Oxide-Metal Transitions probed by operando/in-situ X-ray Absorption Spectroscopy (XAS) and Raman techniques: Case Studies on Cell Reversal Tolerant Pt-Ir catalysts and Cu_xO foams for CO_2RR

Dissertation

To obtain the academic degree

Doctor of Natural Sciences

(Dr. rer. nat.)

submitted to the Department of Chemistry,

Institute of Physical Chemistry,

University of Hamburg

by

Sonja Katharina Blaseio

Dissertation submitted to the University of Hamburg

Hamburg 2025

First Reviewer:	Prof. Dr. Mehtap Oezaslan
Second Reviewer:	Prof. Dr. Katsuyoshi Kakinuma
Thesis Defense Committee:	
	Prof. Dr. Mehtap Oezaslan
	Prof. Dr. Michael Fröba
	Prof. Dr. Alf Mews
Date of Disputation:	05.09.2025
Date of Approval:	15.12.2025

The results presented in this dissertation were obtained from August 2020 until October 2024 supervised by Prof. Dr. Mehtap Oezaslan at the Technical Electrocatalysis Laboratory, Institute of Physical Chemistry, Department of Chemistry, University of Hamburg (until September 2024 located at the Institute of Technical Chemistry, TU Braunschweig).

I. List of Publications

Original Articles

S. Blaseio, C. Dosche, M. Rahaman, K. Kiran, A. Dworzak, B. Mahrt, P. Broekmann, A. Dutta and M. Oezaslan, Impact of Cu^{+} and Cu^{2+} species on the oxide-metal transition processes of Cu_xO foams during the CO_2RR probed by operando Quick-XAS, *J. Mater. Chem. A*, 2024, **12**, 28177–28192.

S. Ibrahim, D. Crespo, **S. Blaseio**, A. Hockmann, G. Hilt and M. Oezaslan, Nanoporous Copper for the Electrosynthesis of Cyclic Carbonates from CO_2 and Epoxides, *ChemElectroChem*, 2024, **11**, e202400098.

M. Janssen, J. Klein, A. Dworzak, **S. Blaseio** and M. Oezaslan, Insights into the Structure - Composition - Activity Relationship of PtCo Alloy Nanoparticles towards Oxygen Reduction Reaction (ORR), *ECS Trans.*, 2023, **111**, 3–15.

J. K. Mathiesen, J. Quinson, **S. Blaseio**, E. T. S. Kjær, A. Dworzak, S. R. Cooper, J. K. Pedersen, B. Wang, F. Bizzotto, J. Schröder, T. L. Kinnibrugh, S. B. Simonsen, L. Theil Kuhn, J. J. K. Kirkensgaard, J. Rossmeisl, M. Oezaslan, M. Arenz and K. M. Ø. Jensen, Chemical Insights into the Formation of Colloidal Iridium Nanoparticles from In Situ X-ray Total Scattering: Influence of Precursors and Cations on the Reaction Pathway, *J. Am. Chem. Soc.*, 2023, **145**, 1769–1782.

W. J. Tipping, L. T. Wilson, **S. K. Blaseio**, N. C. O. Tomkinson, K. Faulds and D. Graham, Ratiometric sensing of fluoride ions using Raman spectroscopy, *Chem. Commun.*, 2020, **56**, 14463–14466.

Conference Contributions

Oral presentations

S. Blaseio, A. Dutta, C. Dosche, M. Rahaman, K. Kiran, A. Dworzak, B. Mahrt, P. Broekmann, M. Oezaslan; Oxide-Metal Transition Processes of Cu_xO Foams during CO_2RR probed by operando Quick-XAS, ECS PRiME, Honolulu/US, 2024.

S. Blaseio, G. Ioselli, P. Seidel, J. Klein, Q. Guo, H. Valle Casara and M. Oezaslan; Mechanistic Insights into the Bifunctionality of Cell-Reversal Tolerant Pt-Ir Alloy Catalysts during HOR and OER Using Operando Quick-XANES, ECS PRiME, Honolulu/US, 2024.

S. Blaseio, A. Dutta, C. Dosche, M. Rahaman, K. Kiran, A. Dworzak, B. Mahrt, P. Broekmann, M. Oezaslan; Understanding the oxide-metal transition of Cu_xO foams during CO_2RR; Small Molecule Activation Workshop, Berlin/DE, 2024.

Poster Presentations

S. Blaseio, A. Dutta, C. Dosche, M. Rahaman, K. Kiran, A. Dworzak, B. Mahrt, P. Broekmann, M. Oezaslan; Oxide-Metal Transition Processes of Cu_xO Foams during CO_2RR probed by *operando* Quick-XAS, Electrochemistry 2024, Braunschweig/DE, 2024.

S. Blaseio, G. Ioselli, P. Seidel, J. Klein, Q. Guo, H. Valle Casara and M. Oezaslan; Mechanistic Insights into the Bifunctionality of Cell-Reversal Tolerant Pt-Ir Alloy Catalysts during HOR and OER Using Operando Quick-XANES, Electrochemistry 2024, Braunschweig/DE, 2024.

S. Blaseio, A. Dutta, C. Dosche, M. Rahaman, K. Kiran, A. Dworzak, B. Mahrt, P. Broekmann, M. Oezaslan; Understanding the oxide-metal transition of Cu_xO foams during CO_2RR; IUPAC Congress, Den Haag/NL, 2023.

S. Blaseio, A. Dutta, M. Rahaman, K. Kiran, A. Dworzak, B. Mahrt, P. Broekmann, M. Oezaslan; Investigating transition processes of Cu/Cu-oxide foams during CO_2RR by operando Quick-X-ray Absorption Spectroscopy (Quick-XAS), SNI2022, Berlin/DE, 2022.

S. Blaseio, M. Oezaslan; Operando Quick-X-ray Absorption Spectroscopy (XAS) Investigation on Cu/Cu oxide foams during CO_2RR; 55. Jahrestreffen Deutscher Katalytiker, Weimar/DE, 2022.

II. Contents

I. List of Publications iii
II. Contents v
III. List of Abbreviations viii
IV. List of Symbols x
V. Zusammenfassung xi
VI. Abstract xiv
1. Introduction 16
1.1. General Research Goals and Motivation 16
1.2. Proton-Exchange Membrane Fuel Cell (PEMFC) 19
1.2.1. Hydrogen Starvation and Mitigation Strategies 21
1.2.2. Unitized Regenerative Fuel Cell 25
1.2.3. Hydrogen Oxidation and Evolution Reactions (HER/HOR) on Platinum 28
1.2.4. Oxygen Reduction Reaction (ORR) on Platinum 30
1.2.5. Oxygen Evolution Reaction (OER) on Iridium oxide (IrO_x) 31
1.3. Electrochemical CO_2 Reduction 36
1.3.1. Nanostructured and oxide-derived Cu-based materials 39
1.3.2. Reduction of Cu_2O and CuO during CO_2RR 40
1.3.3. Influence of the Electrochemical Protocol on the Reduction of Cu_xO 42
2. Research Objectives 43
3. Experimental Methods 45
3.1. Ex-situ Characterization 45
3.1.1. Transmission electron microscopy (TEM) and Energy dispersive X-ray spectroscopy (EDX) of Pt-Ir NPs 45
3.1.2. Scanning electron microscopy (SEM) 45
3.1.3. X-ray Diffraction (XRD) 45
3.1.4. µ-X-ray Fluorescence (µ-XRF) 46
3.1.5. X-ray Photoelectron Spectroscopy (XPS) and Auger 46
3.1.6. Raman Spectroscopy of Cu_xO foams 47
3.2. X-ray Absorption Spectroscopy (XAS) 48
3.2.1. Set-up of the electrochemical XAS flow-cell 49
3.2.2. XAS Data Acquisition in the case studies 51
3.2.3. XAS Data Processing, Analysis and Interpretation 52
3.2.4. Multivariate Curve Resolution – Alternating Least Squares (MCR-ALS) Analysis 57

3.3. Raman Spectroscopy 59

3.3.1. The Raman Scattering Process 59

3.3.2. Molecular vibrations 60

3.3.3. Surface Enhanced Raman Spectroscopy (SERS) 61

3.3.4. Set-up of a Confocal Raman Microscope 61

3.3.5. Design and set-up of the spectro-electrochemical Raman Cell 62

3.3.6. In-situ Raman Data Collection of the Pt-Ir, Pt and Ir thin films 64

4. Results and Discussion 65

4.1. Mechanistic Insights into the HER-OER Bifunctionality of Cell-Reversal Tolerant Pt-Ir NPs using operando Quick-XANES 65

4.1.1. Initial structure of the as-prepared Pt-Ir nanoparticles 66

4.1.2. Bifunctionality of PtIr NPs towards HOR and OER 68

4.1.3. *Operando* Quick-XANES potential jump experiments between HER and OER 69

4.1.4. *Operando* Quick-XANES potential jump experiments between HER and OER with reduced Ir content 76

4.1.5. *Operando* Quick-XANES potential jump experiments between HER and OER with monometallic Pt and Ir NPs 79

4.1.6. Discussion 83

4.2. Bimetallic Pt-Ir Oxide Surfaces under Oxygen Reduction/ Evolution Reactions (ORR/OER) using in-situ Raman spectroscopy and DFT 89

4.2.1. Morphology and structure of the bimetallic Pt-Ir thin films 90

4.2.2. Activities of the Pt-Ir, Pt and Ir thin films towards ORR and OER 92

4.2.3. In-situ Raman spectroscopy of Pt-Ir, Ir and Pt thin films 93

4.2.4. DFT Calculations of Ir, Pt and Pt-Ir model structures 103

4.2.5. Discussion 107

4.3. Impact of Cu^{+} and Cu^{2+} species on the oxide-metal transition processes of Cu_xO foams during the CO_2RR probed by *operando* Quick-XAS 112

4.3.1. Ex-situ Characterization of the Annealed Cu_xO foams 113

4.3.2. CO_2 Electrolysis Product Distribution 116

4.3.3. Potential Increment Experiments (ΔE = 100 mV) from + 0.4 V_{RHE} to – 1.2 V_{RHE} 117

4.3.4. Potential Step Experiments (ΔE > 100 mV) 121

4.3.5. Potential Jump Experiments ($\Delta E \geq$ 500 mV) 124

4.3.6. Discussion 128

5. Conclusions 133

6. Outlook 137

7. References 140

8. List of Figures 157

9. List of Tables 163
10. Appendix 164
10.1. Supporting Information Chapter 4.1. 164
10.2. Supporting Information Chapter 4.2. 189
10.3. Supporting Information Chapter 4.3. 213
11. Hazardous Materials 240
11.1. Hazardous Statements 242
11.2. Precautionary Statements 243
12. Acknowledgements 245
13. Declaration on oath 246

III. List of Abbreviations

AEM	Adsorbed evolution mechanism
CCD	Charge-coupled device
CCS	Carbon capture and storage
CE	Counter electrode
CG	Constant gas
CL	Catalyst layer
CO_2RR	CO_2 reduction reaction
CO_2R	CO_2 reduction
COR	Carbon oxidation reaction
CPET	Concerted proton–electron transfer
CR	Cell reversal
DFT	Density functional theory
ECSA	Electrochemically active surface area
EXAFS	Extended X-ray absorption fine structure
FT	Fourier transformation
GDL	Gas diffusion layer
HER	Hydrogen evolution reaction
HOR	Hydrogen oxidation reaction
H_{UPD}	Hydrogen underpotential deposition
LCF	Linear combination fit
LOM	Lattice oxygen participating mechanism
MA	Mass activity
MEA	Membrane electrode assembly
MCR-ALS	Multivariate curve resolution-alternating least squares
NA	Numerical aperture
NP	Nanoparticle
OCP	Open circuit potential
OER	Oxygen evolution reaction
ORR	Oxygen reduction reaction
PEM	Proton-exchange membrane
PEMFC	Proton-exchange membrane fuel cell
PFSA	Perfluorosulfonic acid
PTFE	Polytetrafluoroethylene
RE	Reference electrode
RDE	Rotating disk electrode
rds	Rate determining step
SA	Specific activity
SERS	Surface enhanced Raman spectroscopy
SUSD	Start up shut down
URFC	Unitized regenerative fuel cell

WE	Working electrode
XANES	X-ray absorption near edge structure
XAS	X-ray Absorption Spectroscopy
XPS	X-ray photoelectron spectroscopy
XRD	X-ray diffraction

IV. List of Symbols

Symbol		Unit
α	polarizability	$C \cdot m^2 \cdot V^{-1}$
C	Product matrix containing concentration profile	-
$\boldsymbol{\chi}$	EXAFS oscillations	-
$\tilde{\boldsymbol{\chi}}(\boldsymbol{r})$	Pseudo radial distribution function	$Å^{-3}$
d	distance	m
D	Data matrix	-
E_0	Binding energy	eV
E	Matrix of noise in the data set	-
$F(k)$	Backscattering amplitude of an atom	m
$\hbar$	Planck's constant ($6.62607015 \times 10^{-34}$)	J s
I	Intensity	$W \cdot m^{-2}$
k	Photo-electron wavenumber	m^{-1}
λ	wavelength	m
lof	Lack of fit	%
m	mass	g
φ	Phase shift	°
μ	linear absorption coefficient	m^{-1}
μ_{IND}	Induced dipole moment	C m
N	Number	-
ν	frequency	Hz
π	Pi (3.14159)	-
Q	Vibrational amplitude	m
R^2	Data variance	-
r	distance	m
S_0	Amplitude reduction factor	-
σ^2	Mean-square disorder of neighbor distance	$Å^2$
σ	Debye-Weller-like factor	$Å^2$
S^T	Product matrix containing component spectra	-
θ	Bragg angle	°

V. Zusammenfassung

In Anbetracht des fortschreitenden Klimawandels ist die Entwicklung effizienter elektrochemischer Energiesysteme wie Brennstoffzellen und Elektrolyseure von entscheidender Bedeutung. Ein Schlüsselfaktor, der die Leistung dieser Geräte beeinflusst, ist das aktive Katalysatormaterial. Um diese Elektrokatalysatoren zu verbessern und vollständig zu verstehen, muss die Beziehung zwischen Zusammensetzung/Struktur und Aktivität unter realistischen Betriebsbedingungen bewertet werden. Diese Arbeit konzentriert sich insbesondere auf das Verständnis der Oxid-Metall-Übergangsprozesse von Elektrokatalysatoren in drei Fallstudien unter Verwendung von in-situ/*operando* Raman- und Röntgenabsorptionsspektroskopie (XAS).

In der ersten Fallstudie wird der Übergang der chemischen Zustände von Pt-Ir Nanopartikeln, die durch zwei Synthesewege hergestellt wurden, während der Wasserstoffentwicklungsreaktion (HER) und der Sauerstoffentwicklungsreaktion (OER) untersucht, um die Bedingungen unter Wasserstoffmangel (H_2 starvation) nachzuahmen. Dieser Wasserstoffmangel an der Anode führt zur Korrosion des Kohlenstoffträgermaterials. Eine Möglichkeit, um die Stabilität der Anode zu verbessern ist die Verwendung eines Co-Katalysators wie IrO_x zur Beschleunigung der OER. Zur Nachahmung des Verhaltens unter Wasserstoffmangel, wird innerhalb weniger Sekunden zwischen HER- und OER-Bedingungen gewechselt. Um bifunktionale Eigenschaften, Änderungen des Oxidationszustands der Pt-Ir-Elektrokatalysatoren und elektronische Wechselwirkungen zwischen beiden Metallen zu untersuchen wird zeitaufgelöste *operando* Quick-XAS eingesetzt. Unsere Ergebnisse zeigen, dass sich während der HER bei allen Katalysatoren in kurzer Zeit metallisches Pt bildet, unabhängig von der Haltezeit und dem Pt:Ir-Verhältnis. Im Gegensatz dazu erfolgt die entsprechende Oxidation zu Pt^{2+}-Spezies bei + 1.55 V_{RHE} (OER) mit einer deutlich verzögerten Rate. Interessant ist, dass das Verhalten von Ir während HER und OER stark von der Kristallinität der Pt-Ir NPs abhängt. Kleinere, amorphe Pt-Ir NPs bestehen, während OER hauptsächlich aus Ir^{4+}-Spezies, die während HER reversibel und teilweise zu Ir^{3+}-Spezies reduziert werden. Es wurde eine schnelle Oxidationskinetik von Ir^{3+} zu Ir^{4+} bei + 1.55 V_{RHE} im Vergleich zum entsprechenden Reduktionsübergang bei – 0.02 V_{RHE} festgestellt. Kristallinere und größere Pt-Ir NPs zeigen sehr langsame Oxidationsprozesse von Ir^0 und Ir^{3+} zu Ir^{4+} Spezies während der OER. Darüber hinaus zeigt diese Fallstudie den Einfluss von elektronischen Effekten zwischen Pt und Ir während der elektrochemischen Reaktionen.

In der zweiten Fallstudie werden Pt-Ir-Dünnschichten, als bifunktionale Modellkatalysatorsysteme für die Sauerstoffreaktionen in regenerativen Brennstoffzellen untersucht. Die verwendete Raman-Spektroskopie ist eine vielseitige Technik zur in-situ-Messung der potenzialaufgelösten elektronischen und strukturellen Wechselwirkungen von Pt und Ir in den gesputterten bimetallischen PtIr- und Pt_3Ir-Dünnschichten, die als Modellkatalysatorsystem für die ORR/OER fungieren. Darüber hinaus wurde die Dichtefunktionaltheorie (DFT) angewandt, um Modelle von tetrameren Iridium-, Platin- und Platin-Iridium-Oxo-Hydroxy-Komplexen zu erstellen und ihre jeweiligen Raman-Spektren zu berechnen. Während der ORR bildet sich ein amorphes bimetallisches Pt-Ir-Oxid auf der Oberfläche der Dünnschichten. Zwischen 1.4 und 1.5 V_{RHE} deuten die beobachteten Veränderungen in den Raman-Spektren auf eine weitere elektrochemische Oberflächenoxidation der Pt-Ir-Filme hin, die sich deutlich von dem Verhalten der reinen gesputterten Ir- und Pt-Dünnschichten unterscheidet. Bei Potentialen kurz vor und während der OER weisen die DFT-Berechnungen auf die Bildung von wasserhaltigen PtO_6-IrO_6-Ketten hin, die über ihre Kanten miteinander verbunden sind. Die Pt- und Ir-Zentren sind durch μ-Oxo-Sauerstoffbindungen verbunden, die es den Pt- und Ir-Zentren ermöglichen, elektronisch in Wechselwirkungen zu stehen. Die theoretischen Streck- und Deformationsschwingungen dieser Pt-O-Ir-Bindungen sind die intensivsten Schwingungen und stehen in guter Übereinstimmung mit den beobachteten Raman-Banden. Der Vergleich zwischen den experimentellen Raman-Banden für die symmetrische Streckschwingung von Ir-O-Pt und Ir-O-Ir zeigt eine deutliche Rotverschiebung um 38 cm^{-1} während der OER, was sich durch die DFT-Berechnungen bestätigen lässt. Diese Rotverschiebung ist wahrscheinlich auf Veränderungen der Elektronendichteverteilung, der Polarität und der Bindungslänge von Ir-O-Pt zurückzuführen.

Im dritten Teil der Arbeit werden dynamische und zeitaufgelöste Oxid-Metall-Übergänge von Cu_xO-Schäumen für die CO_2-Reduktionsreaktion mittels *operando* Quick-XAS untersucht. Die Cu_xO-Schäume wurden durch thermisches Behandeln von galvanisch abgeschiedenem Cu zwischen 100 und 450 °C in Sauerstoffatmosphäre hergestellt, um das Cu^0:Cu^+:Cu^{2+}-Verhältnis und insbesondere die Kristallinität von CuO zu variieren. Mit diesen unterschiedlichen chemischen Zuständen und Strukturen wurde die Kinetik des Oxid-Metall-Übergangs während verschiedener kathodischer Protokolle „potential increment“ ($\Delta E = 100$ mV), „steps“ ($\Delta E > 100$ mV) und „jumps“ ($\Delta E > 500$ mV) mittels Quick-XAS umfassend untersucht. Unsere Ergebnisse zeigen, dass die Kinetik des Oxid-Metall-Übergangs stark von der anfänglichen Konzentration der Cu^{2+}-Spezies und dessen Struktur (geordnet oder amorph) sowie von der Art des chronoamperometrischen Experiments abhängt. Ein anfänglich hoher Anteil an kristalliner

CuO-Spezies führt im Vergleich zu amorphem CuO zu einer signifikanten Verschiebung des Oxid-Metall-Übergangspotenzials zu niedrigeren kathodischen Werten, was auf eine niedrigere Energiebarriere für die Reduktion hindeutet. Darüber hinaus zeigte diese Fallstudie, dass die verschiedenen chronoamperometrischen Experimente die elektrochemische Stabilität der Cu^{+}-Spezies in den Cu_xO-Schäumen während der CO_2-Elektrolyse stark beeinflussen. Kleinere Potenzialstufen erhöhen die Bildung von Cu^{+}-Spezies und führen zu einer verlangsamten Reduktionskinetik.

Auf der Grundlage dieser Fallstudien werden grundlegende Einblicke in die Oxid-Metall-Übergangsprozesse und die Beziehung zwischen Struktur/Zusammensetzung und Reaktivität von drei verschiedenen Elektrokatalysatoren für Brennstoffzellenanwendungen und CO_2-Elektrolyse gewonnen, was zur Entwicklung neuer aktiver Elektrokatalysatormaterialien beiträgt.

VI. Abstract

In consideration of the climate change, the development of efficient electrochemical energy conversion devices, such as fuel cells and electrolyzers is essential. A key factor influencing the performance of these devices is the active catalyst material. In order to improve and fully understand these electrocatalysts under working conditions, the composition/structure – activity relationship needs to be evaluated under realistic operating conditions. In particular, this thesis focusses on understanding oxide-metal transition processes of electrocatalysts in three case studies using in-situ/*operando* Raman and X-ray absorption spectroscopy (XAS) techniques.

In the first case study, the transition of the chemical states for cell reversal tolerant Pt-Ir NPs prepared by two synthesis routes are evaluated during the hydrogen evolution reaction (HER) and oxygen evolution reaction (OER) to mimic the conditions under fuel starvation. Hydrogen starvation at the anode causes the oxidation of the carbon support. Thus, one mitigation strategy is the utilization of a co-catalyst such as IrO_x to accelerate the OER. To mimic these conditions, time-resolved *operando* Quick-XAS is employed to study bifunctional properties, changes in oxidation state of the Pt-Ir electrocatalysts and electronic interactions between both metals, while switching between HER and OER conditions within a few seconds. Our results show that during HER metallic Pt is rapidly formed for all catalysts independent of the holding time and Pt:Ir ratio. In contrast, the respective oxidation to Pt^{2+} species at + 1.55 V_{RHE} (OER) occurs at a much slower rate. Very interestingly, the behavior of Ir during HER and OER is strongly dependent on the crystallinity of the Pt-Ir NPs. Smaller, amorphous Pt-Ir NPs consist of mostly Ir^{4+} species during OER, which are reversibly and partially reduced to Ir^{3+} species during HER. Rapid Ir^{3+} to Ir^{4+} oxidation kinetics at + 1.55 V_{RHE} compared to the respective reduction transition at – 0.02 V_{RHE} were found. More crystalline and larger Pt-Ir NPs exhibit very sluggish oxidation processes of Ir^0 and Ir^{3+} to Ir^{4+} species during OER. In addition, this case study reveals the influence of electronic effects between Pt and Ir during the electrochemical reactions.

In the second case study, Pt-Ir thin films prepared by magnetron sputtering are investigated as bifunctional model catalyst systems for the oxygen reactions in unitized regenerative fuel cells. Raman spectroscopy is a powerful technique to monitor in-situ the potential-resolved electronic and structural interactions of Pt and Ir in the sputtered bimetallic PtIr and Pt_3Ir thin films as model catalyst system for the oxygen reduction reaction (ORR) and OER. In addition, density functional theory (DFT) was applied to construct models of tetrameric iridium, platinum and platinum-iridium oxo-hydroxy complexes and calculate their respective Raman spectra. During the ORR, an amorphous bimetallic Pt-Ir oxide forms on the surface of the thin films. Between

1.4 and 1.5 V_{RHE} the observed changes in the Raman spectra signify the further electrochemical surface oxidation of Pt-Ir films, which clearly differs from the behavior of the pure sputtered Ir and Pt thin films. At potentials just before and during OER, the DFT calculations indicate the formation of hydrous PtO_6-IrO_6 edge-sharing chains. The Pt and Ir centers are connected by μ-oxo oxygen bond linkages, allowing the Pt and Ir centers to electronically couple to each other. The theoretical stretching and bending motions of these Pt-O-Ir bonds are the most intense vibrations and are in very good agreement with the observed Raman bands. Very remarkably, the comparison between the experimental Raman bands for symmetric stretching of Ir-O-Pt and Ir-O-Ir shows a clear red shift by 38 cm^{-1} during the OER, which is also confirmed by the DFT calculations. This red shift is most likely based on changes in electron density distribution, polarity and bond length of the Ir-O-Pt.

In the third part of the thesis, dynamic and time-resolved oxide-metal transitions of Cu_xO foam precursor catalysts for the CO_2 reduction reaction are studied by *operando* Quick-XAS. The Cu_xO foams were prepared by thermal annealing of electrodeposited Cu between 100 and 450 °C in air to vary the Cu^0:Cu^+:Cu^{2+} ratio and especially the crystallinity of CuO. With these different chemical states and structures, the oxide-metal transition kinetics during cathodic potential increment ($\Delta E = 100$ mV), step ($\Delta E > 100$ mV), and jump ($\Delta E > 500$ mV) experiments were comprehensively investigated using Quick-XAS. First, our results demonstrate that the oxide-metal transition kinetics strongly depend on the initial abundance of Cu^{2+} species and precursor structure (ordered vs. amorphous) as well as on the type of chronoamperometric experiment. More precisely, compared to amorphous CuO, a high initial population of crystalline CuO species leads to a significant shift of the *oxide-metal transition potential* towards lower cathodic values, signifying a lower energy barrier to reduction. In addition, this case study revealed that the different chronoamperometric experiments strongly influence the electrochemical stability of Cu^+ species within the Cu_xO foams during CO_2 electrolysis. Smaller potential steps increase the formation of Cu^+ species and lead to a slowdown in the reduction kinetics.

Based on these case studies fundamental insights into the oxide-metal transition processes and structure/composition – reactivity relationship of three different electrocatalysts for fuel cell applications and CO_2 electrolysis were obtained, aiding to the development of new active electrocatalyst materials.

1. Introduction

1.1. General Research Goals and Motivation

In consideration of the still progressing climate change and ambitious 'amended Federal Climate Protection Act', stating that Germany has to achieve greenhouse gas neutrality until 2045, there is an increasing demand for carbon neutral electricity production, transport and direct utilization of CO_2 into valuable products such as hydrocarbons as fuels and/or basic chemicals.[1,2] In 2021, worldwide the highest carbon dioxide (CO_2) emissions originated from electricity and heat (16.30 billion t) followed by transport (7.84 billion t) and manufacturing (6.38 billion tons), indicating the demand for carbon neutral alternatives in the near-future.[3] For the energy transformation, hydrogen (H_2) can play an important role in energy storage, as fuel in the transport or feedstock in the industrial sector for e.g. ammonia synthesis or steel production. Therefore, in Germany the 'National Hydrogen Strategy' was established in 2020, setting out a framework for the generation, transport and use of H_2 enabling the relevant innovations and investments that are needed to meet the climate targets.[4] The main goals of the strategy are making hydrogen a competitive option, developing a domestic market for hydrogen technology in Germany and paving the way for imports.[4] In 2023, the strategy was revised and specific targets for 2030 were established. These include the accelerated market ramp-up of hydrogen, securing the availability of hydrogen, building of a hydrogen infrastructure as well as establishing hydrogen in the heavy duty transport sector, industry, aviation and shipping sectors.[5] In addition, the government's goal is to make Germany the leading provider of hydrogen technologies such as fuel cells and electrolyzers until 2030.[5] All of these are ambitious goals especially since at the beginning of 2024 the capacity of all electrolyzers in Germany was only around 66 MW, which is not even 1 % of the 10 GW goal set to be reached within the next 5 years.[6]

A promising approach for energy storage application of fuel cells is the unitized regenerative fuel cell (URFC).[7] By using excess energy from renewable sources, H_2 and O_2 are produced by water electrolysis and when needed the same device can produce electricity from H_2 and O_2 in a fuel cell. A decoupling of energy storage capacity, high scale-up efficiency, low weight and volume are some of the advantages over the widespread lithium-ion batteries.[7] Poor efficiencies and stability issues, due to harsh operating conditions at the oxygen electrode are some of the challenges that need to be addressed before URFCs become commercially competitive.[7]

In order to meet the climate targets in the traffic and transport sector, the emissions need to decrease by 42 % until 2030 compared to the level in 1990.[8] Furthermore, in the last ten years less than 1.000 fuel cell cars and in 2024 only a third of the newly registered cars in Germany

(381.000) were battery electric cars, showing that further action is needed in the development of emission-free vehicles.[4,5,9–11] Proton exchange membrane fuel cells (PEMFCs) have several advantages for the use in vehicles such as hydrogen having a very high specific energy, that is three times higher than that of gasoline, while also having a greater efficiency compared to the combustion engine.[12] Compared to battery vehicles, a much faster refueling time, a longer range, improved safety and longer life time of a PEMFC are reasons why the focus of fuel cell powertrains in the transport sector is nowadays more on heavy duty, aviation and shipping applications.[12] However, the still very poor H_2 infrastructure (only 84 H_2 service stations in Germany in February 2025[13]) and thus H_2 availability as well as the higher cost mainly caused by the usage of platinum (Pt) catalysts and low manufacturing quantities are some of the reasons why fuel cells are hardly used in the transportation sector today.[12] In addition, PEMFC degradation during abnormal operating conditions such as fuel starvation or start up and shut down (SUSD) of the fuel cell, but also long-term operation needs to be improved. The main factors affecting the stability of a PEMFC are the chemical degradation of the ionomer membrane, platinum dissolution/redeposition, Pt nanoparticle detachment and coalescence as well as carbon corrosion at the anode and cathode.[14] Hence, more research into the stability of the catalyst material especially under abnormal operating conditions such as hydrogen (fuel) starvation is needed and material design strategies need to be developed to avoid degradation of the catalyst material.

In addition, to the plans of reducing greenhouse gas emissions in the future, the Paris climate agreement also states to remove already emitted carbon dioxide from the atmosphere.[15] This can be done by carbon capture and storage (CCS) followed by converting CO_2 into valuable products by e.g. CO_2 electrolysis.[16] CCS is regarded as a component to achieve negative emissions in the next decades when CO_2 emissions cannot be avoided and need compensation as well as if the target of retaining the global warming to 1.5 °C is failed.[17] In the traditional chemical industry, thermally activated CO_2 hydrogenation using H_2 as a reductant in the reverse water gas shift reaction produces syngas (CO and H_2), when the obtained water is constantly removed. This syngas is then used for several chemical processes such as Fischer-Tropsch, methanol synthesis or methanation.[16] All of these industrial processes run at a very high temperature and pressure requiring a lot of energy input.[16] Thus, the electrochemical CO_2 reduction (CO_2R) commencing at ambient conditions provides an alternative with several advantages such as the combination of water splitting and hydrogenation in a single process, it enables products of higher value that cannot be prepared by the thermal processes and it allows for a quick adaptation of the production to match the overproduction of electricity from

renewable energy sources.[16] However, electrochemical CO_2R technologies need much more work in providing a low-cost and scalable alternative to the thermal processes. Additionally, a fundamental understanding of CO_2R mechanisms and insides into the active catalyst structure, composition, oxidation states and adsorbed intermediates under working conditions (in-situ/*operando*) is required.[16]

In general, in electrocatalysis understanding the structure and composition of the active catalyst species and their reaction mechanisms are crucial for the design of high-performance electrocatalysts for renewable energy technologies such as fuel cells and electrolyzers mentioned above. Therefore, in-situ/*operando* techniques are commonly employed to enhance the knowledge of the active (electro-)catalyst under working/operating conditions. Throughout this thesis the term "in-situ" is defined as the real-time measurement of an (electro)catalyst under the relevant reaction conditions. On the other hand, "*operando*" refers to the measurement of a working (electro)catalyst under the same reaction conditions as those inside a catalytic reactor e.g. an electrochemical cell, electrolyzer or fuel cell. Using *operando* methods minimizes the experimental gap between instrumental requirements and realistic catalytic conditions.[18] The use of in-situ*/operando* techniques has enabled valuable insights into the structure/composition – reactivity relationship under real-time conditions. While many different techniques exist to study electrocatalysts under working conditions, this thesis focusses on the use of Raman and X-ray absorption spectroscopies (XAS) to study electrocatalysts for the use in PEMFCs and CO_2 electrolysis. In particular, oxide-metal transition processes of PEMFC anode, URFC oxygen electrode as well as CO_2 electrolysis catalyst materials were investigated in *operando* and in-situ in three case studies.

1.2. Proton-Exchange Membrane Fuel Cell (PEMFC)

In a fuel cell chemical energy from hydrogen is converted to electric energy. The most promising type of fuel cell is the proton-exchange membrane fuel cell (PEMFC). A schematic drawing of a PEMFC is shown in **Figure 1**. Overall, in PEMFCs hydrogen (H_2) and oxygen (O_2) are converted into water:

$$2\,H_2 + O_2 \rightarrow 2\,H_2O \tag{1}$$

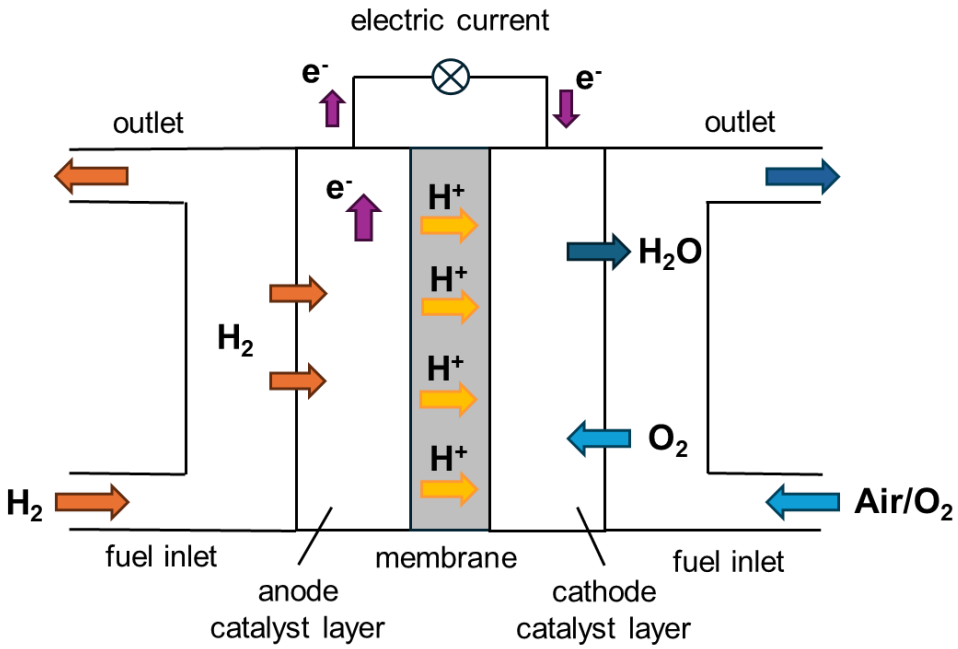

Figure 1. Schematic drawing of a PEMFC.

This overall reaction is split into two half-cell reactions, which are separated by a proton-conducting membrane. At the anode the hydrogen oxidation reaction (HOR) takes place

$$2\,H_2 \rightarrow 4\,H^+ + 4\,e^- \,. \tag{2}$$

The produced protons diffuse to the cathode through a conductive membrane where they react with O_2 to water in the oxygen reduction reaction (ORR):

$$O_2 + 4\,H^+ + 4\,e^- \rightarrow 2\,H_2O \tag{3}$$

In the following section the components of a PEMFC with their respective functions are briefly outlined. In principle, PEMFCs consist of bipolar plates, gas diffusion layers (GDLs), catalyst layers (CLs) at the anode and cathode as well as the proton-exchange membrane (PEM) separating the anode and cathode. The bipolar plates provide mechanical support along with H_2 and air supply at the anode and cathode, respectively. The introduced gas is then diffusing

through the GDLs, which consist of 100 – 300 µm thick carbon fibers creating a highly porous structure.[19] The GDLs not only supply the reactant gas, they also provide a passage for water and heat removal, mechanical support for the membrane electrode assembly (MEA), transport of electrons and protection of the catalyst layers from corrosion and mechanical erosion.[19] A schematic of the MEA is displayed in **Figure 2**. It comprises the anode and cathode GDLs and CLs as well as the PEM. After the H_2 diffuses through the anode GDL, the HOR takes place at the so-called triple-phase boundary, where the active catalyst nanoparticles (NPs), reactants and ionomer film meet to form the protons and electrons. While the electrons are transported through an external load, the protons are diffusing through the ionomer film and membrane to the cathode compartment. The protons and oxygen combine to form water at the triple-phase boundary at the cathode side, which is where the ORR reaction takes place. In PEMFCs for both reactions (HOR and ORR) mainly platinum (Pt)-based catalysts are used.[20,21]

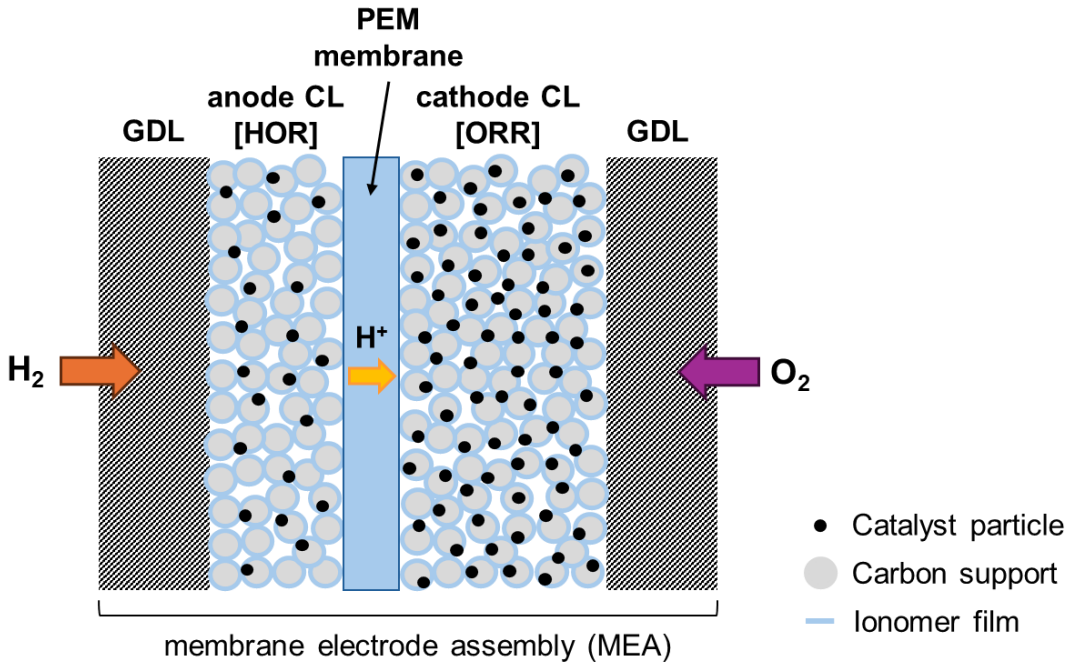

Figure 2. Schematic drawing of a membrane electrode assembly (MEA). The black dots represent the catalyst nanoparticles, grey spheres depict the carbon support, and the light blue lines show the ionomer film inside the catalyst layer, which usually contains the same polymer (Nafion) as the membrane.

The membrane separating anode and cathode is a proton-conductive membrane that consists of a polytetrafluoroethylene (PTFE) backbone with sulfonic acid end-groups (SO_3H) on the side chains, known as perfluorinated sulfonic-acid (PFSA) membranes. These sulfonic acid end-groups are responsible for the proton conductivity of the membrane, while together with the covalently bonded backbone a natural phase separation between backbone and side chains

occurs. This phase separation gives PFSAs their unique ion-transport capabilities. The most commonly used PFSA membrane is Nafion.[22]

***Table 1**. Reaction equations and respective standard potentials for the HOR and ORR.[23]*

	Reaction	**Standard Potential**
anode (HOR)	$2\,H_2 \rightarrow 4\,H^+ + 4\,e^-$	$E_0 = 0$ V
cathode (ORR)	$O_2 + 4\,H^+ + 4\,e^- \rightarrow 2\,H_2O$	$E_0 = 1.23$ V
overall	$2\,H_2 + O_2 \rightarrow 2\,H_2O$	

The total thermodynamic cell voltage of a PEMFC is 1.23 V, combined from the standard potential for the HOR (0 V) and ORR (1.23 V) as tabulated in the electrochemical series (**Table 1**).[23] However, voltage losses in PEMFCs due to overpotentials caused by slow reaction rates and mass transfer limitations result in a lower voltage compared to the thermodynamically predicted value. These overpotentials mainly occur from the cathode, where the sluggish ORR takes place. Therefore, the cathode catalyst loading is usually 6 – 8-times higher compared to the anode loading.[24,25] Since, both cathode and anode catalysts are commonly containing platinum NPs supported on carbon that are scarce and costly, it is necessary to further reduce the platinum loading especially at the cathode. Highly active ORR catalysts are required to maintain sufficient ORR activity and durability during PEMFC operation. However, also at the anode degradation of the catalyst occurs especially during abnormal working conditions such as startup/shutdown (SUSD) or fuel starvation. Fuel starvation is most problematic at the anode, as the fuel cell voltage reverses causing a fast degradation of the catalyst layer. The conditions and consequences of hydrogen (H_2) starvation are outlined in detail in the following section.

1.2.1. Hydrogen Starvation and Mitigation Strategies

One of the major challenges for PEMFC applications remains global and/or local hydrogen starvation. Insufficient supply of H_2 or nonuniform gas distribution causes major damage to the system.[26,27] Several causes for H_2 starvation are proposed in the literature, for example insufficient fuel supply, blocked flow field channels by water or ice, blocked pathways in the GDLs and the catalyst pores as well as abnormal operating conditions such as SUSD processes.[28,29] During normal fuel cell operation voltages are typically in the range of 0.5 – 1.0 V_{RHE}, while H_2 starvation results in a rapid (several milliseconds to few seconds) increases in voltage above 1.4 V_{RHE} at the anode (**Figure 3**).[30,31] This abnormal decrease in cell potential is known as cell reversal (CR).

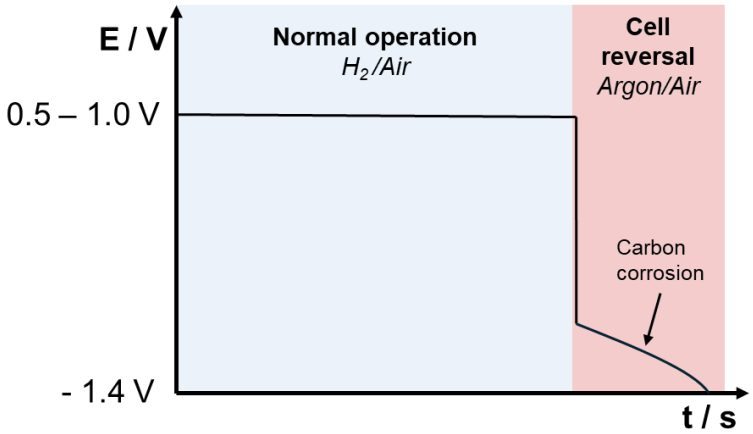

Figure 3. Schematic fuel cell voltage changes with time under normal operation and hydrogen starvation/cell reversal.

To continuously provide protons and electrons to the cathode during H_2 starvation, the carbon oxidation reaction (COR) commences as an alternative reaction at the anode:[14]

$$C + 2\,H_2O \rightarrow CO_2 + 4H^+ + 4e^- \,. \qquad (4)$$

As shown in **Figure 4**, during carbon corrosion the carbon of the support material reacts with water to generate CO_2. Consequently, this degradation of the support material results in agglomeration of Pt NPs, electrochemical Ostwald ripening, corrosion of the metal bipolar plates leading to a failure of the fuel cell performance.[28,30,32,33] In addition to the loss of catalyst particles, the carbon oxidation is accompanied by very high overpotentials and energy loss as heat, leading to local membrane damage.[34]

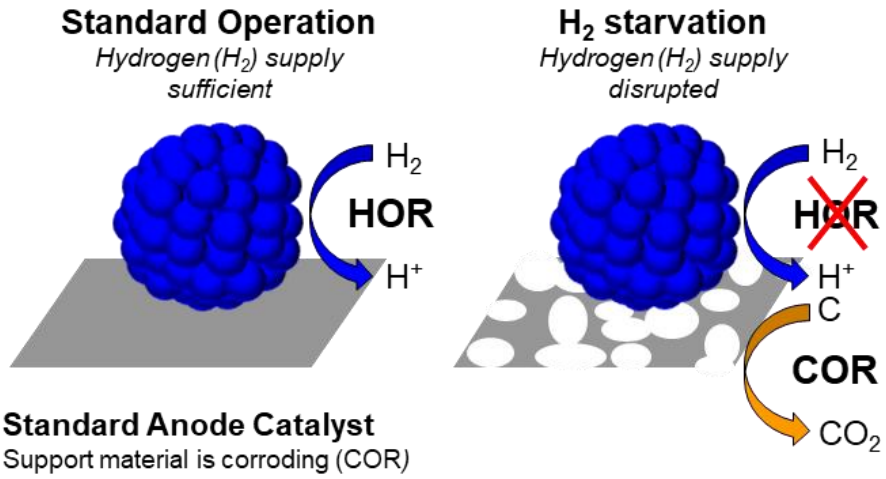

Figure 4. Schematic representation of standard operation at the anode catalyst (**left**) and carbon corrosion occurring as a result of hydrogen starvation (**right**). The blue sphere shows a Pt NP and the grey rectangle the carbon support, that is highly corroded during COR.

To prevent and control fuel starvation, several system mitigation strategies can be employed. These include constantly monitoring the voltage of individual cells and entire stacks as well as analyzing the exhaust gas for CO_2 content.[29] Abnormal cells can then be switched off immediately to prevent severe irreversible damage. However, these system-based strategies are relatively slow and only work for global fuel starvation of the entire anode. Local starvation caused by blocked pathways in the GDLs and the catalyst pores can be as damaging to the CL and long-term durability of the fuel cell, that cannot be mitigated by design strategies.[35]
Therefore, reversal tolerant anode materials have been developed to intrinsically protect the anode catalyst layer from CR events. Several approaches for resistant anode materials exist for example the utilization of more corrosion-resistant support materials[36–38] such as ruthenium-titanium oxides[39] or Nb doped tin oxide[40], support materials with hydrogen spillover effects,[41] or hydrophobic additives[42]. One promising approach is the utilization of a co-catalyst such as IrO_x to accelerate the oxygen evolution reaction (OER) as an alternative source for protons and electrons.[29,31,43,44] The OER also known as water splitting,

$$2\,H_2O \rightarrow O_2 + 4\,H^+ + 4\,e^- \tag{5}$$

is the reverse reaction of the ORR (**Equation (3)**) and thus has the same standard potential (E^0 = 1.23 V).[23] Thermodynamically, the COR could commence at 0.21 V, but significant kinetic barriers of this reaction make carbon corrosion only possible at potentials above 1.0 V_{RHE}.[23,29] Therefore, the OER can compete and commence instead of the COR once a suitable OER catalyst such as IrO_x is incorporated into the CL. As shown in **Figure 5**, the iridium can be (i) physically mixed into the platinum-based catalyst layer as IrO_x, (ii) added to the same carbon support material as Pt NPs or (iii) alloyed with Pt NPs.[45–50]

To date, the most commonly employed strategies for CR tolerant CLs are physical mixing or co-deposition of iridium oxide and platinum. Deposition of Ir or IrO_x NPs on a Pt/C catalyst has been shown to increase the reversal time by 4-fold compared to physical mixing of commercial catalysts, due to the more uniform distribution of the co-deposited iridium in the catalyst layer.[34,51,52] In addition, physical mixing of various iridium oxides with different structures and oxidation states were studied by Marić et al.[53] and Tovini et al.[54] indicating that non-reducible highly crystalline IrO_2 is increasing the reversal tolerance under prolonged PEMFC operating conditions. Even though amorphous iridium oxyhydroxide ($IrO_x(OH)_y$) containing mostly Ir^{3+} species shows initially the highest cell reversal tolerance by a high activity for the OER, it gets reduced to less stable metallic iridium under prolonged exposure to a hydrogen atmosphere in a fuel cell anode.[53] Metallic iridium is generally disfavored as it is

less stable, easier dissolved from the electrode, not very active for the OER and can even crossover to the cathode compartment.[54] Thus, the oxidation state, structure and stability of the iridium (oxide) play a critical role in the cell reversal tolerance.

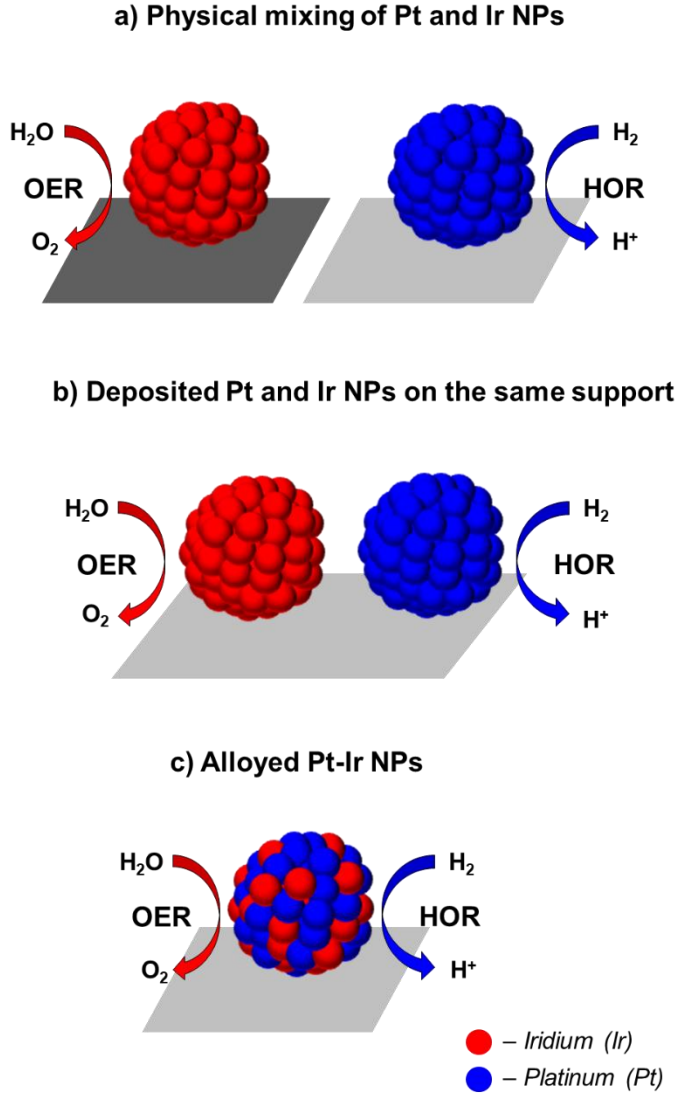

Figure 5. Schematic representation of the incorporation of an iridium co-catalyst into the anode catalyst layer by (**a**) physical mixing, (**b**) addition to the same support and (**c**) alloying with Pt NPs.

Besides the changes in chemical state of iridium, the platinum oxidation state alters significantly between normal operation under hydrogen atmosphere and the cell reversal that is accompanied by a rapid increase in cell potential. Several experimental studies suggest a transition from pure metallic Pt to amorphous platinum oxide is commencing from around 0.7 V_{RHE}.[55,56] As outlined by studies using XPS and EXAFS analysis, prolonged exposure (>10 min) to potentials higher than 1.25 V_{RHE} results in the formation of PtO_2.[57,58] Especially under extended cell reversal times, strong surface oxidation of the platinum takes place.[51,59] Upon returning to normal cell operation, platinum oxide is reduced back to the metallic state. These oxide-metal phase

transitions were shown for example by Fuchs et al.[60], Martens et al.[61] or Ehelebe et al.[62] to enhance platinum dissolution.

Bimetallic Pt-Ir alloys have not been studied extensively under HOR or OER conditions. Zhang et al. observed, that Pt-Ir alloy NPs show an increase in OER performance with increasing amounts of IrO_x surface species formed during the reaction.[45] Additionally, the study indicates that surface alloying effects of Pt and Ir change the rate determining step for the OER from the adsorption of hydroxyl groups to the dissociation of water, which was explained by a partial electron transfer from Ir onto Pt.[45] On the other hand, Ioroi et al.[49] and Bhuvanendran et al.[63] found a positive shift in Pt 4f and negative shift in Ir 4f binding energies for the Pt-Ir alloy compared to the respective monometallic Pt and Ir. In both studies this was attributed to an interatomic charge transfer from Pt to Ir within the Pt-Ir alloy.[49,63] These findings illustrate that the electronic interactions between Pt and Ir especially within Pt-Ir alloys are still under discussion in literature.

Although many studies demonstrate an increase in cell reversal tolerance by employing an iridium based co-catalyst,[27,29,34,43,51–54,64,65] no *operando* spectroscopic studies have so far been conducted to understand the surface oxidation states and electron transfer processes especially between the two metals and metal oxides within alloyed Pt-Ir NPs during the HOR and OER reactions.

1.2.2. Unitized Regenerative Fuel Cell

Another application of bifunctional Pt-Ir catalysts is the use in a Unitized Regenerative Fuel Cell (URFC). The URFC combines a water electrolyzer and fuel cell in one device to form a combined hydrogen battery system. There are two operating modes for URFCs. The constant electrode mode is capable of higher efficiencies with the downside of lower lifetimes as the electrodes are exposed to larger potential ranges and risk of hydrogen and oxygen mixing.[66] The second configuration is the constant gas (CG) mode, that allows fast switching between fuel cell and electrolyzer as well as longer life times.[67] A schematic of a URFC in the CG mode is displayed in **Figure 6** and comprises of a H_2 electrode at which the hydrogen evolution reaction (HER) and HOR takes place. At the other electrode the oxygen reactions (OER/ORR) commence. In fuel cell mode the HOR and ORR reactions occur as outlined above for the PEMFC, while in water electrolysis mode, hydrogen and oxygen are produced for storage.

For the H_2 electrode Pt-based PEMFC catalysts can be employed as both the HER and HOR are catalyzed by platinum. [20,21] The oxygen electrode is more complex, since platinum only catalyzes the ORR sufficiently, while its activity for the water splitting reaction is limited.[68]

Thus, a bifunctional ORR/OER catalyst is required at the oxygen electrode. As iridium oxide is one of the most active OER catalysts in acidic environment, it is incorporated into the catalyst layer of the oxygen electrode.[45–49,69–71]

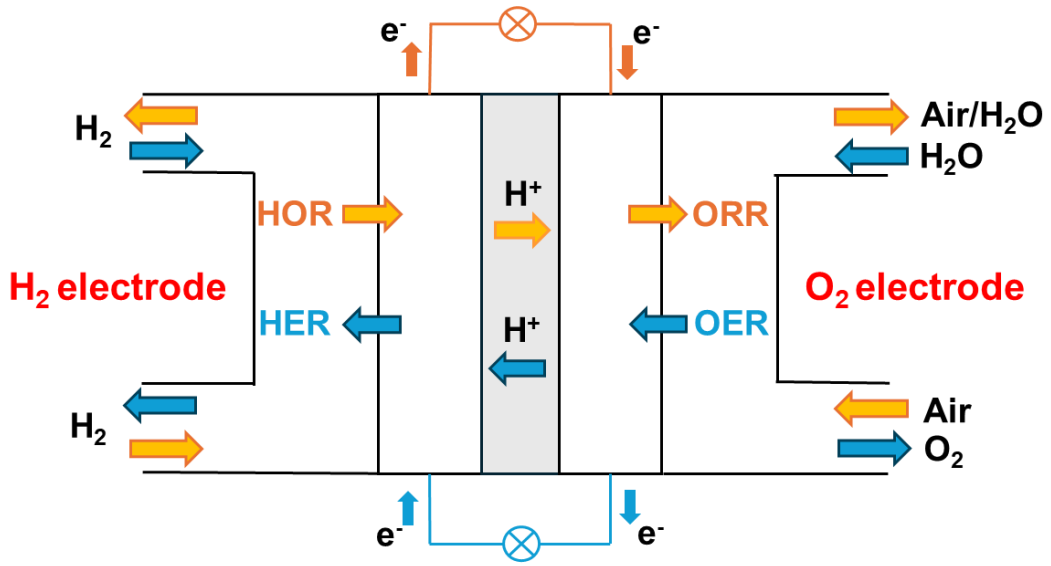

HOR/HER: $2\,H_2 \rightleftharpoons 4\,H^+ + 4\,e^-$ (E_0 = 0 V)

ORR/OER: $O_2 + 4\,H^+ + 4\,e^- \rightleftharpoons 2\,H_2O$ (E_0 = 1.23 V)

Figure 6. Schematic drawing of a URFC in constant gas (CG) mode with the HOR/HER and ORR/OER reaction equations and respective standard potentials.

To incorporate iridium into the electrode the same design strategies as outlined in **Figure 5** can be employed. Initially electrodes made from basic mixtures of Pt black and Ir black or IrO_2 were investigated, showing improved OER activity and degraded ORR performance compared to pure Pt electrodes due to the added iridium.[47,49] Several studies using Ir and Pt layers show the same results, an enhanced OER performance with increased Ir content, while the ORR performance is decreasing.[69,72] Depositing platinum on iridium or iridium oxide shows a slightly different behavior.[50,73] Wesselmark et al. found that an irreversible formation of hydrous IrO_x increases the ORR activity and stabilizes the platinum, due to a better wetting of the electrode.[73] On the other hand Da Silva et al. showed that Pt deposited on crystalline IrO_2 exhibited better ORR performance compared to deposited on hydrous IrO_x.[50] However, no conclusions on the reasoning were made. [50] Generally, this study on the stability of the electrode found that dissolution of Ir occurs mostly in the OER region, while Pt dissolution is highest when cycling through both the ORR and OER regions.[50] This indicates that for platinum oxide-metal transitions enhance the dissolution of platinum significantly between ORR and OER conditions, demonstrating that this transition is not only relevant for the stability of bifunctional

cell reversal tolerant anode catalysts (HOR/OER), but also for oxygen electrode catalysts. Furthermore, Pt-Ir alloys have been studied more extensively for the ORR/OER bifunctionality of the oxygen electrode in the URFC. Du et al. observed a decrease in ORR and increase in OER performance with increased Ir content similar to the studies using physically mixed Pt and Ir.[46] However, the OER activity was always lower compared to iridium oxide (IrO_x) catalysts and severe degradation during accelerated stress tests occurred.[46] In contrast, Zhang et al. observed that for all Ir concentrations of Pt-Ir alloy NPs an increase in OER performance compared to monometallic Ir occurs.[45] Additionally, the study indicates that surface alloying effects of Pt and Ir change the rate determining step for the OER from the adsorption of hydroxyl groups to the dissociation of water, which was explained by a partial electron transfer from iridium to platinum.[45] This suggests that in a Pt-Ir alloy Ir is more oxidized compared to Pt. On the other hand, Ioroi et al. demonstrate that the ORR activity of PtIr alloy NPs increases with 5 – 20 % iridium in the alloy.[49] At higher Ir concentrations the activity decreases again, which is explained by the strong influence of Ir-OH surface groups on neighboring Pt surface atoms.[49] In contrast to Zhang et al., the authors showed an interatomic charge transfer from platinum to iridium by a positive shift in Pt 4f and negative shift in Ir 4f binding energies by XPS analysis.[49] Overall, these findings illustrate that the electronic interactions between Pt and Ir as well as the ORR and OER on these bimetallic Pt-Ir alloys are so far not yet fully understood.

Furthermore, under these ORR and OER conditions, the metallic state for both Pt and Ir is not stable and Pt and Ir (surface) oxides are formed.[57,74,75] Experimentally the oxidation mechanism of single crystalline Ir(111) has been studied by surface X-ray diffraction (XRD).[76] He et al. found that first a hexagonal trilayer of O-Ir-O forms, followed by a phase transition to a multilayered oxide with corundum Ir_2O_3 structure as an intermediate, before thermodynamically stable bulk rutile IrO_2 is formed.[76] The initial formation of the O-Ir-O trilayer has been confirmed by DFT.[77] However, under electrochemical potential in electrolyte it was found by using XPS and atomic force microscopy (AFM), that independent of the initial iridium surface orientation and oxidation state (single crystal or IrO_2) always the same roughened/buckled surface oxide containing mostly Ir^{4+} species are formed under OER relevant potentials [74] In addition, Pavlovic et al. have extensively investigated amorphous IrO_x during OER in alkaline and acidic media using in-situ Raman spectroscopy.[78,79] From the studies on anodic IrO_x deposited on an Ir or Au foil, it was found that in aqueous electrolyte IrO_x is heavily hydrated in the form of polymeric edge sharing IrO_6 octahedra, that are connected via μ-oxo type bridges.[78,79] These polymeric IrO_6 chains were found to have a flexible ligand

environment, which facilitates the exchange of oxygen atoms during OER.[78,79] The formation of this structure manifests in a broad range of Raman bands observed between 300 and 800 cm^{-1} for IrO_x, which were confirmed by Zhao et al..[80]

The oxidation of platinum is commencing differently to iridium. It was shown by scanning tunnelling microscopy (STM) that on a Pt(111) surface, first Pt oxide chains form that buckle out of the surface plane forming Y shaped branched structures.[81] These findings were confirmed by DFT calculations[77,82] and further suggest that a transition to a 2D PtO_2 film occurs as the oxidation of the surface progresses. This electrochemical oxidation process on single crystalline Pt(111) and Pt(100) was investigated experimentally by Huang et al. using in-situ Raman spectroscopy.[83] The study confirmed that first, between 1.0 and 1.2 V_{RHE} a 2D (su)peroxo-like 2D platinum surface oxide is observed. From 1.3 V_{RHE} the separate formation of an amorphous hydrous α-PtO_2 3D oxide commences independently, with a broad Raman band around 500 – 590 cm^{-1}, that could not be resolved further.[83]

However, the oxidation of bimetallic Pt-Ir surfaces has so far only been investigated by DFT. For example Kafka et al. showed that alloying Pt with Ir has a positive ΔG of mixing.[84] Under anodic potentials these repulsive interactions push platinum out of the alloy thereby facilitating the separate oxide formation (PtO_2 and IrO_2).[84] These findings are in agreement with DFT calculations by Wittemann et al. showing that thermodynamically rutile IrO_2 is the most stable on bimetallic PtIr(111) and Pt_3Ir(111), while α-PtO_2 is only meta stable.[77]

1.2.3. Hydrogen Oxidation and Evolution Reactions (HER/HOR) on Platinum

The hydrogen oxidation reaction on platinum, even though completely facile in acidic media, is still difficult to quantify kinetically using the standard rotating disk electrode (RDE) set-up, due to the insufficient mass-transport limiting current.[21,85] The reaction pathway for the HOR/HER consists of three elementary steps and is called Tafel-Heyrovsky-Volmer mechanism:[86–88]

Tafel reaction/Dissociative adsorption:

$$H_2 \rightleftharpoons 2H_{ads} \tag{6}$$

Heyrovsky reaction/Oxidative adsorption:

$$H_2 \rightleftharpoons H_{ads} + H^+ + e^- \tag{7}$$

Volmer reaction/Oxidative desorption:

$$H_{ads} \rightleftharpoons H^+ + e^- \tag{8}$$

In the Tafel-Volmer pathway H_2 is adsorbed and dissociates into two hydrogen atoms. This is followed by two separate one electron oxidation steps of the *H adatoms.[85] In contrast, the Heyrovsky-Volmer mechanism combines both a simultaneous one electron oxidation and adsorption of a hydrogen atom and is followed by another oxidation of the adsorbed hydrogen.[85] By using a dual path kinetic equation it was found that the Tafel reaction is responsible for the high activities on platinum at small overpotentials (– 40 to + 40 mV), while the Heyrovsky pathway is only significant at higher overpotentials (> 100 mV).[85,89]

Furthermore, on platinum there are two types of *H adatoms that are adsorbing on different sites and thus have different adsorption energies.[21,90] It was found that only hydrogen adsorbed at the ontop sites (**Figure 7**) functions as an intermediate in the HOR/HER on platinum.[91,92] In contrast, hydrogen that is underpotentially adsorbed (H_{UPD}) is found in hollow or bridge sites and is not a precursor for the HER and HOR.[21,93] Even though the H_{UPD} hydrogen is not directly involved in the reaction, it still weakens the adsorption of the atop site hydrogen by lateral repulsions.[89] This facilitates the desorption of the atop site hydrogen and contributes to the sharply increasing current near the equilibrium potential.[21] Platinum shows exceptionally high HER/HOR activity, which is the result of the hydrogen dissociative adsorption on atop sites that are not blocked by the stronger bound hollow and bridge site hydrogen atoms.[21]

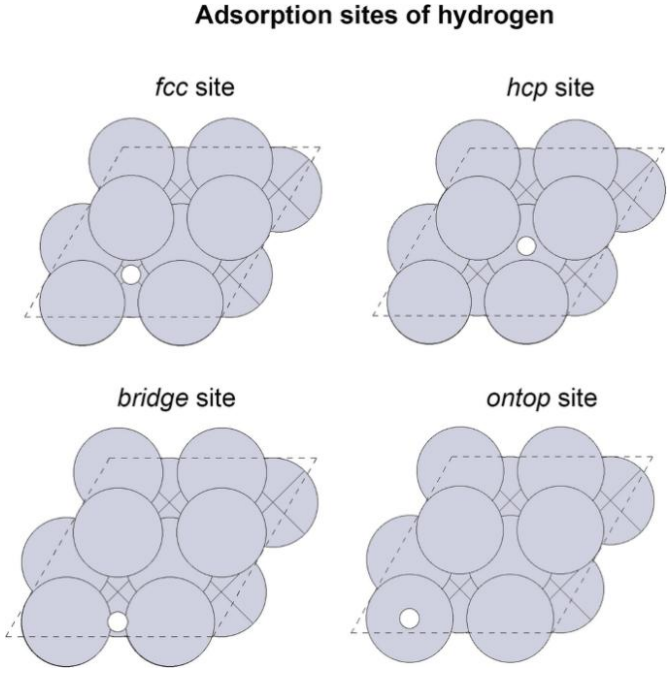

Figure 7. Possible adsorption sites of hydrogen on a platinum (111) surface. Reprinted from Komanicky et al.[90]

1.2.4. Oxygen Reduction Reaction (ORR) on Platinum

The most commonly accepted ORR reaction pathways on platinum surfaces developed by Marković et al.[94] and Wroblowa et al.[95] are displayed in **Figure 8**. In this reaction scheme O_2 is adsorbed to the catalyst surface and reduced to water by either the direct 4-electron route (without intermediates, k_1) or via the formation of intermediate peroxide (k_2 and k_3) known as the 2-electron pathway. Intermediate H_2O_2 can also be released as a product (k_5) and not react further to form water or disproportionate back to oxygen (k_4).

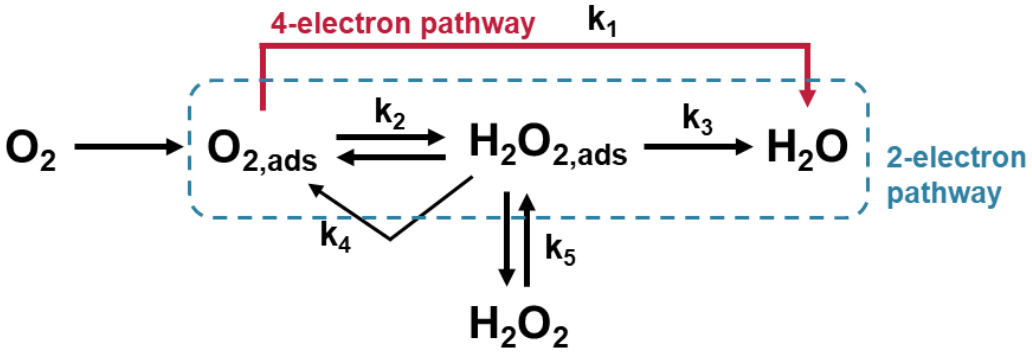

Figure 8. Reaction pathway for the Oxygen reduction reaction (ORR) proposed by Marković et al.[94] and Wroblowa et al.[95]

The most common elementary steps for each of the reaction pathways are:[96]

2-electron pathway:

$$O_2 + 2H^+ + 2e^- \rightarrow OOH_{ads} + H^+ + e^- \rightarrow H_2O_2 \quad (6)$$

4-electron pathway:

$$\frac{1}{2}O_2 + 2H^+ + 2e^- \rightarrow O_{ads} + 2H^+ + 2e^- \rightarrow OH_{ads} + H^+ + e^- \rightarrow H_2O \quad (7)$$

$$O_2 + 4H^+ + 4e^- \rightarrow OOH_{ads} + 3H^+ + 3e^- \rightarrow O_{ads} + 2H^+ + 2e^- \rightarrow OH_{ads} + H^+ + e^- \rightarrow 2H_2O \quad (8)$$

Research on the ORR mechanism began over 60 years ago and pathways developed back then are still the most widely accepted ones today.[97–99] These studies established that oxygen mainly reduces to water, but the reaction kinetics and H_2O:H_2O_2 product ratio was found to be dependent on the formation of platinum oxides at the surface, impurities in the solution that are adsorbed onto the electrode surface or in the presence of strongly adsorbing anions.[100–102]

As intermediate species during the ORR adsorbed hydroperoxyl ($*OOH_{ads}$) in acidic and superoxide radicals $*O_2^-{}_{ads}$ in alkaline electrolytes were suggested.[99,103,104] These intermediates were confirmed by several studies and showed enhanced H_2O_2 production.[98,100,105,106] Thus, in

these studies the main ORR path was proposed to be the 2-electron path with step-wise peroxide formation.[98,100,105,106]

Along the 4-electron pathway there are two possible mechanisms discussed in literature. These are dependent on whether the $*OOH_{ads}$ is broken during the reaction or not, which is controlled by the adsorption configuration of O_2 on the catalyst surface. In the first scenario oxygen is adsorbed by the dissociative side-on, that weakens the O=O double bond resulting in water as the product.[107] In the second scenario oxygen is adsorbed by the associative end-on, where oxygen is adsorbed as *OOH, which can result in H_2O_2 and H_2O.[107] In PEMFCs or URFCs the 4-electron pathway with H_2O as a product is desired, since peroxides strongly damage the PFSA membrane.[108]

Spectroscopically the presence of $*O_{2ads}$, $*O_2^-{}_{ads}$ $*OH_{ads}$ and $*OOH_{ads}$ in alkaline, neutral and acidic electrolyte during ORR was confirmed, supporting the outlined mechanisms.[83,109–112] Besides the investigations of the reaction intermediates, the focus lies strongly on determining the influence of strongly adsorbing anions such as the perchlorate anion, $*OH_{ads}$ and oxygen coverage on the surface.[83,105,113] Weakening of the adsorption energy of these site blocking species such as the *O or *OH coverage is a common design criteria of novel ORR catalysts.[114,115] This can be achieved for example by using modifications in the surface structure, atomic arrangement, strain, ligand effects or Pt alloys.[20,100,104,116–118] However, despite extensive research efforts, the detailed mechanism of the ORR is still not fully understood, and further experimental and theoretical work is required.

1.2.5. Oxygen Evolution Reaction (OER) on Iridium oxide (IrO_x)

Initially, for the OER several different basic reaction mechanisms were proposed. These are based on theoretical density functional theory (DFT) or kinetic analysis and include the oxide pathway, electrochemical oxide pathway, electrochemical metal peroxide pathway and DFT-predicted peroxide pathway mechanisms outlined in **Figure 9**.[119–122] For iridium based OER, the most widely excepted pathway is the DFT-predicted peroxide path developed by Rossmeisl et al.[121] and is often also referred to as the adsorbed evolution mechanism (AEM). The mechanism involves four concerted proton-electron transfers (**IV**, **Figure 9** and **Figure 10**) and commences with the adsorption of a water molecule onto the catalytically active site. The adsorbed H_2O decomposes into adsorbed *OH, that will then undergo a deprotonation to adsorbed *O. This adsorbed oxygen reacts with another water molecule forming adsorbed *OOH species. A further deprotonation of the peroxide leads to the generation of oxygen and recovery of the active site.

I)	Oxide Path	II)	Electrochemical Oxide Path
1)	$H_2O + M \rightarrow M\text{-}OH + H^+ + e^-$	1)	$H_2O + M \rightarrow M\text{-}OH + H^+ + e^-$
2)	$2\,M\text{-}OH \rightarrow M\text{-}O + M + H_2O$	2)	$M\text{-}OH \rightarrow M\text{-}O + H^+ + e^-$
3)	$2\,M\text{-}O \rightarrow 2\,M + O_2$	3)	$2\,M\text{-}O \rightarrow 2\,M + O_2$
III)	**Electrochemical Metal Peroxide Path**	**IV)**	**DFT-predicted Peroxide Path**
1)	$H_2O + M \rightarrow M\text{-}OH + H^+ + e^-$	1)	$H_2O + M \rightarrow M\text{-}OH + H^+ + e^-$
2)	$2\,M\text{-}OH \rightarrow M\text{-}O + M + H_2O$	2)	$M\text{-}OH \rightarrow M\text{-}O + H^+ + e^-$
3)	$M\text{-}O + H_2O \rightarrow M\text{-}OOH + H^+ + e^-$	3)	$M\text{-}O + H_2O \rightarrow M\text{-}OOH + H^+ + e^-$
4)	$2\,M\text{-}OOH \rightarrow M\text{-}O + H_2O + O_2 + M$	4)	$M\text{-}OOH \rightarrow M + O_2 + H^+ + e^-$

Figure 9. Proposed reaction mechanisms for the oxygen evolution reaction. Reproduced from Reier et al.[120]

This very simplified DFT model of the OER reaction mechanism did not consider reaction kinetics and changes in the catalyst surface states depending on the reaction environment. Lastly, the computational hydrogen electrode as a simplified treatment of potential cannot consider decoupled proton and electron pathways limiting the DFT model.[123] Since in this thesis the OER is only studied in acidic environment, the discussion in this section focusses on catalytic OER cycles via H_2O oxidation and does not include alkaline OER commencing from OH^- oxidation.

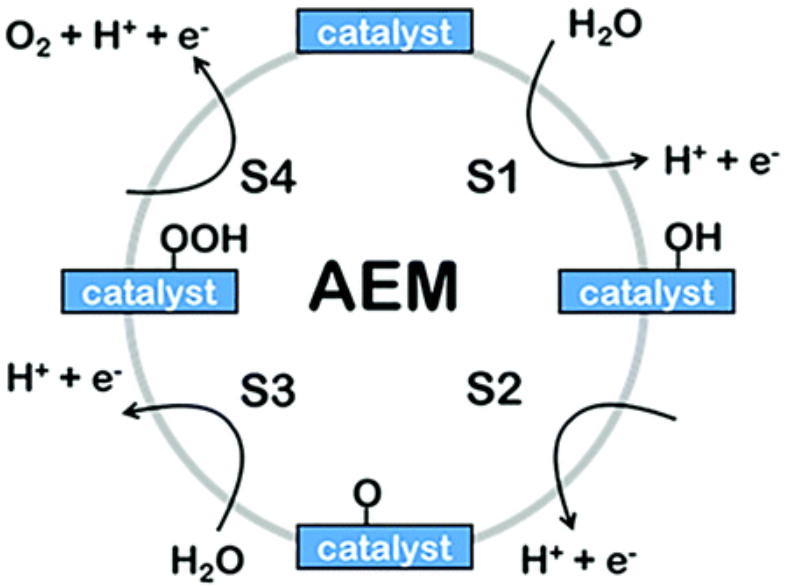

Figure 10. Primary pathway of the AEM proposed by Rossmeisl et al.[121] Reprinted from Shi et al.[124]

In recent literature, based on spectroscopic and computational data there are four catalytic cycles proposed for the acidic OER mechanism over iridium oxide. These are illustrated in

Figure 11 and show that in all cycles the oxidation state of the active iridium center plays a critical role in the OER mechanism.

The first cycle (**Figure 11a**) involves a surface adsorbate, driven by the redox of the iridium center. It begins with the oxidation of a Ir^{3+} center as a water molecule adsorbs and dissociates to Ir^{4+}-O^{2-}H, eliminating first one and then the other proton together with an electron each via concerted proton–electron transfers (CPET). This forms an oxidized Ir^{5+}=O^{2-} center, which then reacts with another water molecule reducing the iridium back to Ir^{4+}-O^{2-}OH.[121,125–131] By returning to the Ir^{3+} state O_2 is released. Generally, this cycle is consistent with the single-site mechanism commonly used by DFT calculations.[123,132,133]

The second catalytic cycle (**Figure 11b**) is very similar, but in this cycle the oxygen is the redox species, resulting in different oxidation states of the Ir center throughout the OER. Similar to the first cycle, the Ir^{3+} center is oxidized to Ir^{4+}-O^{2-}H by water adsorption and release of a proton and an electron via CPET. But in contrast to the first cycle, this is followed by an oxidation of the oxygen atom forming Ir^{4+}=O^{-} containing an electrophilic oxygen species as the reactive intermediate retaining the Ir center in the 4+ oxidation state.[121,125–127,130,131,133–136] The electrophilic Ir^{4+}=O^{-} reacts with another water molecule via a CPET step to form Ir^{4+}-O^{2-}OH and in the next step eliminates oxygen while reducing to the Ir^{3+} state. It is the only proposed mechanism without Ir^{5+} species involved.

In contrast to the first two cycles in the third cycle (**Figure 11c**) the redox involves Ir=O states. In the first step the Ir^{4+}=O of an iridium oxide gets oxidized to Ir^{5+}=O via an electron transfer step followed by the formation of the reactive oxyl species (Ir^{4+}-$O^{\bullet 1-}$) that reacts with a water molecule via a proton transfer forming Ir^{3+}-O^{-}OH.[79,125,129,130,137] This species releases oxygen with a water molecule and returns to the initial state (Ir^{4+}=O) by a CPET. This route is believed to occur at very high over potentials (>2.4 V_{RHE}) where the accumulation of charge is likely to occur.[137,138]

The last cycle is the most complex as it proceeds via the release and refill of oxygen vacancies at the iridium oxide surface. It is also called lattice oxygen participated mechanism (LOM). Depending on how many lattice oxygen atoms are participating in the reaction, two pathways are considered. The outer circle in **Figure 11d** is considered first. As in the previous catalytic cycle the first step is an electron transfer, however here it is irreversible and oxidizes Ir^{3+} to O-Ir^{4+}-O. The lattice bridging iridium sites are attacked by a water molecule forming O-Ir^{5+}(-OH)-O via a CPET, followed by a transformation to O-Ir^{6+}(=O)-O.[139–145] From this O_2 is released leaving O-Ir^{4+} with a vacant site, that is subsequently filled by the attack of a water molecule regaining O-Ir^{4+}-O. In the second inner cycle of **Figure 11d**, first the bridging oxygen

leaches out from the lattice leaving a vacant site, the subsequently released O_2 consists of two lattice oxygens forming two vacant sites on the iridium that are filled from two water molecules by a CPET.[146]

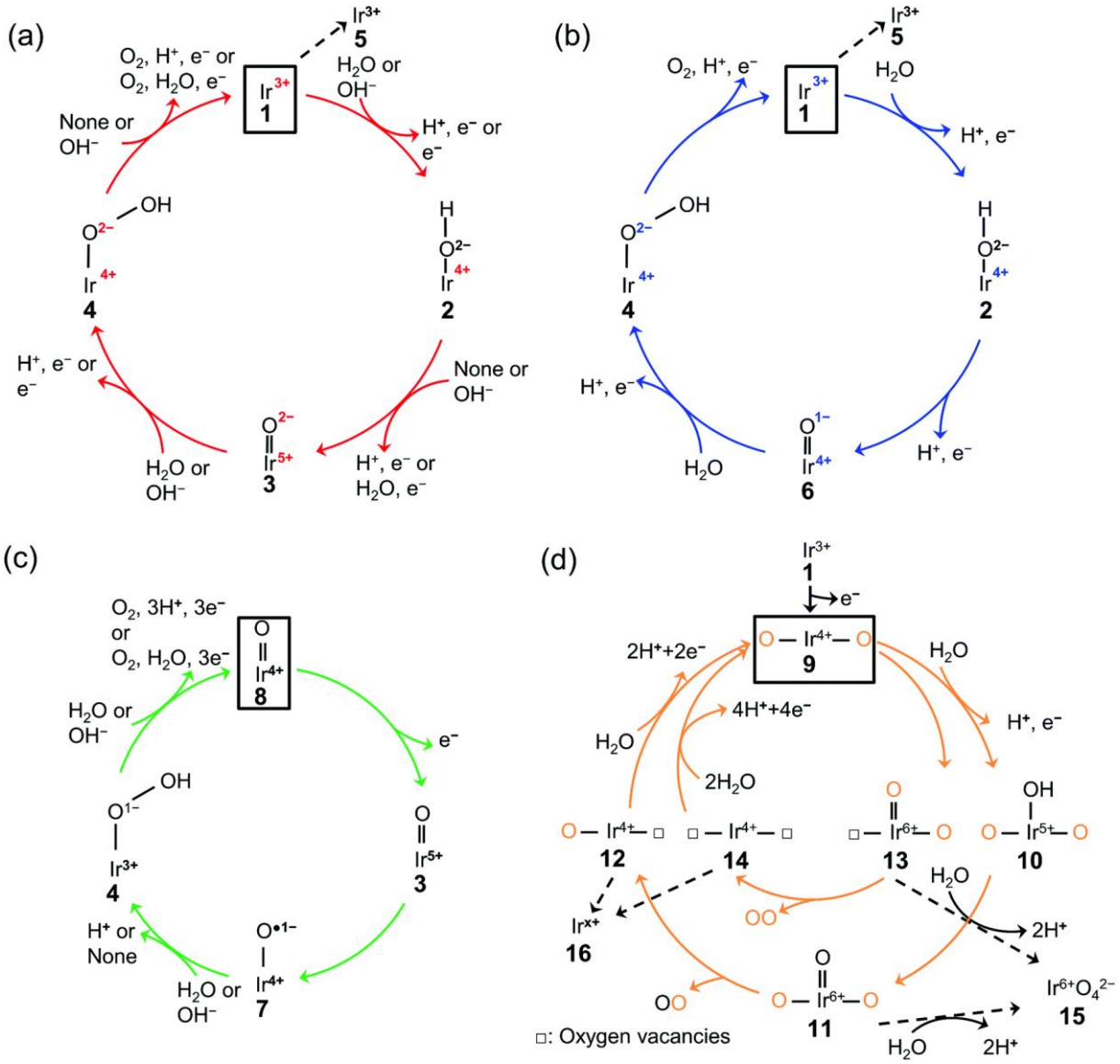

Figure 11. Proposed mechanism of the oxygen evolution reaction (OER) over iridium oxide. Four different colors (red, blue, green, and orange) were used to illustrate four catalytic cycles. (**a**) The red-colored cycle is driven by the redox of the iridium center. (**b**) The blue-colored one proceeds via the redox of the adsorbed O species. (**c**) The green-colored cycle is characterized by the redox of the Ir=O state. (**d**) The orange-colored cycle involves the lattice oxygen, where the orange and black O represent the lattice oxygen and adsorbed oxygen species, respectively. The squares represent the initial state of each cycle, and the dashed lines indicate the dissolution path of iridium species. Reprinted from Naito et al.[123]

Overall, the discrepancies between these catalytic cycles illustrate that the mechanism of the OER is still not fully understood to date. Furthermore, for iridium oxide many oxidation state transitions (Ir^{3+}, Ir^{4+}, Ir^{5+} and Ir^{6+}) are under discussion that need to be systematically

investigated by e.g. spectroscopic studies to get a full picture on the active sites, surface intermediates and rate determining steps (rds). In recent years spectroscopic evidence of the Ir^{5+} state by in-situ and *operando* techniques implies that the rds occurs on the Ir^{5+} site.[128–130,139,147–151] Stabilizing these high-valent states of IrO_x by a second element could improve the OER performance and long term durability, as Ir^{3+} and Ir^{6+} species were found to dissolve more easily into the solution compared to the other oxidation states.[139,143]

1.3. Electrochemical CO_2 Reduction

*Parts of this chapter are reprinted in an adapted form from Blaseio et al. in J. Mater. Chem. A, 2024, **12**, 28177–28192. https://doi.org/10.1039/D4TA02217C*

One approach in the reduction of the still increasing CO_2 emissions is the direct conversion of CO_2 into valuable products, such as hydrocarbons as fuels and/or basic chemicals such as CO, formic acid, or alcohols for industrial applications. As a promising approach commencing at ambient conditions, this can be accomplished by utilizing the electrochemical CO_2 reduction reaction (CO_2RR) and thus has become an expanding field of research. Compared to PEMFCs, the commercialization of large-scale CO_2 electrolysis facilities is not as advanced, and the reactions are much more complex. Thus, the focus still lies more on advancing the fundamental understanding of the active catalyst, CO_2RR reaction mechanisms and modifying the catalyst's selectivity. Most of the research into the CO_2RR is carried out using copper (Cu)-based materials, as it has a unique ability to convert CO_2 to valuable chemicals such as hydrocarbons and fuels.[16,152]

In an aqueous electrolysis cell, at the cathode the CO_2 reduction occurs with the general form

$$xCO_2 + nH^+ + ne^- \rightarrow product + yH_2O \ . \quad (9)$$

At the anode water splitting occurs (**Equation (5)**) that provides the protons and electrons to sum up the overall CO_2RR reaction:

$$xCO_2 + yH_2O \rightarrow product + zO_2 \ . \quad (10)$$

Many CO_2RR products exist, some of which are summarized in **Table 2** with the corresponding reaction equation. All acidic products are considered in the fully protonated form, as together with the OER they must add to the overall CO_2RR reaction (**Equation (10)**). CO reduction reaction products from stepwise reduced CO_2 are not included in the table, but this reaction is also considered as a likely pathway during CO_2R.[153] Currently, the desired products tend to be the production of specialty chemicals such as formic acid and propanol, due to the economic feasibility.[16] Renewable, large scale syngas and methane production is in strong economic competition with the traditional, still relatively cheap synthesis using coal and natural gas.[16] The most promising products in terms of impact for the mass market and feasibility are ethanol and ethylene.[16] Since ethylene is a precursor for many polymers the demand is high, while it is produced by the very energy intensive steam cracking process.[154] Ethanol is primarily produced by biofuel today, but sold at a price that is much higher than the minimum energy for production by electrochemical CO_2 reduction.[16] Thus, a large focus in research in CO_2R is on the production of C_{2+} products.

***Table 2**. Possible electrochemical cathode reactions and products obtained during CO_2RR.*[16,152,155–158]

Reaction	Product name
$2H^+ + 2e^- \rightarrow H_2$	Hydrogen (competing HER)
$CO_2 + 2H^+ + 2e^- \rightarrow HCOOH_{(aq)}$	Formic acid
$CO_2 + 2H^+ + 2e^- \rightarrow CO + H_2O$	Carbon monoxide
$CO_2 + 6H^+ + 6e^- \rightarrow CH_3OH_{(aq)} + H_2O$	Methanol (MeOH)
$CO_2 + 8H^+ + 8e^- \rightarrow CH_{4(g)} + H_2O$	Methane
$2CO_2 + 2H^+ + 2e^- \rightarrow (COOH)_{2(s)}$	Oxalic acid
$2CO_2 + 8H^+ + 8e^- \rightarrow CH_3COOH_{(aq)} + 2H_2O$	Acetic acid
$2CO_2 + 10H^+ + 10e^- \rightarrow CH_3CHO_{(aq)} + 3H_2O$	Acetaldehyde
$2CO_2 + 12H^+ + 12e^- \rightarrow C_2H_5OH_{(aq)} + 3H_2O$	Ethanol (EtOH)
$2CO_2 + 12H^+ + 12e^- \rightarrow C_2H_{4(g)} + 4H_2O$	Ethylene
$3CO_2 + 16H^+ + 16e^- \rightarrow C_2H_5CHO_{(aq)} + 5H_2O$	Propionaldehyde
$3CO_2 + 18H^+ + 18e^- \rightarrow C_3H_7OH_{(aq)} + 5H_2O$	Propanol (PrOH)

To find a suitable electrode material, Hori et al. thoroughly investigated several polycrystalline metal electrodes and only copper was able to produce hydrocarbons, aldehydes and alcohols (C_{2+} products) in sufficient quantities.[152] Thus, Cu is the only pure metal that can produce products requiring more than a 2-electron transfer. This unique ability is assumed to be the result of Cu being the only metal that has a negative adsorption energy for *CO, while it is positive for *H.[159] In addition, CO adsorption on Cu is suppressing the competing HER, due to site blocking effects and changes in *H binding energy.[16,160]

Despite many years of research in the last decades, the mechanism of CO_2RR on polycrystalline Cu is still not fully understood and no general consensus on the very complex mechanistic pathways has been achieved. To demonstrate this, **Figure 12** displays the many suggested reaction paths for C_1 and C_2 products, compiled from several works by Nitopi and Bertheussen et al., demonstrating the complexity of the CO_2 reduction processes.[16] Most mechanisms agree that CO_2 adsorption is a limiting step for 2-electron products and that how the CO_2 binds via the C or O atom determines the formation of formate or CO.[16] CO is generally

agreed as a key intermediate for both pathways to higher value C_1 and C_{2+} products. In addition, the C_1 and C_{2+} product formation pathways seem to be independent from each other, while nanostructured electrodes typically exhibit a suppressed C_1 pathway.[16] The mechanism for C_{2+} products diverges completely after the C-C coupling step, highlighting that especially for the higher value products there is still no general understanding on which parameters influence the selectivity between the various oxygenates and hydrocarbons.[16]

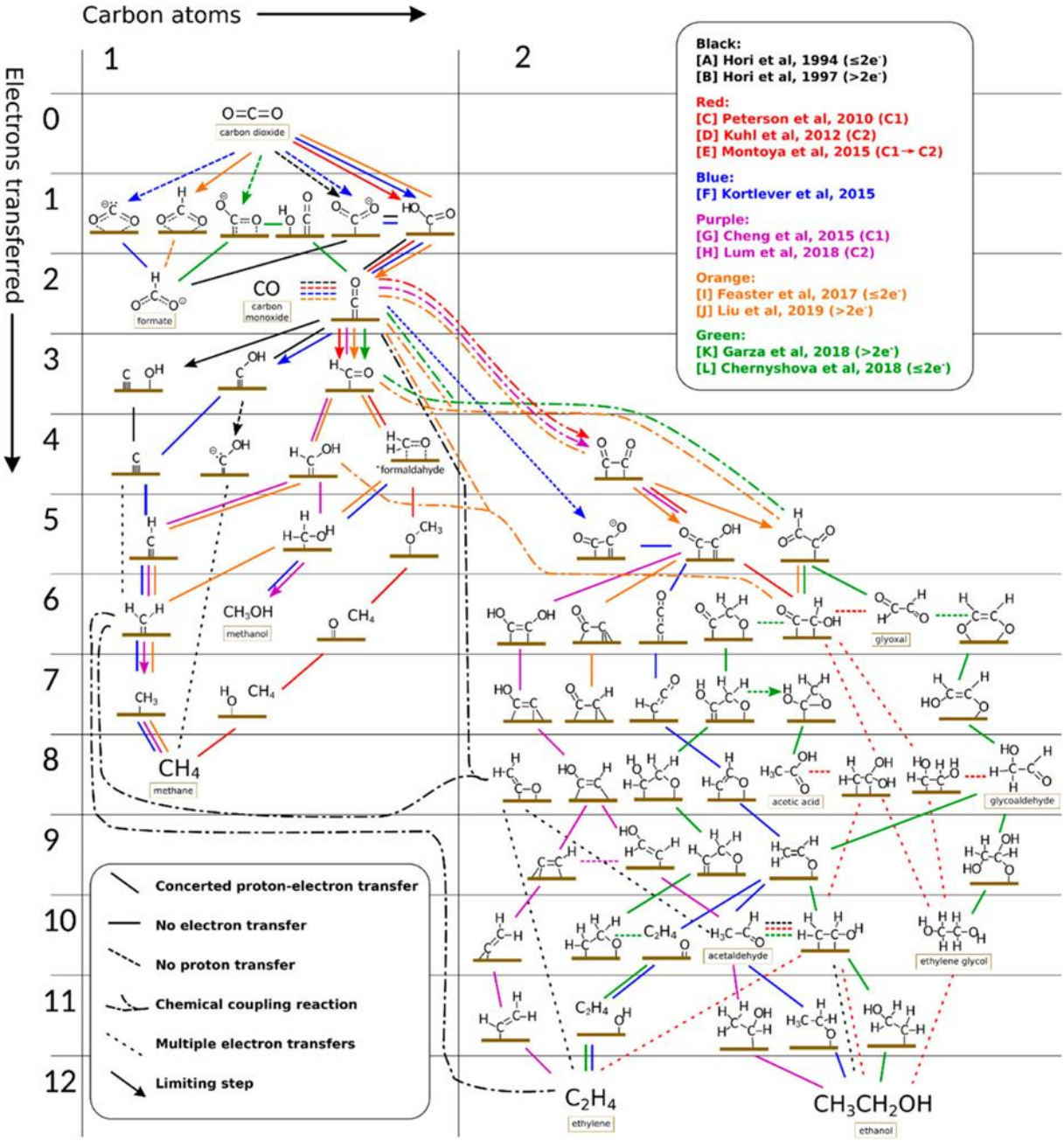

Figure 12. Possible mechanistic pathways of CO_2RR to C_1 and C_2 products on polycrystalline copper grouped into different colored reaction schemes combined from the works in the top-right legend. Reprinted from Nitopi and Bertheussen et al.[16]

1.3.1. Nanostructured and oxide-derived Cu-based materials

Not only the electrode material determines the resulting CO_2RR selectivity, efficiency and stability, but also the morphological characteristics such as shape, size and composition strongly influence the product distribution.[16,158,161,162] Similar to electrocatalysts developed for other reactions nanoparticles are intensively investigated for the CO_2RR, due to the high surface area to bulk ratio allowing greater utilization by mass. In addition, an impact on the reactivity is found due to a lower coordination of surface atoms as a result of an increase in undercoordinated sites.[163] This can change the electronic structure and in turn enhance the reactivity of the NPs. However, as discussed previously the CO_2RR is very complex, including many proton and electron transfers, making it very difficult to predict the effect of changes in electronic structure on the catalyst performance. Several studies on Cu NPs have been performed, but tend to show different trends.[16,164–166] Reske et al. studied the product distribution in dependence of the nanoparticle size, but no clear trend with changing size could be observed.[164] On the other hand, Manthiram et. al. observed an enhanced methane production on Cu NPs compared to polycrystalline Cu.[165] Overall, studies of Cu NPs show that the mobile Cu surface, especially when CO is present, leads to significant restructuring under reaction conditions causing changes in NP size, shape and distibution.[165,167] Therefore, three-dimensional nanostructured catalyst materials were developed. These nanostructured copper materials are investigated without an oxidative treatment or with partial or complete surface oxidation that creates more active surface sites for a selective CO_2RR.[168,169] The non-oxide derived catalysts are prepared by sputter deposition, anodization, cathodic electrodeposition or dealloying.[161,162,170–172] Even though these catalysts are prepared without a distinct oxidation step, a thin oxide layer readily forms on the Cu surface when exposed to ambient air. Only using the nano structuring is found to increase the selectivity towards C_2 products and reduces C_1 product formation compared to polycrystalline Cu.[16,173]

More commonly in recent years the nano structuring is followed by a thermal annealing, chemical oxidation or oxygen plasma treatment step to generate thin Cu_2O/CuO surface layers.[16,161,174–179] The formation of bulk oxide is usually disfavored as it can cause a reduced electrical conductivity, which results in kinetic stabilization of the oxide phases within the catalyst even at highly reductive potentials.[180,181] For example, Dutta et al. investigated an at 300 °C in air annealed Cu_xO foam by complimentary *operando* XRD, Raman and XAS during CO_2RR.[180] A potential induced oxide-metal transition was required to activate the Cu_xO catalyst towards alcohol formation.[180] In addition, another study on Cu skeletons showed that an oxidative treatment or Cu foam deposition was required to activate the Cu catalyst.[170] This

treatment favored the C_2 pathway while C_1 product formation (methane and methanol) was completely surpressed.[170] Two studies by Ma et al. using nanowires and Rahaman et al. using an annealed copper mesh support these findings showing enhanced selectivity for hydrocarbons and alcohols.[168,182] Even though the copper oxides enhance the formation of C_2 products, they are thermodynamically unstable at potentials applied during CO_2RR. Therefore, the electrochemical reduction during the CO_2RR generates in-situ oxide-derived (OD) Cu catalysts. Interestingly, subsurface oxygen present even under CO_2RR conditions in a 1 – 2 nm amorphous copper layer is proposed to be responsible for an enhanced CO adsorption on the OD-Cu surface.[183,184] However, DFT calculations by Fields et al. indicate that no subsurface oxygen will remain thermodynamically stable under the highly cathodic conditions presents during CO_2RR and is thus unlikely the reason for an enhanced activity of the OD-Cu catalyst.[185] Overall, the stability and role of subsurface oxygen is still controversially discussed in literature.[16,183–186]

1.3.2. Reduction of Cu_2O and CuO during CO_2RR

As outlined in the previous section the copper oxides are not stable and reduced to metallic Cu under cathodic potentials relevant for CO_2RR. This reduction of Cu^{z+} species during CO_2RR needs to be considered in two aspects. Firstly, the thermodynamically predicted stability of Cu_2O and CuO under the conditions present and secondly, the kinetics of the reduction process. The thermodynamic stability is predicted by the Pourbaix diagram displayed in **Figure 13**.[187] From the diagram, the reduction pathway from Cu^{2+} to metallic Cu in the pH range from 2.5 to 16 always commences via intermediate Cu_2O formation. Since CO_2RR experiments are usually carried out in 0.1-0.5 M $KHCO_3$ ≈ pH = 7 – 8, this is the expected pathway for the oxide-metal process and commences via the following two-step reaction

$$2CuO + 2e^- \overset{k_1}{\rightarrow} Cu_2O \tag{11}$$

$$Cu_2O + 2e^- \overset{k_2}{\rightarrow} 2\,Cu \tag{12}$$

From a kinetic point, the electrochemical reduction comprises two rate constants. One for the reduction from Cu^{2+} to Cu^+ species (**Equation (11)**, k_1) and one for Cu^+ to Cu^0 (**Equation (12)**, k_2). Depending on which of the potential-controlled rate constants is the rate determining step, i.e. the slowest step, the formation of Cu^+ can be detected, or it might be too fast to be observed depending on the resolution of the analysis technique used. If k_1 is rate determining, the Cu^+ intermediately rapidly reacts to metallic Cu. On the other hand, if k_2 is the slowest step a fast buildup of Cu^+ occurs that is followed by a slow reduction to Cu^0 species.

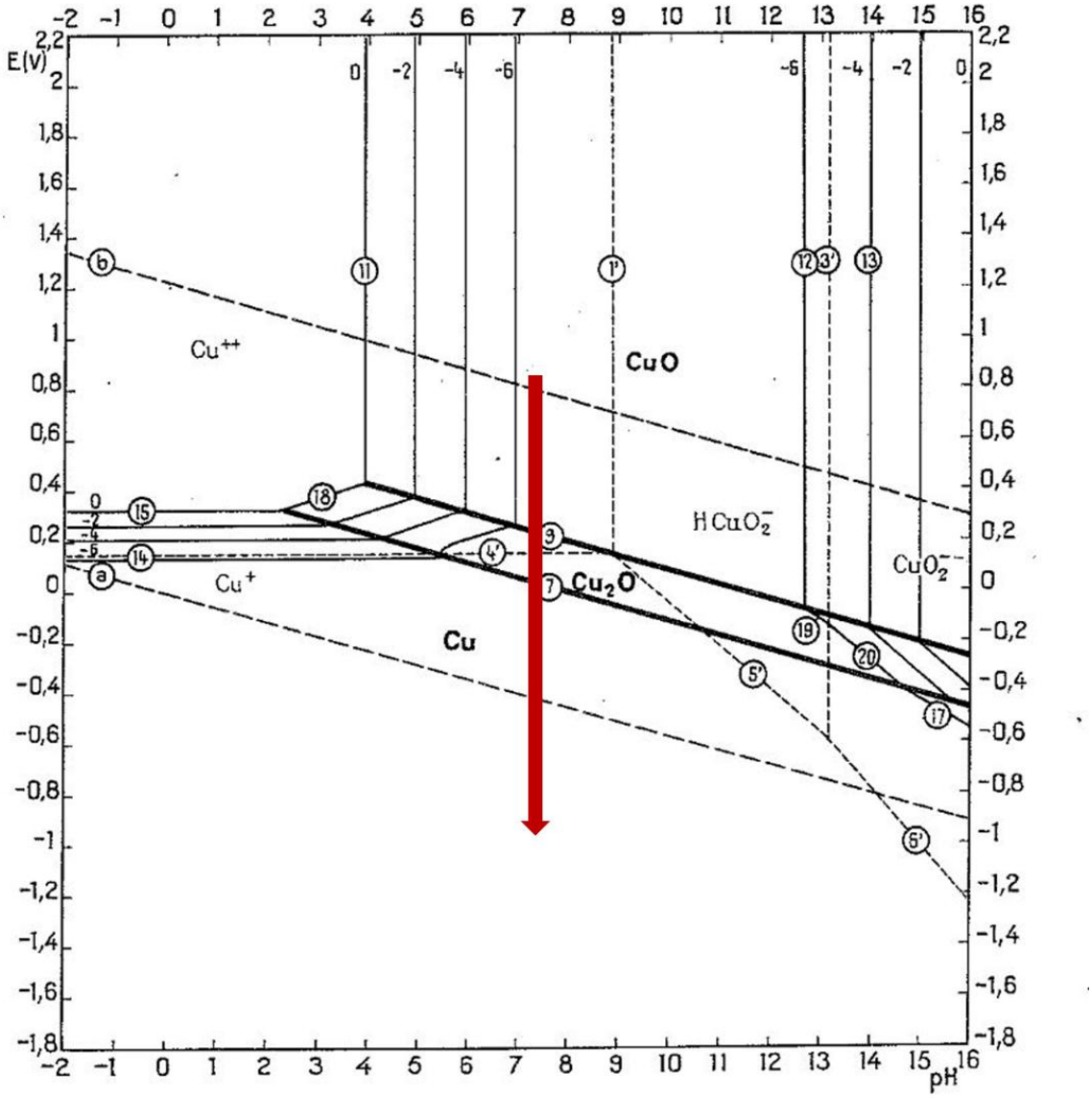

Figure 13. Pourbaix diagram for copper at 25 °C. The red arrow illustrates the transition of CuO to metallic Cu via the formation of Cu_2O as the potential is decreased to cathodic values under common conditions during CO_2RR (pH ≈ 7 – 8, 25 C). Reprinted from Pourbaix.[187]

Considering, that most investigations on OD-Cu catalysts are focused on the influence of the oxidic precursor on the CO_2RR product distribution, faradaic efficiencies and surface structure changes, very little is known on how the reduction of the oxidic precursor is commencing and how it is influencing the CO_2RR.[16] As an example, Velasco-Vélez et al. investigated Cu oxidation state changes during the CO_2RR in 0.1 M $KHCO_3$.[181] For Cu^+ a reduction to metallic Cu was observed at – 0.8 $V_{Ag/AgCl}$ ≈ – 0.2 V_{RHE} (3.4 M KCl).[181] Surprisingly, no reduction of the pure CuO foam could be detected over the entire potential range up to – 0.8 V_{RHE}, which was explained by the formation of a stable carbonate layer formed, passivating the surface of the foam.[181] In addition, Timoshenko et al. and Jeon et al. showed that by time-resolved LCA-XANES analysis at – 1.0 V_{RHE} and – 0.7 V_{RHE} the successive reduction of mainly Cu^+

containing Cu nanocubes and nanocrystals can be studied in detail.[188,189] Both investigations did not make any conclusions on the influence of the different Cu species on the reduction processes. These examples show that the specific role of the oxides as well as the transition processes to metallic Cu during CO_2RR have so far not been fully understood and no general conclusion has been achieved in literature.[170,178–180,183–186,190–193]

1.3.3. Influence of the Electrochemical Protocol on the Reduction of Cu_xO

Another important influence on the reduction behavior of copper oxides is the electrochemical protocol applied. For CO_2RR, research using *operando* techniques has been mainly conducted using chronoamperometric methods (**Figure 14**). Most commonly small potential shifts instead of jumping directly to highly cathodic potentials are employed.[180,181,194] The smaller potential steps allow for a more gradual reduction. One method mainly used by Roldan Cuenya et al. is to apply anodic pulses to regenerate the oxides in-situ that enhance the selectivity of CO_2RR.[166,189] A mixture of Cu^+ and Cu^{2+} species formed during the anodic pulses is required for an enhanced alcohol formation.[166]

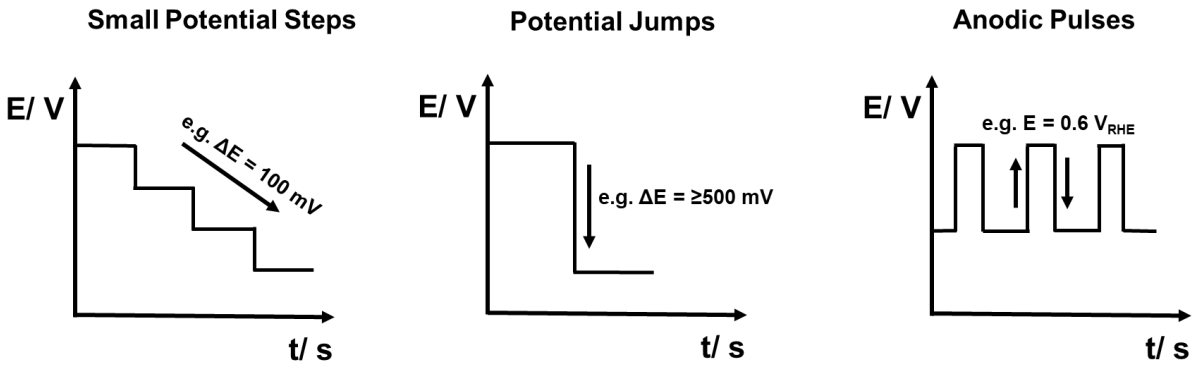

Figure 14. Electrochemical Protocols used to investigate oxide-metal transition processes of Cu_xO type materials and the influence on the CO_2RR product formation.

2. Research Objectives

The general aim of this thesis is to investigate oxide-metal transition processes in three case studies by in-situ/*operando* XAS and Raman spectroscopy techniques: Cell reversal tolerant PEMFC anode, bifunctional oxygen electrode and CO_2 electrolysis catalyst materials are investigated.

To investigate the oxide-metal transitions in the three case studies, in-situ/*operando* Raman and X-ray absorption spectroscopy techniques are employed. These techniques were chosen as they are highly complementary. While XAS is a bulk technique, Raman spectroscopy only probes the surface of the electrocatalyst. In addition, Raman spectroscopy allows the detection of adsorbed intermediates and products as well as the chemical species of the active catalyst.

When employing XAS in electrocatalysis, materials with high surface-to-bulk ratios, such as NPs or nanoporous materials are usually studied to obtain most of the signal from surface atoms that are involved in the electrochemical reaction(s). From XAS not only information on the oxidation states of the active catalyst, but also on the structure (number of neighboring atoms and their distances from the central atom) can be obtained. Furthermore, nowadays XAS spectra can be recorded with very high time resolution and data quality, therefore dynamic studies with changes in conditions within several seconds become feasible. For confocal Raman spectroscopy this is theoretically possible, but changes in the focus plane e.g. by oxide formation make it very difficult to follow surface changes dynamically within a few seconds.

The objective of the first case study is to investigate the transition of the chemical states of cell reversal tolerant Pt-Ir NPs in a three-electrode *operando* XAS cell. To mimic the cell reversal event conditions, time-resolved Quick-XAS will be used to study the bifunctional properties, changes in Pt and Ir oxidation states as well as electronic interactions between both metals during HER (– 0.02 V_{RHE}) and OER (+ 1.55 V_{RHE}), while switching between both conditions as fast as every 3 s. With this study the aim is to gain new insights into the oxide-metal transition kinetics of the bimetallic Pt-Ir NPs under operating conditions thereby advancing the development of cell reversal tolerant catalyst materials.

The aim of the second case study is to investigate sputtered Pt-Ir thin films as bifunctional model catalyst systems for the oxygen electrode (ORR/OER) in the URFC. These nano-structured films show a very low surface-to-bulk ratio and are thus unsuitable for investigation by XAS. One goal of the research is to gain mechanistic insights into the potential-resolved bimetallic Pt-Ir oxides formed in the potential range from 0.3 to 1.6 V_{RHE} using in-situ Raman

spectroscopy. A custom-made three-electrode in-situ Raman cell will be employed for the measurements. In combination with the first case study, we aim to further enhance the knowledge on Pt-Ir oxide formation from metallic under anodic potentials aiding to a more detailed understanding on the surface of the bimetallic Pt-Ir catalysts under operating conditions.

In the third part of the thesis, the dynamic and time-resolved changes of copper oxide (Cu_xO) foam precursor catalysts under CO_2 reduction reaction conditions in a three-electrode *operando* XAS cell are studied. In particular, the dynamic oxide-metal reduction kinetics of differently annealed Cu_xO foams (100 – 450°C) during the CO_2RR will be investigated. These different annealing temperatures result in different Cu^0:Cu^+:Cu^{2+} ratios and crystal structures. Since the influence of these different copper oxides and their crystallinities on the reduction kinetics to metallic Cu were not yet fully investigated, the aim is to understand the influence of these on the oxide-metal reduction kinetics using time-resolved *operando* Quick-XAS. In addition, by employing different types of potential control experiments we will investigate the influence of the electrochemical protocol on the reduction kinetics of the Cu_xO foams.

All in all, both techniques offer great potential for studying the three electrocatalysts under operating conditions and were thus chosen for investigating the oxide-metal transitions of cell reversal tolerant Pt-Ir NPs, bimetallic Pt-Ir thin films for the oxygen reactions and Cu_xO foams during the CO_2RR.

3. Experimental Methods

3.1. Ex-situ Characterization

3.1.1. Transmission electron microscopy (TEM) and Energy dispersive X-ray spectroscopy (EDX) of Pt-Ir NPs

To determine the morphology and mean particles size of the as-synthesized Pt-Ir NPs and commercial reference materials, a JEOL JEM ARM300F2 transmission electron microscope (TEM) operated with an accelerating voltage of 300 kV was employed. Around 800 particles from several TEM images were analyzed using the ImageJ software (version 1.50i). For obtaining the Pt:Ir ratios of the bimetallic NPs, energy dispersive X-ray analysis (EDX) was performed using a Dual-SDD EDX-Detector.

3.1.2. Scanning electron microscopy (SEM)

Pt-Ir thin films

The structure and morphology of Pt-Ir thin films were evaluated by using a Helios G4 CX scanning electron microscope (SEM) equipped with an Everhart-Thornley secondary electron detector and a back-scattering detector. An accelerating voltage of 5 kV and a current of 100 pA were applied and the SEM images were acquired at a working distance of 4.1 mm.

Cu_xO foams

The structure and morphology of annealed Cu_xO foams were evaluated by using a Zeiss Gemini 450 scanning electron microscope equipped with an InLens secondary electron detector and a back-scattering detector. An accelerating voltage of 5 kV and currents of 75 pA were applied at a working distance of 5 mm.

3.1.3. X-ray Diffraction (XRD)

Pt-Ir NPs and Pt-Ir thin films

X-ray diffraction (XRD) data of sputtered Pt-Ir thin films were measured using a 2 Theta-diffractometer (Bruker, D2Phaser) equipped with a Cu Kα X-ray source (wavelength of 1.54 Å) and a position-sensitive detector (SSD160 1D-Detektor) in Bragg-Brentano geometry. The operating voltage and current were 30 kV and 10 mA, respectively. The measurement parameters used were: 2θ range from 10 to 95°, step size of 0.01°, holding time of 7 s per step, divergence slit of 1 mm, secondary soller slit of 2.5°, and sample rotation of 20 rpm. The XRD profiles were analyzed with the software TOPAS (Bruker, version 5). The quantitative Rietveld refinement analysis was conducted with the following fit parameters: background coefficients,

displacement correction, peak shapes and cell parameters. The quality of the fit was evaluated with the R-weighted pattern (Rwp).

Cu_xO foams

Bruker D8 X-ray diffractometer was operated at 40 mA and 40 kV with a Cu Kα radiation (1.540 Å) and scan rate of 0.1° min^{-1} to obtain crystal information of the annealed Cu_xO foams. The XRD profiles were analyzed with TOPAS (Bruker, Version 5).

3.1.4. µ-X-ray Fluorescence (µ-XRF)

Pt-Ir thin films

To determine the bulk Pt:Ir ratios of the thin films, a micro-X-ray fluorescence (µ-XRF) spectrometer (Bruker, M4 Tornado plus) equipped with a rhodium X-ray source operated at 50 kV and 300 µA, a 20 µm polycapillary and two SDD detectors (type: 660 PAR -LE) was used. Pt and Ir Lα data from three randomly distributed point measurements with a spot size of 20 µm and acquisition time of 60 s were analyzed using the software M4 TORNADO (Bruker, version 1.6.621.0).

3.1.5. X-ray Photoelectron Spectroscopy (XPS) and Auger

Pt-Ir thin films

For X-ray photoelectron spectroscopy (XPS) measurements, an ESCALAB 250 Xi instrument (Thermo Fisher) equipped with a 1486.6 eV Kα source was employed. The spot size used was 650 µm and no charge compensation was carried out. The acquisition parameters of Pt 4f, Ir 4f, O 1s and C 1s XPS spectra are listed in **Table S2.1** of the **Appendix Chapter 10.2**. The spectra were analyzed using the software Avantage v5.9952. For background correction, a simple Shirley function was used, while the XPS signals were fitted with mixed Lorentzian–Gaussian functions with optional asymmetric and tailing functions for any metal components. The binding energies of the deconvoluted XPS spectra were referenced to the C 1s peak of the aliphatic hydrocarbon component at 284.8 eV.

Cu_xO foams

ESCALAB 250 Xi X-ray photoelectron spectrometer (Thermo Fisher) equipped with a monochromatic Al Kα X-ray source (1486.6 eV) was used to determine the chemical state of Cu surface species of annealed foams. Experimental parameters for the acquisition of survey and high-resolution XPS spectra of C 1s, O 1s and Cu 2p as well as Auger spectra of Cu LMM are summarized in **Table S3.1** of the **Appendix Chapter 10.3.**. The XPS and Auger data were analyzed using Avantage software (version 5.9952).

3.1.6. Raman Spectroscopy of Cu_xO foams

Raman spectra of the annealed Cu_xO foams were acquired by a WITec alpha300 RSA confocal microscope using an excitation wavelength of 532 nm with a laser power of 1 mW, a 600 l mm^{-1} grating and a Zeiss EC Epiplan-Neofluar Dic 50×/0.8 NA objective.

3.2. X-ray Absorption Spectroscopy (XAS)

In XAS a monochromatic beam of X-rays with energy *E* is focused on a sample of interest. This adsorption can be described by the Lambert-Beer law

$$I(E) = I_0(E)e^{-\mu(E)d} \tag{13}$$

where the incident and transmitted X-Ray intensities are described by $I_0(E)$ and $I(E)$, respectively. $\mu(E)$ is the linear absorption coefficient and d is the sample thickness. With an increasing energy of the incident X-ray beam, the absorption coefficient is decreasing until a critical energy is reached and a sharp increase in the coefficient occurs. This steep increase indicates the ejection of a core electron of an atom upon adsorption of a photon from the incident X-ray beam and is called absorption edge. The region of the sharp increase at the absorption edge is also referred to X-ray absorption near edge structure (XANES) and gives information about the oxidation state, electronic properties and geometry. For atoms in a molecule the absorption coefficient above the absorption edge displays a fine structure, because of scattering of the ejected electron on the neighboring atoms. This fine structure is known as extended X-ray absorption fine structure (EXAFS) and provides information on the type and number of neighboring atoms as well as their distances from the central atom (**Figure 15**).

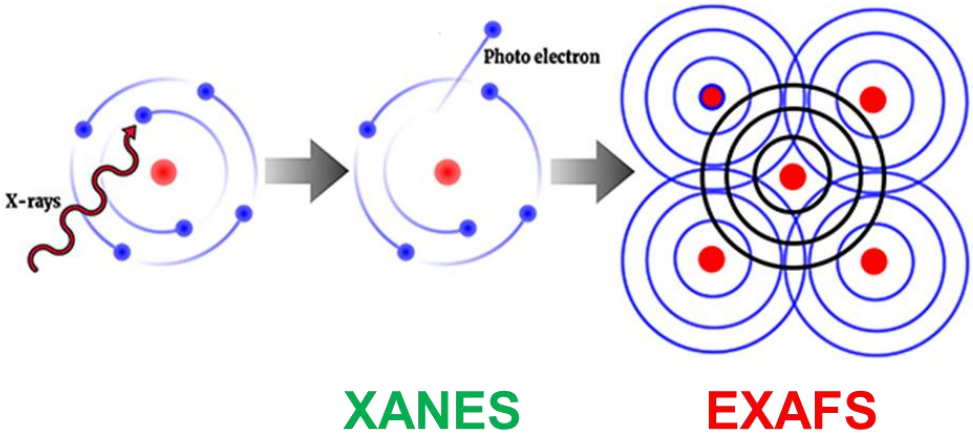

Figure 15. Schematic representation of the X-ray absorption process and subsequent scattering of the ejected electron. Reprinted from Diamond Light Source.[195]

In a XAS experiment, the Bragg diffraction from crystals is used to select a specific photon energy from the broad spectral range. The Bragg equation demonstrates that a beam of the wavelength λ is reflected into the angle 2θ:

$$n\lambda = 2d \sin(\theta) \tag{14}$$

where *n* is an integer and *d* is the interplanar spacing. Usually, two crystals are employed, one is used as a primary monochromator and the second one suppresses the higher harmonics such as 2λ or 3λ. In a Quick-XAS set-up the angle (*2θ*) changes very rapidly, reducing the measurement time.

One ionization chamber before and one after the sample measure the incident (I_0) and transmitted (I) X-ray intensities, as well as a reference sample. Most commonly this is the element of interest in its non-oxidized or reduced form e.g. metal foils in the metallic state. Absorption can also be measured using processes that are proportional to it. For example, X-ray fluorescence can be measured and related back to the absorption process. Fluorescence radiation is obtained by an outer shell electron filling the hole of the core electron shell, which produces the fluorescence radiation with a wavelength that is characteristic of the energy difference between the two shells and can be easily separated from the absorbed radiation. Most commonly the fluorescence detector is assembled perpendicular to the incident beam, to minimize interference from reflected radiation (**Figure 16)**. Measurement in fluorescence mode can be especially useful when the sample concentration is low, or the sample thickness is large.

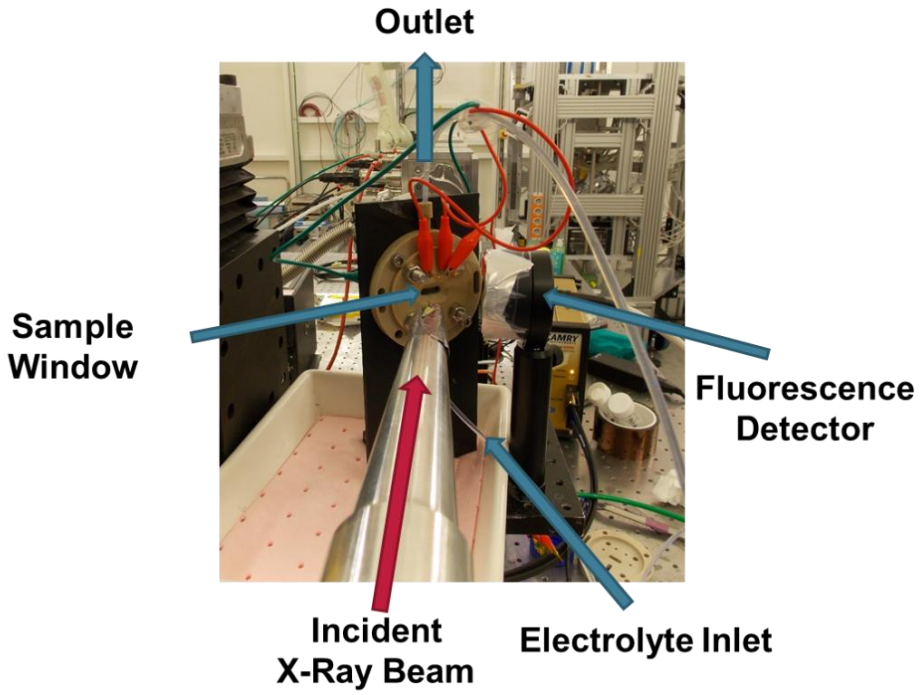

Figure 16. Set-up of the custom-made electrochemical XAS flow-cell at beamline P64 at DESY.

3.2.1. Set-up of the electrochemical XAS flow-cell

Exemplarily, the set-up of the electrochemical XAS flow-cell at the beamline P64 at DESY is shown in **Figure 16**. During operation a constant flow of electrolyte (~1 – 2 ml min^{-1}) is pumped through the cell by a syringe pump. The cell potential is controlled by a potentiostat,

while XAS spectra at the desired edge are collected. The cell was mounted at a 45° angle to the incident X-ray beam, allowing to collect XAS data in transmission and fluorescence mode.

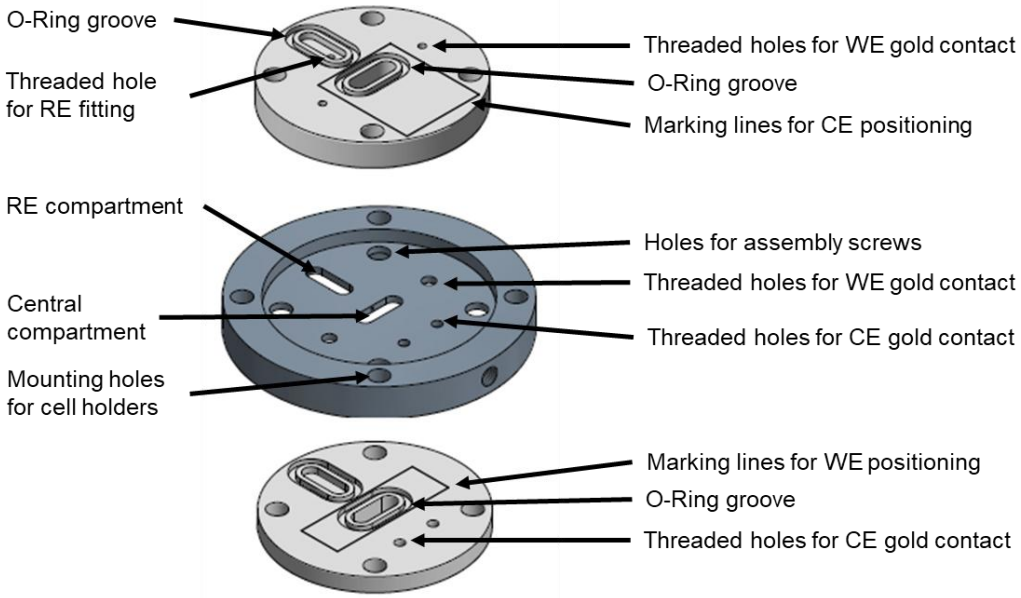

Figure 17. Drawings of the three parts of the electrochemical XAS flow-cell. WE = working electrode, RE = reference electrode and CE = counter electrode.

The design of the XAS flow-cell was based on Binninger et al.[196] and developed previously in the group. The drawings of the three parts of the cell are displayed in **Figure 17**. During assembly the parts are connected by four equally distributed screws. The top part of the cell holds the fitting for the reference electrode (RE), a marked space to place the counter electrode (CE) and O-ring grooves to seal the RE and CE compartments. As CE, a graphite or gold sheet can be used. The middle part contains the RE and central compartment through which the electrolyte is pumped by the syringe pump (**Figure 18**). The central compartment/sample window is elongated to simultaneously measure XAS data in transmission and fluorescence mode. The thickness of the electrolyte layer can be adjusted to 1 or 2 mm using a middle part with the respective thickness. The choice of the middle part thickness depends on the sample thickness, material, the absorption edge that is measured and whether the detection is carried out in transmission or fluorescence mode. On the rim of the middle part, four holes are placed for mounting the cell to a holder. The third part of the cell contains the marked space of the working electrode (WE) and two O-Ring grooves for sealing the RE and WE compartments. The CE and WE are connected to the potentiostat by two gold contact pins each.

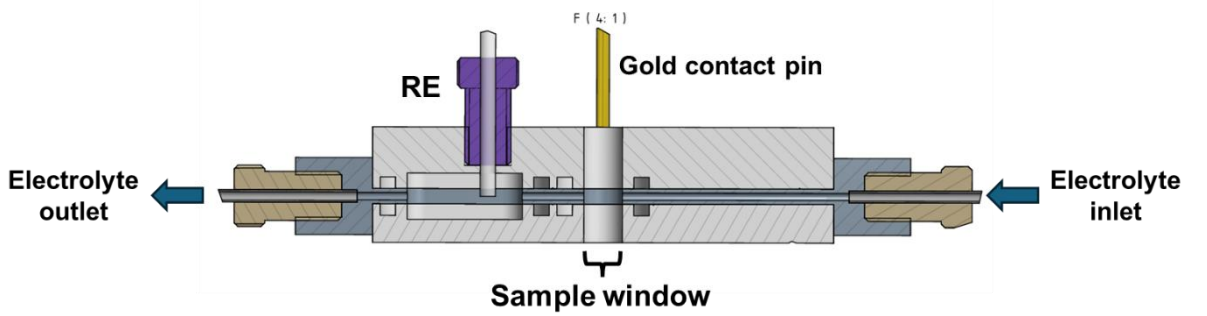

Figure 18. Cross section drawing of the electrochemical XAS flow-cell with arrows showing the flow of electrolyte through the cell. RE = reference electrode.

3.2.2. XAS Data Acquisition in the case studies

Pt-Ir NPs

Quick-XANES data recorded at the Ir and Pt L3 edges were obtained at beamline P64 of the DESY Synchrotron, Germany.[197] The storage ring was operated with a beam current of 100 mA at an energy of 6.0 GeV. The beamline was equipped with a von Hamos-type spectrometer and an Oscillating Channel-Cut Si(111) QEXAFS monochromator, which enabled recording both Pt and Ir L3 edges in one scan every second.[198,199] To measure XANES spectra in fluorescence mode, a passivated implanted planar silicon (PIPS) Canberra 100 element detector was used.

The custom-made spectro-electrochemical flow cell outlined in **Section 3.2.1.** was used for the *operando* Quick-XAS measurements. The carbon-supported bimetallic Pt-Ir, Ir or Pt NPs with a loading of 300 μg_{metal} cm^{-2} were dropcasted onto a gas diffusion layer (GDL) (SGL Carbon, 29BC) and used as the working electrode. A graphite sheet functioned as a counter electrode and a mercury/mercury sulfate (MMS) reference electrode (ALS-Japan, RE-2CP) was employed. The catalyst ink was prepared by dispersing the Pt-Ir, Pt or Ir NPs with a 1:1 mixture of 2-propanol:water and 10 µL of a 5 wt.% Nafion solution. As an electrolyte, argon saturated 0.1 M $HClO_4$ solution was pumped with a constant flow rate of 2 mL min^{-1} through the cell by a syringe pump (KD Scientific, Legato 210). The potential was jumped repeatedly every 3 s or 10 s between -0.02 V_{RHE} (HER) and $+1.55$ V_{RHE} (OER) using a potentiostat (Gamry, Reference 600). The start of the Quick-XANES data recording was manually synchronized with the potentiostat. Due to the small resistance (≤ 5 Ω) in the XAS cell, no iR-corrections of the potentials were carried out.

Cu_xO foams

*This section is reprinted from Blaseio et al. in J. Mater. Chem. A, 2024, **12**, 28177–28192.*
https://doi.org/10.1039/D4TA02217C

Quick-XAS data recorded at the Cu K-edge was obtained at the SuperXAS (X10DA) beamline of the Swiss Light Source (SLS), Switzerland. The storage ring was operated with a beam current of 400 mA and an energy of 2.4 GeV. A fast oscillating channel cut crystal monochromator allowed recording one spectrum in 1 s. The ionization chambers for the detection of the incident and transmitted X-ray radiation were filled with N_2.

The custom-made spectro-electrochemical flow cell (outlined in **Section 3.2.1**) was used. In the experiments, the Cu_xO foams were used as a working electrode, a gold foil as the counter electrode and a non-leakage Ag/AgCl (3 M KCl, EDAQ) as the reference electrode. The electrolyte thickness in the X-ray window was adjusted to 1 mm. A Cu foam thickness of 30 – 40 µm allowed to measure XAS spectra in transmission mode with sufficient signal-to-noise ratio. As electrolyte a CO_2-saturated 0.5 M $KHCO_3$ solution (pH = 7.2) was used, which was pumped with a constant flow through the cell by a syringe pump. For the potential increment, step and jump conditions, the following electrochemical experiments were carried out:

(i) Potential increment: ΔE = 100 mV, from + 0.4 V_{RHE} → – 1.2 V_{RHE}

(ii) Potential step: OCP → – 0.2 V_{RHE} → – 0.5 V_{RHE} → – 1.3 V_{RHE}

(iii) Potential jump: OCP → – 0.5 V_{RHE} or – 1.3 V_{RHE}.

3.2.3. XAS Data Processing, Analysis and Interpretation

In the first step, the raw collected XAS data are background subtracted and normalized with respect to $\mu_0(E)$. The contribution of Compton-scattering to the absorption coefficient below the absorption edge (pre-edge) is subtracted from the XAS spectrum (**Figure 19**). Depending on the shape of the pre-edge several functions can be used to approximate the shape of the pre-edge region. Most commonly this is a linear function and is extrapolated to all energies in the measurement range. Similarly, dependent on the shape a polynomial is regressed to the data in the post-edge region to normalize the data. The normalization constant ($\mu_0(E_0)$) is determined by extrapolating the pre- and post-edge lines to E_0 (binding energy) and subtracting the y-intersections of the pre-edge and post-edge lines with E_0. To obtain the normalized spectrum, the pre-edge function is then subtracted from the measured XAS data, which sets the pre-edge values to y = 0. This pre-edge subtracted data is then divided by the normalization constant, $\mu_0(E_0)$.

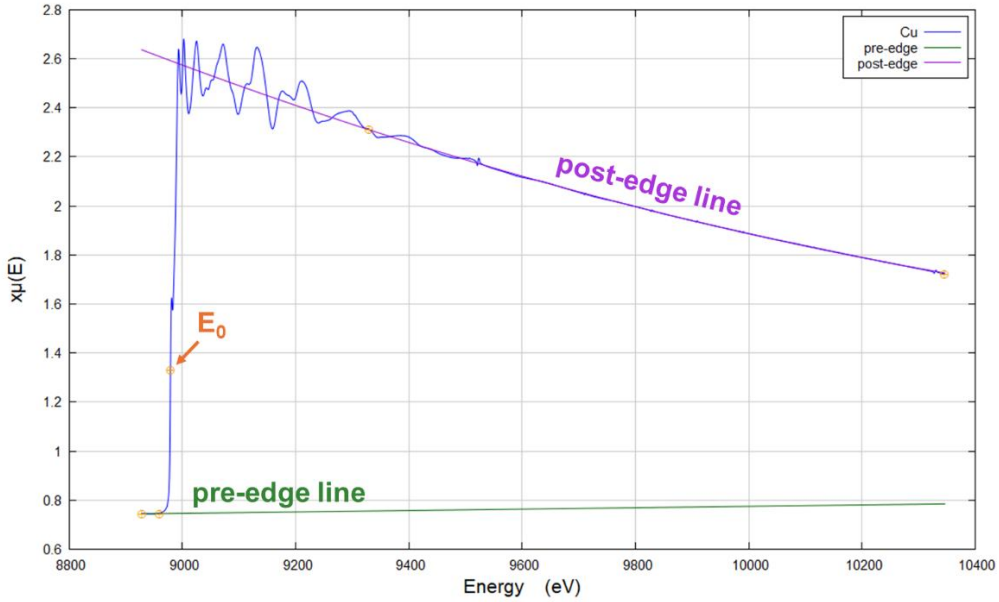

Figure 19. XAS data of a Cu foil at the Cu K-edge (blue). Showing the pre-edge line (green), post-edge line (purple) and binding energy (E_0, orange).

To display the normalized XAS data it is common to plot the post-edge part of the spectrum placed on y = 1.[200] This is done by subtracting the difference in slope and quadrature between pre- and post-edge lines from the data for energy values bigger than E_0. After normalization, the XANES region of the spectrum (**Figure 20**) can be evaluated by linear combination fitting (LCF) or multivariate curve resolution – alternating least squares (MCR-ALS) analysis described in **Section 3.2.4**. LCF analysis is a simple linear combination of standard spectra fitted to an unknown spectrum, to obtain quantities of standards in a mixture.

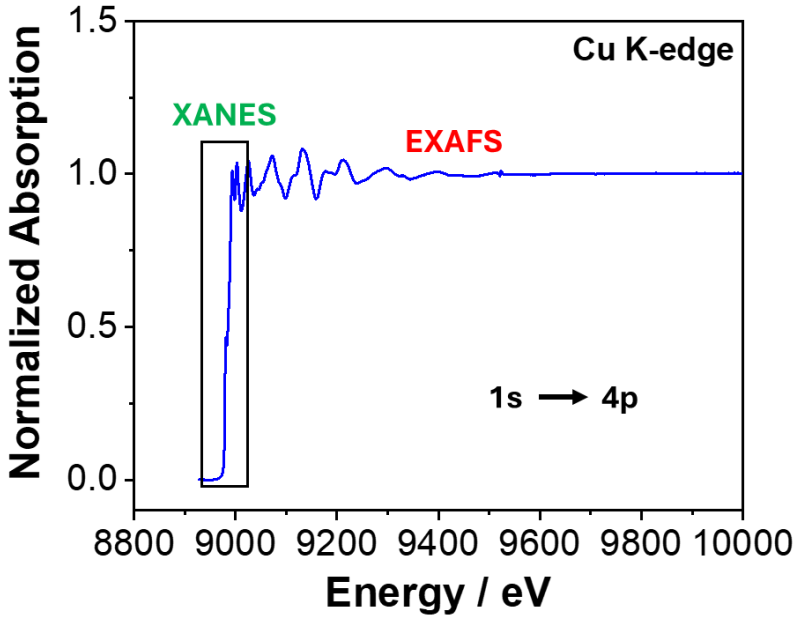

Figure 20. Normalized XAS spectrum at the Cu K-edge. Showing the XANES (green) and EXAFS region (red) as well as the orbital transition (1s → 4p) observed at this absorption edge.

For EXAFS analysis, further data processing steps are needed. First, the atomic background, which contains scattering of the ejected photoelectron from valence electrons and unspecific background factors from the spectrometer or detectors, needs to be removed. These low frequency oscillations cannot be measured directly and thus its analytical form must be determined by a least-square adjustment of a spline to the experimental data for completely removing the background (**Figure 21**).

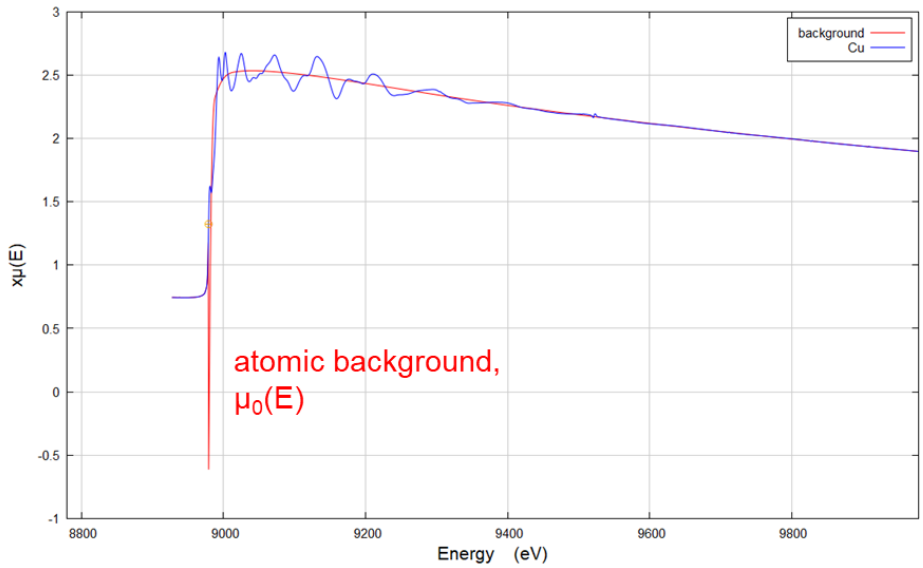

Figure 21. XAS data of a Cu foil at the Cu K-edge (blue). Showing the atomic background ($\mu_0(E)$).

With the atomic background ($\mu_0(E)$) the EXAFS function

$$\chi(E) = \frac{\mu(E) - \mu_0(E)}{\mu_0(E)} \tag{15}$$

is obtained. In the next step, $\chi(E)$ is converted into a k-dependent function $\chi(k)$ by using the relation

$$k = \sqrt{\frac{2m}{\hbar^2}(E - E_0^{exp})} \tag{16}$$

where m is the mass of the electron and $\hbar$ is the Plank's constant. E_0^{exp} is the experimentally determined absorption edge energy (orange label, **Figure 19**). Thus, $E - E_0^{exp}$ is the kinetic energy of the ejected electron. To obtain a pseudo radial distribution function, Fourier transformation (FT) of $\chi(k)$ is carried out according to

$$\tilde{\chi}(r) = \frac{1}{\sqrt{2\pi}} \int_0^\infty k^n \chi(k) e^{2ikr} dk\,. \tag{17}$$

Prior to the Fourier transformation the experimental spectrum is weighed by different powers of k^n (n = 0, 1, 2 or 3) to account for the weakening of the oscillations with increasing values of k. As a rule of thumb, for light elements a k-weight of 1 is used, while for transition metals usually a k-weight of 2 is employed. For very heavy elements k^3 is used. An example of k-dependent $\chi(k)$ and FT-transformed $\tilde{\chi}(r)$ data is shown in **Figure 22**.

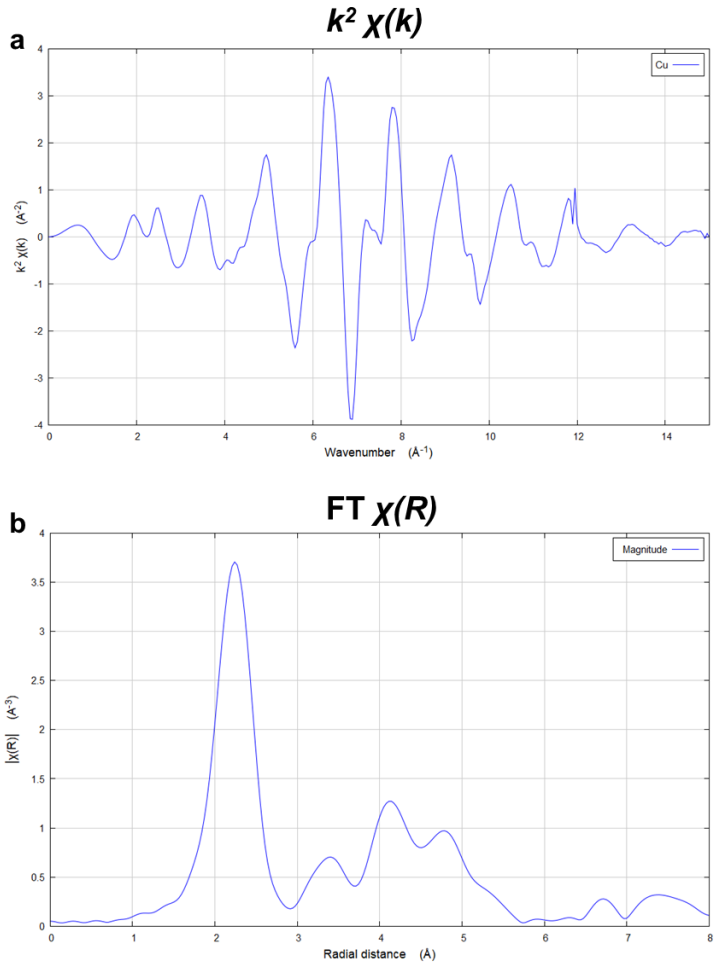

Figure 22. (**a**) k²-weighted Cu K edge EXAFS data in k-space and (**b**) corresponding Fourier-transformed EXAFS data of a Cu foil.

In order to obtain structural information from the EXAFS data, the theoretical EXAFS formula

$$\chi(k) = \sum_j S_0 \frac{N_j}{kr_j^2} F_j(k) e^{-2\sigma_j^2 k^2} e^{\frac{2r_j}{\lambda(k)}} sin\left[2kr_j + \varphi_{ij}(k)\right] \quad (18)$$

is fitted to the experimental data. S_0 is the amplitude reduction factor and accounts for the inelastic scattering effects. The backscattering amplitude $F_j(k)$ of an atom of type j and its total phase shift $\varphi_{ij}(k)$ are element specific parameters and are usually determined from a well-defined reference substance. While the number of neighboring atoms (N_j), and their distances

from the absorbing atom (r_j) and the degree of disorder (σ^2) are structural parameters and evaluated during the EXAFS fit analysis.

Pt-Ir NPs

For extracting, separating the Pt and Ir L3 edges, aligning, averaging and edge step normalization of the raw data, the ProQEXAFS software was employed.[201] For the potential jump experiments with 10 s holding time, two Quick-XANES spectra were averaged, while the spectra recorded every second were directly used for analyzing the 3 s experiments. The normalized XANES data was analyzed using multivariate curve resolution–alternating least squares (MCR-ALS) with the MCR-ALS GUI 2.0 MATLAB script.[202–204] This enables to establish the contribution of the different oxidation states of Ir and Pt species based on the reference spectra of metal foils and metal salts ($IrCl_3$ and IrO_2 or K_2PtCl_4 and K_2PtCl_6) (**Figure S3.1** in the **Appendix Chapter 10.1**), respectively. $IrCl_3$ and IrO_2 were mixed with a binder (cellulose) and measured as pellets, while K_2PtCl_4 and K_2PtCl_6 were recorded in a methanol solution in transmission mode. Ex-situ XANES spectra were analyzed with the software ATHENA by linear combination fit (LCF) method using these reference spectra.[200]

Cu_xO foams

*This paragraph is reprinted from Blaseio et al. in J. Mater. Chem. A, 2024, **12**, 28177–28192. https://doi.org/10.1039/D4TA02217C*

For background subtraction and edge step normalization of the Cu K-edge XAS spectra, the ProQEXAFS software suite[201] was used. The normalized data was analyzed using the MCR-ALS GUI 2.0 MATLAB script, performing MCR-ALS on the Quick-XANES data (see **Section 3.2.4**).[202–204] In addition, conversion of the energy units (eV) to photon electron wave factor k units ($Å^{-1}$) was carried out using the ATHENA software (Version: 0.9.26).[200] The resulting $\chi(k)$ functions were weighted with k^2 to account for the dampening of the XAS amplitude with increasing k. Using Fourier-transformation, the EXAFS spectra were transformed to obtain pseudo radial structure functions (RSFs). For EXAFS analysis the amplitude reduction factor (S_0^2) was determined from a Cu foil to be 0.89. The coordination number (N), interatomic bond length (R), mean squared bond length disorder (σ^2), and correction to the energy origin (ΔE_0), together with the error bars were established for Cu-Cu and Cu-O scattering pairs by fitting the theoretical EXAFS signals to the data in R-space using the ARTEMIS software[200] (Version: 0.9.26). Ex-situ XAS data of the reference materials (Cu foil, Cu_2O and CuO) and thermally annealed Cu_xO foams were collected every second for 6 – 10 min and subsequently averaged. Powder materials (Cu_2O, CuO) were mixed with a

binder (cellulose) and measured as a pellet. The IFEFF6 data for EXAFS fitting analysis, were determined from Cu (#9008468), Cu_2O (#1010963) and CuO (#9008961) taken from the crystal open database (COD).[205–207]

3.2.4. Multivariate Curve Resolution – Alternating Least Squares (MCR-ALS) Analysis

MCR-ALS is a MATLAB powered algorithm that can manage big coherent data sets. It is used to determine chemical constituents or species of an unresolved mixture, when no prior knowledge is available about the nature and composition of the mixture.[202] In order to apply MCR-ALS to a data set, only two requirements need to be fulfilled. The first requirement is that the experimental data must be structured as a two-way data matrix or multiset structure. Secondly, the data set should be explainable by a bilinear model using a limited number of components. For XAS data both requirements are usually fulfilled and thus MCR-ALS is becoming increasingly popular for analyzing dynamic Quick-XAS data sets.[147,203,204,208]

In MCR analysis relevant information of pure components in a mixture system is extracted through a bilinear model decomposition of the experimental data matrix D into product matrices C and S^T according to

$$D = CS^T + E\,. \tag{19}$$

C and S^T are the product matrices that contain the pure profiles of the components linked to the row mode (concentration profile) and column mode (spectra), respectively. E is the matrix of the noise in the data set, which cannot be explained by the components.[202] An example of an XAS data set D as well as by MCR-ALS analysis obtained components (S^T) and concentration profile (C) is outlined in **Figure 23**.

To solve the MCR bilinear model, constrained ALS algorithm is employed.[202] In the case of XAS data, several constraints can be applied: (i) non-negativity of the concentration and MCR-

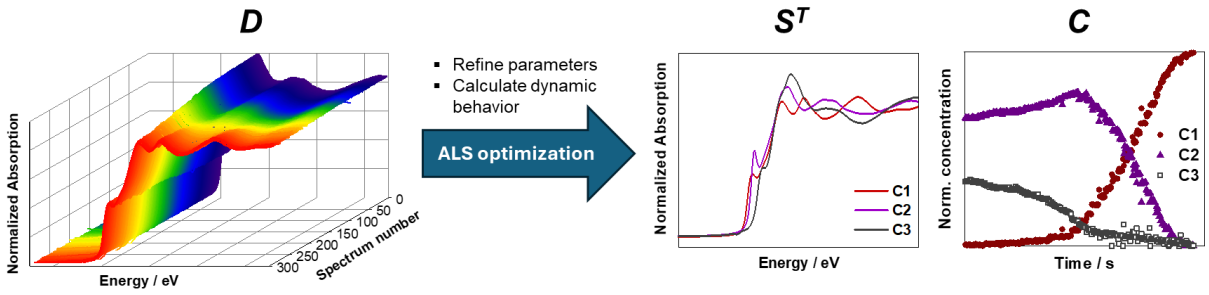

Figure 23. Schematic representation of the MCR-ALS analysis, outlining data set D, the obtained components (S^T) and concentration profiles (C) of the respective components by the constrained ALS optimization.

ALS spectra (C and S^T matrices), (ii) the total concentration of the components sums up to 1 (100 %) and if applicable (iii) unimodality.

The quality of the MCR-ALS model can be assessed by two parameters that show the dissimilarity between experimental data matrix and the MCR-ALS output. The first parameter is the data variance (R^2):

$$R^2 = 100 \sqrt{\frac{\sum_{i,j} d_{ij}^2 - \sum_{i,j} e_{ij}^2}{\sum_{i,j} d_{ij}^2}}. \quad (20)$$

The second parameter is the lack of fit to the data:

$$lof(\%) = 100 \sqrt{\frac{\sum_{i,j} e_{ij}^2}{\sum_{i,j} d_{ij}^2}}. \quad (21)$$

In both formulas d_{ij} is an element of the experimental data matrix and e_{ij} is the residual value obtained from the difference between the experimental data and the reproduced data (CS^T).[202] Detailed examples of the MCR-ALS analysis in MATLAB using XAS data from the case studies are outlined in the **Appendix Chapters 10.1** and **10.3**.

3.3. Raman Spectroscopy

3.3.1. The Raman Scattering Process

The light scattering process (**Figure 24**) during Raman measurements involves an incident (laser) light consisting of an electromagnetic field, which induces an oscillating dipole in the molecule. The induced dipole moment is a result of the molecular polarizability α, which is the ability of the electron cloud to deform about the molecule, when an electric field is applied.[209] Most of these light-scattered photons will be elastically scattered, i.e. will have the same energy as the incident radiation, which is known as Rayleigh scattering. Whereas Raman scattering consists of photons that have either a lower energy (longer wavelength) or a higher energy (shorter wavelength) compared to the incident photons. Hence, Raman scattering can be further divided into Stokes and anti-Stokes Raman scattering, where Stokes scattering consists of the lower energy and anti-Stokes of the higher energy radiation. Both the Raman and Rayleigh scattering involve excitation to a virtual energy state, followed by scattering of a photon.

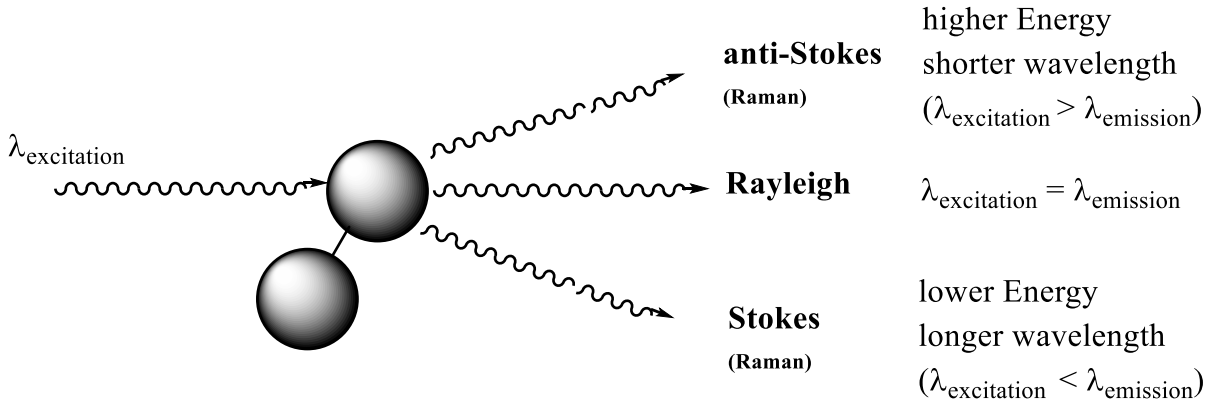

Figure 24. Schematic representation of the light scattering process.

As outlined in **Figure 25**, in Stokes Raman scattering the molecule is excited from a ground state and relaxes back into the first vibrational state. Thus, the energy of the scattered light is smaller compared to the energy of the incident photon. During anti-Stokes Raman scattering, the molecule is already in a vibrational excited state and relaxes back into the ground vibrational state. Thus, the photon scattered has a higher energy than the incident one (**Figure 25**). Since more molecules at room temperature are in the ground state, Stokes scattering is more intense than anti-Stokes scattering.

The intensity (I_R) of Raman scattered radiation is given by:

$$I_R = v^4 I_0 N \left(\frac{\delta\alpha}{\delta Q}\right)^2 \quad (22)$$

where I_0 is the incident laser intensity, N is the number of scattering molecules in a given state, ν is the frequency of the exciting laser, α is the polarizability of the molecules and Q is the vibrational amplitude. This equation shows that a laser with a shorter wavelength e.g. 457 nm generates a greater intensity of the Raman signal. However, a short wavelength means the light is more energetic and can give strong fluorescence interference or cause burning of the sample under investigation. Thus, using a longer wavelength into the near-infrared (NIR) region can be used to overcome these issues.

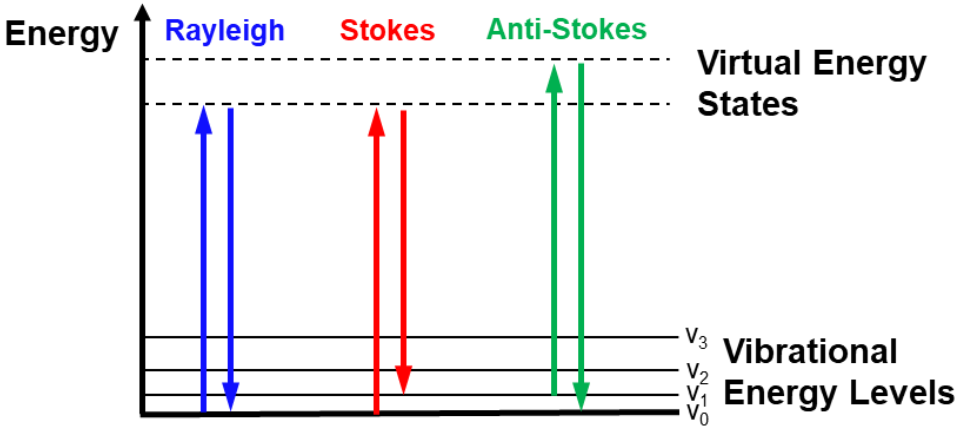

Figure 25. Schematic representation of the Raman (Stokes/Anti-Stokes) and Rayleigh scattering processes.

When the incident light interacts with a polarizable analyte molecule, it induces an oscillating dipole. Since the electric field of the light is oscillating as a function of time at a frequency ν_0, it induces an oscillating dipole moment at the same frequency. The magnitude of this dipole moment (μ_{IND}) is proportional to the applied electric field (E) and the polarizability of the molecular electron cloud (α), which is an intrinsic property of the molecule. This induced dipole scatters the light in all directions.

3.3.2. Molecular vibrations

Whether a molecule is Raman active depends on the symmetry of the molecule. The symmetry of a molecule can be determined by group theory and the allocation of point groups. Additionally, for molecules with a center of symmetry, the mutual exclusion rule applies, which states that no vibrations can be both infra-red and Raman active.

Bulk metals in the metallic state show no Raman active bands, since as outlined above a change in polarization is an essential requirement for a Raman spectrum. Pure metals do not show a polarizability change and therefore do not show Raman peaks. Thus, in electrochemical Raman measurements metallic surfaces cannot be observed directly. However, potential dependent adsorbates or oxide species formed/reduced can still be monitored.

3.3.3. Surface Enhanced Raman Spectroscopy (SERS)

In general, the SERS effect describes the enhancement of the Raman scattering signal of an analyte in close proximity to a nanostructured metallic surface. This enhancement is generally agreed to result from an amplification of electromagnetic fields, which are generated by the excitation of localized surface plasmons.[210] The main factor for the enhancement is explained by electromagnetic mechanisms exhibited by nanostructured metallic materials.[210] Essentially, the vibration of the electrons within a metal lead to a large enhancement of the localized electric field and in turn enhance the scattering intensity of the molecules within the range.[211–213] The SERS effect leads to a total field enhancement up to the fourth power, making it a very significant effect. As the range of the enhancement is limited (10 – 100 Å), SERS is considered as a very surface-sensitive technique.[214,215]

Most commonly SERS is used with metallic nanoparticles as a further effect of the enhancement occurs. The free electrons on the surface of a metallic nanoparticle are excited by electromagnetic wave irradiation and thereby undergo collective oscillation. This oscillation generates an electromagnetic wave. When the frequency of the incident light wave is the same as the intrinsic frequency of the oscillating electrons an enhancement factor of the Raman scattering signal of an analyte molecule in the radiation range of $10^6 - 10^{11}$ can be achieved.[210,216] This enhancement is known as surface plasmon resonance.

3.3.4. Set-up of a Confocal Raman Microscope

A standard set-up of a confocal Raman microscope and an image of the WITec alpha300 RSA microscope used in the experiments in this thesis can be seen in **Figure 26**. The instrument combines a Raman spectrometer with a confocal microscope, allowing the laser beam to be focused onto the sample by the microscope lens. This generates a better resolution of the Raman spectra, compared with a traditional Raman spectrometer. In the case of the in-situ electrochemical Raman spectroscopy, a water immersion objective was used. Water has a higher refractive index than air and thus a higher Numerical Aperture (NA) of the objective is achieved leading to a better resolution. When coupled to a camera, the confocal Raman microscope can image or map samples, while collecting the Raman spectra. In general, spectral collection is achieved by a charge coupled device (CCD). Before collecting, the Raman scattered light is separated into each wavelength by a pinhole and spectrometer. This then generates the total Raman spectrum.

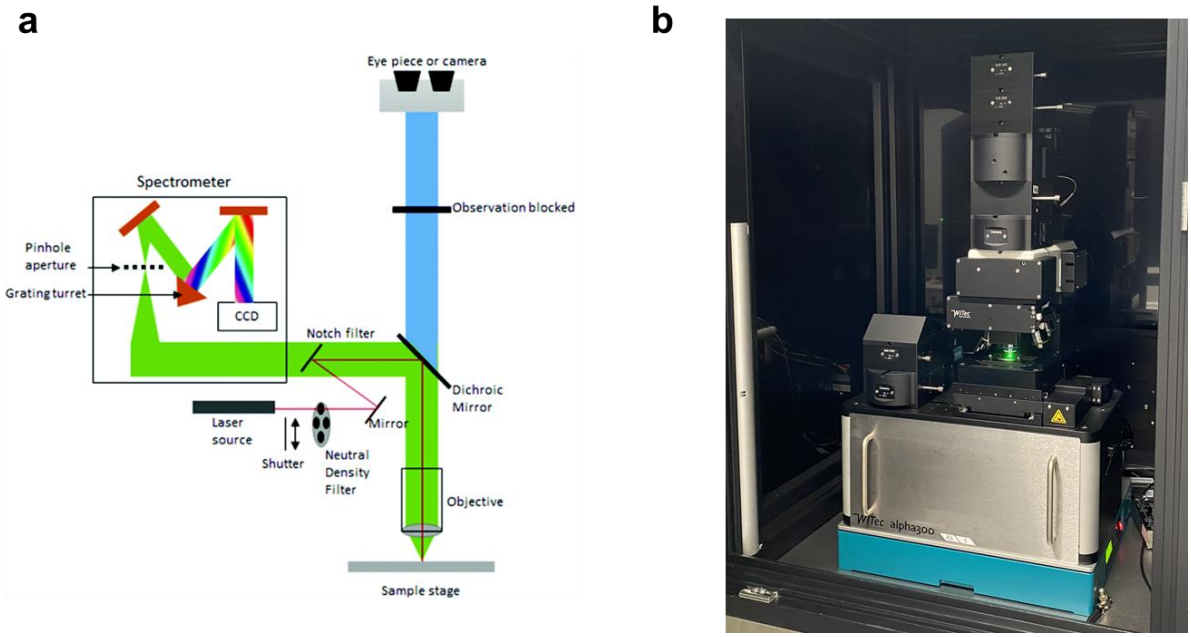

Figure 26. (**a**) Standard configuration of a Raman microscope. Reprinted from Smith et al.[217](**b**) Image of WITec alpha300 RSA confocal microscope.

3.3.5. Design and set-up of the spectro-electrochemical Raman Cell

In order to measure in-situ Raman data, a spectro-electrochemical Raman Cell was designed based on the VDI 2221 guideline.[218] The development process of this guideline is described only very briefly. After an initial phase of defining and clarifying the specifications, principal solutions and function structures are developed. Followed by a design phase, where realizable modules are arranged, and key modules are developed to obtain an overall layout of the design. The requirements for the development of the electrochemical Raman cell are summarized in **Table 3**.

Table 3. *Requirement list for the design of the electrochemical Raman cell.*

Requirements	**Parameter/Data**
Dimensions of the Cell	max. 70 x 70 x 22 mm
Dimensions of the Zeiss 63× Objective	M27 (Ø 27 mm); working distance 2.5 mm
4 screws with equal pressure	
Reference Electrode (Ag/AgCl)	Ø 2 mm; length: 44 mm
O-Rings	stable in acids at pH = 1
Material	stable in acids at pH = 1
Space for counter electrode/gold mesh and connection to potentiostat with screw	M3
Sample thickness	2 mm

Based on these the design of the Raman cell shown in **Figure 27** was developed. The cell consists of two parts that are held together by four M4 screws to obtain equal pressure distribution on all O-Rings. The top part contains the compartment for the counter electrode, which consists of a gold mesh and a gold wire that is connected to a cable lug allowing a simple connection to the potentiostat. Furthermore, it includes a threaded hole on the same side for inserting the reference electrode using M6 fittings. A groove for an O-ring is placed at the bottom of the top part. This O-ring is used to seal the sample from the top, preventing leakage of the electrolyte between the two cell parts. All O-ring grooves in the cell were designed based on DIN ISO 3601-1.[219] The bottom part comprises the holder for the sample (working electrode) and a groove for a second O-ring below the sample preventing electrolyte leaking through the contacting hole at the bottom of the cell. An extra larger O-Ring (d = 45 mm) is placed around the working electrode holder and provides an extra barrier for leakage between the top and bottom parts. This groove is designed to be gas tight and thus the bottom part of the cell can, with a further developed top compartment, in future be used for experiments with gas saturation. A picture of the assembled electrochemical cell at the WITec alpha300 RSA microscope is displayed in **Figure 28**.

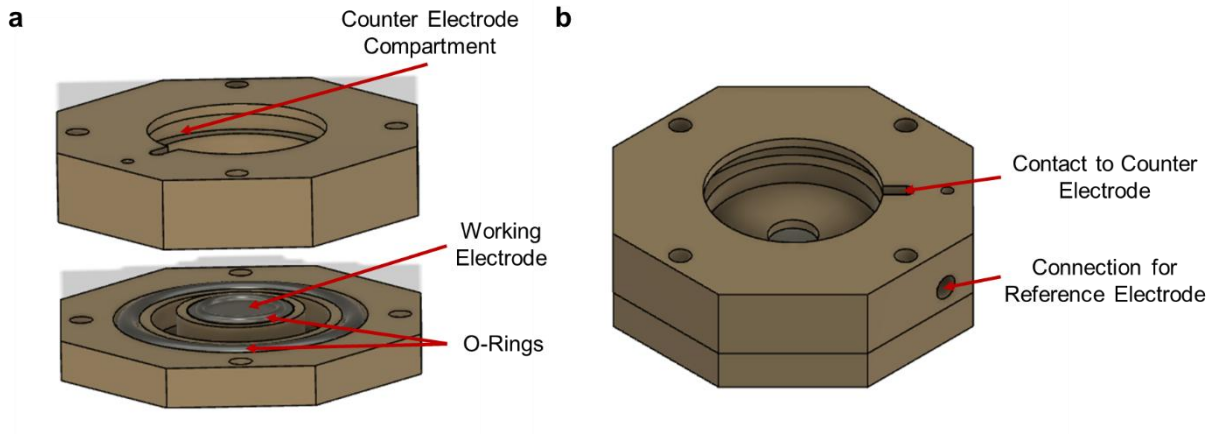

Figure 27. Schematic drawings of the electrochemical Raman Cell in exploded view (**a**) and oblique view (**b**). For the manufacturing of the cell Polyetherketon (PEEK) was used and O-rings made from Viton® are employed, which are stable in acids at pH = 1.

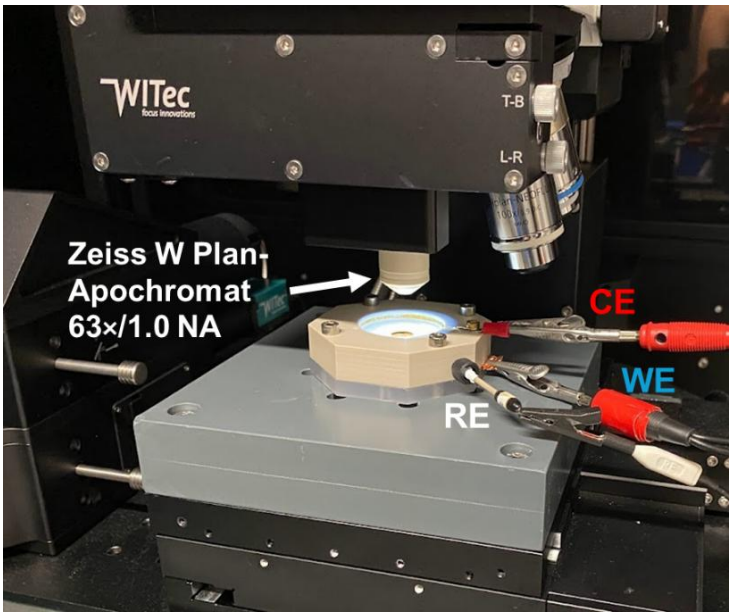

Figure 28. Image of the spectro-electrochemical Raman cell under WITec alpha300 RSA confocal microscope. CE = Counter Electrode, WE = Working Electrode and RE = Reference Electrode.

3.3.6. In-situ Raman Data Collection of the Pt-Ir, Pt and Ir thin films

Electrochemical measurements were conducted in a three-electrode custom-made spectro-electrochemical cell (**Figure 28**) using a potentiostat (Gamry, Reference 600). The sputtered Pt-Ir thin films on the GDL (Freudenberg, H23C6) were used as the working electrode and a gold mesh as the counter electrode. As a reference electrode a mercury-mercury sulfate electrode (ALS-Japan, RE-2CP) was employed. All measurements were conducted in 0.1 M $HClO_4$. A chronoamperometric method was used by increasing the potential in 100 mV steps from 0.3 V_{RHE} to 1.6 V_{RHE}. All reported potentials were corrected for the iR drop.

Raman spectra of the Pt-Ir thin films were acquired by a Witec alpha300 RSA confocal microscope using an excitation wavelength of 785 nm with a laser power of 2 mW, a 300 l mm^{-1} grating and Zeiss W Plan-Apochromat 63×/1.0 NA objective. At each potential, Raman spectra were recorded with 5 s acquisition time averaged over 50 exposures. Ex-situ Raman spectra were recorded with a Zeiss EC Epiplan-Neofluar Dic 50×/0.8 NA objective using 1 mW laser power. All Raman spectra were background subtracted and smoothed using Savitsky Golay filtering over a window size of 32 points using the software Project SIX (WITec, version 6.1).

4. Results and Discussion

4.1. Mechanistic Insights into the HER-OER Bifunctionality of Cell-Reversal Tolerant Pt-Ir NPs using operando Quick-XANES

Co-authors' contributions: G. Ioselli and P. Seidel synthesized the Pt-Ir NPs and conducted the electrochemical measurements in the RDE set-up. G. Ioselli and J. Klein supported the *operando* Quick-XAS measurements. M. Oezaslan supervised the work.

In this chapter, the dynamic (oxidation-reduction) transitions and electronic interactions of cell reversal tolerant Pt-Ir NPs during HER and OER are investigated by Quick-XANES. The bimetallic Pt-Ir NPs (1:1 and 3:1 ratios) were prepared by two synthesis routes (surfactant-free colloidal and wet impregnation – annealing). Pt-Ir NPs prepared by the colloidal route are small (<2 nm) and mostly amorphous, while the wet-impregnation method prepares larger Pt-Ir NPs with higher crystallinity. *Operando* Quick-XANES potential jump experiments between – 0.02 V_{RHE} for HER and + 1.55 V_{RHE} for OER with holding times of 3 s and 10 s were conducted. This allows to investigate dynamic oxidation-reduction processes and electronic interactions between both metals. Our results show that at – 0.02 V_{RHE} metallic Pt is rapidly formed for all catalysts independent of the holding time and Pt:Ir ratio. In contrast, the respective oxidation to Pt^{2+} species at + 1.55 V_{RHE} occurs at a much slower rate. Colloidal Pt-Ir NPs consist of mostly Ir^{4+} species during OER, which are reversibly and partially reduced to Ir^{3+} species during HER. Rapid Ir^{3+} to Ir^{4+} oxidation kinetics (~1 – 2 s) at + 1.55 V_{RHE} compared to the respective reduction transition at – 0.02 V_{RHE} were found. More crystalline and larger Pt-Ir NPs exhibit very sluggish oxidation processes of Ir^0 and Ir^{3+} to Ir^{4+} species during OER. In addition, we observe electronic interactions between Pt and Ir within the bimetallic particles.

4.1.1. Initial structure of the as-prepared Pt-Ir nanoparticles

In this work, alloyed Pt-Ir nanoparticles (NPs) with 1:1 and 3:1 ratios were prepared by two different synthetic routes (for experimental details see **Appendix Chapter 10.1**). The first route involves the surfactant-free colloidal synthesis reported previously by Quinson et al.[220–223] and NPs prepared by this route will be referred to as "colloidal" throughout this work. From the TEM images (**Figure 29 a**,**b**), colloidal NPs are well dispersed on the carbon substrate and have a very small particle diameter of ~ 2 nm irrespective of the Pt:Ir ratio (TEM Pt_3Ir-colloidal in **Figure S1.2a**,**b** of the **Appendix Chapter 10.1**). XRD profiles (**Figure S1.3)** of these colloidal NPs show very broad peaks, confirming the small crystallite size and indicate an amorphous structure. For the PtIr-colloidal NPs, Rietveld refinement analysis was not possible due to peak broadening. An increase in the amount of platinum results in slightly sharper diffraction peaks, indicating a more crystalline structure for the Pt_3Ir-colloidal NPs. Rietveld refinement confirms the small crystallite size of 2 nm and the expected alloy composition of $Pt_{77}Ir_{23}$ obtained by Vegard's law (**Table S1.1**).

The second synthesis route involves the wet-impregnation – freeze drying – thermal annealing synthesis method,[224,225] that will be referred to as "WI" throughout this work. As shown in **Figure 29 c**,**d** and **S1.2c**,**d**, NPs prepared by this route have a larger size distribution with an average diameter of 3 – 4 nm. XRD data of these PtIr- and Pt_3Ir-WI NPs reveal sharper diffraction peaks, indicating a more crystalline structure and larger crystallite size (**Figure S1.3**). Quantitative Rietveld refinement confirms the larger crystallite size of 3 – 4 nm. The alloy composition of the main phase ($Pt_{56}Ir_{44}$) deviates only slightly from the expected ratio for the PtIr-WI NPs. The Pt_3Ir-WI NPs show a slight enrichment of Pt within the alloy ($Pt_{80}Ir_{20}$). In addition, elemental analysis using energy-dispersive X-ray spectroscopy (EDX) shows that the Pt:Ir ratios (1:1 and 3:1) for all Pt-Ir NPs are as expected (± 2 wt.%, **Table S1.2**).

To understand the initial chemical state of the platinum and iridium species within the bimetallic Pt-Ir NPs, ex-situ XANES spectra were collected for 10 min at the Pt and Ir L3 edges and subsequently analyzed by the linear combination fit (LCF) method. The ex-situ XANES spectra and respective LCF analysis for all Pt-Ir NPs are shown in **Figure S1.4**. Generally, both the Pt and Ir L3 edges show the transition of an electron from the 2p → 5d orbital upon absorption of the X-ray radiation.[226] In case of metallic Ir, this process occurs at 11 215 eV and for metallic Pt at 11 564 eV. Thus, an increase, shift and/or broadening in absorption edge are associated with a higher oxidation state of the element. More precisely, for Ir^{3+} and Ir^{4+} species the energy of the maximum white line position is shifted to 11 218 eV and 11 220 eV, respectively. The

absolute energy shifts for the oxidized platinum species are very similar with 11 567 eV (Pt^{2+}) and 11 568 eV (Pt^{4+}).

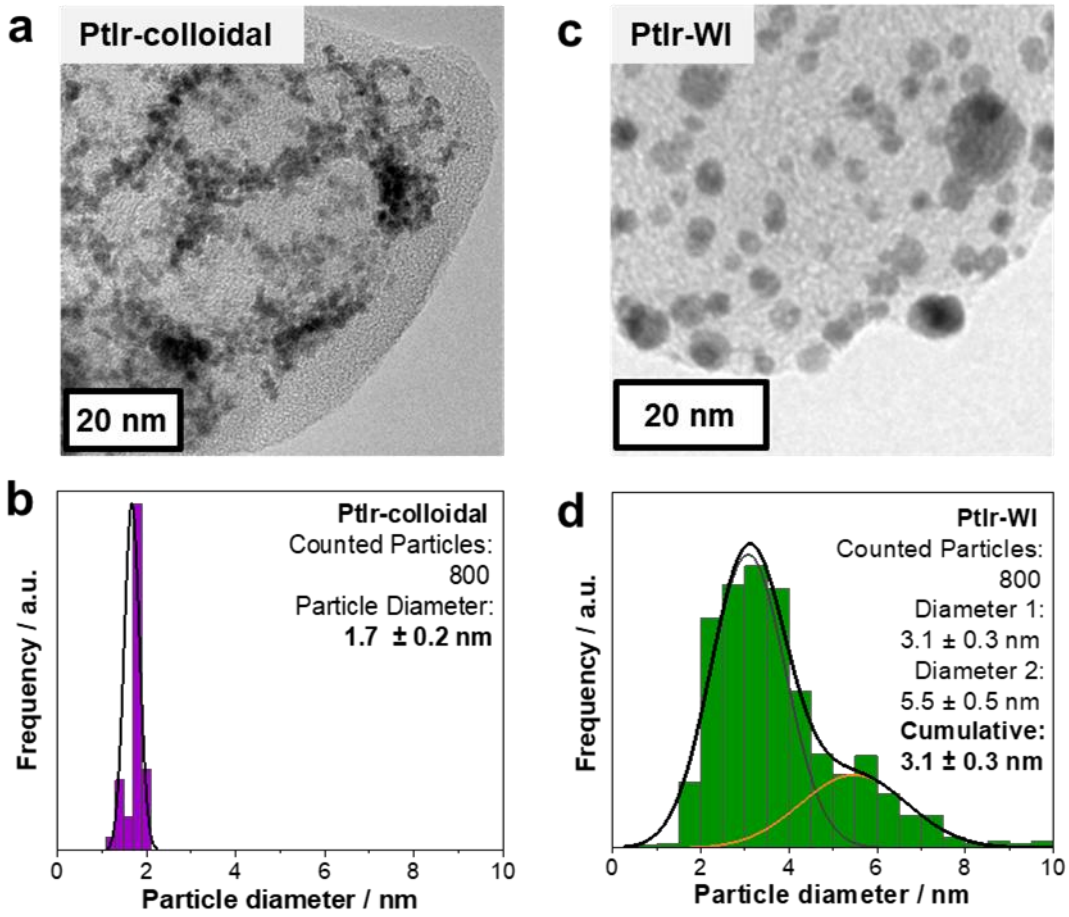

Figure 29. TEM micrographs (**top panel**) and respective particle size distributions (**bottom panel**) of the PtIr-colloidal (**a,b**) and PtIr-WI (**c,d**) NPs supported on carbon. The PtIr-WI NPs show two different particle size distributions i.e. a smaller diameter with 3.1 ± 0.3 nm (dark grey line) and a larger diameter with 5.5 ± 0.5 nm (orange line). For the cumulative particle size, the two diameters were weight based on the particle count resulting in 3.1 ± 0.3 nm (black line).

All ex-situ Pt L3 edge XANES spectra of the PtIr and Pt_3Ir NPs prepared by the colloidal and wet-impregnation routes are essentially identical and have a higher white line compared to metallic Pt, indicating the presence of oxidized platinum species (**Figure S1.4a**). This is confirmed by the LCF analysis, which results in a contribution of around 60 ± 2 % Pt^0 and 40 ± 2 % Pt^{2+} species irrespective of the Pt:Ir ratio and synthesis route. The ex-situ Ir L3 edge XANES spectra of the colloidal NPs have a much higher white line, are much broader and are shifted to higher energies, compared to the ones prepared by the wet-impregnation route (**Figure S1.4b**). This points out a difference in the contribution of Ir^0, Ir^{3+} and Ir^{4+} species between the two synthesis routes. LCF analysis (**Figure S1.4d**) indicates, that no metallic Ir is found for the PtIr- and Pt_3Ir-colloidal NPs, while the NPs prepared by the WI synthesis contain

~20 – 30 % Ir^0 species. In addition, the Ir^{4+} species content is around 4-times higher for the colloidal NPs compared to the WI NPs. The most dominant species with the largest contribution (~50 – 70 %) is the Ir^{3+} species independent of the synthesis route of the Pt-Ir NPs.

Altogether, Pt-Ir NPs prepared by the WI route are larger (4 nm vs. 2 nm) and more crystalline compared to the colloidal ones. In case of platinum, the extent of oxidation of the Pt-Ir NPs is very similar (40 % Pt^{2+} species) and independent of the synthesis route. For iridium, the synthesis route determines the oxidation state. PtIr- and Pt_3Ir-colloidal NPs are fully oxidized to Ir^{3+} and Ir^{4+} species. In contrast, the NPs prepared by the WI route consist of partially metallic Ir (20 – 30 %), a high contribution of Ir^{3+} species (almost 70 %) and only very minimal amounts of Ir^{4+}species (≤10 %).

4.1.2. Bifunctionality of PtIr NPs towards HOR and OER

In order to establish the catalytic activity of the bimetallic Pt-Ir NPs, polarization curves for HOR and OER were collected (for experimental details see **Appendix Chapter 10.1.)**. The HOR polarization curves for the PtIr NPs prepared by both the WI and colloidal routes as well as commercial Pt NPs and IrO_x references in H_2-saturated 0.1 M $HClO_4$ are presented in **Figure 30a**. For all platinum containing materials, the polarization curves reach a plateau at ~0.05 V_{RHE} and overlap with the diffusion limiting current (j_{diff}), indicating that the HOR is completely controlled by mass transport. Since IrO_2 is not active for the HOR, no Faradaic oxidative current is observed.

The OER polarization curves for the same materials (PtIr-colloidal, PtIr-WI, Pt-TEC and IrO_x-TEC) in argon-saturated 0.1 M $HClO_4$ are displayed in **Figure 30b**. Obviously, all iridium-containing catalysts show sufficient OER activity, while the Pt NPs are less active, evident by the very limited oxidative current. The Pt-Ir surface area-based specific activities (SAs) at 1.50 $V_{RHE,iRfree}$, are shown in **Figure 30c** and follow the order: PtIr-WI > PtIr-colloidal >> Pt NPs. Note that for IrO_x-TEC no H_{UPD} can be obtained due to the absence of metallic Ir. The Ir-based mass activities (MA) are plotted in **Figure 30d**. The pure IrO_x has the highest MA with 91 ± 4 A g^{-1}_{Ir}, followed by the bimetallic PtIr-colloidal NPs (63 ± 6 A g^{-1}_{Ir}) and PtIr-WI with a MA of 46 ± 11 A g^{-1}_{Ir} at 1.50 $V_{RHE,iR\text{-}free}$. The apparent differences in MA and SA can be explained by the particle size effect. The PtIr-WI NPs, have a smaller H_{UPD} as a result of the larger particle diameter resulting in an increased SA compared to the smaller colloidal NPs that have a larger H_{UPD}.

Overall, the Pt-Ir NPs prepared by both routes show activities towards HOR as well as OER, confirming the bifunctionality for both reactions. This establishes the ability of the Pt-Ir NPs to

catalyze the HOR during normal operation of a PEM fuel cell and OER during the cell reversal event.

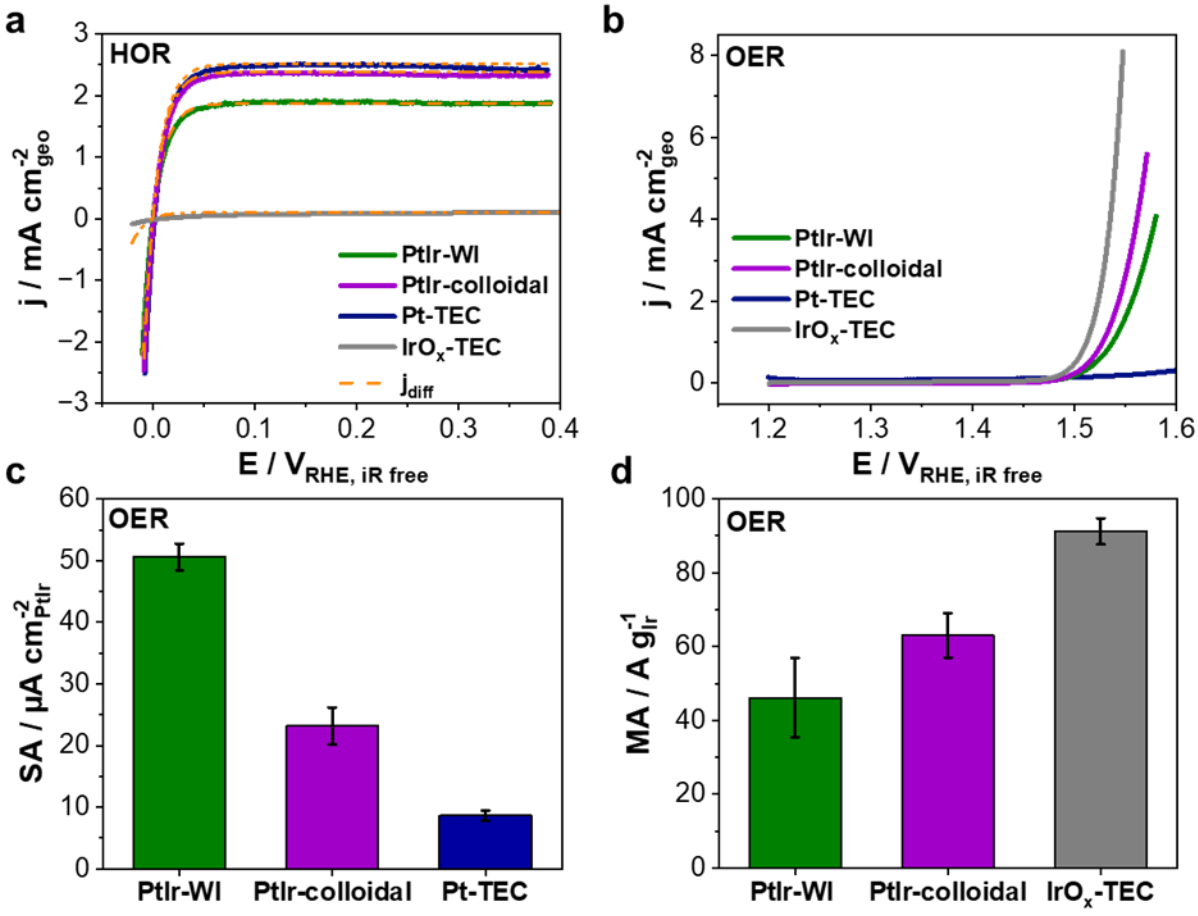

Figure 30. (**a**) HOR and (**b**) OER polarization curves of the PtIr-WI (green line), PtIr-colloidal (purple line), commercial IrO_x-TEC (grey line) and commercial Pt-TEC (blue line). The catalyst loading was 8 μg_{metal} cm^{-2}_{geo}. For HOR, LSVs were measured from – 0.02 to + 0.4 $V_{RHE,\ iR\text{-}free}$ at a scan rate of 10 mV s^{-1} and 1600 rpm in H_2-saturated 0.1 M $HClO_4$. The data of the Pt-Ir NPs is overlaying with the diffusion limiting currents (j_{diff}, orange dashed line). The OER polarization curves were measured from 1.2 to 1.6 $V_{RHE,\ iR\ free}$ at 6 mV s^{-1} and 2000 rpm in argon-saturated 0.1 M $HClO_4$. (**c**) Specific activities (SA) and (**d**) Ir-based mass activities (MA) towards OER were determined at 1.50 $V_{RHE,\ iR\text{-}free}$.

4.1.3. *Operando* Quick-XANES potential jump experiments between HER and OER

In order to investigate the dynamic oxidation state changes between HER and OER occurring within a few seconds, *operando* Quick-XANES spectra at the Pt and Ir L3 edges were recorded during chronoamperometric jump experiments between HER (– 0.02 V_{RHE}) and OER (+ 1.55 V_{RHE}) in argon saturated 0.1 M $HClO_4$. Since the spectro-electrochemical set-up does not allow for fast gas switching from hydrogen to argon and sufficient saturation time, the HER was studied instead of the HOR. Each potential was held for 3 s and the alteration (between

HER and OER) was repeated for 60 s. A schematic representation of the chronoamperometric potential jump experiments is displayed in **Figure S1.5**.

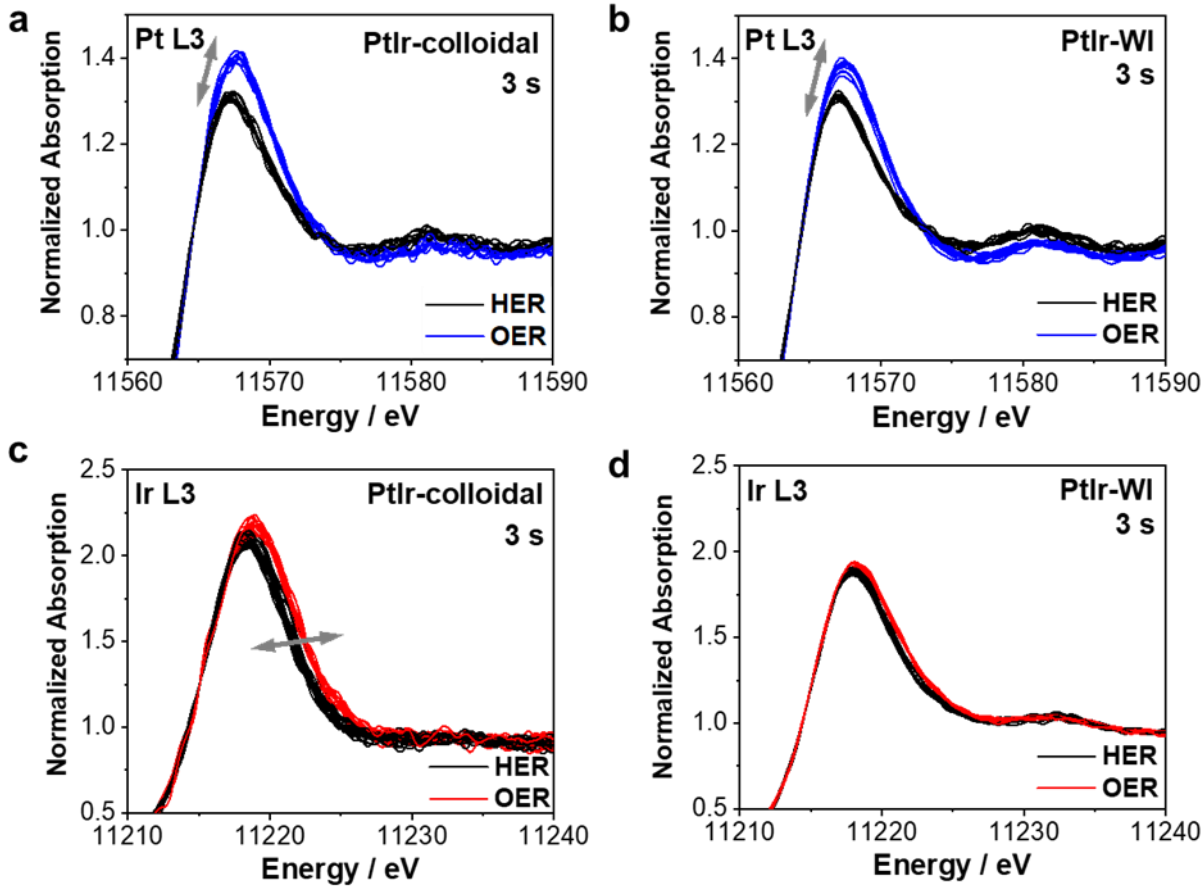

Figure 31. *Operando* Quick-XANES spectra of the PtIr-colloidal (**a,c**) and PtIr-WI (**b,d**) NPs recorded at the Pt and Ir L3 edges. Spectra were collected every second and subsequently averaged over 3 s during the potential jump experiments between HER (– 0.02 V_{RHE}, black) and OER (+ 1.55 V_{RHE}, blue or red for Pt or Ir, respectively) with holding times of 3 s in argon-saturated 0.1 M $HClO_4$ and subsequently averaged by three.

For the PtIr NPs prepared by the colloidal and WI routes, the *operando* Ir and Pt L3 edges Quick-XANES spectra recorded at – 0.02 V_{RHE} (HER, in black) and + 1.55 V_{RHE} (OER, in blue or red for Pt or Ir, respectively) during the potential jump experiment are displayed in **Figure 31.** The same normalized spectra with a larger energy range are displayed in **Figure S1.6**. Independent of the synthesis route (colloidal or WI), the XANES spectra obtained at the Pt L3 edge (**Figure 31a**,**b**) reveal a similar reversible increase-decrease in white line intensity (WLI) upon oxidation during OER. More precisely, the black spectra (HER) have a WLI of around 1.3, while for the blue spectra (OER) it increases to ~1.45, which is accompanied by a slight shift in the position of the maximum of the white line to higher energies. This WLI during OER is comparable to the ex-situ Pt L3 edge XANES spectra, indicating that the reduction of the Pt^{2+} species commences as soon as – 0.02 V_{RHE} are applied.

In contrast, Ir L3 edge XANES spectra recorded of the PtIr-colloidal NPs displayed in **Figure 31c** show a slight increase in WLI (~2.15 to 2.25) and shift in the position of the maximum accompanied by a distinct broadening upon jumping the potential to + 1.55 V_{RHE} (OER, red spectra). This high WLI (>2.15) indicates that there are little changes in the Ir L3 edge XANES spectra compared to the ex-situ measurement. The pronounced broadening of the iridium L3 edge XAS spectrum has been confirmed experimentally and by theoretical calculations and is attributed to a surface oxidation involving the transition from Ir^{3+}-OH to Ir^{4+}-O surface species.[227,228] The Ir L3 edge XANES spectra of the PtIr-WI (**Figure 31d**) exhibit a much lower WLI (~2.0) compared to the PtIr-colloidal during both reactions, showing only minimal broadening and almost no change in white line during OER. This lower WLI matches the ex-situ XANES spectra, indicating little structural changes of the PtIr-WI NPs upon exposure to the electrolyte and HER/OER potentials.

Dynamic oxidation state changes of PtIr-colloidal NPs

To determine the dynamic changes in the chemical state of the Pt and Ir species the XANES spectra obtained were analyzed using MCR-ALS analysis. A detailed example of the MCR-ALS analysis using MATLAB is shown in **Figure S1.7**.

The normalized concentration profiles obtained by the MCR-ALS analysis of the Pt and Ir L3 edges XANES spectra for the PtIr-colloidal NPs during the first 25 s are displayed in **Figure 32**. For platinum, the MCR-ALS analysis was conducted using Pt^0 (Pt foil) and Pt^{2+} (K_2PtCl_4) references and the normalized concentrations of these species are shown in **Figure 32a**. During HER the dominant species is metallic Pt with around 90 %, while around 10 % remain in the Pt^{2+} state. Upon jumping the potential to + 1.55 V_{RHE} the oxidation of metallic Pt commences, resulting in a Pt^{2+} species concentration of around 50 – 60 % (40 – 50 % Pt^0). This behavior is fully reversible for 60 s as demonstrated in **Figure S1.8a**. It is noted that Pt^{4+} species are usually expected under these OER conditions,[55,57,58] but the short oxidation time of 3 s during OER is not sufficient to form the thermodynamically stable PtO_2. For instance, potential jump experiments with holding times of 180 s show that Pt^{4+} is formed after ~20 – 30 s at + 1.55 V_{RHE} (**Figure S1.9**). To validate our hypothesis, we plotted the ΔXANES of the Pt L3 edge spectra recorded during OER for 3 s and 180 s using metallic Pt as a reference (**Figure S1.10**). The ΔXANES data with the 3 s intervals shows a small peak around the absorption edge that has been reported by Ramaker et al. and is assigned to adsorbed OH groups on the Pt surface.[229] As the holding time is increased from 3 s to 180 s this peak is no longer observed. A positive amplitude ~+ 5 eV and negative amplitude with around + 15 eV above the absorption edge is

observed for both holding times, showing the presence of Pt-O.[229] These amplitudes are increasing with the holding time, correlating to an increase in oxygen atoms. Similar results were also found by Imai et al.[230] showing by XAS of 2 nm Pt NPs that PtO_2 formation only commences after 100 s. We thus conclude that for holding times below 20 s only kinetically controlled Pt^{2+} species are formed.

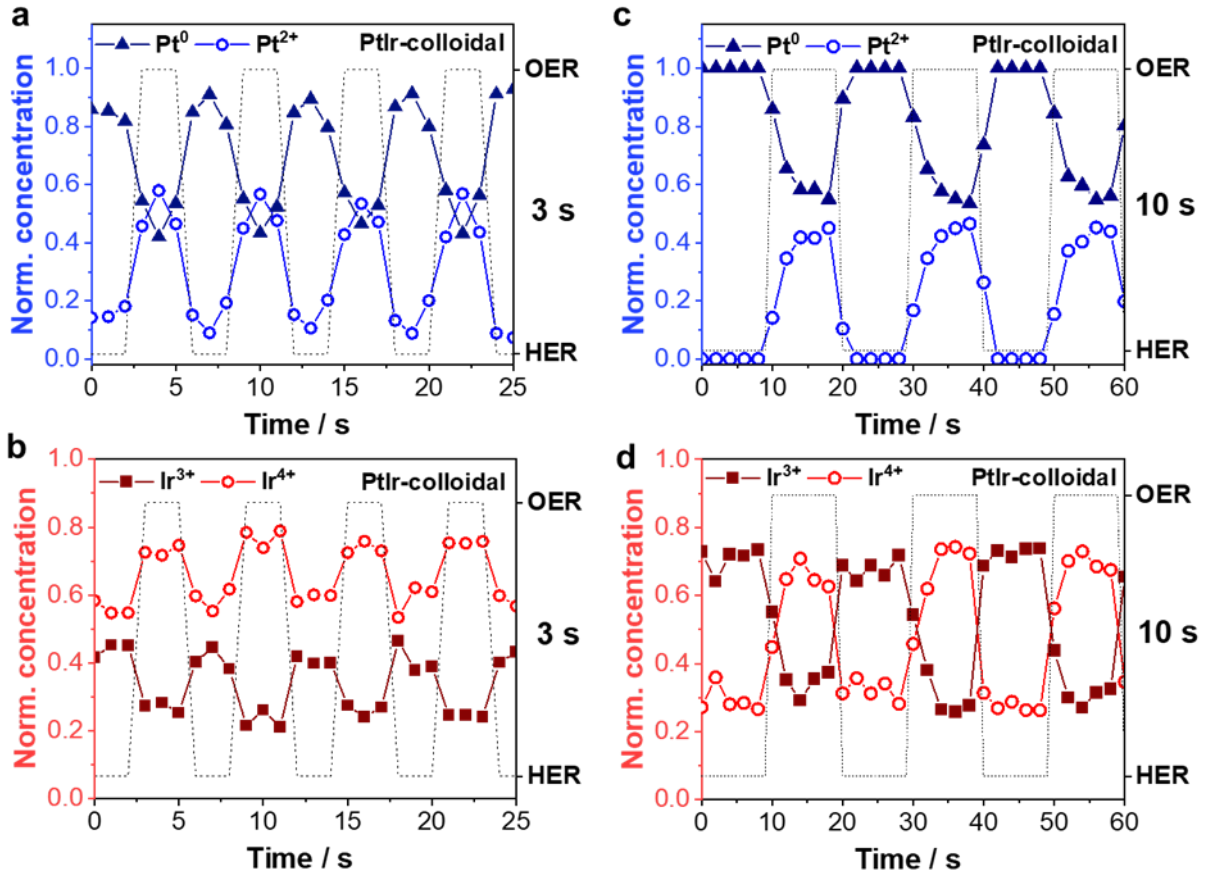

Figure 32. Concentration profiles of the Pt^0 and Pt^{2+} (**top**) as well as Ir^{3+} and Ir^{4+} (**bottom**) species obtained by the MCR-ALS analysis of the Pt and Ir L3 edge XANES spectra for the PtIr-colloidal NPs in dependence of the time during the potential jump experiments with 3 s intervals for the first 25 s (**a**,**b**) and the potential jump experiments with 10 s intervals (**c**,**d**). For MCR-ALS analysis of the 3 s jumps one XANES spectrum recorded every second was used. For the 10 s experiment the spectra were averaged to every two seconds, resulting in one point every two seconds. The black dashed lines show the holding times of the potential jumps between HER (– 0.02 V_{RHE}) and OER (+ 1.55 V_{RHE}) in argon-saturated 0.1 M $HClO_4$.

For the PtIr-colloidal the concentration profile of the Ir^{3+} and Ir^{4+} species are plotted in **Figure 32b**. Note that metallic Ir is not found to be present for this sample, which is consistent with the relatively high WLI of the Ir L3 edge XANES spectra and ex-situ LCF analysis of the pristine catalyst. During the HER "more" reduced Ir^{3+} species (~40 %) compared to the amount at + 1.55 V_{RHE} are present, while 60 % are in the Ir^{4+} state. Around 20 % of this Ir^{3+} is oxidized to Ir^{4+} species during OER, making Ir^{4+} the dominant species during OER. The overall Ir^{3+}:Ir^{4+}

species ratio under OER conditions is 20:80. Both states are highly reversable by jumping the potential between HER and OER for 60 s (**Figure S1.8b**).

A similar potential jump experiment between HER and OER was conducted with a holding time of 10 s. The Ir and Pt L3 edges XANES spectra collected from the PtIr-colloidal NPs during the entire experiment of 60 s are displayed in **Figure S1.11a**,**b**. Essentially, very similar XANES spectra are obtained for both Pt and Ir during HER and OER. However, for the Ir L3 edge XANES spectra (**Figure S1.11b**) the broadening and shift in energy at + 1.55 V_{RHE} is much more pronounced compared to the spectra obtained during the 3 s potential jump experiments. The respective normalized concentration profiles obtained from the MCR-ALS analysis are displayed in **Figure 32c**,**d**. For platinum, a very similar behavior compared to the 3 s potential jump experiment is observed for the PtIr-colloidal NPs. During HER, platinum is fully reduced to Pt^0 species. Upon jumping the potential to + 1.55 V_{RHE} (OER) a limited exponential growth to ~50 % Pt^{2+} species commences over 10 s at + 1.55 V_{RHE}. The reduction back to metallic platinum is always much more rapid within the first 2 – 4 s at – 0.02 V_{RHE}. This behavior is repeated for at least three cycles of 10 s potential jumping between HER and OER. For iridium, the normalized Ir^{3+} and Ir^{4+} concentrations reveal that a longer holding time at – 0.02 V_{RHE} results in more reduced Ir^{3+} species (~70 %) compared to the short 3 s potential jump experiment. Jumping to + 1.55 V_{RHE} causes 40 % of these Ir^{3+} species to be oxidized to a total of 70 % Ir^{4+} species making it the dominant species for the OER. This oxidation-reduction behavior is reversible for 60 s. Increasing the holding time at OER even further to 180 s all Ir^{3+} species are fully oxidized to Ir^{4+}. Jumping the potential to – 0.02 V_{RHE} shows that 30 % of the formed Ir^{4+} species are reduced within 20 s to Ir^{3+} species. This apparent discrepancy between the amount of Ir^{3+} species formed during HER in the 10 s potential jump experiment compared to the 180 s jumps can be explained by the higher concentration of irreversibly formed Ir^{4+} species during the longer potential hold under OER conditions.

Overall, the PtIr-colloidal NPs show a dynamic oxidation-reduction behavior upon jumping between – 0.02 V_{RHE} (HER) and + 1.55 V_{RHE} (OER). More precisely, for iridium a longer holding time of 10 s at – 0.02 V_{RHE} results in more (70 %) Ir^{3+} species compared to only 40 % that are detected during the 3 s potential jump experiment, indicating sluggish reduction kinetics. The oxidation from Ir^{3+} to Ir^{4+} species during OER is rapid and independent of the holding time. Platinum is (almost) fully reduced to metallic platinum (90 – 100 %) during HER, while at + 1.55 V_{RHE} around 50 – 60 % are oxidized in the Pt^{2+} state independent of the holding time (3 s or 10 s).

Metal-oxide transitions of PtIr-WI

The first 35 s of the Pt^0 and Pt^{2+} species concentrations, obtained by the MCR-ALS analysis of the Pt L3 edge XANES spectra during the 3 s potential jump experiment from the PtIr-WI NPs are displayed in **Figure 33a**. A very similar behavior compared to the PtIr-colloidal NPs is found. During HER a high contribution of metallic platinum (~90 %) with minimal amounts of ~10 % Pt^{2+} species is observed. Increasing the potential to + 1.55 V_{RHE} (OER) the oxidation to Pt^{2+} species with a similar concentration of ~50 – 60 % compared to the same experiment with the PtIr-colloidal NPs is found. This behavior is fully reversable and alternates with the applied potential for 60 s (**Figure S1.8c**). Thus, the oxidation-reduction behavior of the Pt species during the 3 s potential jump experiments is very similar for particles prepared by the colloidal and WI routes, indicating that it is independent of the particle size and crystallinity of the PtIr NPs.

For PtIr-WI the behavior of the iridium species is completely different compared to the PtIr NPs prepared by the colloidal route. Metallic Ir species are observed from the start of the experiment at a concentration of around 30 %, which is slightly higher compared to the Ir^0 species concentration found ex-situ (23 ± 2 %). Throughout the first 20 s during the 3 s potential jumps the concentration of Ir^0 species decreases irreversibly to ~20 % forming Ir^{3+} and Ir^{4+} species (**Figure 33b**). The remaining 20 % Ir^0 species remain constant for the rest of the experiment. During this initial time, also some very subtle reversible oxidation of ≤10 % Ir^{3+} species to Ir^{4+} are observed throughout the 3 s hold at + 1.55 V_{RHE}. However, please note that these transitions are very close to the experimental error.

From around 20 s, the Ir^{3+} and Ir^{4+} species start to alternate clearer with the applied potential jumps, which is better observed in the 60 s concentration profile shown in **Figure S1.8d**. Around 25 – 35 % Ir^{4+} species form reversibly during OER, while around 45 – 55 % remain as Ir^{3+} species, resulting in a total Ir^0:Ir^{3+}:Ir^{4+} ratio of around 20:50:30. After the initial activation for 20 s, during HER the Ir^{4+} species are reduced back to 10 – 15 %, while a total of 65 – 70 % Ir^{3+} species are formed. The dominant species of these NPs are the Ir^{3+} species during both potential regimes, that even during OER are present with a concentration of 50 %.

In addition, potential jump experiments with holding times of 10 s were carried out with the PtIr-WI NPs. Similar XANES spectra (**Figure S1.11c**,**d)** were obtained during HER. The WLI of the spectra collected during OER are slightly higher in comparison to the ones obtained during the 3 s jump experiment, indicating a higher contribution of Pt^{2+} species with longer

holding times. For iridium, the slight broadening of the XANES spectra during OER becomes more apparent with the longer holding time (10 s) at + 1.55 V_{RHE}.

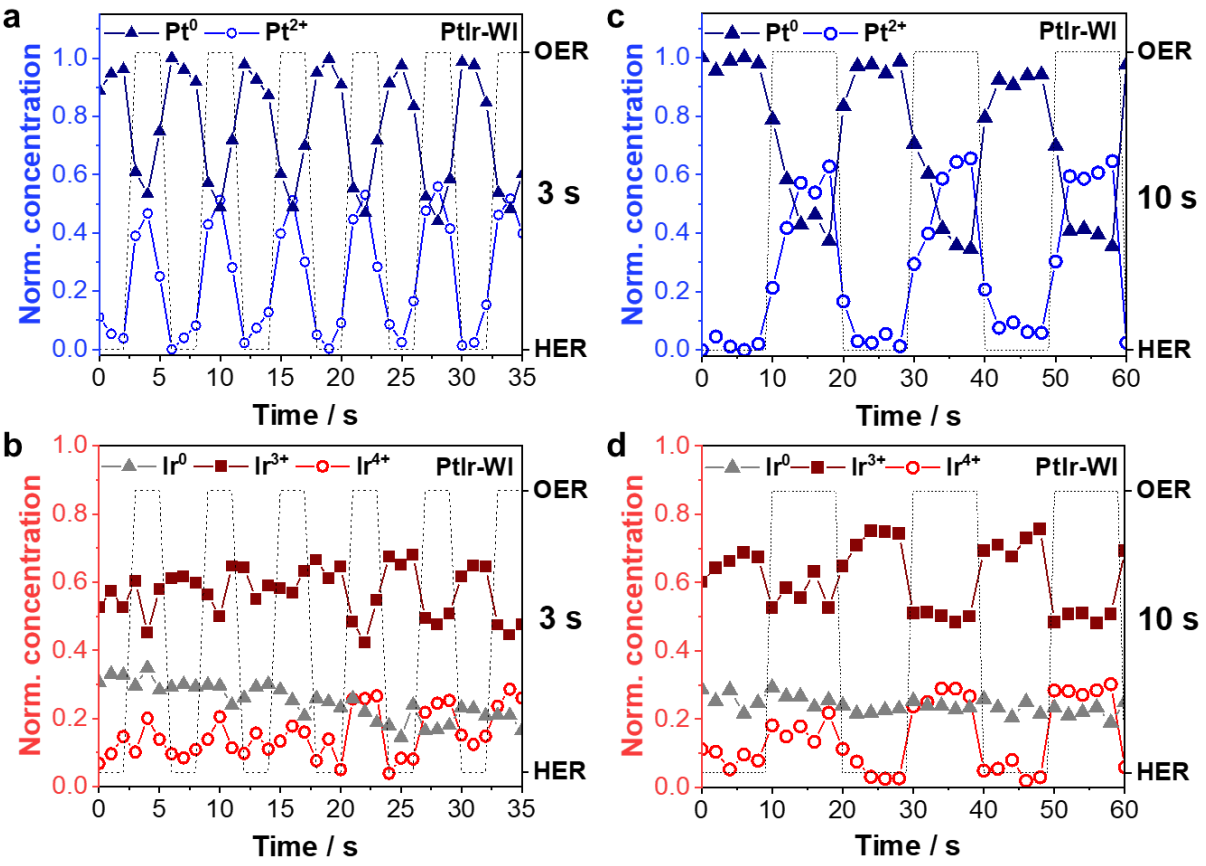

Figure 33 Normalized Pt^0 and Pt^{2+} (**top**) as well as Ir^0, Ir^{3+} and Ir^{4+} (**bottom**) species concentrations obtained by the MCR-ALS analysis of the XANES spectra collected from the PtIr-WI NPs in dependence of the time during the potential jump experiments with 3 s for the first 35 s (**a**,**b**) and the potential jump experiments with 10 s for 60 s (**c**,**d**). For MCR-ALS analysis of the 3 s jumps one Pt and Ir L3 edge XANES spectrum recorded every second was used. For the 10 s experiment the spectra were averaged to every two seconds, resulting in one point every two seconds. The black dashed lines show the holding times of the potential jumps between HER (– 0.02 V_{RHE}) and OER (+ 1.55 V_{RHE}) in argon-saturated 0.1 M $HClO_4$.

The normalized concentration of the platinum species determined by the MCR-ALS analysis of the Pt L3 edge XANES spectra is displayed in **Figure 33c**. The evaluation proves that platinum is fully reduced to metallic Pt during HER. Around 60 – 70 % Pt^{2+} species are gradually formed over 10 s at + 1.55 V_{RHE} (OER). This concentration in Pt^{2+} species is higher compared to the 3 s jumps confirming the observed increase in WLI of the XANES spectra because of the longer holding time at this highly anodic potential.

The MCR-ALS analysis of the Ir L3 edge XANES spectra (**Figure 33d**) confirms the sluggish oxidation-reduction behavior that was already observed for the iridium species during the 3 s potential jumps. A stable contribution of metallic iridium (~20 %) is detected throughout the

experiment. The longer holding time at + 1.55 V_{RHE} does not increase the amount of formed Ir^{4+} species (~30 %), while 50 % remain in the Ir^{3+} state. Similar to the PtIr-colloidal NPs, with a longer holding time of 10 s slightly more Ir^{3+} (around 75 – 80 %) is formed at – 0.02 V_{RHE}, whereas Ir^{4+} is not detected during HER. The dominant species at both potentials (– 0.02 V_{RHE} and + 1.55 V_{RHE}) is the Ir^{3+} species, while after 20 s around 20 % Ir^{4+} is reversibly formed during OER. This sluggish oxidation kinetics of the Ir^{3+} to Ir^{4+} transition may be explained by the high crystallinity of the sample.

Overall, the larger PtIr-WI NPs show sluggish oxidation and reduction kinetics of the iridium species. The NPs contain a high initial amount of ~20 % Ir^0 species that are stable over the entire 60 s of HER and OER potential jump experiments, independent of the holding time (3 s or 10 s). The dominant species of these nanoparticles are the Ir^{3+} species (≥50 %) and only small amounts of Ir^{4+} species are formed at + 1.55 V_{RHE}. For platinum oxidation from metallic Pt to 50 – 60 % Pt^{2+} species at + 1.55 V_{RHE} and consecutive reduction at – 0.02 V_{RHE} commences. A longer holding time (10 s) results in a higher final concentration of Pt^{2+} species of around 60 – 70 %.

4.1.4. *Operando* Quick-XANES potential jump experiments between HER and OER with reduced Ir content

Since Ir is a very scarce metal and even more expensive than Pt, nanoparticles with a Pt:Ir ratio of 3:1 were prepared by the same synthesis routes (colloidal and WI). HER-OER potential jump experiments with holding times of 3 s and 10 s were conducted to investigate the functionality.

The Pt and Ir L3 edges Quick-XANES spectra collected from the Pt_3Ir NPs prepared by the colloidal and WI routes during the 3 s potential jump experiments between HER and OER are displayed in **Figure S1.12**. The Pt L3 edge XANES spectra recorded of the Pt_3Ir-colloidal and Pt_3Ir-WI NPs show a similar behavior compared to the PtIr NPs prepared by both routes. The spectra recorded at + 1.55 V_{RHE} show a slightly shifted absorption edge and higher white line intensity (~1.4) compared to the HER spectra, indicating the presence of oxidized platinum species. The Ir L3 edge XANES spectra of the Pt_3Ir-colloidal NPs (**Figure S1.12b**) display significant broadening between HER and OER with the applied potential jumps of 3 s. In contrast, the Ir L3 edge XANES spectra of the Pt_3Ir-WI NPs display no changes with the applied potential and have a low WLI of 2.0 that is similar to the ex-situ XANES spectrum of this sample.

Dynamic oxidation state transitions of Pt_3Ir-colloidal

The time-dependent concentrations of the Pt^0 and Pt^{2+} species determined by the MCR-ALS analysis of the Quick-XANES spectra for the Pt_3Ir-colloidal NPs are displayed in **Figure 34a**. During the HER, platinum is fully reduced to metallic. Upon increasing the potential to + 1.55 V_{RHE} (OER) gradual oxidation to a maximum concentration of ~40 – 50 % Pt^{2+} species occurs throughout the first two 3 s holds. From the third 3 s potential jump to OER, the maximum concentration of Pt^{2+} species obtained during OER slightly increases to ~60 % over the 3 s holding time. After returning to – 0.02 V_{RHE} an instant reduction of the formed PtO to fully reduced metallic platinum commences. This oxidation-reduction behavior is repeated for each 3 s jump in potential between HER and OER for 60 s (**Figure S1.13a**). Increasing the holding time of the potential jumps to 10 s results in a higher WLI of the Pt L3 edge XANES spectra at + 1.55 V_{RHE} (**Figure S1.14a**). During OER for around 6 s a limited exponential growth with a fast oxidation to 75 % Pt^{2+} species occurs that then slowly increases further to 80 % for the remaining 4 s at + 1.55 V_{RHE} (**Figure S1.15a**).

The concentration profile of the Ir^{3+} and Ir^{4+} species of the Ir L3 edge XANES spectra from the Pt_3Ir-colloidal NPs displayed in **Figure 34b** show that from the first jump to – 0.02 V_{RHE} (HER) 50 % Ir^{3+} and 50 % Ir^{4+} species are found. Jumping the potential to + 1.55 V_{RHE} (OER) results in an oxidation of ~25 % Ir^{3+} to Ir^{4+} species summing up to a total Ir^{3+}:Ir^{4+} ratio of 25:75. This alternation between HER and OER is maintained throughout the entire 60 s of the experiment (**Figure S1.13b)**. In line with the ex-situ LCF analysis of the Pt_3Ir-colloidal NPs, metallic iridium is not observed. The reduction of the Ir^{4+} to Ir^{3+} species during HER is stronger for longer holding times (10 s) at – 0.02 V_{RHE}, evident by the more pronounced narrowing and shift in the position of the Ir L3 edge absorption maximum to lower energies during HER (**Figure S1.12b**). MCR-ALS analysis of these XANES spectra displayed in **Figure S1.15b** indicates 70 % Ir^{3+} and 30 % Ir^{4+} species at – 0.02 V_{RHE} that is reversed to a Ir^{3+}:Ir^{4+} ratio of 30:70 during OER.

Comparing the time-dependent concentrations of the iridium species of the colloidal Pt_3Ir NPs to the PtIr NPs, the same reversible oxidation-reduction behavior is observed between OER and HER with a holding time of 3 s. This suggests that the kinetics of the iridium oxidation are independent of the Pt:Ir ratio. For the Pt_3Ir NPs, more Ir^{3+} species are observed during longer holding times at – 0.02 V_{RHE} confirming the sluggish reduction kinetics of the Ir^{4+} species for the PtIr NPs.

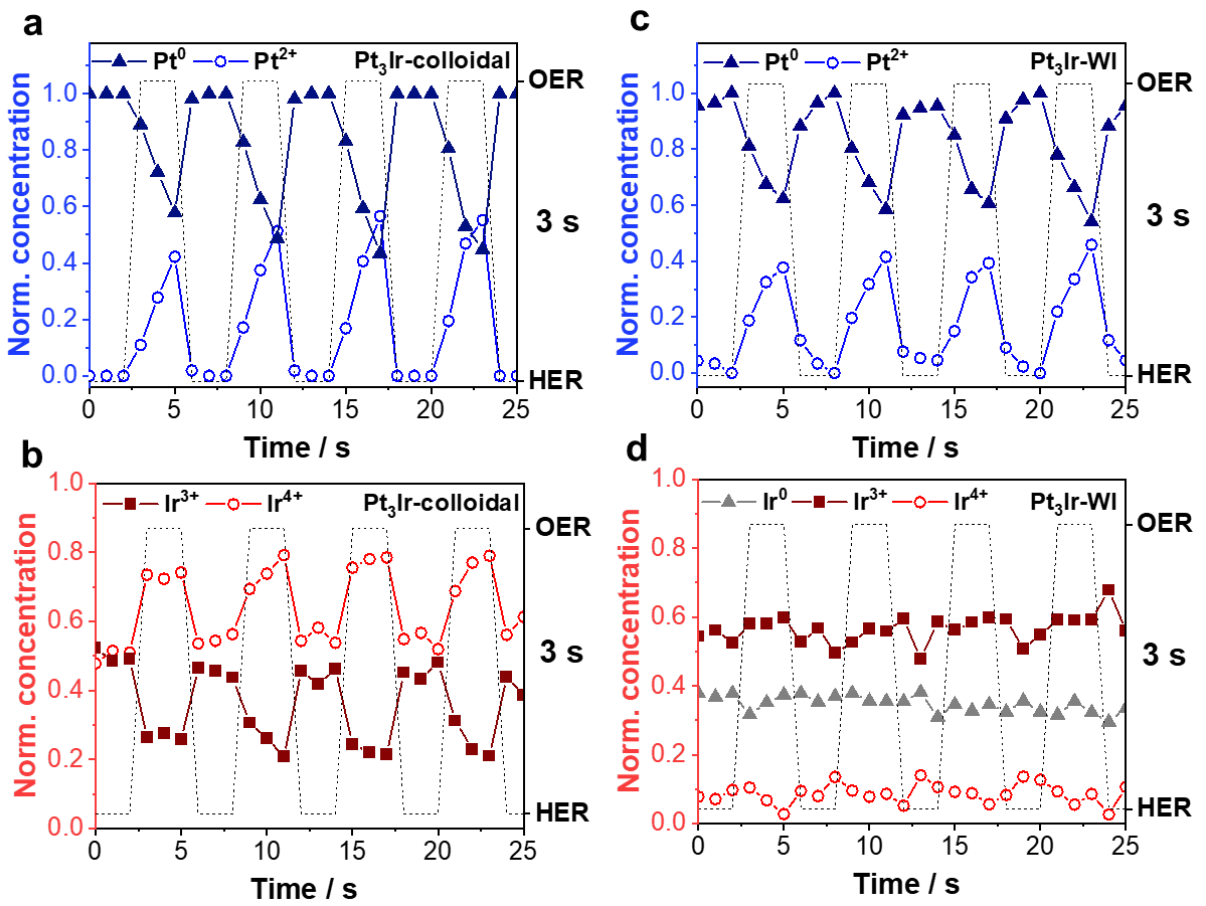

Figure 34. Normalized Pt^0 and Pt^{2+} (**top**) as well as normalized Ir^0, Ir^{3+} and Ir^{4+} (**bottom**) concentrations obtained by the MCR-ALS analysis of the XANES spectra collected from the Pt_3Ir-colloidal (**a**,**b**) and Pt_3Ir-WI NPs (**c**,**d**) during the 3 s potential jump experiments for the first 25 s. For the MCR-ALS analysis one XANES spectrum recorded every second was used resulting in one point per second. The black dashed lines show the holding times of the chronoamperometric potential jumps between HER (– 0.02 V_{RHE}) and OER (+ 1.55 V_{RHE}) in argon-saturated 0.1 M $HClO_4$.

Sluggish oxidation behavior of Pt_3Ir-WI

The Pt^0 and Pt^{2+} species concentrations obtained by the MCR-ALS for the Pt_3Ir-WI NPs during the 3 s potential jump experiments (**Figure 34c**) exhibit the same gradual oxidation to ~40 % Pt^{2+} species at + 1.55 V_{RHE} (OER) as the Pt_3Ir-colloidal NPs (60 % remain as metallic Pt). At – 0.02 V_{RHE} (HER) platinum is fully reduced to the metallic state. However, the reduction to Pt^0 species is progressing at a slightly slower rate compared to the Pt_3Ir-colloidal NPs. More precisely, the reduction requires 1 – 2 s to complete, while for the Pt_3Ir NPs prepared by the colloidal route the reduction was instant (within the first second). After 40 s the maximum concentration of Pt^{2+} species at + 1.55 V_{RHE} increases to ~55 % (**Figure S1.13c**). Increasing the holding time to 10 s a higher white line of the Pt L3 edge XANES spectra compared to the 3 s potential jump experiment are found during OER (**Figure S1.14c**). This is corroborated by the MCR-ALS analysis showing a higher maximum in Pt^{2+} concentration. Like the Pt_3Ir-colloidal

NPs a limited exponential growth in Pt^{2+} concentration to 75 % is observed during 10 s at + 1.55 V_{RHE}. The remaining 25 % stay in the metallic state and the behavior is repeated for 60 s. The concentration profiles of the Ir^{z+} species for the first 25 s are shown in **Figure 34d**. In contrast to all other Pt-Ir NPs, the Ir^0, Ir^{3+} and Ir^{4+} species concentrations of the Pt_3Ir-WI NPs do not change significantly with the applied potential within the full 60 s recorded (**Figure S1.13d**). In line with the content found by ex-situ LCF analysis, a high concentration of ~30 % metallic Ir, (30 ± 2 %) and very low content (~10 %) of Ir^{4+} species are observed. The highest contribution is found for the Ir^{3+} species with ~60 %. Even with a holding time of 10 s, the iridium species concentrations do not change for the first 30 s of jumping between HER and OER (**Figure S1.15d**). Afterwards around 10 % Ir^{4+} species are reversibly formed at + 1.55 V_{RHE} and the Ir^{3+} concentration reduces from 65 to 55 %, while the concentration of metallic Ir is constant (30 %) throughout the experiment.

We can sum up that the Pt_3Ir NPs prepared by the WI synthesis route only show pronounced changes in the concentration of the platinum species. More precisely, during the 3 s jump experiments initially for the first 40 s only ~40 – 50 % Pt^{2+} species alternate with the HER and OER jumps, while for iridium no changes in the concentration of the Ir^0, Ir^{3+} and Ir^{4+} species are detected by the MCR-ALS analysis.

4.1.5. *Operando* Quick-XANES potential jump experiments between HER and OER with monometallic Pt and Ir NPs

Next, we compare the results of the bimetallic Pt-Ir NPs to commercial and colloidal monometallic Pt and Ir NPs. The TEM images and particle size distributions of the monometallic Pt NPs prepared by the colloidal route (2.2 ± 0.2 nm) and commercial Pt-TEC NPs (2.7 ± 0.1 nm) are displayed in **Figure S1.16**. At – 0.02 V_{RHE} during the 3 s potential jumps mostly metallic platinum is observed during HER (**Figure 35**). The formation of the metallic Pt is again very rapid within a few seconds. Thus, no difference in platinum oxidation state and reduction kinetics between bimetallic Pt-Ir NPs and both monometallic Pt NPs (Pt-TEC and Pt-colloidal) are observed during the 3 s potential jump experiment. At + 1.55 V_{RHE} a slow and gradual oxidation from Pt^0 to Pt^{2+} species over the entire 3 s is observed with both monometallic Pt NPs (Pt-TEC and Pt-colloidal). This oxidation behavior is similar to the Pt_3Ir NPs prepared by both the WI and colloidal synthesis. For the Pt-colloidal NPs the total amount of Pt^{2+} species formed (40 %) during OER is slightly lower compared to all other samples. We suspect that this is caused by agglomeration of the more amorphous Pt NPs under the harsh anodic conditions.

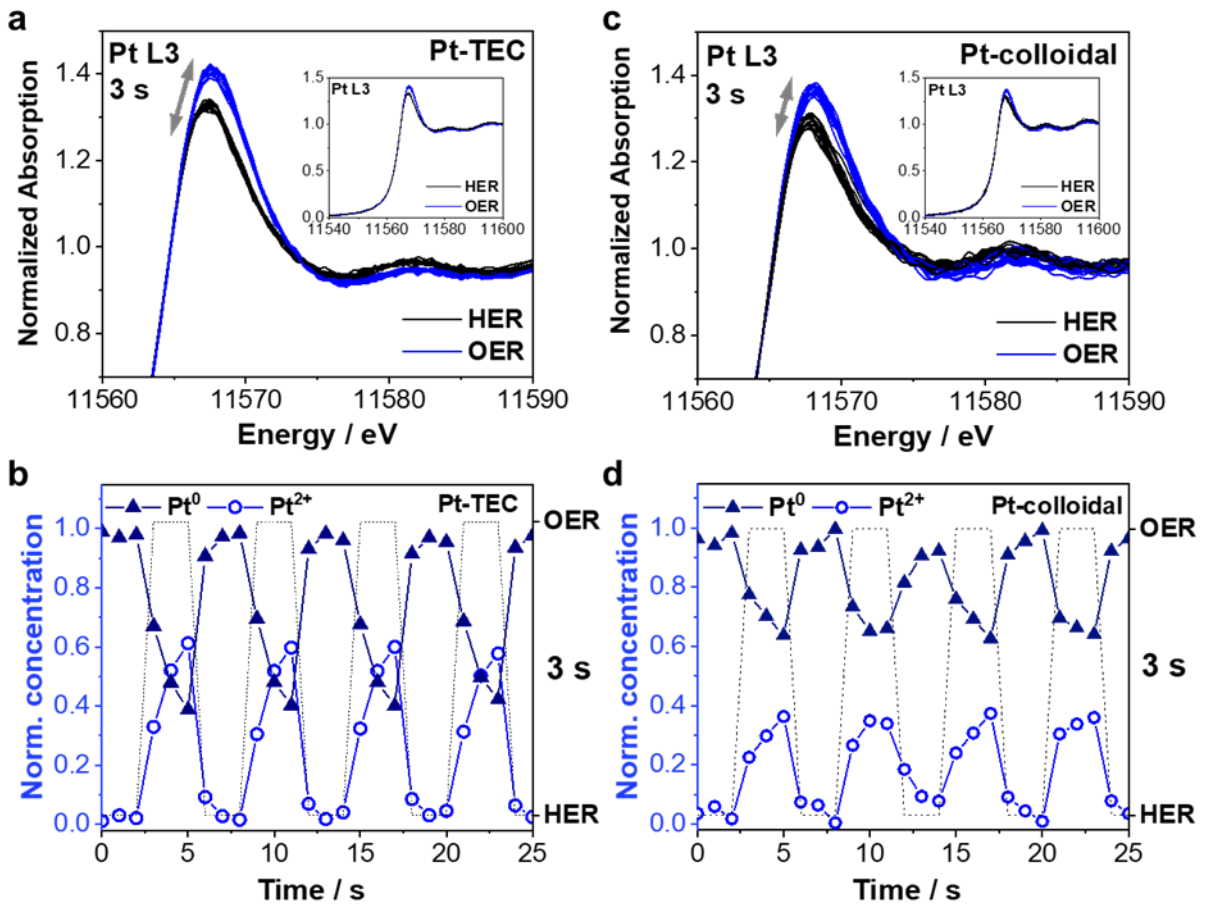

Figure 35. *Operando* Quick-XANES potential jump experiments for 3 s with commercial Pt-TEC (**a**,**b**) and Pt-colloidal NPs (**c**,**d**). Pt L3 edge XANES spectra (**top panel**) were collected every second and subsequently averaged by three. XANES spectra collected during HER are displayed in black and during OER in blue. The insets display the same XANES spectra with a longer energy range. Normalized Pt^0 and Pt^{2+} concentrations obtained by the MCR-ALS analysis in dependence of the time (**bottom panel**). For MCR-ALS analysis one spectrum recorded every second was used. The black dashed lines show the holding times of the potential jumps between HER (– 0.02 V_{RHE}) and OER (+ 1.55 V_{RHE}) in argon-saturated 0.1 M $HClO_4$.

The same 3 s potential jump experiments were conducted with the commercial IrO_x-TEC, which has an amorphous structure and highly agglomerated particles (TEM, **Figure S1.17**) as well as Ir NPs prepared by the colloidal synthesis route with a size of 1.6 ± 0.2 nm (**Figure S1.17**). While the former has a lower surface-to-bulk ratio due to the agglomeration, the latter involves mostly surface atoms, which results in totally different oxidation-reduction behavior during 3 s HER-OER jump experiments. As displayed in **Figure 36a**, the agglomerated IrO_x-TEC shows a very small shift in absorption maximum of the Ir L3 edge XANES spectra recorded during OER and a WLI of ~2.4 expected for purely Ir^{4+} containing samples (also compare IrO_2 **Figure S1.1**).[147,228]

In contrast, the Ir L3 edges XANES spectra of the Ir-colloidal NPs shown in **Figure 36b** display a totally different behavior. Initially, the first Quick-XANES spectrum of these NPs shows a similar WLI of ~2.2 compared to the ex-situ Ir L3 edge XANES spectra recorded of the bimetallic PtIr-colloidal and Pt_3Ir-colloidal NPs (compare **Figure S1.4**). Upon jumping to OER the WLI increases to ~2.3, indicating oxidation of iridium species to Ir^{4+}. However, after holding to + 1.55 V_{RHE} for 3 s and a consecutive potential jump to – 0.02 V_{RHE}, the initial state is not regained and the WLI remains higher, suggesting irreversible oxidation of the iridium species. This process repeats for ~7 cycles of 3 s HER-OER potential jumps, resulting in an irreversible increase in WLI with every jump to OER. From the 8th cycle, no further oxidation occurs at + 1.55 V_{RHE} and two distinct spectra are obtained under HER and OER conditions with a very high WLI >2.6. After the irreversible oxidation is complete, a 3 s potential jump from – 0.02 V_{RHE} to + 1.55 V_{RHE} results in a reversible increase in WLI to ~2.75, strong broadening and a shift in absorption maximum from 11 219 to 11 221 eV (Δ3 eV). This strongly suggests the presence of Ir^{5+} species under OER conditions. Since this high WLI (above 2.5) is only observed for the small Ir-colloidal NPs, we conclude that these Ir^{5+} species only form on the surface of the 2 nm NPs and are thus not observed as pronounced for the larger, agglomerated IrO_x-TEC. This is in agreement to recent studies proposing the involvement of Ir^{5+} species in the OER mechanism during the O-O coupling step of the OER.[129,130,139,147,149,150]

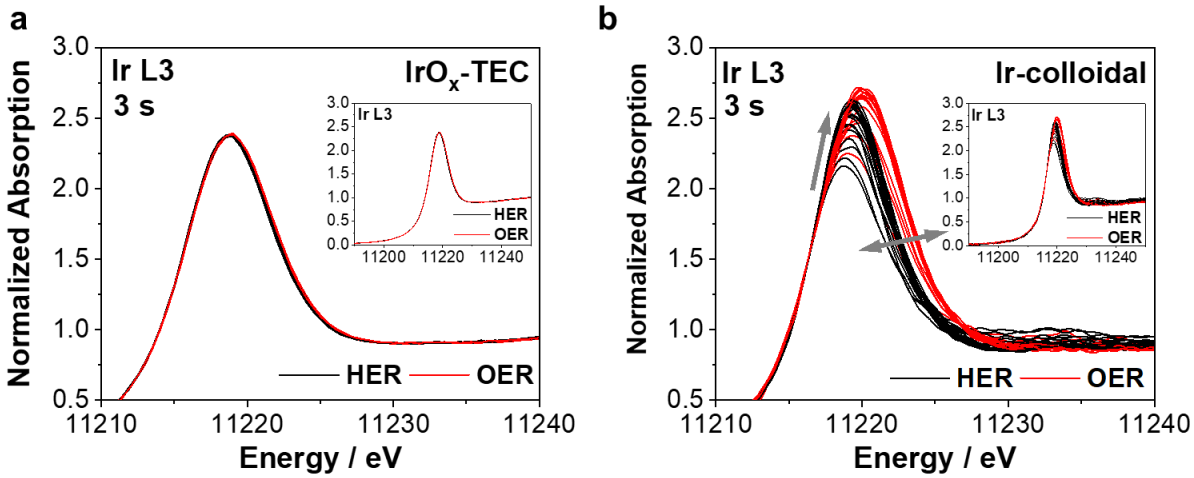

Figure 36. *Operando* Ir L3 edge Quick-XANES spectra collected of the commercial IrO_x-TEC (**a**) and Ir-colloidal NPs (**b**). Spectra were recorded every second and subsequently averaged over 3 s during the potential jump experiments between HER (– 0.02 V_{RHE}, black) and OER (+ 1.55 V_{RHE}, red) with holding times of 3 s in argon-saturated 0.1 M $HClO_4$. The insets display the same XANES spectra with a longer energy range.

In summary, the monometallic Pt-TEC and Pt-colloidal NPs exhibit a similar oxidation-reduction behavior (metallic Pt during HER and gradual formation of Pt^{2+} species during OER)

to the Pt_3Ir NPs during the 3 s potential jump experiments. The commercial IrO_x-TEC shows little changes in the Ir L3 edge XANES spectra, due to their agglomerated structure. In contrast, the 2 nm Ir-colloidal NPs show an initial irreversible oxidation to Ir^{5+} species evident by the irreversibly increasing WLI throughout the 3 s potential jump experiment. These Ir^{5+} species are not observed for the bimetallic Pt-Ir NPs leading to the assumption that electronic interaction between Pt and Ir retain Ir in the Ir^{4+} state.

4.1.6. Discussion

The principal findings of this study are summarized in **Figure 37**, showing schematically the oxidation state changes of the Pt and Ir species between HER and OER for the PtIr NPs prepared by the colloidal and WI synthesis routes. In this work, the differences between the two synthesis routes in respect to the activity towards HOR and OER, the dynamic changes in Pt^{z+} and Ir^{z+} species when jumping between both reactions and relating these findings to the cell reversal event are highlighted.

In addition to the activity of the bifunctional PtIr NPs towards the OER, stability, reversibility and oxidation-reduction kinetics are crucial parameters for a suitable catalyst material that protects the platinum under cell reversal conditions. For understanding this dynamic behavior, the bifunctional Pt-Ir catalysts were investigated under mimicked H_2 starvation conditions by *operando* Quick-XANES using potential jump experiments. The main focus of this work is to investigate the behavior of the Ir and Pt species during the 3 s potential jump experiments, which closely reflect the rapid reversal time during H_2 starvation.

First, our results demonstrate that the two synthesis routes (colloidal and WI) produce nanoparticles with different sizes and morphologies. While Pt-Ir NPs prepared by the colloidal route have a particle size of ≤2 nm with an amorphous structure, the WI synthesis generates more crystalline particles with a larger diameter of 3 – 4 nm. LCF analysis of the Pt L3 edge XANES spectra reveals that the amount of metallic Pt (~40 %) and Pt^{2+} species (~60 %) is almost identical for all as-prepared Pt-Ir NPs and thus independent of the synthesis route and Pt:Ir ratio. For iridium the synthesis route strongly influences the oxidation state. PtIr-colloidal NPs contain only Ir^{3+} and Ir^{4+} species and are thus fully oxidized to IrO_x leading to an almost 30 % higher MA_{OER} (63 ± 6 A g^{-1}_{Ir}) compared to the more crystalline and reduced PtIr NPs that were prepared by the WI route (46 ± 11 A g_{Ir}^{-1}). These pristine PtIr-WI NPs consist of around 20 – 30 % metallic Ir, while the dominant species is the Ir^{3+} species with almost 70 % and only minimal amounts (≤10 %) of Ir^{4+} species. The enhanced OER activity of the PtIr-colloidal NPs suggests that these might provide better protection during H_2 starvation. In addition, HOR polarization curves of both catalysts overlap with the diffusion limiting current, demonstrating the bifunctionality towards both the HOR and OER.

For platinum the behavior of both types of NPs is very similar during the 3 s potential jump experiments (**Figure 37**). During HER at – 0.02 V_{RHE} the dominant species found is metallic Pt with minimal amounts (10 %) of Pt^{2+} species. Several experimental studies suggest a transition from metallic Pt to amorphous platinum oxide is commencing from around

0.7 V_{RHE}.[55,56] Below this potential and especially during potentials relevant for HER and HOR, it is mainly understood that platinum is in the metallic state, agreeing with our results.[231,232] The remaining very small amount of Pt^{2+} species are either present as an amorphous Pt species that are not fully reduced during these short holding times of 3 s or within the experimental error of the XANES measurement. During the 3 s potential jump experiments at + 1.55 V_{RHE} metallic platinum of the bimetallic PtIr NPs of both synthesis routes is rapidly oxidized to ~50 % Pt^{2+} species. The formation of the Pt^{2+} species during OER are readily reversible within one to two seconds at – 0.02 V_{RHE}. These oxidation-reduction cycles are repeatable for several potential jumps between HER (– 0.02 V_{RHE}) and OER (+ 1.55 V_{RHE}) without potential-dependent changes in the Pt^0:Pt^{2+} ratios.

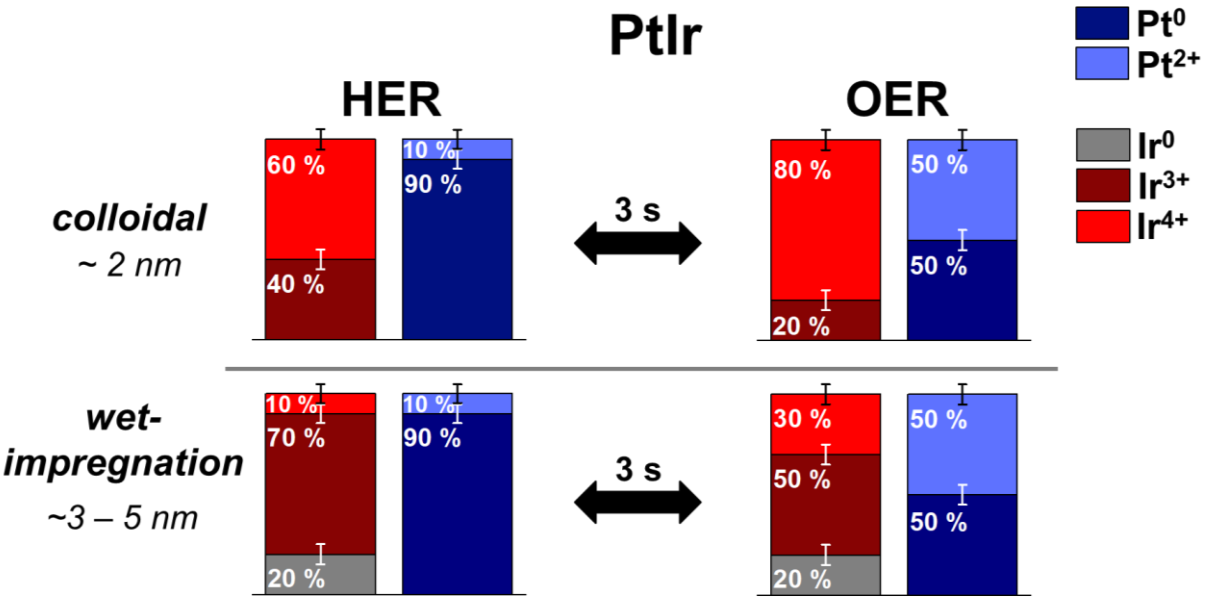

Figure 37. Bifunctionality model for the PtIr NPs prepared by the colloidal and Wet-Impregnation (WI) synthesis routes. Proportion of Ir^0, Ir^{3+} and Ir^{4+} species as well as Pt^0 and Pt^{2+} species present during HER (– 0.02 V_{RHE}) and OER (+ 1.55 V_{RHE}) are schematically represented by the bar diagrams.

Next, the behavior of the iridium species of the bimetallic PtIr NPs during the HER and OER is discussed. The most apparent difference between the bimetallic PtIr-WI and PtIr-colloidal NPs is the absence of metallic Ir in the latter (**Figure 37**). These colloidal NPs are fully oxidized to ~40 % Ir^{3+} and ~60 % Ir^{4+} species e.g. as IrO_x, since no other anions are found after the synthesis. This ratio is not altered at – 0.02 V_{RHE} during the 3 s potential jump experiments. Jumping to + 1.55 V_{RHE} (OER) oxidizes 20 % Ir^{3+} to Ir^{4+} species, resulting in a total of 20 % Ir^{3+} and 80 % Ir^{4+} species. This makes Ir^{4+} the dominant species under OER conditions. The same amount of Ir^{4+} species (20 %) are partially reduced to Ir^{3+} species within the first second under HER conditions. These transitions of Ir^{3+} to Ir^{4+} species at + 1.55 V_{RHE} are in line with

our in-situ Raman and DFT investigations on Ir and Pt-Ir thin films (**Chapter 4.2**) as well as several *operando*/in-situ Raman[78,79,137,233] and XAS[129,130,148,149,233] studies of different iridium oxides prior and during OER in literature.

For the PtIr-WI NPs, the proportion of metallic Ir (~20 %) is stable for all holding times under HER and OER conditions. The dominant species under HER conditions for this sample is the Ir^{3+} species with ~70 %. This high Ir^{3+} species concentration shows very sluggish oxidation kinetics towards Ir^{4+} during OER: It requires four 3 s jumps to + 1.55 V_{RHE} (20 s) before the oxidation of 20 % Ir^{3+} to Ir^{4+} species commences for the PtIr-WI NPs. These are then reduced back to the same amount of Ir^{3+} species during HER.

To enhance the knowledge on the fast transition processes of the Pt and Ir species under HER-OER conditions, several effects were investigated. First, we will discuss the influence of the holding time during HER and OER on the oxidation-reduction behavior of the bimetallic PtIr NPs. Next, the influence of an increased platinum content is examined. Lastly, a comparison of the 3 s potential jump experiments between the bimetallic Pt-Ir NPs and monometallic Ir as well as Pt is made.

Increasing the holding time during HER and OER

Independent of the synthesis route of the PtIr NPs, an increase in the holding time to 10 s results in similar amounts of oxidized Pt^{2+} species (~50 %). However, the oxidation is occurring with a limited exponential growth over time. For the first ~6 s slightly faster oxidation to 40 – 50 % Pt^{2+} species commences, followed by a slowed oxidation of a further 10 % up to 10 s. Overall, for the PtIr NPs the Pt^0 to Pt^{2+} species oxidation is still slower compared to the 3 s jumps, which could be the result of the remaining 10 % Pt^{2+} species that are not reduced during 3 s at – 0.02 V_{RHE}. This remaining surface oxide is likely amorphous with more defects resulting in a faster oxidation at + 1.55 V_{RHE}. When platinum is fully reduced to metallic Pt before applying + 1.55 V_{RHE}, such as during the 10 s potential jumps, less defects are present resulting in slower oxidation kinetics.

A key finding from the 3 s and 10 s potential jump experiments is that during OER (at + 1.55 V_{RHE}) metallic platinum is oxidized to Pt^{2+} species (**Figure 37**). Surprisingly, the presence of Pt^{4+} species as part of a PtO_2 lattice was not observed. We showed that these short holding times (≤10 s) are not sufficient to form the thermodynamically stable PtO_2 that is only observed in the potential jump experiments with 180 s holding time at + 1.55 V_{RHE}. Thus, we conclude that the Pt^{2+} species formed during the fast potential jump experiments with 3 s or 10 s holding times are kinetically stabilized and will oxidize to Pt^{4+} species under prolonged

exposure to anodic potentials. This behavior was already observed by Imai et al. demonstrating that Pt NPs only form Pt-O and Pt-OH species below 100 s at + 1.4 V_{RHE}.[230]

Returning to the iridium species for the PtIr-colloidal NPs a longer holding time of 10 s during OER does not increase the amount of Ir^{4+} species (80 %) formed at + 1.55 V_{RHE}. However, when increasing the holding time at – 0.02 V_{RHE} to 10 s, almost double the amount of reduced Ir^{3+} species (70 %) are formed compared to a holding time of 3 s (~40 %). This reduction of the Ir^{4+} species takes ~4 – 6 s, while the respective oxidation only requires ~2 s supporting this effect. Therefore, the reduction kinetics from Ir^{4+} to Ir^{3+} species are slower compared to the respective oxidation transition, that occurs instantly within one second during the 3 s potential jump experiments. The formation of IrO_x is irreversible and only transitions of the Ir^{3+} and Ir^{4+} species are observed. Increasing the holding time of the potential jumps further to 180 s the Ir^{3+} species are fully oxidized to Ir^{4+} species within ~20 s.

For the PtIr-WI NPs an increase in the holding time to 10 s results in an earlier start in the alternating transition of 20 % Ir^{3+} to Ir^{4+} species from the first jump to OER. Like the colloidal NPs, the amount of Ir^{4+} species formed under OER potentials (~30 %) is not influenced by a longer holding time of 10 s. The presence of ~20 % metallic Ir remains constant throughout the potential jump experiment.

For all PtIr NPs, no metallic iridium is formed during the potential jump experiments between HER and OER. This indicates that once formed Ir^{3+} and Ir^{4+} species are not readily reduced at – 0.02 V_{RHE} independent of the synthesis route, holding time and iridium content, which is in line with previous literature.[234]

Increasing the platinum content (Pt_3Ir)

Independent of the synthesis route (WI or colloidal, **Figure S1.18**) for the Pt_3Ir NPs platinum is fully reduced to metallic Pt under HER conditions even during the shorter 3 s potential jump experiments. For both Pt_3Ir NPs, the reduction from Pt^{2+} species to metallic Pt at – 0.02 V_{RHE} is instant within the first one or two seconds for all holding times (3 and 10 s), implying fast reduction kinetics. In contrast, the respective oxidation (Pt^0 to Pt^{2+} species) is a gradual, slower process occurring over the entire time of the potential hold (3 or 10 s) at + 1.55 V_{RHE} for the Pt_3Ir NPs compared to the PtIr NPs (WI and colloidal). However, for these NPs more Pt^{2+} species (~70 – 75 %) are observed during OER in the 10 s potential jump experiment compared to the same experiment with the PtIr NPs and the 3 s potential jumps.

In summary, an increase in platinum content results in a slowdown of the oxidation kinetics during 3 s at + 1.55 V_{RHE}, while similar total amounts of Pt^{2+} species (~40 – 60 %) are observed

for all bimetallic NPs (PtIr and Pt_3Ir) independent of the synthesis route. The reduced platinum content also results in an increase in Pt^{2+} species during longer holding times (10 s) at + 1.55 V_{RHE}.

For the Pt_3Ir-colloidal NPs (**Figure S1.18**), there is no influence of the platinum content on the transitions between Ir^{3+} to Ir^{4+} species, independent of the holding time (3 or 10 s).

In contrast, for the Pt_3Ir-WI NPs the oxidation of the Ir^{3+} species gets even more hindered. No changes in iridium species are observed for the Pt_3Ir-WI NPs during the 3 s potential jumps and even during 10 s at + 1.55 V_{RHE} only 5 – 10 % of Ir^{3+} are oxidized to Ir^{4+} species. These results confirm the very sluggish oxidation and reduction kinetics for Ir^{3+} species within more crystalline Pt-Ir NPs.

Comparing transition kinetics between bimetallic Pt-Ir and pure Pt and Ir

Similar to the Pt-Ir NPs, both monometallic Pt NPs (Pt-TEC and Pt-colloidal) are rapidly reduced to metallic Pt under HER conditions. At + 1.55 V_{RHE} a slower oxidation from Pt^0 to Pt^{2+} species over the entire 3 s is observed with both monometallic Pt NPs. These gradual oxidation kinetics are comparable to the Pt_3Ir NPs with increased Pt content during the 3 s potential jump experiment, supporting that an increase in platinum content results in a slowdown of the oxidation transitions during OER. Besides these differences in oxidation kinetics, our study reveals that for all bimetallic Pt-Ir and monometallic Pt NPs the formation of the platinum oxides during OER are readily reversible as fast as 3 s at – 0.02 V_{RHE}.

In contrast to recent studies, we did not observe the formation of Ir^{5+} species for bimetallic Pt-Ir NPs under OER conditions independent of the synthesis route and iridium content. These Ir^{5+} species are highly discussed in recent literature[128–130,139,147–151] and especially Diklić et al.[147] and Ooka et al.[150] propose the Ir^{5+} formation as a prerequisite for the OER. By using small Ir-colloidal NPs and applying the same 3 s potential jump experiments between HER and OER, we also observed these Ir^{5+} species at + 1.55 V_{RHE}, evident by the high WLI of ~2.75 and shift of the maximum white line position to 11 221 eV. In addition, we found that for the Ir-colloidal NPs the formation of highly oxidized Ir species (Ir^{4+} and Ir^{5+}) is (partially) irreversible. This is evident by the initial continuous increase in WLI with each consecutive 3 s potential jump to + 1.55 V_{RHE}. However, for the bimetallic Pt-Ir NPs, which have a similar high surface-to-bulk ratio, due to the small particle size Ir^{5+} species formation is not observed. Considering that OER activity is retained for these bimetallic particles, this suggests that the mechanism of the OER is changed on bimetallic Pt-Ir NPs compared to monometallic Ir. Furthermore, this leads to the conclusion that the platinum in the bimetallic NPs is able retain iridium in the $\leq Ir^{4+}$ state. To

investigate the effect of the platinum species (Pt^{2+} and Pt^{4+}) on the oxidation of Ir^{4+} species, DFT calculations are in progress.

Overall, our *operando* Quick-XANES study provides new insights into the bifunctionality as well as the dynamic and reversible oxidation and reduction transitions of bifunctional Pt-Ir NPs between HER and OER within a few seconds. Thereby we uncover that the oxidation of metallic platinum is kinetically controlled, while oxidation of Ir^{3+} species is always rapid. Electronic interactions between platinum and iridium retain iridium in the $\leq Ir^{4+}$ state.

4.2. Bimetallic Pt-Ir Oxide Surfaces under Oxygen Reduction/ Evolution Reactions (ORR/OER) using in-situ Raman spectroscopy and DFT

Co-authors' contributions: G. Sievers and M. Rohloff prepared the Pt-Ir thin films. T. Reetz and H. İ. Sözen conducted DFT calculations and helped writing **Section 4.2.4**. C. Schneemann guided the electrochemical measurements of the thin films in the impinging jet flow cell. C. Dosche measured and analyzed the XPS data as well as advised on the in-situ Raman spectroscopy. T. Klüner and M. Oezaslan supervised the work.

In the second case study, bimetallic platinum-iridium electrocatalysts are investigated under the oxygen reduction/evolution reactions (ORR/OER). In-situ Raman spectroscopy is used, to monitor the potential-resolved electronic and structural interactions of Pt and Ir in the sputtered bimetallic Pt-Ir thin films under these conditions. In addition, density functional theory (DFT) was applied to construct models of tetrameric iridium, platinum and platinum-iridium oxo-hydroxy complexes and calculate their respective Raman spectra. During the ORR, an amorphous bimetallic Pt-Ir oxide forms on the surface of the thin films. Between 1.4 and 1.5 V_{RHE} the observed changes in the Raman spectra signify the further electrochemical surface oxidation of the Pt-Ir films, which clearly differs from the behavior of the pure sputtered Ir and Pt thin films. At potentials just before and during OER, the DFT calculations indicate the formation of hydrous PtO_6-IrO_6 edge-sharing chains. The theoretical stretching and bending motions of these Pt-O-Ir bonds are the most intense vibrations and are in very good agreement with the observed Raman bands. Very remarkably, the comparison between the experimental Raman bands for symmetric stretching of Ir-O-Pt and Ir-O-Ir shows a clear red shift by 38 cm^{-1} during the OER, which is also confirmed by the DFT calculations. This red shift is most likely based on changes in electron density distribution and bond strength of the Ir-O-Pt.

4.2.1. Morphology and structure of the bimetallic Pt-Ir thin films

The bulk composition and structure of Pt-Ir thin films were investigated by SEM, XRD and μ-XRF techniques. The bimetallic Pt-Ir thin films were prepared by alternating magnetron sputtering of Pt and Ir targets for 50 cycles onto a PTFE/carbon-based gas diffusion layer (GDL, for experimental details see **Appendix Chapter 10.2**). Iridium was always the last in the alternating cycle process between Pt and Ir. Sputtered thin films with atomic Pt:Ir ratios of 1:1 and 3:1 will be referred to as PtIr(1:1) and PtIr(3:1) throughout the manuscript. For comparison, monometallic Pt and Ir thin films were prepared.

At low magnification, the top view SEM images of the PtIr(1:1) and PtIr(3:1) thin films (**Figure S2.1a** and **b**) show the typical surface with a "cauliflower" growth. The rough surface forms by the individual grains as they are deposited onto the GDL during sputtering. Quantitative μ-XRF analysis (**Table S2.2**) confirms that the bulk Pt:Ir ratios are in line with the expected values of 1:1 (Pt: 47 ± 2 at.% and Ir: 53 ± 2 at.%) and 3:1 (Pt: 75 ± 1 at.% and Ir: 25 ± 1 at.%).

Furthermore, the crystal phase and crystallite sizes of the sputtered Pt-Ir, Pt and Ir thin films were established by XRD. All XRD profiles of the bimetallic Pt-Ir as well as monometallic Ir and Pt thin films with the respective fits obtained from the quantitative Rietveld refinement analysis are displayed in **Figure S2.1c**. The peaks at 2θ values of ~40°, ~46°, ~67°, ~82° and ~86° correspond to the lattice planes of (111), (200), (220), (311) and (222) of a face-centered cubic (fcc) disordered Pt, Ir and PtIr alloy unit cell with a space group of $Fm\bar{3}m$. All thin films show broadened peaks, indicating small crystallite sizes. **Table S2.3** summarizes the best fit results of the quantitative Rietveld refinement analysis and respective alloy composition via Vegard's law for the PtIr(1:1), PtIr(3:1), Pt and Ir thin films. Both bimetallic Pt-Ir thin films contain at least two fcc disordered Pt-Ir alloy crystal phases. The PtIr(1:1) thin film consists of a ratio of 1:1 by $Pt_{95}Ir_{05}$ alloy phase (mean crystallite size of 6.1 ± 0.2 nm) and $Pt_{40}Ir_{60}$ alloy phase (7.2 ± 0.2 nm), while 40 wt.% $Pt_{52}Ir_{48}$ phase (8.2 ± 0.3 nm) and 60 wt.% monometallic Pt (6.0 ± 0.1 nm) are present for PtIr(3:1) thin film. The monometallic Pt and Ir thin films show slightly smaller mean crystallite of 5.1 ± 0.1 nm and 4.5 ± 0.1 nm, respectively.

Surface-sensitive XPS measurements were employed to investigate the surface composition and oxidation state of Pt and Ir species. High-resolution Pt and Ir 4f XPS data of the PtIr(1:1) and PtIr(3:1) thin films are displayed in **Figure 38a** and **b**, respectively. Deconvolution of the Pt $4f_{7/2}$ XPS spectra implies the presence of three components at binding energies (BEs) of 71.1 eV, 71.4 eV and 72.5 eV, corresponding to metallic Pt, Pt^{2+} and Pt^{4+} species,

respectively.[235,236] The Ir $4f_{7/2}$ XPS spectra can be deconvoluted by three chemical species at BEs of 60.6 eV, 61.3 eV and 62.2 eV that are attributed to metallic Ir, Ir^{3+} and Ir^{4+} species, respectively.[235,237] Based on quantification of the Pt and Ir $4f_{7/2}$ XPS data, the surface Pt:Ir ratio was determined to be 29:71 at.% for PtIr(1:1), while for the PtIr(3:1) a higher Pt contribution at the surface is observed (Pt:Ir = 44:56 at.%). For both thin films, the surface is enriched with iridium compared to the bulk. This can be related to the preparation of the thin films with the last step of Ir in the 50 cycles of sputtering.

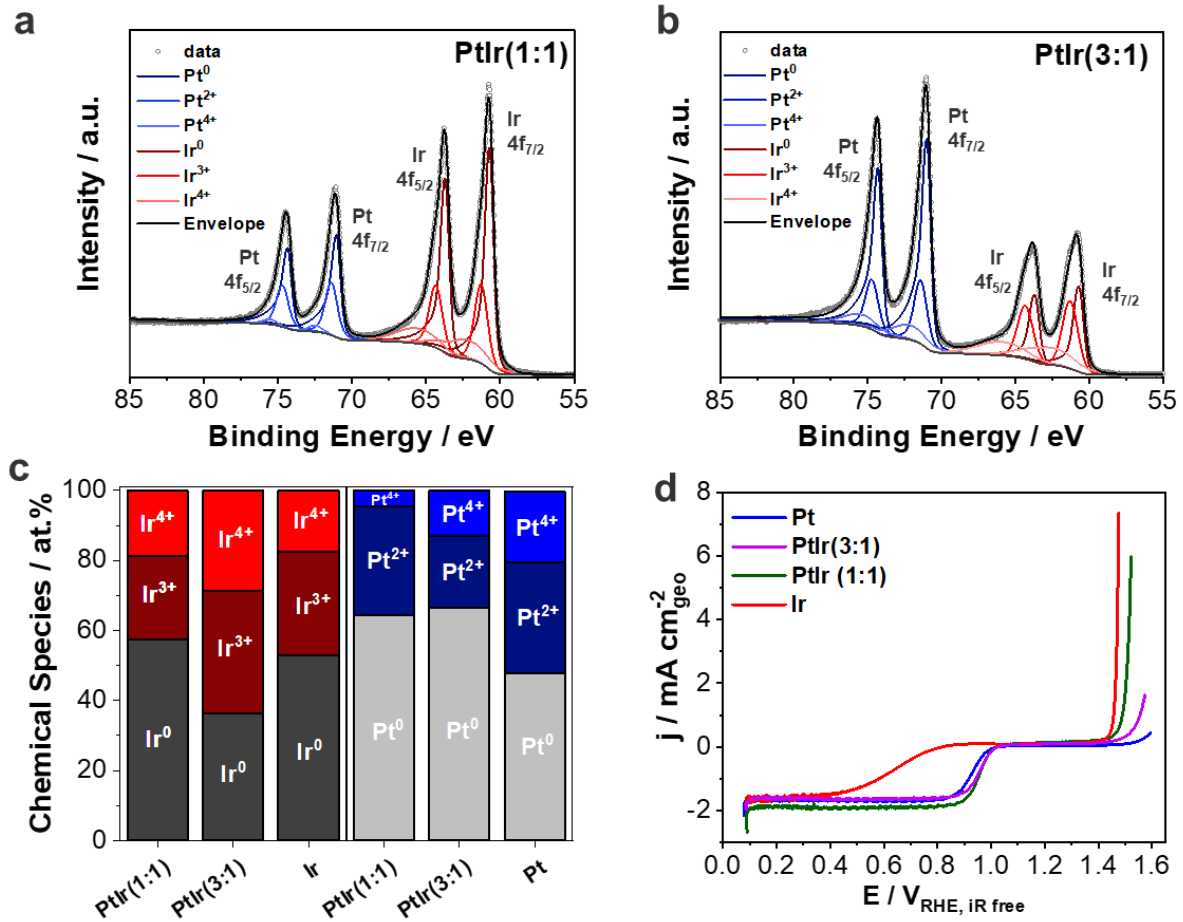

Figure 38. (**a** and **b**) Ex-situ high-resolution Pt and Ir 4f XPS spectra of the Pt-Ir thin films. Light grey circles represent the measured data, the envelope is shown in black and Pt^0, Pt^{2+} and Pt^{4+} species are plotted in blue, while Ir^0, Ir^{3+} and Ir^{4+} species are displayed in red. (**c**) Quantitative surface analysis of the high-resolution Pt and Ir $4f_{7/2}$ XPS spectra, determining each species (Pt^0, Pt^{2+}, Pt^{4+} and Ir^0, Ir^{3+}, Ir^{4+}). High-resolution Pt and Ir 4f XPS spectra of the monometallic Pt and Ir thin films are displayed in **Figure S2.2**. (**d**) ORR and OER polarization curves of the Pt (blue), PtIr(1:1) (green), PtIr(3:1) (pink) and Ir (red) thin films. The polarization curves were recorded in one scan from 0.05 to 1.6 $V_{RHE,\ iR\ free}$ at a scan rate of 1 mV s^{-1} and a flow rate of 1 mL min^{-1} in O_2-saturated 0.1 M $HClO_4$ using an impinging jet flow cell.

Quantitative XPS analysis of the different oxidation states of Pt and Ir are displayed in **Figure 38c**. The surface of the PtIr(1:1) thin film contains around 58 at.% Ir^0, 24 at.% Ir^{3+} and 18 at.% Ir^{4+} species. In contrast, for the PtIr(3:1) thin film, the quantification of the Ir $4f_{7/2}$ XPS data

reveals a high contribution (64 at.%) of the oxidized Ir species (35 at.% Ir^{3+} and 29 at.% Ir^{4+}) and only 36 wt.% metallic Ir. For platinum, the metallic contribution of both bimetallic Pt-Ir thin films is comparable (~65 at.%), while around 35 at.% are oxidized to Pt^{2+} and Pt^{4+} species. As expected for samples stored in air, iridium is more oxidized compared to platinum, due its strong oxophilic character.[238]

The Ir and Pt 4f XPS data for both monometallic thin films are displayed in **Figure S2.2**. The monometallic Ir thin film shows a similar contribution of the three chemical species (Ir^0, $Ir^{3+}$and Ir^{4+}) compared to the PtIr(1:1). For monometallic platinum this is different. A much higher concentration of oxidized Pt^{2+} and Pt^{4+} species (52 at.%) are observed compared to both bimetallic Pt-Ir films. This reveals a preferential oxidation of Ir for the bimetallic thin films, while Pt tends to appear more reduced. However, this could have occurred due to the enrichment of iridium or it being sputtered last on the surface, which protects the platinum in the sub-surface from air oxidation.

Overall, the ex-situ characterization highlights that the Pt-Ir thin films exhibit a rough, oxidized surface. Bulk XRD analysis showed that both bimetallic films are composed of one Pt-rich and one fcc Pt-Ir alloy phase with average crystallite sizes between 5 and 8 nm. Surface-sensitive XPS analysis reveals the significant air oxidation of the surfaces of all thin films and their enrichment of iridium oxide surface species.

4.2.2. Activities of the Pt-Ir, Pt and Ir thin films towards ORR and OER

To establish the catalytic activity of the bimetallic Pt-Ir thin films, polarization curves for ORR and OER were collected in O_2-saturated 0.1 M $HClO_4$ using an impinging jet flow cell (**Figure 38d**, for experimental details see **Appendix Chapter 10.2**). The electrochemically active surface area was determined by the underpotential deposition of hydrogen (H_{UPD}) obtained from the cyclic voltammetry (CV) measurements between 0.06 and 0.40 V_{RHE} shown in **Figure S2.3**. We note that due to the presence of Ir-OH surface coverage CO stripping experiments would have been a more suitable method to determine the ECSA.[68,239,240] Nevertheless, the general trend is still observed from the H_{UPD}-based ECSA.

In **Figure S2.3**, the CV profiles of monometallic and bimetallic thin films show the characteristic features of metallic Pt and Pt-Ir, related to the underpotential hydrogen (H_{UPD}) region (0.06 – 0.40 V_{RHE}), capacitive double layer region (0.40 – 0.60 V_{RHE}) and (hydr)oxide formation/reduction above 0.6 V_{RHE}. Only the monometallic Ir thin film shows a strong oxide surface with a redox couple of Ir^{3+}/Ir^{4+} between 0.7 and 1.0 $V_{RHE,iR\text{-}free}$ and minor H_{UPD} region below 0.3 $V_{RHE,iR\text{-}free}$. In addition, the CV profiles exhibit varying current densities in the

capacitive double layer region (0.4 – 0.6 V_{RHE}), indicating different contributions of sputtered films and PTFE/carbon-based GDL substrate. More precisely, the capacitive current density for monometallic Pt is the lowest, signifying the formation of a dense bulk metal film due to the continuous dissolution/re-deposition of amorphous Pt species during pre-conditioning step (100 potential cycles between 0.05 and 1.40 V_{RHE}, **Figure S2.4**). In contrast, the bimetallic and Ir thin films show larger capacitive current density, indicating less dense metal film with a significant contribution of the GDL substrate exposed to the electrolyte solution.

In **Figure 38d**, the polarization curves show catalytic activity towards ORR for all platinum containing films with different extents. Since IrO_x is not active, no ORR activity is observed. Due to the strong oxidation of the Ir surface, no ORR activity is observed. **Table S2.4** sums up the Pt-Ir-based surface area specific ORR activities (SA_{ORR}) determined from the H_{UPD}-based kinetic current at 0.90 $V_{RHE, iR\text{-}free}$. The Koutecký-Levich equation was applied to determine the limiting current density (j_{lim}) and kinetic current density (j_{kin}). Very recently, we have demonstrated that the j_{lim} characteristics measured in our impinging jet flow cell are in very good agreement with the data from computational fluid dynamics (CFD) and our developed universal analytical model.[241] It is noted that the SA_{ORR} decreases in the sequence of PtIr(3:1) (88 μA cm^{-2}_{Hupd}) > PtIr(1:1) (57 μA cm^{-2}_{Hupd}) > Pt (54 μA cm^{-2}_{Hupd}) >> Ir (3 μA cm^{-2}_{Hupd}). The observed ORR activity difference can be explained by 2 – 3-times higher surface area and larger roughness factor (RF) of the bimetallic thin films compared to the monometallic Pt. In other words, the RF values determined by the ratio between H_{upd} and geometric surface area are 19 for pure Pt, 56 for PtIr(1:1) and 39 for PtIr(3:1).

At 1.50 $V_{RHE, iR\text{-}free}$ the monometallic Ir thin film shows the highest SA_{OER} with 245 μA cm^{-2}_{Hupd}. Combining platinum with iridium in a 1:1 ratio reduces the SA_{OER} by 7-fold (34 μA cm^{-2}_{Hupd}), while a further increase in platinum content leads to much lower SA_{OER} with 8 μA cm^{-2}_{Hupd}. This value is only slightly higher compared to that for the monometallic Pt thin film (4 μA cm^{-2}_{Hupd}).

Altogether, the Pt-Ir thin films show catalytic activities towards ORR and OER in different extents, demonstrating their unique bifunctionality for unitized regenerative fuel cells.

4.2.3. In-situ Raman spectroscopy of Pt-Ir, Ir and Pt thin films

Surface-sensitive Raman spectroscopy technique was used to understand the bifunctionality, in-situ formation of catalytically active Pt-Ir oxide sites and its electronic structure for the ORR and OER between 0.3 and 1.6 V_{RHE} in 0.1 M $HClO_4$. The high roughness factor (RF) and small crystallite sizes derived from the CV and XRD data show the nano-structuring of the sputtered

film surface, allowing to detect in-situ sufficient Raman scattering signal of the catalytically active metal oxide species formed during ORR and OER.

Initially, the PtIr(1:1), PtIr(3:1), Pt and Ir thin films were investigated ex-situ and at open circuit potential (OCP), see **Figure S2.5**. From the ex-situ data, all thin films show broad Raman bands between 400 cm^{-1} and 700 cm^{-1}, indicating the presence of disordered amorphous Pt and Ir oxide species. Single crystalline structures of these oxides would exhibit sharp distinct Raman peaks.[242–244] Platinum oxide only forms as amorphous oxide in all platinum containing thin films, as it does not exhibit any sharp and resolved Raman bands. All iridium containing thin films show two distinct bands at 550 cm^{-1} (E_g) and 704 cm^{-1} (B_{2g}), indicating the formation of some ordered rutile IrO_2 on the surface (for peak assignments see **Table S2.5**).[242,243] Upon exposure to 0.1 M $HClO_4$ (**Figure S2.5b**), the peak at 704 cm^{-1} immediately disappears, indicating the hydration of structured rutile IrO_2 structure to form hydrous IrO_x.[78] Note, that the weak band at 933 cm^{-1} is assigned to ClO_4^- of the 0.1 M $HClO_4$ electrolyte solution (**Figure S2.6**).[83,109,245,246]

To investigate the potential-dependent surface changes and oxide formation for each of the thin films, a chronoamperometric method was applied, where the potential was shifted in 100 mV steps from 0.3 to 1.6 V_{RHE} in 0.1 M $HClO_4$. Each potential was held for 5 minutes, while Raman spectra were accumulated every 5 s. The detailed evolution of the Raman spectra recorded from all thin films between 0.8 and 1.6 V_{RHE} are illustrated in **Figure S2.7**. To obtain a fundamental understanding of the oxide formation on the thin films under ORR and OER conditions, the in-situ Raman spectra of the monometallic Pt and Ir thin films are described first.

In-situ Raman spectra of monometallic thin films

Iridium: Potential-resolved in-situ Raman spectra for the Ir thin film at low potentials (below 0.8 V_{RHE}) are displayed in **Figure S2.8**. At 0.2 V_{RHE} the broad amorphous peak of around 548 cm^{-1} (already observed at OCP) disappears and a sharp band at 564 cm^{-1} emerges and is retained until 0.6 V_{RHE}. From 0.8 V_{RHE} to higher potentials, where the transition of Ir^{3+} to Ir^{4+} species occurs, a broadening of the Raman bands is observed. At this potential, a second distinct peak at 498 cm^{-1} is obtained, while simultaneously two bands at 295 and 336 cm^{-1} appear. In the potential region, where ORR commences (0.8 to 1.2 V_{RHE}, **Figure 38b**), this broad peak structure between 400 and 700 cm^{-1} is retained, while the band at 564 cm^{-1} shifts to 548 cm^{-1} at 1.0 V_{RHE}. From 1.3 V_{RHE} to higher potentials, the Raman spectra change significantly (**Figure S2.7a**), indicating the second oxidation wave of the Ir thin film. More precisely, three distinct peaks at 465 cm^{-1}, 498 cm^{-1} and 681 cm^{-1} appear, while the bands at 548 cm^{-1} and

602 cm^{-1} diminish. These spectral features are retained until 1.5 V_{RHE}. Increasing the potential to 1.6 V_{RHE}, only the Raman band at 681 cm^{-1} shifts by 14 cm^{-1} to 695 cm^{-1}, the remaining spectrum remains unchanged (**Figure 39a**).

Generally, our results for the Ir thin film between 0.8 and 1.6 V_{RHE} are in good agreement with the formation of hydrous IrO_x species proposed by Pavlovic et al. and Zhao et al.[78,80] For instance, the sharp Raman band at 564 cm^{-1} observed below 0.8 V_{RHE} was previously reported for IrO_2 in several studies in acidic[214,233] and alkaline[79] environments. In all studies, this peak was attributed to highly stable Ir^{3+}-OH species. At 0.8 V_{RHE}, a second band at 498 cm^{-1} and a general broadening of the sharp band occur similar to a IrO_2 study reported by Zou et al.[214] This additional Raman band is assigned to the Ir-O stretching frequency and is associated with the formation of Ir^{4+} centers.[78,80] This suggests that the transition of Ir^{3+} to Ir^{4+} species already takes place starting from 0.8 V_{RHE}. A shoulder at 602 cm^{-1} appears, which is related to an Ir^{3+}-O-Ir^{4+} stretch and gets more pronounced, when the potential is increased further.[78]
At 1.0 V_{RHE} the peak at 564 cm^{-1} red shifts to 548 cm^{-1} which could indicate either the formation of some rutile-type IrO_2 or the association with Ir^{3+} centers.[78,80] In addition, a new band at 465 cm^{-1} is formed, that is discussed in literature to be associated with adsorbed perchlorate anions on IrO_x surfaces.[246] Two Ir^{4+}-O bending vibrations appear simultaneously at 295 cm^{-1} and 336 cm^{-1}. The bending and stretching motions are shown schematically in **Figure S2.9**. This arrangement of the Raman peaks remains during the entire potential range of the ORR (from 0.8 to 1.2 V_{RHE}).

The assignments of the Raman bands detected at 1.2 V_{RHE} and 1.6 V_{RHE} are summarized in **Table 4** and are mainly based on the works on the oxidation of anodically deposited IrO_x films for OER by Pavlovic et al.[78] and Zhao et al.[24] We chose these potentials due to the observed significant changes in the Raman spectra, which is correlated with the formation of catalytically active species during ORR (<1.23 V_{RHE}) and OER (~1.6 V_{RHE}).

At 1.3 V_{RHE} the oxidation of the remaining Ir^{3+} to Ir^{4+} centers continuous, as evidence by the disappearing of the Raman band associated with the Ir^{3+} center at 602 cm^{-1} and presence of two strong bands at 498 cm^{-1} and 681 cm^{-1}. Both bands are related to Ir-O stretching frequencies with only Ir^{4+} centers.[78] Up to 1.5 V_{RHE} the peak positions remain unchanged, indicating that the octahedral IrO_x lattice with Ir-O. At a potential of 1.6 V_{RHE}, the band at 681 cm^{-1} slightly shifts to a higher energy at 695 cm^{-1}, signifying the gradual oxidation of some Ir^{4+} to Ir^{5+} centers. According to the DFT calculations, a blue shift in the predicted Raman spectrum is either due

to the presence of Ir^{4+}-Ir^{5+}-Ir^{4+} trimer compared to the Ir^{4+}-Ir^{4+}-Ir^{4+} trimer or associated with a shortening/strengthening of the Ir-O bond length.[78,247]

Table 4. *Raman peaks and corresponding mode of vibration of the Ir thin film by applying a potential of 1.2 V_{RHE} and 1.6 V_{RHE}. Assignments are based on the works reported by Pavlovic et al.[78] and Zhao et al.[80].*

Potential	Raman shift / cm^{-1}	Type of vibration
1.2 V_{RHE}	295	Ir^{4+}-O-Ir^{4+} bend
	336	Ir^{4+}-O-Ir^{4+} bend
	465	$ClO^-_{4(ads)}$
	498	Ir^{4+}-O-Ir^{4+} stretch
	548	rutile IrO_2 (E_g)
	602	Ir^{3+}-O-Ir^{4+} stretch
	681 (very weak)	Ir^{4+}-O-Ir^{4+} stretch
1.6 V_{RHE}	465	$ClO^-_{4(ads)}$
	498	Ir^{4+}-O-Ir^{4+} stretch
	695	Ir^{4+}-O-Ir^{5+} stretch

Overall, various Raman bands present at around 550 cm^{-1} are related to a mixture of Ir^{3+}/Ir^{4+} species within a hydrated IrO_x structure at the potential range of the ORR. With increasing the potential until the OER sets in, all Raman bands corresponding to Ir^{3+} centers diminish and simultaneously the formation of Ir^{4+} centers is observed by two strong bands at 498 cm^{-1} and 695 cm^{-1}.

Platinum: The in-situ Raman spectra from the monometallic Pt thin film between 0.3 and 0.8 V_{RHE} are displayed in **Figure S2.10**. Evidently, more Raman peaks are obtained at these potentials compared to the pure Ir thin film. Especially in the region between 700 and 1000 cm^{-1}, several strong bands appear and tend to change Raman their frequency with the applied potential. At 0.4 V_{RHE} several bands between 400 and 600 cm^{-1} appear simultaneously and are getting more pronounced, as the potential is increased further to 0.8 V_{RHE}. The in-situ Raman spectra obtained from the monometallic Pt thin film between 0.8 and 1.6 V_{RHE} are plotted in **Figure 39b**. At 1.0 V_{RHE} a broad band with a maximum at 558 cm^{-1} is present, while all Raman peaks between 700 and 1000 cm^{-1} disappear. From 1.2 V_{RHE} to higher potentials, a shoulder forms at 725 cm^{-1} and the broad Raman peak at 558 cm^{-1} is retained until 1.3 V_{RHE}. Increasing the potential to 1.4 V_{RHE} results in the formation of a new peak at 675 cm^{-1}, which gradually grows in intensity with higher potential up to 1.6 V_{RHE}.

First, the strong Raman bands between 700 cm^{-1} and 1100 cm^{-1} in the potential range of 0.3 – 1.0 V_{RHE} are associated with surface adsorbed -OH,[109,110] -OOH,[83,110,245] -HO_2[109] and -O_2^- [83,110] species and the respective peak assignments are summarized in **Table S2.6**. The tendency to potential-induced Raman shift is due to the more amorphous structure and different surface sites present on the rough platinum surface. All of these adsorbed oxygen species are related to ORR intermediates.[248,249] Simultaneously with the formation of adsorbed oxygen species, several bands between 400 and 600 cm^{-1} start to appear from 0.4 V_{RHE} onwards. The observed Raman bands in this region are usually assigned to Pt-O bonds of the Pt oxides.[244] In addition, water adsorbed via the oxygen atom (Pt-OH_2) can also be found around 500 cm^{-1}.[250]

At 0.8 V_{RHE}, the Raman bands for the adsorbed oxygen species between 700 and 900 cm^{-1} are still more intense compared to the Raman bands between 400 and 600 cm^{-1} associated with Pt-oxide formation (**Figure 39b**).[83,244] Thus, a mixture of metallic and oxidized Pt surface is present up to this potential, indicating the formation of some surface oxide species. From 1.0 V_{RHE} to higher potential, the peaks of the adsorbed oxygen species diminish, while a broad band with a maximum at 558 cm^{-1} appears. As shown by several in-situ Raman investigations on pure platinum, this indicates the formation of amorphous platinum oxide.[83,110,214,251–253] Huang et al.[83] and Zhang et al.[251] suggest that that the -OH species are involved in the electrochemical oxide formation on the platinum surface, including those from the surrounding water molecules. Thus, the broad Raman peak at around 550 – 600 cm^{-1} is assigned to a combination of $Pt(OH)_4$ and amorphous PtO_x previously reported in both studies.[83,251] Raman peak positions at 1.2 V_{RHE} and 1.6 V_{RHE} with the respective assignment are listed in **Table 5**.

Table 5. *For the monometallic Pt thin film, Raman peaks and corresponding mode of vibration observed at 1.2 V_{RHE} and 1.6 V_{RHE} in 0.1 M $HClO_4$. Assignments are based on Huang et al.[83], Zhang et al.[251], Graham et al.[244] and our own DFT calculations.*

Potential	Raman shift / cm^{-1}	Type of vibration
1.2 V_{RHE}	558	amorphous Pt-O; $Pt(OH)_4$ [83,251]
1.6 V_{RHE}	558	amorphous Pt-O; $Pt(OH)_4$ [83,251]
	600	Pt-O-Pt symmetric stretch + Pt-O-Pt bend
	675	Pt-O-Pt symmetric stretch + Pt-O-Pt bend
	725	Pt_3O_4 [244]

At 1.3 V_{RHE}, a second peak at 600 cm^{-1} emerges with low intensity that is assigned to Pt-O-Pt stretch of a hydrated α-PtO_2 type cluster. The peak identification based on our DFT calculations

is outlined in the subsequent section. The shoulder at 725 cm^{-1}, that starts to form from 1.2 V_{RHE} and diminishes at 1.6 V_{RHE} again corresponds to the Pt_3O_4 oxide containing mixed Pt^{2+} and Pt^{4+} species.[244] This suggests that as an intermediate of α-PtO_2, the formation of Pt_3O_4 commences. No further peak shifts and/or other peaks are visible at these anodic potentials. Only from 1.4 V_{RHE} to more positive direction, another Raman band at 675 cm^{-1} appears and is related to the Pt-O-Pt stretch of a hydrated α-PtO_2 type cluster.

To sum up, the Pt thin film shows intermediates and precursors of adsorbed (hydr-) oxygen species for the ORR up to 1.0 V_{RHE}. At higher anodic potentials, first amorphous PtO_x forms (broad band at around 558 cm^{-1}) followed by the formation of hydrated α-PtO_2 starting from 1.4 V_{RHE}. At potentials relevant for the OER, a mixture of disordered PtO_x and hydrated α-PtO_2 is found by the in-situ Raman data.

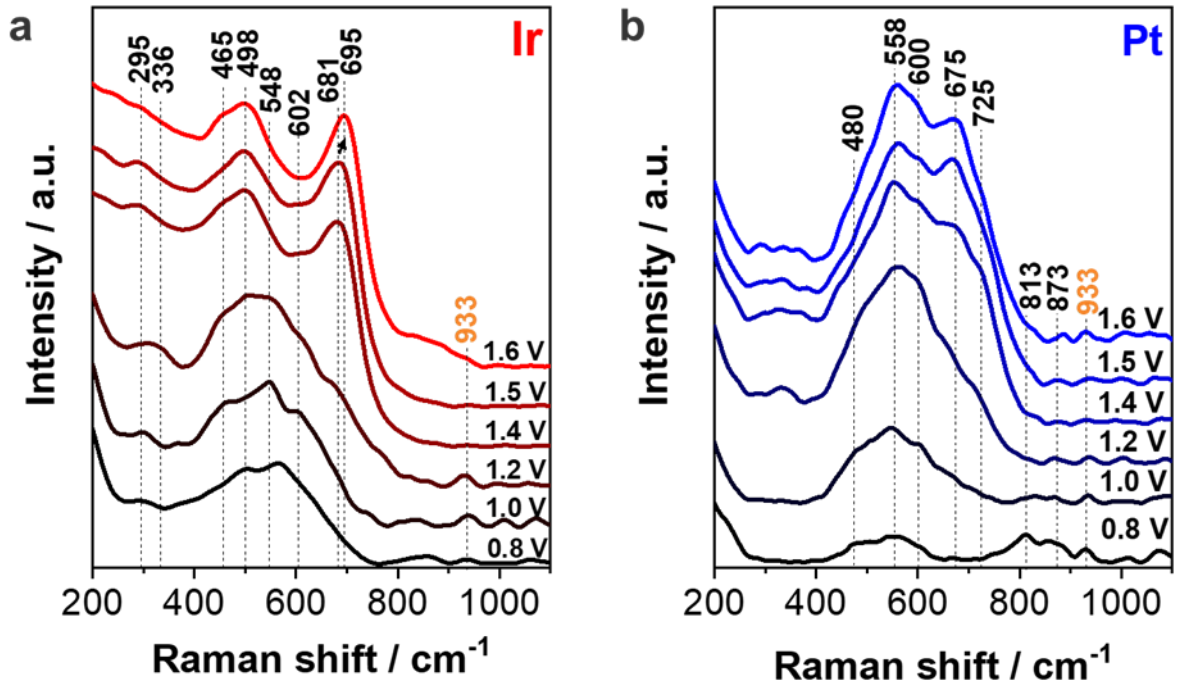

Figure 39. In-situ Raman spectra collected from (**a**) monometallic Ir and (**b**) monometallic Pt thin films in the potential range of 0.8 – 1.6 V_{RHE} in 0.1 M $HClO_4$. Peak assignments of the respective Raman data at 1.2 and 1.6 V_{RHE} are shown in **Tables 4** and **5**. The position at 933 cm^{-1} is ascribed to the adsorbed ClO_4^- anion.

In-situ Raman spectra of bimetallic PtIr(1:1) thin film

The potential-resolved in-situ Raman spectra obtained from the bimetallic Pt-Ir thin films were comprehensively investigated during ORR and OER in 0.1 M $HClO_4$. Similar to the monometallic Ir thin film at low potentials (0.3 – 0.8 V_{RHE}), the Raman spectra recorded of the PtIr(1:1) are almost identical showing one sharp Raman band at 568 cm^{-1} (**Figure S2.11**). In

contrast to the Pt thin film, no clearly resolved Raman bands between 700 and 1100 cm^{-1} appear in the potential range from 0.3 to 1.0 V_{RHE}. **Figure 40a** displays the potential-dependent Raman spectra for the PtIr(1:1) thin film between 0.8 and 1.6 V_{RHE}. At 1.0 V_{RHE}, the sharp band at 568 cm^{-1} broadens to a more intense peak with a maximum at 554 cm^{-1}, which remains unchanged until 1.2 V_{RHE}. Simultaneously, two smaller bands appear at 301 cm^{-1} and 349 cm^{-1}, indicating an assignment to the same bond. In addition to the bands at 301 cm^{-1}, 349 cm^{-1} and 554 cm^{-1}, only one further shoulder at ~710 cm^{-1} is observed at 1.2 V_{RHE}. The next significant change in the Raman spectrum is observed by applying a potential of 1.4 V_{RHE}. A red-shift of the shoulder as a distinct Raman peak to 657 cm^{-1} and the evolution of two new bands at 447 cm^{-1} and 510 cm^{-1} are clearly visible. Up to 1.6 V_{RHE}, the in-situ Raman spectra for the PtIr(1:1) thin film remain unchanged.

The sharp Raman band observed below 0.8 V_{RHE}, similar to the one obtained for the monometallic Ir thin film, is attributed to pure Ir^{3+}-OH species.[79,214,233] The absence of bands between 700 and 1100 cm^{-1} associated with on platinum adsorbed -OH,[109,110] -OOH,[83,110,245] $-HO_2$[109] and $-O_2^-$ [83,110] the surface enrichment of IrO_x, matching the findings from the ex-situ XPS data. Since sufficient ORR activity is still present (see **Figure 38d**) despite the lack of formation of adsorbed oxygen intermediates, we can conclude that the platinum is still in the metallic state. Only from 1.0 V_{RHE} to higher potentials, a broad, more intense Raman peak with a maximum at 554 cm^{-1} appears, that is assigned to the formation of a mixed amorphous Pt-Ir oxide lattice. Note, that this bimetallic oxide formation is delayed by 200 mV on the potential scale compared to the monometallic Ir and Pt thin film (**Figure S2.7**). At 1.2 V_{RHE} an additional shoulder is observed at 710 cm^{-1}, which is attributed to symmetric stretches of the μ-oxo bridging oxygen between Pt and Ir atoms based on our DFT studies. All Raman band assignments at 1.2 V_{RHE} and 1.6 V_{RHE} are shown in **Table 6**. Until 1.3 V_{RHE} these features remain essentially unchanged (**Figure S2.7c**).

From 1.4 V_{RHE} to higher anodic potential, three new Raman bands at 657 cm^{-1}, 510 cm^{-1} and 447 cm^{-1} appear, indicating changes in the lattice structure as a result of a further electrochemical oxidation of the bimetallic thin film. More precisely, from 1.2 to 1.5 V_{RHE} the band at 710 cm^{-1} red shifts to higher energy at 657 cm^{-1} associated with Ir-O-Pt stretches of the bimetallic Pt-Ir oxide. This significant red shift indicates the weakening of the Pt-O-Ir bond accompanying the oxidation of the thin film. The Raman band appearing at 510 cm^{-1} is similar to the Ir-O-Ir stretching vibration at 498 cm^{-1} observed for the monometallic Ir thin film. Based on this comparison, we ascribe this peak to the bimetallic Ir-O-Pt stretching frequency that is shifted to lower energy compared to the same frequency of the monometallic Ir thin film. The

peak at 447 cm^{-1} is corresponds to the respective Ir-O-Pt bending vibration. The peak at 554 cm^{-1} remains constant over this potential range and could originate from an underlying amorphous Pt-Ir oxide phase.

Table 6. *Potential-dependent Raman peaks and corresponding mode of vibration for the PtIr(1:1) thin film at 1.2 V_{RHE} and 1.6 V_{RHE} in 0.1 M $HClO_4$.*

Potential	Raman shift / cm^{-1}	Type of vibration
1.2 V_{RHE}	554	amorphous Pt-Ir oxide
	710	Ir-O-Pt symmetric stretch
1.6 V_{RHE}	447	Ir-O-Pt bend
	510	Ir-O-Pt bend + Ir-O-Pt antisymmetric stretch
	554	Ir-O-Pt bend + Ir-O-Pt antisymmetric stretch
	657	Ir-O-Pt symmetric stretch

Altogether, the PtIr(1:1) thin film shows one broad Raman band with a maximum at 554 cm^{-1} during the ORR (up to 1.2 V_{RHE}), revealing the appearance of an amorphous Pt-Ir oxide. The peaks associated with ORR intermediates, that are observed for the monometallic Pt thin film are completely suppressed due to the surface enrichment of IrO_x. Therefore, the observed high ORR activity is very likely related to the low coverage of the metallic Pt sites with oxygen adsorbates and the surface roughening. In addition, the oxidation of the Ir^{3+}-OH band starts to only from 1.0 V_{RHE}, which is significantly delayed on the potential scale by ~200 mV compared to the monometallic Ir thin film. Electrochemical oxidation of the bimetallic film during potentials relevant for OER results in three main peaks at 510 cm^{-1} (dominant peak), 554 cm^{-1} and 657 cm^{-1} associated with a bimetallic Pt-O-Ir lattice as well as the underlying amorphous Pt-Ir oxide phase.

Influence of the reduction of Ir content on the ORR and OER intermediates

To evaluate the effect of a lower Ir content as a costly and very scarce metal on the formation of ORR and OER surface species, potential-resolved in-situ Raman spectra for the PtIr(3:1) thin film were performed in 0.1 M $HClO_4$ (**Figure 40b**). At potentials below 0.8 V_{RHE} (displayed in **Figure S2.12**), the same sharp Raman band at 568 cm^{-1} is observed compared to the monometallic Ir and bimetallic PtIr(1:1) thin films. Similarly to the PtIr(1:1) thin film, no clearly resolved Raman bands between 700 and 1100 cm^{-1} are found in the potential range from 0.3 to 1.0 V_{RHE}. Increasing the potential to 1.0 V_{RHE}, only a broad Raman peak with a maximum at 554 cm^{-1} appears. This remains unchanged until 1.2 V_{RHE} are applied, where an additional shoulder forms at 710 cm^{-1}. When the potential is further increased to 1.5 V_{RHE}, this Raman

frequency is red shifted to 657 cm^{-1}. At 1.5 V_{RHE}, additional peaks (510 cm^{-1} and 602 cm^{-1}) are clearly observed. These peak features are still visible by applying potentials up to 1.6 V_{RHE}. Obviously, for the PtIr(3:1) thin film the most dominant Raman band is observed at 657 cm^{-1} compared to the PtIr(1:1) at 510 cm^{-1} under similar OER conditions.

We explained the observed Raman bands as a function of the potential as follows. At potentials up to 0.8 V_{RHE}, the sharp Raman band at 568 cm^{-1} is assigned to the presence of Ir^{3+}-OH species, in comparison to the Ir and PtIr(1:1) thin films. Similarly, no strong bands for the Pt-O surface species are detected between 700 and 1100 cm^{-1}. This is very surprising, because of the high platinum content (75 at.%) in the PtIr(3:1) thin film. However, the strong oxophilicity of surface-enriched IrO_x suppresses the adsorption of oxygen-based species on platinum. Increasing the potential to 1.0 V_{RHE}, a broad Raman peak with a maximum at 554 cm^{-1} appears, which is associated with the formation of an amorphous Pt-Ir oxide. At 1.2 V_{RHE} a weak shoulder develops around 710 cm^{-1} (**Table 7**) and corresponds to bridging Ir-O-Pt stretches of a bimetallic Pt-Ir oxide.

Table 7. *For the PtIr(3:1) thin film, Raman peaks and corresponding mode of vibration at 1.2 V_{RHE} and 1.6 V_{RHE} in 0.1 M $HClO_4$.*

Potential	Raman shift / cm^{-1}	Type of vibration
1.2 V_{RHE}	554	amorphous Pt-Ir oxide
	710	Ir-O-Pt symmetric stretch + Pt-O-Pt symmetric stretch
1.6 V_{RHE}	510	Ir-O-Pt bend + Ir-O-Pt antisymmetric stretch
	550	Ir-O-Pt bend + Ir-O-Pt antisymmetric stretch
	602	Ir-O-Pt symmetric stretch + Pt-O-Pt symmetric stretch
	657	Ir-O-Pt symmetric stretch + Pt-O-Pt symmetric stretch

In general, the Raman band structure after additional electrochemical oxidation from 1.4 V_{RHE} to higher potentials is different to the one from the PtIr(1:1), except for the Raman band at 657 cm^{-1}, that is observed for both thin films. In contrast to the PtIr(1:1), this distinct peak becomes the most intense band at 1.6 V_{RHE} (OER) in the Raman spectrum for the PtIr(3:1) thin film and corresponds to Ir-O-Pt stretches. A further peak, that has not been observed for the PtIr(1:1), appears at 602 cm^{-1} by applying a potential equal to or higher than 1.4 V_{RHE}. Based

on the results from the monometallic Pt thin film, we assigned this peak to the Pt-O stretching frequency of the monometallic hydrated α-PtO_2. The tendency of the platinum oxide formation is more pronounced for the PtIr(3:1) due to the higher Pt surface concentration (see ex-situ XPS, **Figure 38c**). Furthermore, the band at 510 cm^{-1} only becomes observable with a low intensity at potentials above 1.5 V_{RHE}, indicating some structural differences between the Pt-Ir oxide species formed with different atomic Pt:Ir ratios.

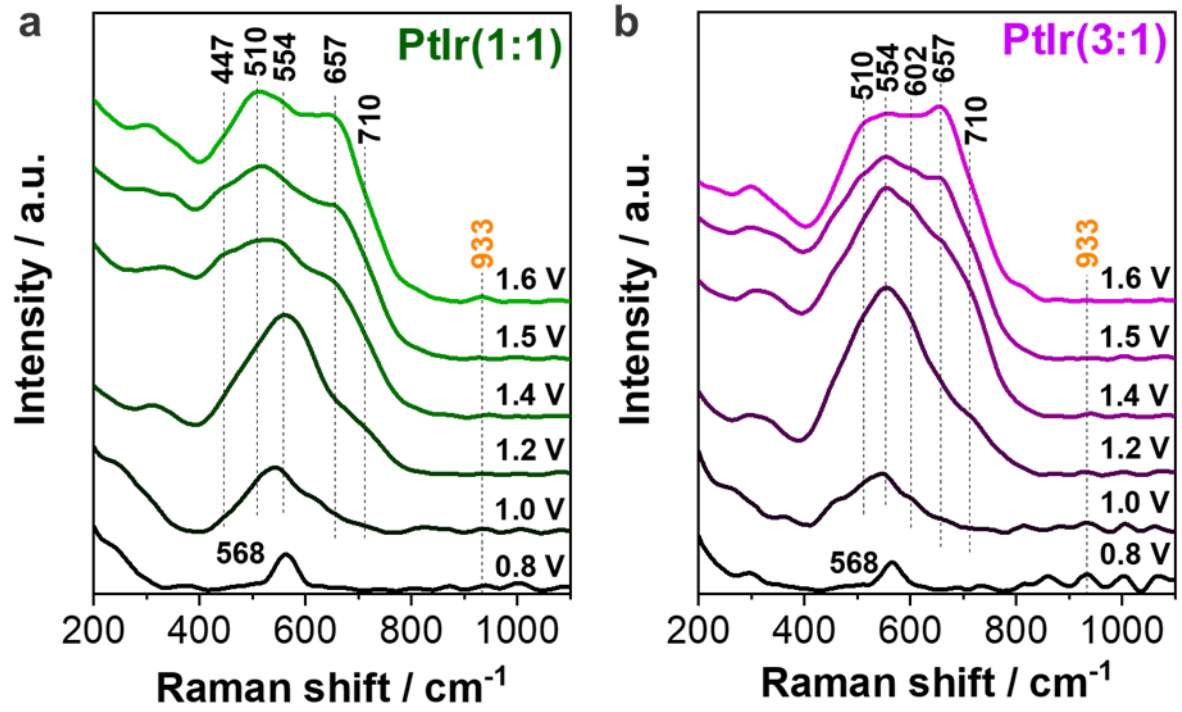

Figure 40. In-situ Raman spectra collected from (a) PtIr(1:1) and (b) PtIr(3:1) thin films in the potential range of 0.8 – 1.6 V_{RHE} in 0.1 M $HClO_4$. Peak assignments of the respective thin films at 1.2 V_{RHE} and 1.6 V_{RHE} are shown in **Tables 6** and **7**. The position at 933 cm^{-1} is related to the adsorbed ClO_4^- anion.

Altogether, during ORR the in-situ Raman spectrum of the PtIr(3:1) thin film shows mainly one broad peak at 554 cm^{-1} that corresponds to an amorphous Pt-Ir oxide. Similar to the PtIr(1:1) thin film, the absence of adsorbed ORR intermediates on the Pt sites is observed due to the increased presence of IrO_x surface. At 1.6 V_{RHE} (OER), several Raman peaks at 510, 554, 602 and 657 cm^{-1} are detected, related to the formation of bimetallic Pt-Ir oxide species. The band at 657 cm^{-1} is associated with the Ir-O-Pt stretching frequency of a bimetallic Pt-Ir oxide is the most dominant in the Raman spectrum, while the band at 602 cm^{-1} is associated with monometallic hydrated α-PtO_2.

4.2.4. DFT Calculations of Ir, Pt and Pt-Ir model structures

Density functional theory (DFT) calculations were conducted to obtain a better understanding of the catalytically active Pt-Ir sites for ORR and OER (for experimental details see **Appendix Chapter 10.2**). Calculations of the model structures and predicted Raman spectra are based on the μ-oxo bridge-connected IrO_6 octahedra as a simple model proposed by Pavlovic et al.[78], which yield a good agreement with experimental data in their study. The undercoordinated oxygen atoms of the cluster model were saturated with hydrogen atoms to either form OH or H_2O. Terminating hydroxy groups were attached to the bottom side of the metal centers as well as the axial dangling bonds to simulate a polymeric oxide structure. On the other hand, the top side was saturated with water to mimic the surface. Four different cluster systems were theoretically modeled, which are rutile-IrO_2, α-PtO_2 and two bimetallic Pt-Ir oxides with rutile structure of Pt:Ir ratios of 1:1 and 3:1. In order to optimize the computational efforts the smallest cluster sizes were defined as tetramers, to model the system with sufficient accuracy. In agreement with the work by Pavlovic et al., when using dimers as model structures, the intensities could be very low, making the comparison very difficult.[78] In their study, trimers were employed to model the IrO_x system and were found to successfully replicate important features of the experimental Raman spectra.

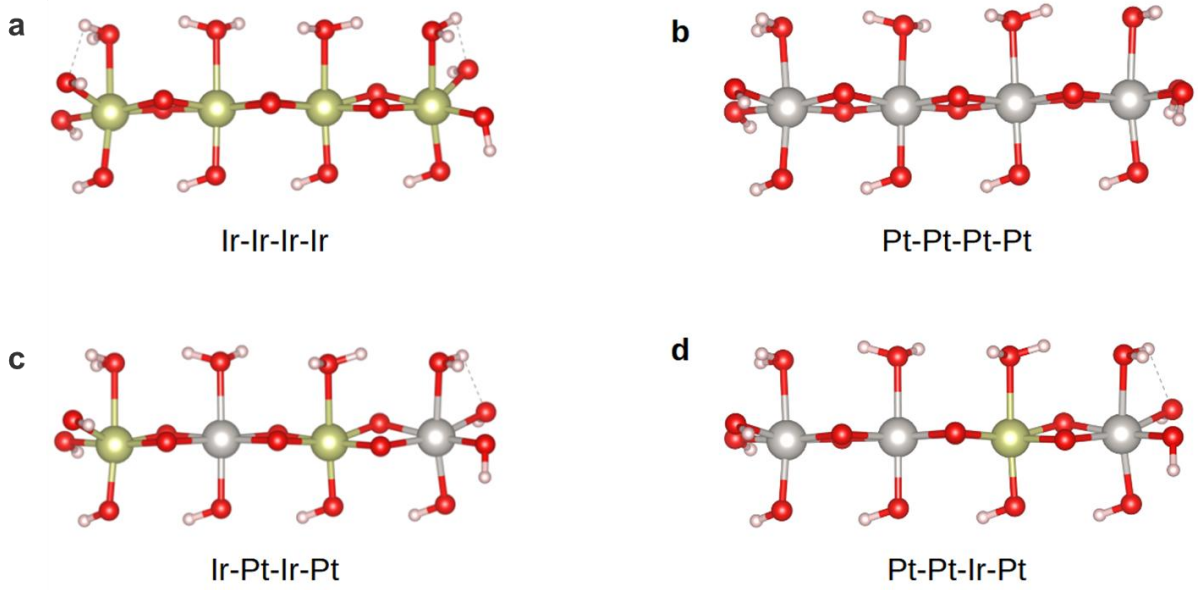

Figure 41. Optimized tetramer geometries of (**a**) iridium oxo-hydroxo complex, (**b**) platinum oxo-hydroxo complex, (**c - d**) bimetallic platinum-iridium oxo-hydroxo complex with (**c**) 1:1 and (**d**) 3:1 Pt:Ir ratios employed for the calculations of the predicted Raman spectra. Iridium, platinum, oxygen and hydrogen are denoted with gold, silver, red and white spheres, respectively. For geometry optimization, the bottom -OH groups were fixed, allowing only the μ-oxo bridges and top-side H_2O molecules to freely vibrate.

First, geometry optimizations were performed on the four tetramer models such as Ir-Ir-Ir-Ir, Pt-Pt-Pt-Pt, Ir-Pt-Ir-Pt and Pt-Pt-Ir-Pt. Thereby, the hydrogen atoms were optimized, while all other atoms were constrained. The -OH groups at the bottom of the cluster were then fixed to simulate the bulk phase and the upper layer was completely relaxed. The final and stable geometries of all oxo-hydroxo tetramer models are illustrated in **Figure 41**.

The average Ir-O bond distance in the monometallic iridium tetramer system is 1.85 – 2.06 Å, while the distance of Ir-H_2O is between 2.23 – 2.28 Å. For the α-PtO_2, these values are 1.95 – 2.00 Å and 2.18 – 2.20 Å, respectively. In general, the Pt-O bond distances are shorter, indicating a stronger bonding to oxygen. The Ir-O-Pt bonds in the mixed clusters show bond lengths from 1.84 – 2.06 Å. Obviously, there is no clear tendency for either Ir-O or Pt-O bonds being longer or shorter in the mixed cluster. On the other hand, the water ligands show a clear difference in average bond lengths of 2.28 Å and 2.18 Å for the monometallic iridium and platinum centers, respectively.

Raman spectra were calculated for all optimized oxo-hydroxo tetramer clusters, while the bottom -OH groups were fixed, allowing only the μ-oxo bridges and top-side H_2O molecules to freely move. The predicted spectra of these four tetramer clusters are displayed in **Figure 42**. A list of the most prominent peaks of the calculated Raman frequencies and corresponding vibrations are given in **Tables S2.7** to **S2.10**. It is noted that for all complexes, the strong vibrations of the bridging μ-oxo bonds are showing the most prominent peaks in the DFT-predicted Raman spectra.

In **Figure 42a**, the Raman spectrum of iridium oxo-hydroxo complex as monometallic iridium oxide model is dominated by two distinct peaks at 525 cm^{-1} and 725 cm^{-1}, which can be attributed to antisymmetric and symmetric Ir-O-Ir stretching vibrations, respectively. Compared to the iridium oxide model, the platinum oxo-hydroxo complex based on the α-PtO_2 structure has far less pronounced peaks, see **Figure 42b**. The four distinct high intensity vibrations appear as an integration of broad peaks between 500 and 650 cm^{-1}. Vibrations are on average at a lower wavelength compared to the monometallic iridium oxide cluster. In all high intensity vibrational modes (505, 572, 606, 645 cm^{-1}), the Pt-O-Pt bending motions are observed to some degree, while the dominant contribution originates from the symmetric stretching vibrations.

In **Figure 42c**, the calculated Raman spectrum of the mixed platinum-iridium oxo-hydroxo complex with a Pt:Ir ratio of 1:1 shows a large variety of high intensity peaks with Ir-O-Pt bending vibrations. More precisely, the most dominant peak appears at approximately 600 cm^{-1},

while weaker bending vibrations are found between 400 and 500 cm^{-1}. Some antisymmetric stretching is observed at approximately 550 cm^{-1}. Of special interest is the range between 600 and 700 cm^{-1}, which is composed of three different intense vibrations. It is noted that these individual vibrations are indistinguishable in the Raman spectrum due to the peak integration. All these vibrations have major contributions from the symmetric Ir-O-Pt stretching motions. Peaks in this range of wavelengths are either absent or only partly covered in the calculated monometallic platinum and iridium oxo-hydroxo complexes, leading to new Raman band structures not observed for the monometallic platinum and iridium oxo-hydroxo complexes.

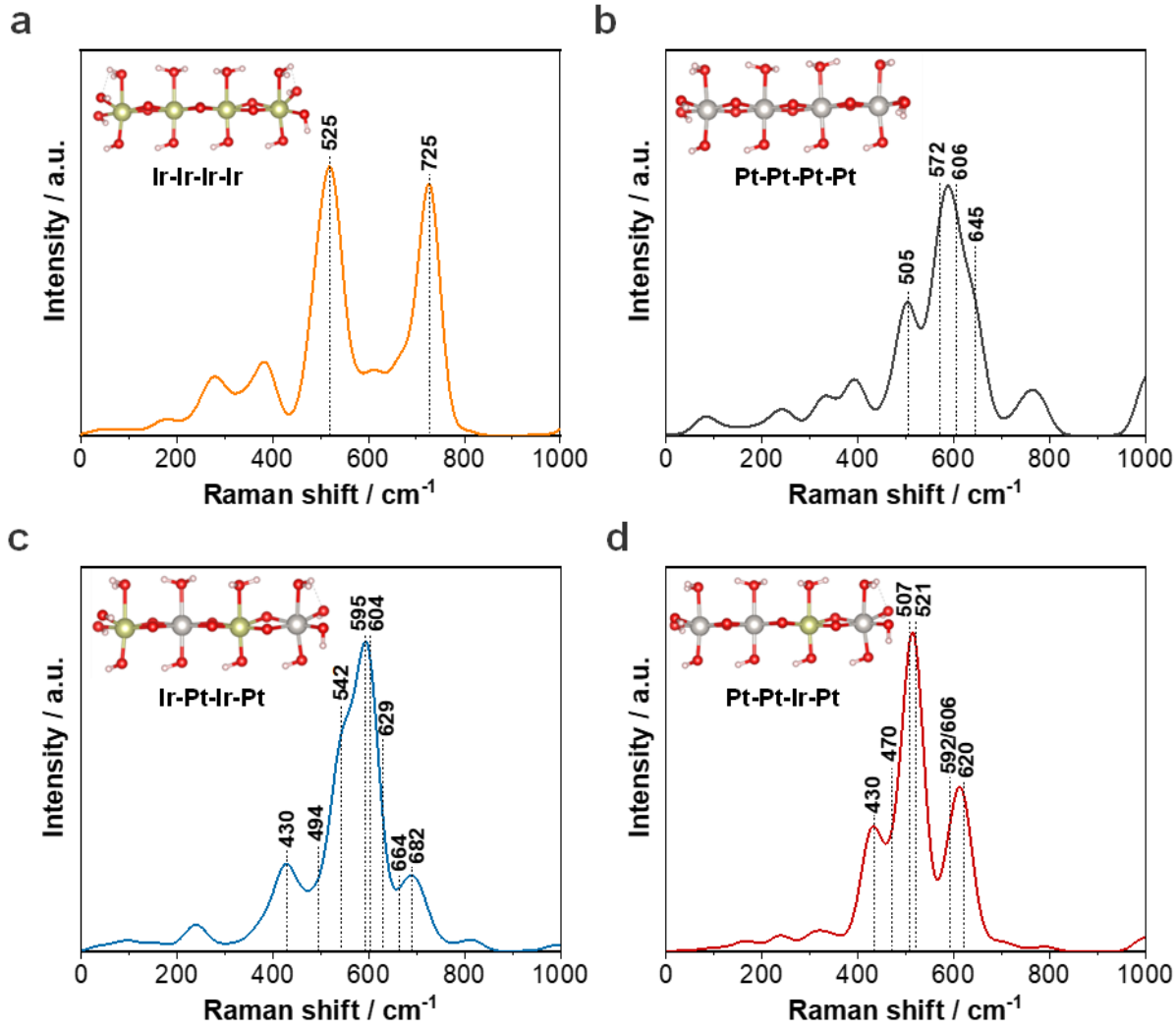

Figure 42. DFT-based calculated Raman spectra of the tetramer complexes of (**a**) iridium oxo-hydroxo, (**b**) platinum oxo-hydroxo, (**c - d**) bimetallic platinum-iridium oxo-hydroxo with Pt:Ir ratios of (**c**) 1:1 and (**d**) 3:1. Assignments of the Raman frequencies to the respective motions are displayed in **Tables S2.7 – S2.10**. Note that individual vibrations become noticeable as integration in a broad Raman band.

For the mixed platinum-iridium oxo-hydroxide complex with the central atom structure of Pt-Pt-Ir-Pt, the predicted Raman spectrum shows multiple peaks similar to those of the 1:1 Pt:Ir cluster model, see **Figure 42d**. Due to additional Pt-O-Pt interactions, some new frequencies

emerge, for example, at 507 cm^{-1}. In addition to the Pt-O-Ir stretching and bending vibrations, major contributions of μ-oxo bridged Pt-O-Pt stretching and bending motions are clearly observed between 600 and 700 cm^{-1}. Furthermore, a shift in intensities is highlighted by comparing platinum-iridium oxo-hydroxo clusters of 1:1 and 3:1. More precisely, the most intense peak for the Ir-Pt-Ir-Pt oxo-hydroxo cluster appears at around 600 cm^{-1}. In contrast, the Pt-Pt-Ir-Pt oxo-hydroxo cluster shows the highest intensity at 515 cm^{-1}, which is likely caused by the larger proportion of lower energy of the Pt-O-Pt vibrations.

To summarize, we constructed tetrameric iridium, platinum and two bimetallic platinum-iridium model clusters based on DFT calculations. The metal centers are connected by μ-oxo bridge linkages. The calculated Raman spectra of the monometallic clusters are significantly different to the bimetallic ones, due to the variations of the bending and stretching frequencies of the strong μ-oxo bridge vibrations. For the bimetallic cluster with 3:1 Pt:Ir ratio, additional monometallic Pt-O-Pt bending and stretching motions contribute to the Raman spectrum.

4.2.5. Discussion

In this work, the potential-dependent formation of the catalytically active sites of bimetallic Pt-Ir thin films and their electronic structure was comprehensively evaluated for the ORR and OER using in-situ Raman spectroscopy and DFT. In general, in-situ Raman spectroscopy is a powerful technique to uncover the differences in ORR and OER activities between the bimetallic and monometallic surfaces based on the nature of vibrations, bond strengths and oxygen coverage.

First, our results demonstrate that the Pt-Ir, Pt and Ir thin films exhibit rough and significantly oxidized surfaces. For both PtIr(1:1) and PtIr(3:1), ex-situ XPS analysis reveals a surface enrichment of iridium compared to the bulk. The electrochemical activity data pointed out a superior activity towards ORR for the Pt-Ir thin films, while their OER activity is still sufficient, confirming the bifunctionality to accelerate both reactions. In other words, the OER activity strongly reduces with a decreasing amount of iridium and the observed ORR activity is highest for the bimetallic PtIr(3:1) thin film. Ex-situ Raman spectra of the thin films show the presence of mostly disordered amorphous Pt and Ir oxides, while all iridium containing films also have two distinct bands for rutile IrO_2 structure (E_g and B_{2g}). These findings indicate the existence of two separate Pt oxide and Ir oxide phases at the surface of the bimetallic PtIr(1:1) and PtIr(3:1) thin films under ambient conditions. The formation of separate phases is most likely related to the alternating sputter processes of Ir and Pt without heating.

In-situ Raman spectroscopy data before and during ORR (0.3 to 1.2 V_{RHE})

Between 0.3 and 0.8 V_{RHE}, the bimetallic PtIr(1:1) and PtIr(3:1) thin films exhibit a similar behavior to the monometallic Ir. All of them show a sharp band, associated with highly stabilized Ir^{3+}-OH species at 564 cm^{-1} and 568 cm^{-1}, respectively. The Raman spectrum of the Ir film at 0.8 V_{RHE} shows significant broadening around the sharp band at 564 cm^{-1} together with the evolution of a new band at 498 cm^{-1}. These are associated with the μ-oxo bond of Ir^{4+} centers.[78] In contrast, the bimetallic thin films do not show the formation of a broad peak until 1.0 V_{RHE}, indicating a higher activation barrier for the electrochemical oxidation of Ir^{3+} to Ir^{4+} in these atomic arrangements.

Due to the absence of further peaks in the Raman spectrum of the bimetallic films between 0.3 and 0.8 V_{RHE}, we conclude that platinum is fully reduced to metallic. Furthermore, the presence of Ir^{3+}-OH surface species for bimetallic thin films suppresses the increased adsorption of observable ORR intermediates like -OOH, -OH, $-O_2^-$ and $-HO_2$ species on the active Pt

sites.[83,109,110,245] The monometallic Pt film already shows ORR intermediates between 700 and 1100 cm^{-1}, when a potential is applied from 0.3 to 0.8 V_{RHE}. Interestingly, the low coverage of oxygen-containing adsorbates on the active Pt sites and high surface roughness might be the cause of the superior ORR activity for PtIr(3:1) compared to monometallic Pt and PtIr(1:1).

Very interestingly, at 1.0 V_{RHE} an amorphous Pt-Ir oxide is formed on the surface of the PtIr(1:1) and PtIr(3:1) thin films, evident by the broad Raman band with a maximum at 554 cm^{-1}. This broad band resembles closer to that observed for the monometallic Pt film (at around 558 cm^{-1}), but is slightly blue shifted to a lower frequency. Up to 1.3 V_{RHE} the Raman spectra of the Pt and Pt-Ir thin films remain essentially unchanged. In contrast, the Raman peaks for the monometallic Ir film appear in a much broader frequency range and tend to move with the applied potential between 0.8 and 1.2 V_{RHE}, indicating the formation of more flexibly bound oxygen species within the IrO_x compared to a rigid crystalline IrO_2 lattice.[78,247]

Altogether, at potentials below 0.8 V_{RHE} mixed Ir^{3+}-OH and metallic Pt are observed at the surface of the bimetallic thin films. These neighboring Ir^{3+}-OH species reduce the coverage of ORR intermediate species on the low-coordinated active Pt sites, resulting in enhanced ORR kinetics.

In-situ Raman spectroscopy data before and during OER (1.3 to 1.6 V_{RHE})

In general, thermodynamically single crystalline rutile IrO_2 forms under OER conditions.[77,84] The Raman bands are located at 561, 728 and 752 cm^{-1}, corresponding to E_g, B_{2g} and A_{1g}, respectively.[242,243] On the other hand, PtO_2 exists in two structures, namely α-PtO_2 and β-PtO_2. The observed two strong Raman peaks at 511 cm^{-1} (A_{1g}) and 550 cm^{-1} (E_g) are ascribed to the formation of the thermodynamically stable α-PtO_2 under OER conditions.[77,83,84,244]

Before the OER sets in, the second oxidation wave commences at 1.4 V_{RHE} and is anodically shifted by 100 mV for the bimetallic PtIr(1:1) thin film compared to monometallic Ir (1.3 V_{RHE}). Mainly three new Raman bands at ~510 cm^{-1}, ~550 cm^{-1} and 657 cm^{-1} appear, which do not alter up to 1.6 V_{RHE} and are different from those observed for both monometallic Pt and Ir. Very importantly, our experimental data and DFT calculations point out that the potential-induced formation of bimetallic Pt-O-Ir phases occurs, where the predicted Pt-O-Ir stretching and bending vibrations are estimated to be at three distinct peaks at 542 cm^{-1}, ~600 cm^{-1} and ~682 cm^{-1}. This observation is clearly different from the appearance of separate Ir or Pt oxide during the ORR. Therefore, we can conclude that the OER kinetics are governed

by the platinum-iridium oxo-hydroxy structure as the catalytically active site for the PtIr(1:1) thin film.

From 1.5 V_{RHE} to higher potentials, an increase in platinum concentration for the PtIr(3:1) thin film shows distinct Raman peaks at ~510 cm^{-1}, ~550 cm^{-1}, ~602 cm^{-1} and 657 cm^{-1}, indicating structural differences in the surface oxide compared to both monometallic and PtIr(1:1) films. However, the peak at 510 cm^{-1} is much less pronounced compared to the other bands. To get an understanding of the observed Raman bands, we calculated a cluster with three Pt centers and one Ir center (Pt-Pt-Ir-Pt). As a result, the contributions of Pt-O-Pt stretching and bending frequencies combined with Pt-O-Ir stretching frequencies lead to a slight red shift of the Raman bands compared to the Ir-Pt-Ir-Pt cluster, indicating the weakening of the Pt-O compared to the Ir-O bond. Similar to monometallic Pt, stronger contributions of the Pt-O-Pt bending frequencies to the calculated Raman bands are observed. Based on these findings, we were able to clearly assign the additional experimental Raman band at 602 cm^{-1} to the Pt-O-Pt stretching frequency. Therefore, the PtIr(3:1) thin film shows the potential-induced formation of Pt-O-Pt and Pt-O-Ir surface species from 1.3 to 1.6 V_{RHE}.

Comparison between experiment and DFT during OER

In principle, both bimetallic Pt-Ir thin films show very similar Raman bands at ~510 cm^{-1}, 554 cm^{-1} and 657 cm^{-1} (**Figure 43a**) during the OER (1.6 V_{RHE}). The two bands at around 510 cm^{-1} and 554 cm^{-1} are assigned to Pt-O-Ir μ-oxo stretching motions of a bimetallic Pt-Ir oxide surface. The plateau between 600 – 650 cm^{-1} comprises several Raman bands and indicates the presence of monometallic hydrated α-PtO_2 phase, as shown by comparison of the Raman spectra of the PtIr(3:1) and monometallic Pt films. The most pronounced Raman band is still observed at 657 cm^{-1} for both PtIr(1:1) and PtIr(3:1). Very remarkably, this peak is red shifted to lower energy by 38 cm^{-1} (≈ 0.48 kJ mol^{-1}) compared to the same Ir-O-Ir band at 695 cm^{-1}, highlighting a change in the metal-oxygen bond strength between monometallic Ir and Pt-O-Ir bond. In the DFT-predicted Raman spectra (**Figure 43b)**, the Ir-O-Ir stretching frequency is found at 725 cm^{-1}, while this band is red shifted by 43 cm^{-1} to 682 cm^{-1} for the bimetallic cluster. The main vibrations contributing to these two frequencies are shown in **Figure 43c** and arise from the strong μ-oxo bond stretching motions of the respective complexes.

Based on this significant red shift, we can highlight that the relative reduction in the bond strength is around ~13 % and most likely caused by the weakening and lengthening of the Ir-

O-Pt bond compared to the Ir-O-Ir bond. This weaker and longer metal-oxygen bond by around 0.48 kJ mol^{-1} in the bimetallic thin films results in the observed decrease in OER activity. According to the Sabatier principle[254], the Ir-O-Pt bond seems to be too weak compared to the Ir-O-Ir bond, highlighting an optimum binding strength to accelerate the OER kinetics and resulting in a so-called volcano plot. For instance, rutile-IrO_2 has a much stronger -O* binding compared to α-PtO_2, which is beneficial for improving the OER kinetics.[255,256] In addition, a shortening of the Ir-O bond length results in an activity enhancement.[129,130,228,233,247,257] Although the Pt-O-Ir bond strength is reduced by about 13 % compared to Ir-O-Ir, it is still not sufficient to overcome the OER activity of IrO_x but is significantly more active than pure platinum.

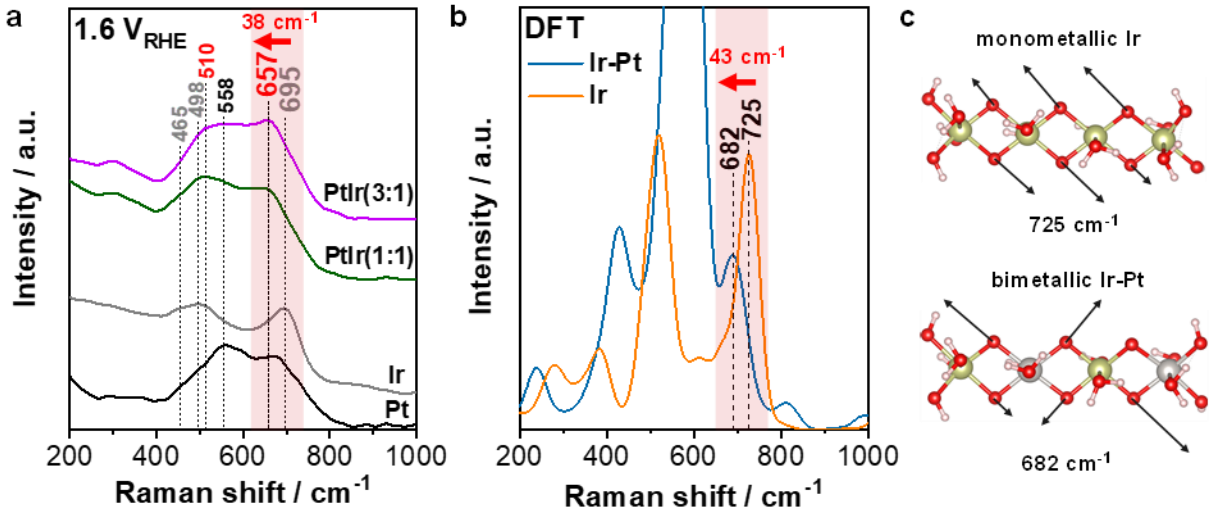

Figure 43. (**a**) Comparison between experiment and theoretical DFT calculations. (**a**) In-situ Raman spectra of all bimetallic Pt-Ir as well as monometallic Pt and Ir thin films recorded at 1.6 V_{RHE} in 0.1 M $HClO_4$. (**b**) Computed Raman spectra of the monometallic iridium oxo-hydroxo complex (orange) and bimetallic platinum-iridium oxo-hydroxy complex (blue). (**c**) Vibrations of the strong movement of the μ-oxo bonds corresponding to the Raman frequencies at 725 cm^{-1} (monometallic Ir complex) and 682 cm^{-1} (bimetallic Ir-Pt complex). The arrows show the direction and magnitude of the atomic movement.

Overall, the in-situ Raman and DFT investigations provide new structural insights on the potential-resolved formation of catalytically active sites for bimetallic Pt-Ir surfaces for both ORR and OER. Independent of the Pt:Ir ratio, the presence of Ir^{3+}-OH reduces the coverage of adsorbed oxygen intermediates on the Pt sites, resulting in an enhancement of ORR activity. At potential higher than 1.0 V_{RHE} amorphous Pt-Ir oxides appear for the first time. Further increase of the potential induces the formation of platinum-iridium oxo-hydroxy type structures instead of separate monometallic Ir and Pt oxide phases. Very remarkably, the unique combination of surface-sensitive in-situ Raman spectroscopy and DFT calculations allows revealing the lower

OER kinetics of the bimetallic surface with weakening of the Ir-O-Pt bond compared to the monometallic IrO_x.

4.3. Impact of Cu^{+} and Cu^{2+} species on the oxide-metal transition processes of Cu_xO foams during the CO_2RR probed by *operando* Quick-XAS

*This chapter is reprinted in an adapted form from Blaseio et al. in J. Mater. Chem. A, 2024, **12**, 28177–28192. https://doi.org/10.1039/D4TA02217C*

Co-authors' contributions: A. Dutta prepared the Cu_xO foams, performed ex-situ XRD and SEM measurements of the Cu_xO foams as well as CO_2RR electrolysis measurements and analysis. C. Dosche conducted ex-situ XPS measurements and quantitative analysis. A. Dutta, M. Rahaman, K. Kiran, A. Dworzak and B. Mahrt supported the *operando* XAS measurements. P. Broekmann and M. Oezaslan supervised the work and contributed to the editing of the manuscript.

In this study the potential-dependent, dynamic reduction processes of differently in air annealed Cu_xO foams (100 – 450 °C) to metallic Cu during CO_2RR are investigated using Quick-XAS. These different annealing temperatures result in different Cu^0:Cu^+:Cu^{2+} ratios and especially alter the crystal structure of CuO. With these different chemical states and structures, the oxide-metal transition kinetics during cathodic potential increment (ΔE = 100 mV), step (ΔE > 100 mV), and jump (ΔE > 500 mV) experiments were comprehensively investigated using MCR-ALS analysis of the Quick-XANES data. The results of this study demonstrate that the oxide-metal transition kinetics strongly depend on the initial abundance of Cu^{2+} species, precursor structure (ordered vs. amorphous) and on the type of chronoamperometric experiment. More precisely, a high initial population of crystalline CuO species leads to a significant shift of the *oxide-metal transition potential* towards lower cathodic values, signifying a lower energy barrier to reduction. In addition, this work revealed that the different chronoamperometric experiments strongly influenced the electrochemical stability of Cu^+ species within the Cu_xO foams during CO_2 electrolysis. Smaller potential steps were found to increase the formation of Cu^+ species, which lead to a slowdown in the reduction kinetics.

4.3.1. Ex-situ Characterization of the Annealed Cu_xO foams

The structure, crystallinity, surface and bulk composition of the Cu_xO foams annealed at 100 °C, 200 °C, 300 °C and 450 °C for 12 h in air were investigated using a variety of ex-situ techniques (for experimental details see **Appendix Chapter 10.3**). Depending on the annealing temperature, the treated Cu_xO foams will be referred to as 100-, 200-, 300-, and 450-foam throughout this thesis chapter.

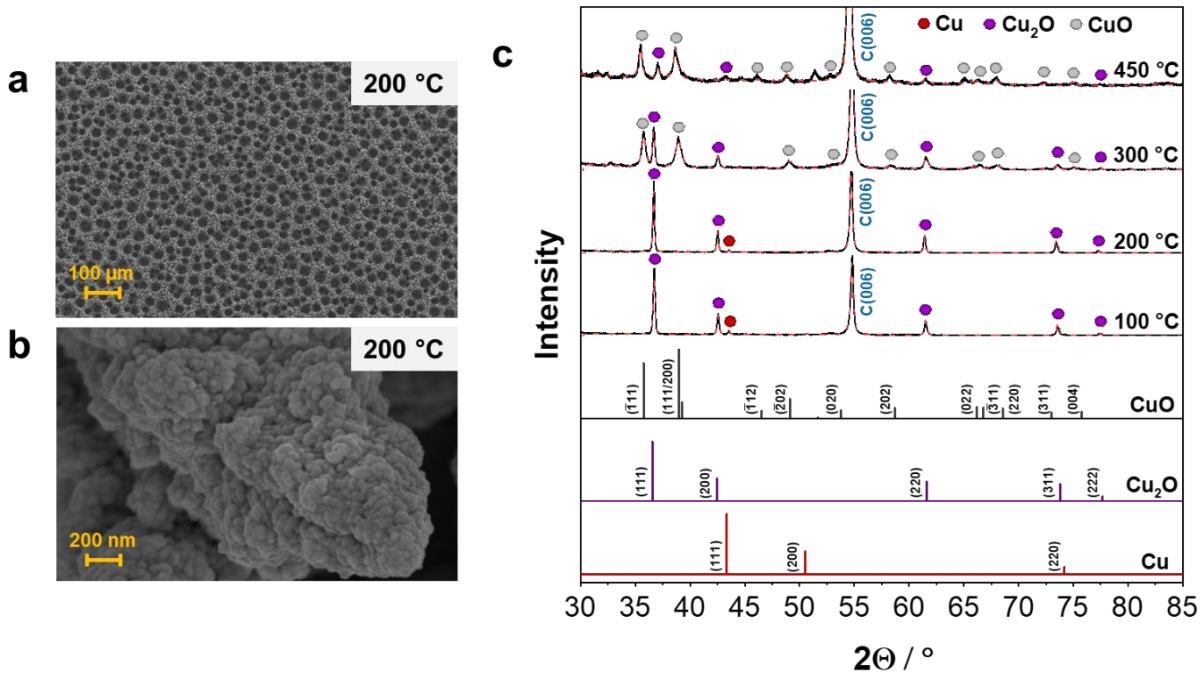

Figure 44. (**a** and **b**) SEM micrographs of the Cu_xO foam annealed at 200 °C for 12 h in air at low and high magnification. (**c**) XRD profiles (black line) of all annealed Cu_xO foams and the corresponding fits (red dashed line) obtained from the quantitative Rietveld refinement analysis. The references of Cu (#9008468, red), Cu_2O (#1010963, purple) and CuO (#9008961, grey) were taken from the crystal open database (COD).[205-207] Note, the peak at a 2θ value of 54° labelled C(006) arises from the carbon substrate. For the 100- and 200-foams, the peaks at 2θ values of 36°, 42°, 61°, 74° and 78° correspond to the lattice planes of (111), (200), (220), (311) and (222) of a primitive cubic Cu_2O unit cell with a space group of $Pn\bar{3}m$. The small peak with 2θ = 43° is assigned to the lattice plane of (111) for face-centered cubic (fcc) copper unit cell with a space group of $Fm\bar{3}m$. For the 300- and 450-foams, the additional peaks at 2θ values of 35°, 39°, 49°, 54°, 59°, 66°, 68° and 76° correspond to the lattice planes of $(\bar{1}11)$, (111/200), $(\bar{2}02)$, (020) (202), ($\bar{3}11$), (220) and (004) of a CuO base-centered monoclinic unit cell with space group C12/c1. For the 450-foam, additional CuO peaks appear at 2θ values of 46°, 65° and 73° that are ascribed to the lattice planes of $(\bar{1}12)$, (022) and (311), respectively. Reprinted from Blaseio et al.[258]

Exemplarily, **Figure 44a**,**b** display the SEM images of the Cu_xO foam annealed at 200 °C, showing a two-level foam architecture of interconnected open-cell pores. This hierarchical open pore network structure is prepared by hydrogen-assisted soft-template electrodeposition process at – 3.0 A cm^{-2} for 5 s.[180] The foam thickness is in the range of several tens of µm and is highly

porous as determined by Dutta et al. using white-light interferometric characterization.[180] The dendritic fine structure is visible in the SEM image at high magnification, see **Figure 44b**. The SEM images of the other annealed Cu_xO foams are collected in **Figure S3.1** of the **Appendix Chapter 10.3.**. Previous works have shown that the dendrites undergo structural and compositional alterations during the annealing process.[180] In other words, the thermal annealing in air induces a coalescence of the initial faceted nano-crystallites, resulting in non-textured dendrite structure (**Figure S3.1a-h**). If the annealing is carried out in air at 200 °C and above, these structural changes are more pronounced and attributed to the concerted mass transport of oxygen and copper into and out of the dendrites at the Cu_2O/CuO interface formed. The loading and thickness of the Cu_xO foams remain unaffected by the thermal annealing in air.

XRD profiles of all annealed foams are displayed in **Figure 44c**. The results of the quantitative Rietveld refinement analysis including the crystal phases, lattice parameters, crystallite sizes and phase quantity are summarized in **Table S3.2**. Obviously, the annealing temperature under oxidative environment controls the composition of the crystal phases between metallic copper, cuprous oxide (Cu_2O) and cupric oxide (CuO). For the 100- and 200-foams (**Figure 45a**), the main crystal phase (≥95 wt.%) is the cuprous oxide with a space group of $Pn\bar{3}m$. Metallic copper ($Fm\bar{3}m$) appears only as minor crystalline component. Note, that we previously showed that the as-deposited Cu foam already contains sufficient amounts of crystalline Cu_2O phases.[180] In contrast, an annealing temperature of more than 200 °C in air leads to a full oxidation of the metallic copper and concurrently to the preferred formation of cupric oxide crystal phase (space group of C12/c1). Hence, the 300-foam contains 21 ± 1 wt.% Cu_2O and 79 ± 1 wt.% CuO, whereas the contribution of the crystalline CuO phase increases to 92 ± 4 wt.% upon annealing at 450 °C, see **Figure 45a**.

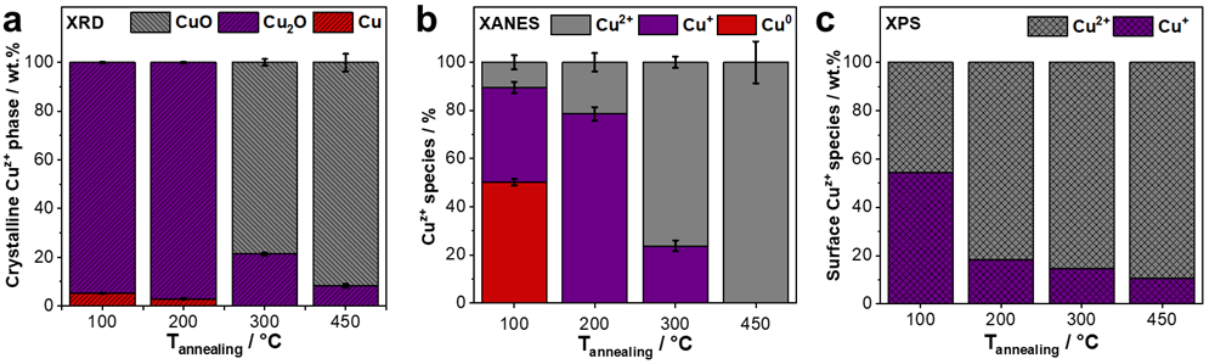

Figure 45. Contributions of the three copper species (Cu^{2+}, Cu^{+}, Cu^{0}) within the in air annealed Cu_xO foams obtained by ex-situ (**a**) quantitative Rietveld refinement analysis of the XRD patterns, (**b**) linear combination fit (LCF) analysis of ex-situ Cu K-edge XANES spectra and (**c**) analysis of the high-resolution Cu $2p_{3/2}$ XPS spectra. Reprinted from Blaseio et al.[252]

As a complementary bulk technique that can detect the nearest neighboring atoms in both amorphous and crystalline structures, the ex-situ Cu K-edge XANES data for all foams were evaluated. By measuring the K-edge, the transition of an electron from 1s to 4p orbital occurring on absorption of the X-ray beam is observed, while the sharp rise in the resulting absorption peak is known as the white line. In **Figure S3.2**, the ex-situ XANES spectra obtained from the 100-, 200-, 300- and 450-foams and the references of Cu foil, Cu_2O and CuO are displayed. Based on the references, the white line intensity increases from Cu^0 to Cu^{2+} as well as a shift in transition energy from 8979.7 eV (Cu^0), 8981.1 eV (Cu_2O) to 8984.3 eV (CuO), which is in excellent agreement with the literature.[179,259] Additionally, the pre-edge at ~8979 eV in the XANES spectra is distinctive for the Cu^+ and Cu^0 species and is usually much less pronounced for CuO.[259] **Figure 45b** shows the contribution of Cu^0, Cu^+ and Cu^{2+} species for the differently annealed Cu_xO foams based on the linear combination fit (LCF) analysis of the ex-situ XANES data using Cu^0, Cu_2O and CuO reference spectra. The 100-foam consists of 50 ± 1 % Cu^0, 39 ± 2 % Cu^+ and only 11 ± 3 % Cu^{2+} species. The apparent discrepancy between the XRD and XANES data can be rationalized by the amorphous structure of metallic copper within the 100-foam. An annealing temperature of 200 °C leads to an entirely oxidized foam (79 ± 3 % Cu^+ and 21 ± 4 % Cu^{2+}). Note, due to the sensitivity the LCF analysis of the XAS data could not detect the minor contribution (3 wt.%) of metallic Cu found by XRD. By raising the temperature to 300 °C and 450 °C, the oxidation state of the Cu species within the foam increases further. The 300-foam still contains 24 ± 2 % Cu^+ and 76 ± 2 % Cu^{2+}, while the foam at 450 °C is entirely oxidized to CuO.

Surface sensitive ex-situ XPS and Raman spectroscopy were employed to evaluate the initial oxidation states of the Cu_xO foams. High-resolution Cu 2p XPS and Cu LMM Auger spectra for each in air annealed Cu_xO foam are plotted in **Figure S3.3**. In **Figure S3.3a**, the deconvolution of Cu $2p_{3/2}$ XPS spectra of the 100-foam indicates two chemical species at binding energies (BEs) of 934.6 eV and 932.0 eV, with the former being assigned to oxidized Cu^{2+} in agreement with other works.[170,260,261] Additionally, the appearance of the Cu^{2+} satellite peaks between 965 – 960 eV as well as 947 – 938 eV support the presence of CuO.[170,260,261] In **Figure S3.3b**, a characteristic shift in kinetic energy (KE) to 916.9 eV is detected in the Cu LMM Auger spectrum, which corresponds to Cu_2O.[260,261] Thus, the second chemical species at BE value of 932.0 eV is assigned to Cu^+. Raising the annealing temperature to 200 °C, the Cu 2p XPS spectrum in **Figure S3.3c** shows a significant increase of the population of Cu^{2+} surface species, which is also confirmed by the intensity increase of the Cu^{2+} satellites and shift of the Auger KE to 917.1 eV. For the 300- and 450-foams, the Cu LMM Auger spectra

(**Figure S3.3f**, **h**) and Cu 2p XPS spectra (**Figure S3.3c**, **e**) reveal the continuous growth of the population of Cu^{2+} surface species. Based on the deconvolution of the Cu $2p_{3/2}$ XPS spectra, the surface compositions of the differently annealed Cu_xO foams are summarized in **Figure 45c**. As expected, metallic Cu on the foam surface is not found for any annealing temperature. Very interestingly, the Cu^+:Cu^{2+} surface ratio alters from 54:46 at 100 °C to 20:80 at 200 °C. At 300 °C and 450 °C, the contribution of Cu^{2+} species further increases to 85 wt.% and 89 wt.%, respectively.

In **Figure S3.4**, Raman spectra of the different in air annealed Cu_xO foams show Cu_2O and CuO surface species. Note, that bulk metallic Cu does not show any Raman active bands due to the polarizability selection rule. In accordance with the XRD data, the 100- and 200-foams show several Raman bands at 110 cm^{-1} (E_μ), 146 cm^{-1} ($T_{1\mu}$), 217 cm^{-1} ($2E_\mu$), 415 cm^{-1} ($4E_\mu$), 623 cm^{-1} ($T_{1\mu}$) and 645 cm^{-1} ($T_{1\mu}$), that are characteristic for crystalline Cu_2O.[262–264] No peaks corresponding to CuO are observed for these two foams. In contrast, the 300- and 450-foams only show characteristic bands for the three Raman active modes of CuO at 298 cm^{-1} (A_g), 346 cm^{-1} (B_g) and 632 cm^{-1} (B_g).[262] These findings are consistent with ex-situ XRD data, as only crystalline copper oxide species exhibit sharp Raman bands described above.

We can sum up that the ex-situ XRD and XANES data reveal different bulk contribution of Cu species within the foams particularly annealed at low temperatures. The direct comparison of ex-situ XRD and XANES data indicates the existence of amorphous CuO species in sufficient amount at lower annealing temperatures, while the formation of only crystalline Cu_2O phases is signified throughout all annealing temperatures. Furthermore, the surface of the annealed foams is more oxidized compared to the bulk with higher amounts (≥ 50 wt.%) of Cu^{2+} species for the 100- and 200-foams.

4.3.2. CO_2 Electrolysis Product Distribution

To understand the structure – performance – selectivity relationship of the differently annealed Cu_xO foams, the Faradaic Efficiencies (FEs) and partial current densities for H_2, C_1 and C_2 product formation at $-0.87\ V_{RHE}$ in CO_2-saturated 0.5 M $KHCO_3$ in dependence of the annealing temperature are displayed in **Figure S3.5**. For experimental details see **Appendix Chapter 10.3**. A notable characteristic of the electrodeposited Cu_xO foam catalysts is the complete suppression of the C_1 (methane) reaction pathway.[161] The FEs for CO_2RR products (C_1 and C_2) are approximately 36 %, 39 %, 38 % and 29 % for the 100-, 200-, 300-, and 450-foams, respectively (**Figure S3.5**). In addition, alcohol formation is observed for all Cu_xO foams after 1 h of CO_2RR without a clear trend and is therefore not discussed in this work.

However, a correlation between C2 products, such as ethylene and ethane and the initial Cu^+ content of the annealed Cu_xO foams (**Figure S3.6**) could be identified. More precisely, the 100-, 200- and 300-foams show increased FEs (~9.0 – 10.0 %, ± 0.4 %) compared to the 450-foam (~7.0 – 8.0 %, ± 0.5 %), which lacks abundant Cu_2O. This suggests that Cu_2O promotes the formation of C_2 products, whereas CuO is less favorable. It is important to note that the FEs for ethylene and ethane in this study are lower than those previously reported by Dutta et al.[161] The overall CO_2RR efficiencies were found to be strongly dependent on surface pore size distribution and catalyst film thickness, which are influenced by the deposition time at constant current density. The Cu_xO foams used in this study were optimized for operando XAS investigations in terms of film thickness, rather than for CO_2RR product distribution. Consequently, thinner films on a graphite substrate were used (see **Figure S3.1**, SEM), which differs from the optimal conditions for high CO_2RR efficiencies. This may have increased the selectivity towards hydrogen as a competing HER on the partially exposed graphite substrate occurs. The effect is even more pronounced for an annealing temperature of 450 °C, which activates the exposed graphite substrate to produce more hydrogen (**Figure S3.5**).

In the next step, we investigated the oxide-metal transition during CO_2RR probed by *operando* Cu K-edge Quick-XAS using different potential control experiments. The different types of experiments conducted (potential increment, step, and jump) are illustrated in **Figure S3.7**.

4.3.3. Potential Increment Experiments (ΔE = 100 mV) from + 0.4 V_{RHE} to – 1.2 V_{RHE}

First, potential increment experiments were carried out, where the potential was shifted in steps of 100 mV from + 0.4 V_{RHE} to – 1.2 V_{RHE}, while each increment was held for 6 – 10 min. In order to determine changes in chemical state of the Cu species, XANES spectra were analyzed using multivariate curve resolution - alternating least squares (MCR-ALS) analysis. A detailed example of the MCR-ALS analysis in MATLAB is shown in **Figure S3.8**. As established by the ex-situ characterization, the initial chemical states of the Cu_xO foams are mixed oxides irrespective of the annealing temperature. Thus, the reference spectra of the three copper species (**Figure S3.2**) were fixed as components to obtain the potential-dependent concentration of each Cu species directly from the MCR-ALS algorithm. The series of potential-resolved XANES spectra of the differently annealed Cu_xO foams as well as the corresponding concentration profiles are presented in **Figure 46**. Additionally, the Cu K-edge XANES spectra assigned to each potential are displayed in **Figure S3.9**. Note, that there are no changes in the XANES spectra of the different Cu_xO foams at OCP (**Figure S3.10**). The left panel of **Figure 46** displays

the potential-resolved XANES spectra of each annealed Cu_xO foam (100 °C – 450 °C). Generally, the series of XANES data show a potential-dependent decrease in white line intensity and shift in transition energy from 8984.3 eV (Cu^{2+}) to 8979.7 eV (Cu^0) for all Cu_xO foams pronounced to different extents. This shift in transition energy indicates a gradual reduction of the Cu^{2+} and Cu^+ species to Cu^0 and is evident to different degrees depending on the annealing temperature.

Based on the LCF analysis of the ex-situ XANES data (**Figure 45b**), the 100-foam initially contains 50 % of metallic Cu. Upon exposure to the electrolyte and anodic potentials, this metallic Cu is partially oxidized to Cu^+ species, signified by the increase in the pre-edge and white line intensity observed at + 0.4 V_{RHE} and OCP (**Figure S3.10**). However, some metallic Cu remains and consequently, the changes of the pre-edge in the course of the potential-dependent XANES spectra are less pronounced due to this initial content of Cu^0 species. For the Cu^{2+} rich foams annealed at 300 °C and 450 °C (**Figure 46e**,**g**), the potential-resolved XANES spectra recorded at anodic potentials show less pronounced pre-edge features at ~8979 eV. With increasing cathodic potential, the reduction of Cu_xO is much more evident by the appearance and shift in pre-edge position of the Cu K-edge XANES spectra.

After the potential-induced reduction process to metallic Cu is complete, no further changes in the XANES spectra are found for all annealed Cu_xO foams, signifying that the metallic Cu is stable at more negative potentials than – 0.8 V_{RHE}, where typically the formation of hydrocarbon sets in.[174,265] This observation is in excellent agreement with our previous works.[169,180]

In the right panel of **Figure 46**, the normalized concentration of the three Cu species obtained from the MCR-ALS analysis in dependence on the applied potential is displayed for the thermally annealed foams. As the potential is stepwise moved in the cathodic direction, a successive decrease in the Cu^{2+} and Cu^+ species concentrations is observed for all Cu_xO foams. Simultaneously, the concentration of Cu^0 is increasing.

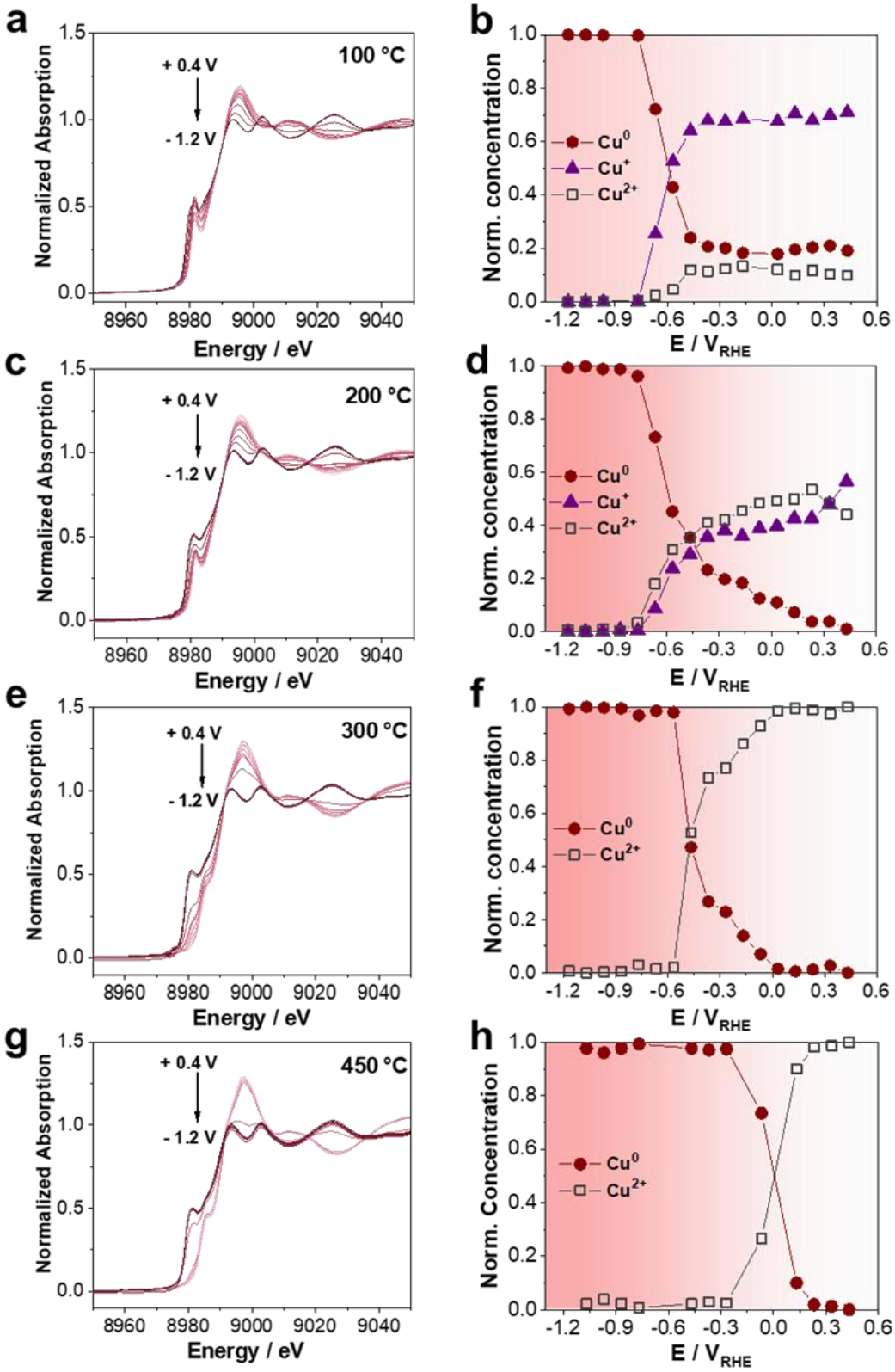

Figure 46. Left panel (a, c, e, g): Series of potential-resolved Cu K-edge XANES spectra of the Cu_xO foams annealed at 100 °C, 200 °C, 300 °C and 450 °C in air. The potential was shifted from + 0.4 V_{RHE} to – 1.2 V_{RHE} at 100 mV and held for 6 – 10 min at each potential, while XAS spectra were collected and subsequently averaged. CO_2-saturated 0.5 M $KHCO_3$ was used as electrolyte solution. **Right panel (b, d, f, h):** Normalized Cu^0, Cu^+ and Cu^{2+} concentration courses obtained by the MCR-ALS analysis of the spectra from the left panel. Reprinted from Blaseio et al.[252]

For the 100-foam (**Figure 46b**), the exposure to the electrolyte and anodic potential leads to an initial oxidation of 30 % Cu^0 to Cu^+ species at + 0.4 V_{RHE}. No change in concentration (20 % Cu^0, 70 % Cu^+ and 10 % Cu^0 species) occurs until – 0.3 V_{RHE}. Thereafter, the successive reduction of Cu^+ and Cu^{2+} species to metallic Cu sets in and is completed at – 0.8 V_{RHE}. For the 200-foam (**Figure 46d**), a simultaneous reduction of both Cu^+ and Cu^{2+} species takes place between + 0.2 V_{RHE} and – 0.8 V_{RHE}, at which this Cu_xO foam is reduced entirely to metallic Cu. As expected from the operando XANES spectra, the initial composition of the 300-foam shows 100 % CuO (**Figure 46f**), which is gradually reduced to metallic Cu from + 0.4 V_{RHE} to – 0.6 V_{RHE}. Here, no formation of Cu^+ species was detected. We note, that this observation is different to our previously published work, where only 80 % of the 300-foam are oxidized to Cu^{2+} species at + 0.5 V_{RHE} with intermediate Cu^+ formation. We attribute this difference to the initial structure, morphology and chemical species of Cu_xO during the annealing process and in contact with the electrolyte solution.[169,170,180] In contrast, the 450-foam (**Figure 46h**), which is also fully oxidized to CuO, shows a completion of the reduction process already at lower anodic potential (– 0.3 V_{RHE}), again without the formation of intermediate Cu^+ species. Overall, for all annealed Cu_xO foams the MCR-ALS analysis points out the appearance of metallic Cu at potentials more negative than – 0.8 V_{RHE}.

Very interestingly, the transition of oxide to metallic copper occurs at different reduction potentials for each of the different annealing temperatures. We defined the point at which half of this transition was completed as the *oxide-metal transition potential*.

According to the thermodynamically based Pourbaix diagram, the transition from Cu^{2+} to Cu^+ takes place at + 0.243 V_{SHE} = – 0.181 V_{RHE} under the presented conditions (pH = 7.2, CO_2-saturated 0.5 M $KHCO_3$).[187] Only from + 0.045 V_{SHE} = – 0.380 V_{RHE} their further electrochemical reduction to Cu^0 sets in.[187] Therefore, the observed differences in the *oxide-metal transition potential* are very likely based on the initial content of Cu^{2+} species for the differently annealed foams.

Figure 47 illustrates the changes in *oxide-metal transition potential* as a function of the annealing temperature and thus the initial concentration of the Cu^{2+} species for all Cu_xO foams obtained from the MCR-ALS analysis. Note, that for Cu^+ such a relation is difficult to establish, since the annealing at 100 °C in air already generates high amounts of crystalline Cu_2O. For the 100-foam at very low Cu^{2+} concentration, the *oxide-metal transition potential* is found to be at – 0.60 V_{RHE}, doubling the annealing temperature to 200 °C and thereby doubling the initial amorphous Cu^{2+} content (surface and bulk obtained from ex-situ XPS, XAS and XRD), only shifts the *oxide-metal transition potential* to – 0.55 V_{RHE}. A further increase to 300 °C and in

Cu^{2+} content to 80 % derived from the LCF analysis reduces the potential to – 0.45 V_{RHE}, so that at least 50 % is in the metallic state. The 450-foam, which contains 100 % Cu^{2+} species in the initial state, shows a considerable shift in the *oxide-metal transition potential* to 0 V_{RHE}. Additionally, the reduction of the Cu_xO foams can also be monitored by EXAFS analysis. The data is shown in **Figure S3.11** and **Tables S3.3 – S3.6**. Exemplary, the EXAFS fit results in k- and R-space for each of the in air annealed Cu_xO foams at + 0.4 V_{RHE}, – 0.1 V_{RHE} and – 1.1 V_{RHE} are displayed in **Figures S3.12 – S3.15**. An increase or decrease in the partial coordination number of Cu-Cu or Cu-O pair indicates the successive reduction of the Cu_xO foams in the cathodic direction, respectively.

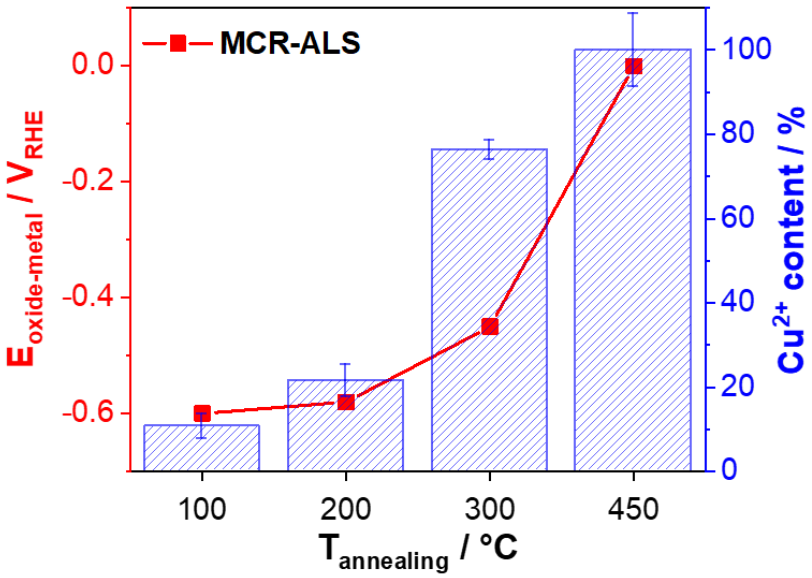

Figure 47. Oxide-metal transition potential in dependence of the annealing temperature for different Cu_xO foams obtained by MCR-ALS (full red squares) analysis. The corresponding Cu^{2+} content of each Cu_xO foam (blue bars) was obtained from LCF analysis of the ex-situ XANES spectra using Cu^0, Cu_2O and CuO as reference materials. Reprinted from Blaseio et al.[252]

Overall, the *oxide-metal transition potential* strongly depends on the annealing temperature and therefore the proportion of Cu^{2+} species in the Cu_xO foams. Higher proportion of Cu^{2+} species causes a shift in the *oxide-metal transition potential* towards lower values during the potential increment experiments (ΔE = 100 mV, from + 0.4 V_{RHE} to – 1.2 V_{RHE}) conducted in CO_2-saturated 0.5 M $KHCO_3$.

4.3.4. Potential Step Experiments (ΔE > 100 mV)

The potential step experiments are the second set of *operando* Quick-XAS measurements carried out to understand the transition of Cu_xO to metallic Cu. The potential was stepwise shifted (more than 100 mV) and held for at least 300 s at each potential (from OCP to

– 1.3 V_{RHE}) using two intermediate steps at – 0.2 V_{RHE} and – 0.5 V_{RHE} in CO_2-saturated 0.5 M $KHCO_3$.

In **Figure 48**, the respective Cu K-edge Quick-XANES spectra and normalized concentration profiles for the 200-foam from the chronoamperometric measurements at different applied potentials are presented. The series of XANES spectra obtained from the first potential step (OCP to – 0.2 V_{RHE} for 700 s) are displayed in **Figure 48a**. From thermodynamic predictions, at this potential the Cu^{2+} species are reduced to Cu^{+} at pH = 7.2.[187] In the inset of **Figure 48a**, the pre-edge intensity at ~8980 eV increases over time at – 0.2 V_{RHE}, indicating the transition from Cu^{2+} to Cu^{+}. Changing the potential from – 0.2 V_{RHE} to – 0.5 V_{RHE} (**Figure 48c**), a slight decrease in the pre-edge intensity was observed within 350 s, which implies a marginal reduction of Cu^{+} to Cu^{0}. Shifting the potential further to – 1.3 V_{RHE}, an instant reduction to Cu^{0} takes place within the first 150 s. This is indicated by the white line intensity and shift in transition energy to a lower value as expected for metallic copper.

Furthermore, for the 200-foam the normalized concentrations of Cu^{0}, Cu^{+} and Cu^{2+} species over time during the chronoamperometric measurements from OCP → – 0.2 V_{RHE} → – 0.5 V_{RHE} → – 1.3 V_{RHE} obtained from the MCR-ALS analysis are displayed in the right column of **Figure *48***. In **Figure 48b**, at – 0.2 V_{RHE} a gradual reduction of the initial 40 % Cu^{2+} to Cu^{+} is observed and as predicted by thermodynamics, no metallic Cu has started to appear.[187] Around 20 % Cu^{2+} remain after 700 s. Jumping to a more cathodic potential of – 0.5 V_{RHE} leads to a slow transition of the remaining 10 % Cu^{2+} to Cu^{+}, while after around 100 s the formation of Cu^{0} commences. Note, that the starting composition at – 0.5 V_{RHE} slightly differs from the previous potential jump (at – 0.2 V_{RHE}), namely ~10 % Cu^{2+} species are reduced. Changing the potential from – 0.5 V_{RHE} to – 1.3 V_{RHE} (**Figure 48f**), a full reduction of the Cu_xO foam is detected after ~150 s. Thus, the 200-foam with a high Cu^{+} content shows a slow transition behavior, which requires highly cathodic potentials to reduce completely from Cu^{+} to Cu^{0}.

The same potential step experiment was carried out for the 450-foam, shown in **Figure S3.16**. As opposed to the 200-foam, this foam contains 100 % of Cu^{2+} species produced by the higher annealing temperature in air. First, only a slight reduction of Cu^{2+} species occurs from OCP to – 0.2 V_{RHE}. About 10 % of the Cu^{2+} species are reduced to Cu^{0} and Cu^{+} species within 350 s. However, when changing the potential from – 0.2 V_{RHE} to – 0.5 V_{RHE}, an instant reduction of Cu^{2+} and Cu^{+} species within less than 2 s is detected. Thus, the higher content of Cu^{2+} species

in the 450-foam leads to a shift in the potential-induced oxide-metal transition to less negative potentials and is much faster compared to the reduction behavior of the 200-foam.

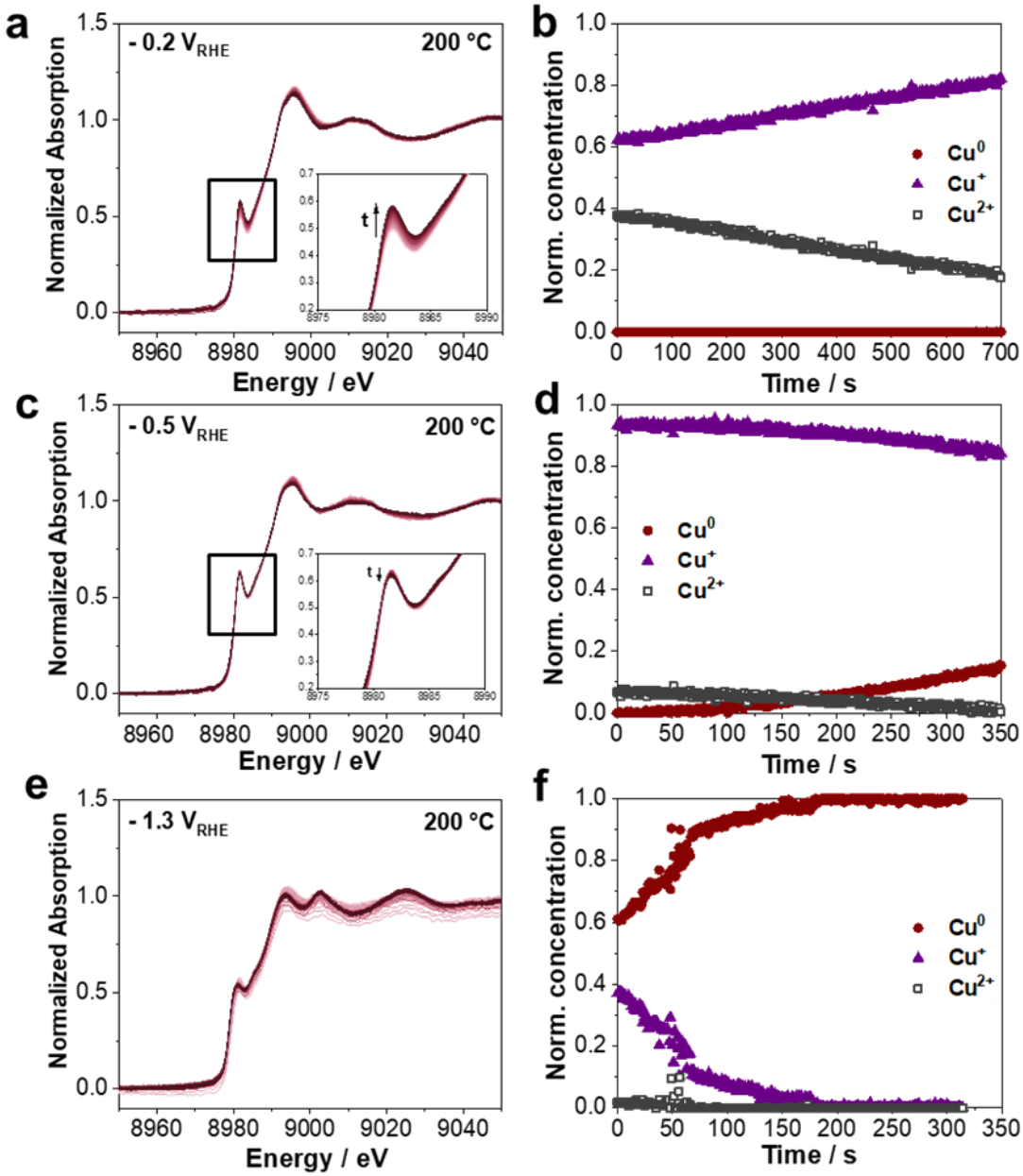

Figure 48. Series of time-resolved Cu K-edge Quick-XANES spectra of 200-foam by jumping from OCP → – 0.2 V_{RHE} (**a**) → – 0.5 V_{RHE} (**c**) → – 1.3 V_{RHE} (**d**) in CO_2-saturated 0.5 M $KHCO_3$. One spectrum was collected every second. (**b, d, f**) Normalized Cu^0, Cu^+ and Cu^{2+} concentrations obtained by the MCR-ALS analysis in dependence of the time at the respective applied potential. Note, the noise in the XAS spectra is caused by the strong bubble formation especially at – 1.3 V_{RHE}, making it difficult to normalize the data in a proper way. Reprinted from Blaseio et al.[252]

Altogether, for the 200-foam an initial reduction of Cu^{2+} to Cu^+ at – 0.2 V_{RHE} and a slow transition of the Cu^+ to metallic at – 0.5 V_{RHE} is observed. In contrast, the 450-foam already rapidly reduces to metallic Cu at – 0.5 V_{RHE}.

4.3.5. Potential Jump Experiments (ΔE ≥ 500 mV)

In order to investigate the oxide-metal transition behavior without applying intermediate potentials, a direct potential jump from OCP to either – 0.5 V_{RHE} or – 1.3 V_{RHE} in CO_2-saturated 0.5 M $KHCO_3$ was performed.

In **Figure 49**, the direct potential jump from OCP to – 0.5 V_{RHE} is plotted for the 200- and 300-foams, whereas the larger jump to – 1.3 V_{RHE} for the 100- and 300-foams is displayed in **Figure 50**. Both, **Figure 49** and **Figure 50** illustrate a series of time-resolved Cu K-edge Quick-XANES spectra collected at the applied potentials with the corresponding normalized concentration profiles and holding times obtained by the MCR-ALS analysis. Again, the composition of each Cu species obtained by the MCR-ALS analysis is determined using the CuO, Cu_2O and metallic Cu references.

Figure 49a illustrates the time-resolved changes in the Quick-XANES data for the 200-foam by jumping the potential from OCP to – 0.5 V_{RHE} for ~300 s. A slow decrease in white line intensity and a shift in edge jump energy from 8982.1 eV (Cu^{z+}) to 8979.7 eV (Cu^0) are observed. Furthermore, the inset in **Figure 49a** shows a decrease in the pre-edge intensity within 300 s at – 0.5 V_{RHE}. Based on the MCR-ALS analysis, initially 63 % Cu^+ and 37 % Cu^{2+} species are present by directly applying the potential of – 0.5 V_{RHE}. This is in good agreement with the initial compositions obtained during the potential increment and step experiments for this Cu_xO foam. First, we observed that the Cu^{2+} species diminishes from 37 % to 0 % at – 0.5 V_{RHE} for around 225 s (**Figure 49b**). Within the holding time of 130 s, a simultaneous increase in Cu^+ species as intermediate is found at a similar rate, at which the initial Cu^{2+} species decreases. From 130 s onwards, the formation of metallic Cu commences and is complete after 285 s at – 0.5 V_{RHE}. As a comparison, the Cu^+ intermediate species were already observed for the 200-foam during the potential step experiment in **Figure 48**. Therefore, we can conclude that the electrochemical reduction of the Cu^{2+} to Cu^+ took place initially followed by the formation of fully metallic Cu under these conditions.

The same potential jump experiment (OCP → – 0.5 V_{RHE}) was carried out with the 300-foam. A series of Cu K-edge Quick-XANES spectra collected for 130 s at – 0.5 V_{RHE} (presented in **Figure 49c**) show a fast decrease in white line intensity and a small shift in transition energy from 8981.5 eV (Cu^{z+}) to 8980.0 eV (Cu^0). This quick potential-induced oxide-metal transition is clearly confirmed by the MCR-ALS analysis (**Figure 49d**). A prompt reduction of the initial Cu_xO to metallic within ~40 s is observed based on the decrease in Cu^+ and Cu^{2+} species and concurrently increase in Cu^0 concentration. It is noted that half of the Cu^{2+} and Cu^+ content was already reduced after around 20 s by jumping the potential from OCP to – 0.5 V_{RHE}. Thus, it is

obvious that the oxide to metal transition processes for the 200- and 300-foams from OCP to – 0.5 V_{RHE} occur with different kinetics depending on the initial chemical state of the copper. More precisely, the oxide-metal transition kinetics of the 200-foam with an initial Cu^{+}:Cu^{2+} ratio of 63:37 is around 6-times slower than that for the 300-foam (Cu^{+}:Cu^{2+} ratio of 20:80).

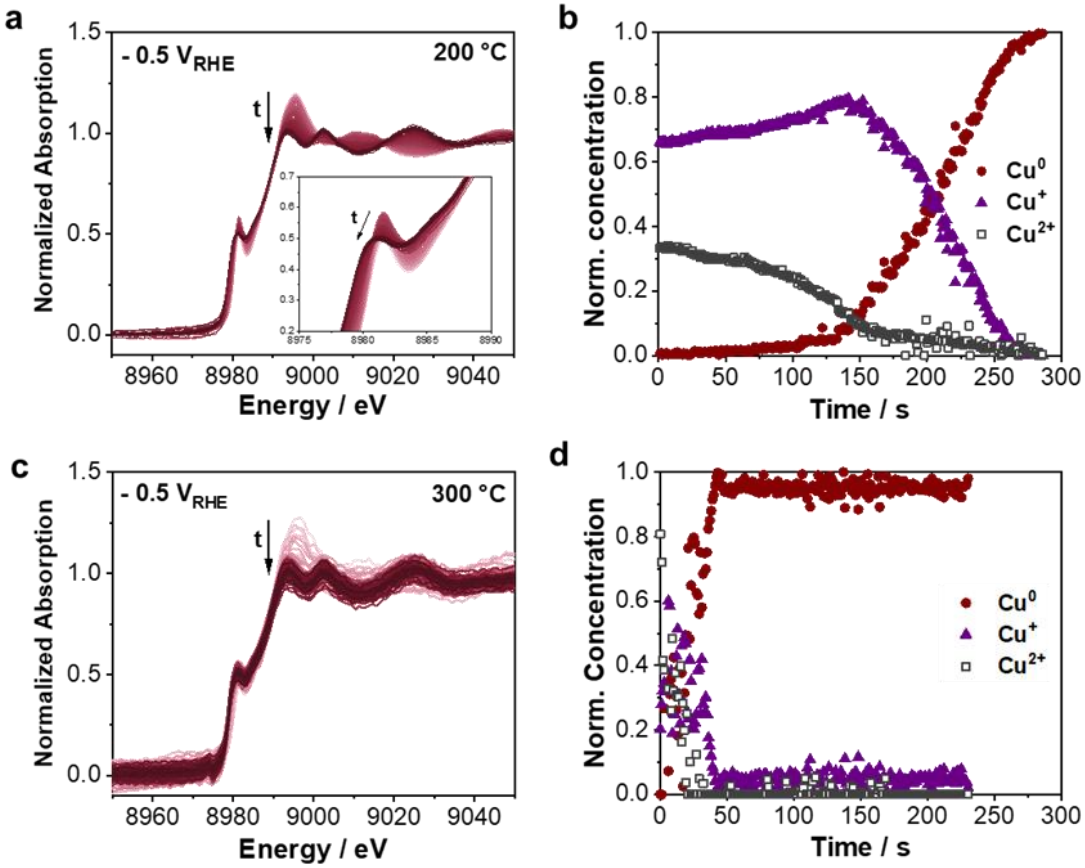

Figure 49. Time-resolved changes in Cu K-edge XANES spectra of the 200-foam (**a, b)** and 300-foam (**c, d**) by direct switching of the potential from OCP → – 0.5 V_{RHE}. One spectrum was collected every second. (**b**, **d**) Normalized concentration profiles of the Cu^{2+}, Cu^{+} and Cu^{0} species obtained by the MCR-ALS analysis. All measurements were performed in CO_2-saturated 0.5 M $KHCO_3$. Note, the noise in the XAS spectra is caused by the strong bubble formation especially at – 0.5 V_{RHE}, making it difficult to normalize the data in a proper way. Reprinted from Blaseio et al.[252]

The transition behavior of the 100-foam from OCP to – 1.3 V_{RHE} is shown in **Figure 50a,b**. From the course of the time-resolved Quick-XANES spectra (**Figure 50a**), a decrease in the white line intensity, but only minimal changes in the pre-edge are observed within the holding time of 125 s at – 1.3 V_{RHE}. Again, for the 100-foam this trend can be explained by the high initial Cu^{0} content (~20 % at – 1.3 V_{RHE} within the first seconds). Evidently, the time-dependent changes in the spectra are less pronounced compared to the entirely oxidized foams, e.g. 300- and 450-foams. From the MCR-ALS analysis (**Figure 50b**), for the 100-foam the reduction to metallic Cu is not fully completed within 125 s at – 1.3 V_{RHE} (~10% Cu^{+} remain), while half the Cu_xO is already transformed to the metallic state after ~ 50 s. Interestingly, if a potential of

– 1.3 V_{RHE} (starting from OCP) was applied instead of – 0.5 V_{RHE} (**Figure 50 c, d**), the oxide-metal transition process for the 300-foam is not getting faster. At – 1.3 V_{RHE} the reduction to metallic Cu species also took place within ~ 40 s, while the Cu^{2+} concentration dropped to 0 % during this time. Similarly, the time at which half of the Cu^{z+} content is reduced to Cu^0 was the same (around 25 s). Note, that compared to the potential jump to – 0.5 V_{RHE} no Cu^+ species are observed for the 300-foam. In **Figure 50c**, the time-dependent XANES spectra clearly support the oxide-metal reduction by the shift and decrease in white line intensity for the 300-foam. Furthermore, the characteristic increase in pre-edge and shift in transition energy from ~8985 eV (mainly Cu^{2+}) to ~8980 eV (Cu^0) corroborate the findings from the MCR-ALS.

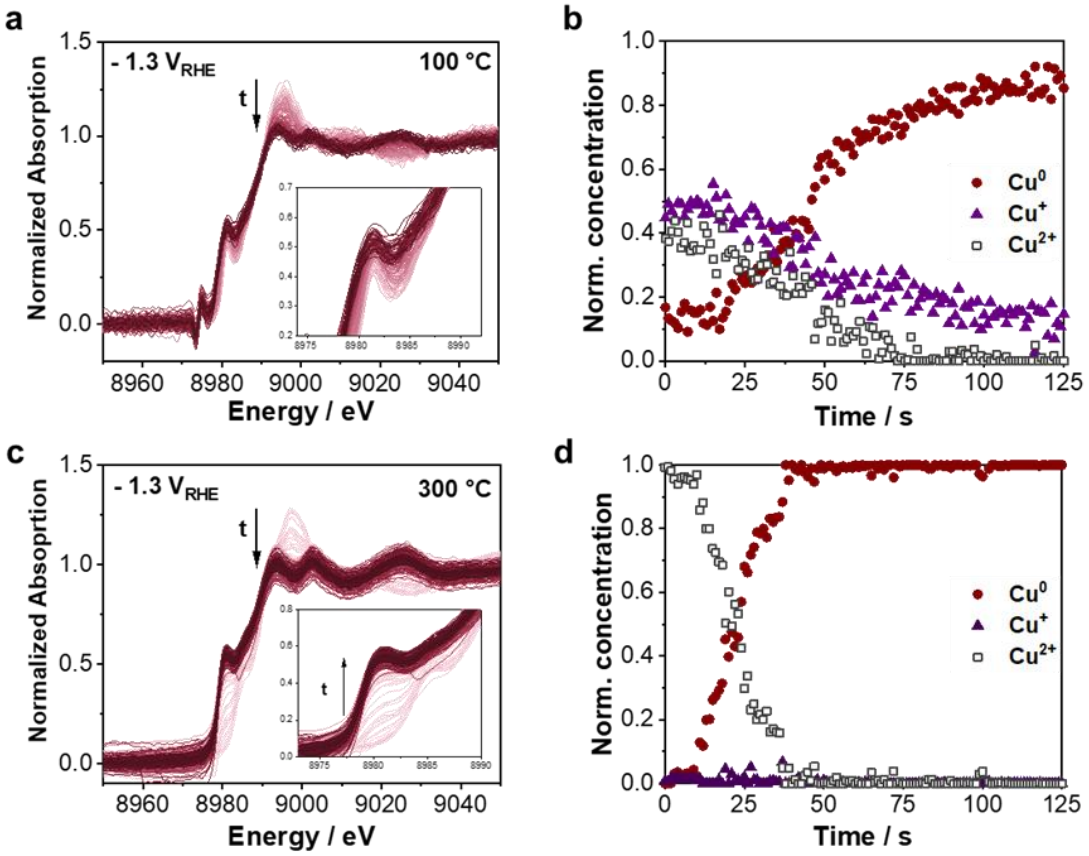

Figure 50. Series of time-resolved Cu K-edge Quick-XANES spectra of 100-foam (**a, b)** and 300-foam (**c, d**) by direct jumping of the potential from OCP → – 1.3 V_{RHE}. One spectrum was collected every second. (**b**, **d**) Normalized concentration profiles of the Cu^{2+}, Cu^+ and Cu^0 species obtained by the MCR-ALS analysis. All measurements were performed in CO_2-saturated 0.5M $KHCO_3$. Note, the noise in the XAS spectra is caused by the strong bubble formation especially at – 1.3 V_{RHE}. This makes it difficult to normalize the data in a proper way. Reprinted from Blaseio et al.[252]

As the potential jump experiments revealed a 6-times slower oxide-metal reduction of the Cu^+ rich 200-foam compared to the Cu^{2+} rich 300-foam at the same potential (– 0.5 V_{RHE}), we can conclude that the abundance of Cu^{2+} species strongly influences the oxide-metal transition kinetics. More precisely, from ex-situ XANES and XPS analyses for the 100- and 200-foams

lower amounts of the Cu^{2+} species (~20 – 40 %) are incorporated in the amorphous oxide mainly located at the surface, while the XRD data does not indicate the formation of crystalline CuO phases. Based on the XRD data, only crystalline Cu_2O phases present throughout these foams, while the 300-foam consists of ~76 wt.% crystalline CuO.

4.3.6. Discussion

Figure 51 and **Figure 52** summarize the principal findings of this study, showing schematically the different reduction rates and lifetimes of Cu^{2+}, Cu^{+} and Cu^{0} species in dependence of the applied potential for the Cu_xO foams annealed at 100 °C, 200 °C, 300 °C and 450 °C for 12 h in air. Especially in this work, the differences observed between small potential increments *vs.* (large) potential steps/jumps are highlighted as well as the shift of the *oxide-metal transition potential* with the annealing temperature and thus the initial ratios of Cu^{0}:Cu^{+}:Cu^{2+} species and structure of these Cu_xO foams.

First, our results demonstrated that the annealing temperature has a strong influence on the Cu^{0}:Cu^{+}:Cu^{2+} ratio within the bulk and surface of the Cu_xO foams as well as the crystal structure of the CuO species. Generally, the content of Cu^{2+} species and their degree of crystallinity increase with higher annealing temperature, while crystalline Cu_2O is present throughout all annealed Cu_xO foams. The results from the ex-situ XRD and Raman data show a high crystallinity of the CuO phase after annealing at and above 300 °C, while at lower temperatures the CuO detected by the XANES and XPS techniques are strongly amorphous (absence of peaks in the XRD profile). Secondly, the annealing at lower temperatures leads to strong differences in the surface and bulk composition of the treated foams. Consequently, more amorphous CuO species on the foam surface are present at lower annealing temperatures. As an excellent example, the 200-foam contains ~80 wt.% of amorphous CuO surface species (via XPS), while the bulk-like XANES data only shows 20 % CuO. These differences in the oxidation state, crystallinity and bulk *vs.* surface Cu oxide as well as the applied electrochemical protocol have a strong influence on the oxide to metal reduction processes during the CO_2RR, which will be discussed now.

The potential increment conditions (ΔE = 100 mV, from + 0.4 V_{RHE} to – 1.2 V_{RHE} for 6 – 10 min at each potential) give insights into the stepwise oxide-metal transition processes of the Cu_xO foams (**Figure 51**). From these experiments, we demonstrated that the higher the annealing temperature of the precursor foam and thus the higher the concentration of crystalline CuO species, the lower the oxide-metal transition potential. Thus, the 100-foam shows the highest cathodic *oxide-metal transition potential*, whereas the lowest overpotential is required for the 450-foam. The difference of the transition potential between the 100- and 450-foams is therefore around – 600 mV. Consequently, highly crystalline CuO phases can be electrochemically reduced at much lower potentials compared to amorphous CuO.

Considering that the oxide-metal transition affects the CO_2RR product distribution and Faradaic efficiencies, it is important to understand the kinetics of this process for the design of efficient electrocatalysts. In all experiments, a chronoamperometry method is applied showing an exponential current decay over time at constant potential due to the transition from the Faradaic current to mass-transport limiting current. According to the thermodynamically predicted Pourbaix diagram, the reduction pathway of Cu^{2+} species to metallic always involves the formation of Cu^{+} intermediate species under these CO_2RR conditions (pH = 7.2, 25 °C).[187] In the first obvious assumption, the electrochemical oxide-metal transition dynamics might comprise two rate constants. One for the reduction rate from Cu^{2+} to Cu^{+} (k_1) and one from Cu^{+} to Cu^{0} (k_2). Depending on which one of the potential-controlled rate constants is the rds, i.e. the slowest step allows to detect Cu^{+} formation, or it might be too fast to be observed with the technique used in this study (resolution of 1 s for each XANES spectrum). If k_1 is rate determining, the Cu^{+} intermediate is rapidly reacting to Cu^{0} species, which cannot be probed within the one second of data acquisition. On the other hand, if k_2 is the slowest step, a fast buildup of Cu^{+} occurs followed by a slow reduction step to metallic. In this work, we can only evaluate the relative relation between k_1 and k_2 to each other.

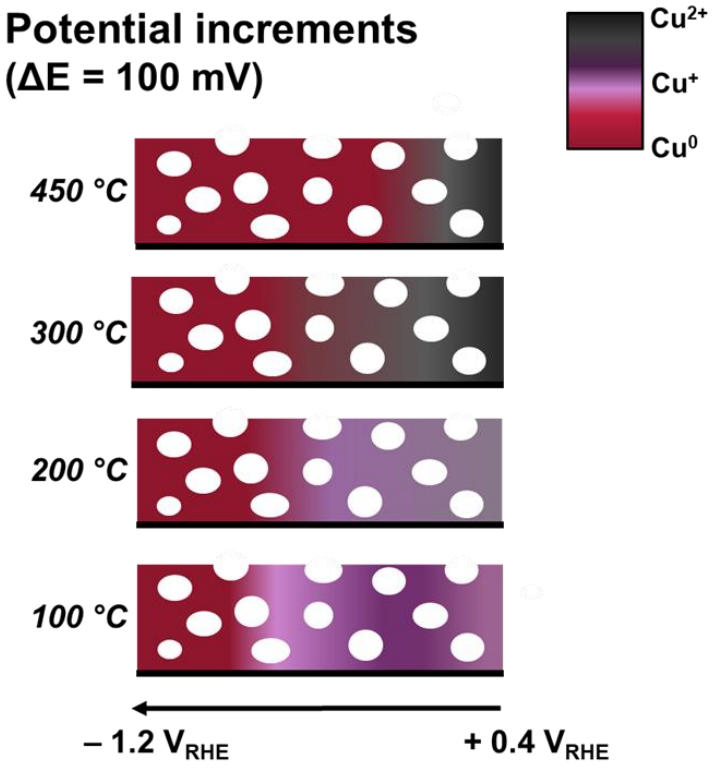

Figure 51. Schematic model showing the potential-dependent oxide-metal transition processes of the four differently annealed Cu_xO foams during the potential increment (ΔE = 100 mV) experiments. The transition of Cu^{2+} to Cu^{0} with intermediate Cu^{+} formation is illustrated. From the ex-situ XANES analysis, the initial Cu^{0}:Cu^{+}:Cu^{2+} ratios of the in air annealed Cu_xO foams are 50:39:11 (100 °C), 0:79:21 (200 °C), 0:24:76 % (300 °C) and 0:0:100 (450 °C), respectively. The pore structure of the foams is depicted by the white spheres. Reprinted from Blaseio et al.[252]

With the potential step (OCP → – 0.2 V_{RHE} → – 0.5 V_{RHE} → – 1.3 V_{RHE}) and potential jump (OCP → – 0.5 V_{RHE} or – 1.3 V_{RHE}) experiments, we gained an understanding of the kinetics during this transition process and the respective lifetime of each Cu^{z+} species without applying intermediate potentials. We could demonstrate, that for the 200-foam first a one-electron-transfer from Cu^{2+} to Cu^{+} sets in, while applying intermediate potentials at – 0.2 V_{RHE} and – 0.5 V_{RHE}. Once the *oxide-metal transition potential* was reached, the further reduction to metallic Cu occurred almost instantly. Again, we found that with increasing annealing temperature, i.e. for the 450-foam compared to the 200-foam, the reduction potential to Cu^0 is shifted to less negative values. We suggest that these observed differences in the kinetics are controlled by the abundance of crystalline CuO species.

With the potential jump conditions (from OCP to – 0.5 V_{RHE} or – 1.3 V_{RHE}), we were able to show the initial Cu^{+} formation/reduction only for the 200- and 100-foams (**Figure 52**). However, for the 300-foam the reduction rate to Cu^{+} species is fast, but can only be detected at the start of the measurement at – 0.5 V_{RHE}. For this annealing temperature, the reduction of Cu^{2+} and Cu^{+} species to metallic Cu was already completed within ~ 40 s, which is 6-times faster compared to the 200-foam using the same protocol (from OCP to – 0.5 V_{RHE}). At – 1.3 V_{RHE} the Cu^{+} formation is too fast to be detected within 1 s of the XAS acquisition. Our observation can be explained by the different reduction rates and lifetimes of Cu^{2+}, Cu^{+} and Cu^0 species during the electrochemical reduction processes. Based on the complimentary ex-situ techniques, the 300-foam mainly consists of the crystalline CuO, while for the 200-foam the Cu^{2+} species are incorporated in the amorphous oxide and mainly located at the surface.

Comparing the potential step (ΔE > 100 mV) and jump experiments (ΔE > 500 mV) for the 200-foam, different oxide to metal reduction behaviors were found (**Figure 52**). For the 200-foam, jumping directly from OCP to – 0.5 V_{RHE} (**Figure 49a**) without any intermediate potential steps shows an initial Cu^{2+} to Cu^{+} transition. Therefore, the rds is the Cu^{+} to Cu^0 reduction, implying a small k_2. Additionally, the metallic Cu formation only sets in after ~130 s, resulting in a buildup of Cu^{+} species by holding the potential at – 0.5 V_{RHE}. For the 200-foam, the complete reduction to metallic Cu is reached after ~285 s in this experiment. Contrarily, during the potential step conditions, where – 0.2 V_{RHE} was applied before – 0.5 V_{RHE}, only around 20 % Cu^0 were formed at – 0.5 V_{RHE} after the same time. Thus, without intermediate potential steps a faster reduction to metallic copper at – 0.5 V_{RHE} occurs, pointing out the strong impact of the previously applied potential to the reduction behavior of Cu^{+}.

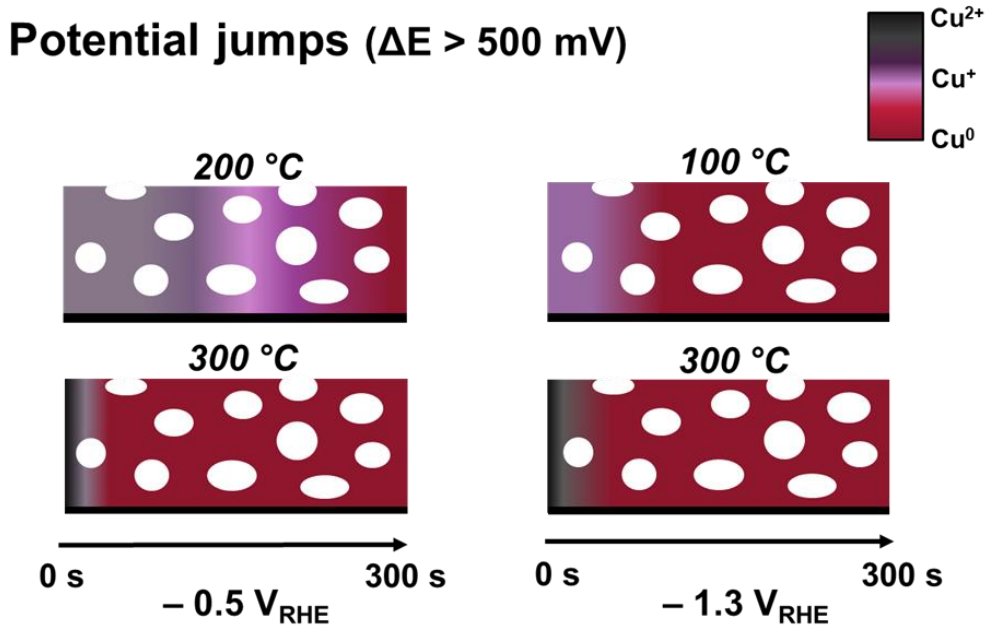

Figure 52. Schematic model showing the time-dependent oxide-metal transition processes of the 100 °C, 200 °C and 300 °C in air annealed Cu_xO foams during the potential jump (ΔE > 500 mV) experiments. The fast transition of Cu^{2+} to Cu^0 vs. slower intermediate Cu^+ formation is illustrated for the two different chronoamperometric experiments used in this study. From the ex-situ XANES analysis, the initial Cu^0:Cu^+:Cu^{2+} ratios of the in air annealed Cu_xO foams are 50:39:11 (100 °C), 0:79:21 (200 °C), 0:24:76 (300 °C) and 0:0:100 (450 °C), respectively. The pore structure of the foams is depicted by the white spheres. Reprinted from Blaseio et al.[252]

Furthermore, for the 300-foam the reduction process becomes much faster if no intermediate potential steps were conducted beforehand. More precisely, the jump from OCP directly to the oxide-metal transition potential of ~ – 0.5 V_{RHE} leads to an instant reduction within 40 s. This is contrary to the observation, where increment potential steps were applied. Here, the reduction to metallic Cu is only complete at – 0.6 V_{RHE}. We note that there is a discrepancy between our previously published XAS analysis of the 300-foam, where a clear intermediate formation of Cu^+ species occurs during the potential step experiments before the reduction to metallic Cu commences.[180] However, initially at + 0.4 V_{RHE} our analysis clearly indicates that this Cu_xO foam is fully oxidized to Cu^{2+} species, while previously around 20 % remain as Cu^+ species even at anodic potentials applied.[180] We explain this observation by the initial structure and chemical species of Cu_xO during the annealing process and in contact with the electrolyte solution. Based on the potential step (ΔE > 100 mV) and jump experiments (ΔE > 500 mV), we suggest that the sluggish reduction kinetics for the 100- and 200-foams are correlated with the surface concentration of amorphous CuO as well as the high abundance of Cu^+ species, which is favorable for the formation of C2 products during CO_2RR. Only the crystalline CuO phase

found for the 300- and 450-foams undergoes very fast reduction kinetics at lower cathodic potentials applied.

Altogether, we reveal a clear dependence of the Cu^0:Cu^+:Cu^{2+} ratio, crystal structure and electrochemical protocol applied on the oxide-metal reduction kinetics for the differently annealed Cu_xO foams. A high concentration of Cu^{2+} species as well-ordered CuO phase is able to influence the rds of the oxide-metal transition, resulting in a shift to lower cathodic potentials and therefore a lower energy barrier to reduction. Comparing the different chronoamperometric protocols, we show that during the smaller potential step and increment experiments, a slowdown of the reduction of the Cu^{2+}/Cu^+ to Cu^0 occurs. Thus, jumping directly to a highly cathodic potential enhances the reduction kinetics of Cu_xO to metallic.

Our operando Quick-XAS study provides deeper insights into the oxide-metal transition dynamics of Cu_xO-derived electrocatalysts and uncovers the impact of the electrochemical protocol on the reduction of the Cu oxide to metallic species as well as the presence of amorphous/crystalline CuO phases during CO_2 electrolysis.

5. Conclusions

Mechanistic Insights into the HER-OER Bifunctionality of Cell-Reversal Tolerant Pt-Ir NPs using operando Quick-XANES (Chapter 4.1)

In this chapter, we investigated the bifunctionality and dynamics of cell reversal tolerant Pt-Ir NPs prepared by two different synthesis routes (colloidal and wet-impregnation). Ex-situ characterization showed that nanoparticles prepared by the colloidal route have a small particle diameter of around 2 nm, are oxidized and mostly amorphous, e.g. as IrO_x. In contrast, nanoparticles synthesized by the wet-impregnation method are around 3 – 4 nm in diameter, more crystalline and around 20 – 30 % of iridium is in the metallic state. The oxidation state of platinum of the as-synthesized Pt-Ir NPs is independent of the synthesis route and around 40 % is oxidized to Pt^{2+} oxide while 60 % are metallic Pt. RDE measurements of the bimetallic catalysts showed that the PtIr NPs prepared by both synthesis routes are active for both the HOR and OER reactions, confirming the bifunctionality of the PtIr NPs.

To investigate the catalytically active species as well as understand dynamic oxidation-reduction processes of the bimetallic Pt-Ir NPs during HER and OER, potential jump experiments between – 0.02 V_{RHE} (HER) and + 1.55 V_{RHE} (OER) with holding times of 3 and 10 s were conducted. Our results demonstrate that during HER fast reduction kinetics to metallic Pt are observed for all samples, independent of the composition and holding time of the potential jumps. During OER different behaviors for the two holding times are found. During the 3 s potential jump experiments a higher amount of iridium results in more rapid oxidation kinetics from Pt^0 to Pt^{2+} species, while a higher Pt content slows down the metal to oxide processes at + 1.55 V_{RHE}. The total amount of Pt^{2+} species formed (~50 – 60 %) during 3 s at OER is independent of the synthesis route, particle size and/or alloying of the platinum with iridium. With increasing platinum content and holding time at + 1.55 V_{RHE} more Pt^{2+} species are observed during OER. Once the holding time is sufficient and overcomes kinetic barriers, thermodynamically stable PtO_2 forms.

For the more amorphous and smaller PtIr and Pt_3Ir NPs prepared by the colloidal route, the reduction of Ir^{4+} to Ir^{3+} species during HER is slower compared to the respective oxidation at + 1.55 V_{RHE}. This leads to a higher Ir^{3+} species concentration during the 10 s potential jump experiments compared to the 3 s potential jumps. Accordingly, the Ir^{4+} species formation during OER is similar for both holding times. The more crystalline Pt-Ir NPs prepared by the WI route show significant kinetic barriers for the oxidation and reduction processes of the iridium species (Ir^0, Ir^{3+} and Ir^{4+}). Furthermore, the chemically active state of iridium promoting OER in the

bimetallic Pt-Ir NPs is involving purely Ir^{3+} and Ir^{4+} species thereby indicating electronic interaction of platinum with iridium, preventing the formation of Ir^{5+} species during OER as well as suggesting a change in the OER mechanism that does not involve Ir^{5+} species. For all iridium-containing NPs, no metallic iridium is formed during the potential jump experiments between HER and OER. This indicates that once formed Ir^{3+}, Ir^{4+} and Ir^{5+} species are not readily reduced at – 0.02 V_{RHE} independent of the synthesis route, holding time and iridium content.

Based on the *operando* Quick-XANES study, our results provide new insights into the dynamic behavior and electronic interactions of bifunctional Pt-Ir NPs during HOR and OER within a few seconds enabling the design of new cell reversal tolerant catalyst materials with low loading of the very costly and scarce iridium.

Bimetallic Pt-Ir Oxide Surfaces under Oxygen Reduction/Evolution Reactions (ORR/OER) using in-situ Raman spectroscopy and DFT (Chapter 4.2)

In the second case study, we investigated the potential-dependent oxidation of sputtered bifunctional Pt-Ir thin films as a model catalyst system for ORR and OER using in-situ Raman spectroscopy and DFT. First, all as-prepared thin films exhibit a rough and significantly oxidized surface with mostly disordered amorphous Pt and Ir oxides, while all iridium containing films also show the presence of rutile IrO_2 structure. The evaluation of the electrochemical activity data highlights the ORR/OER bifunctionality of these bimetallic Pt-Ir thin films.

In-situ Raman spectroscopy is a powerful technique to identify the reaction intermediates on metal-based surfaces. At potentials below 0.8 V_{RHE}, the surface of the bimetallic Pt-Ir thin films contains highly stable Ir^{3+}-OH, which prevents the adsorption of oxygen-containing species onto the active Pt sites. At 1.0 V_{RHE} the first oxidation wave commences with the formation of an amorphous Pt-Ir oxide, evident by a broad Raman band at ~554 cm^{-1}. This is shifted by 200 mV compared to the monometallic Ir film, indicating electronic interactions between platinum and iridium to improve the ORR kinetics. For the PtIr(1:1) thin film, the second oxidation wave commences from 1.4 V_{RHE} to higher potentials relevant for the OER, showing strong changes in the bimetallic oxide structure compared to monometallic Pt and Ir. DFT was used to calculate the Raman spectra for two hydrated platinum-iridium oxo-hydroxy tetramer complexes, where the Pt and Ir atoms are connected to each other by μ-oxo type linkage. Based on the predicted Raman spectra, we could show that the experimental peaks observed correspond to Pt-O-Ir stretching and bending vibrations. One of these stretching frequencies is observed at 657 cm^{-1}, which is red shifted by ~38 cm^{-1} from the same vibration for

monometallic Ir-O-Ir. This shift in the Raman frequency is most likely based on a weakening of the Ir-O-Pt bond by 13 % compared to the monometallic Ir-O-Ir bond, resulting in a lower OER activity of the bimetallic Pt-Ir thin films. For the PtIr(3:1), the second oxidation wave is even further delayed to 1.5 V_{RHE}, which is related to the higher platinum surface concentration. The theoretical calculations indicate the additional Pt-O-Pt stretching and bending vibrations during OER, indicating the presence of less active Pt surface sites.

The unique combination of in-situ Raman and DFT allows uncovering a new mechanistic understanding of the potential-resolved formation of catalytically active sites of bimetallic Pt-Ir materials for ORR and OER. This knowledge will help to boost the performance for unitized regenerative fuel cells in the near future.

Impact of Cu^+ and Cu^{2+} species on the oxide-metal transition processes of Cu_xO foams during the CO_2RR (Chapter 4.3)

*This section is reprinted in an adapted form from Blaseio et al. in J. Mater. Chem. A, 2024, **12**, 28177–28192. https://doi.org/10.1039/D4TA02217C*

In this part of the thesis, the potential and time dependent oxide-metal transition dynamics for the Cu_xO foams annealed in air at four different temperatures ranging from 100 °C to 450 °C probed by operando Quick-XAS were investigated. From the comparison of ex-situ XANES, XRD and XPS analyses, it was pointed out that a rise in annealing temperature leads to an increase in the proportion of Cu^{2+} species and their degree of crystallinity within the Cu_xO foams. More precisely, after annealing at 100 °C and 200 °C these CuO species are amorphous and mainly found at the surface of the foam. Once the annealing temperature reaches 300 °C or higher, the CuO phase is entirely crystalline.

Using potential increment (ΔE = 100 mV), step (ΔE > 100 mV), and jump ($\Delta E \geq$ 500 mV) experiments, deeper insights into the transition kinetics from $Cu^{2+} \rightarrow Cu^{+} \rightarrow Cu^{0}$ in CO_2-saturated 0.5 M $KHCO_3$ were gained. These different types of potential control experiments strongly influence the reduction behavior of Cu_xO to metallic under cathodic conditions. In other words, using smaller increments slows down the reduction kinetics. Additionally, from the potential increment experiments, an increase in initial crystalline CuO species leads to a shift in the oxide-metal transition towards less negative potentials, signifying a lower energy barrier to reduction.

A change in rds during the reduction pathway with the stability of Cu_2O intermediates was identified. For the crystalline CuO rich foams (300 °C and 450 °C), a large rate constant k_2 at highly cathodic potentials results in a very fast transition from Cu^+ to Cu^0. For all in air annealed

Cu_xO foams, we showed that the catalytically active species in the potential range of hydrocarbon formation[168], at – 0.8 V_{RHE} and more negative potentials, is entirely metallic Cu. Overall, the operando Quick-XAS study reveals a clear dependence of the Cu^0:Cu^+:Cu^{2+} ratio and structure of the CuO species as well as a strong influence of the applied potential protocol on the oxide-metal reduction kinetics for the differently annealed Cu_xO foams.

Based on the case studies in this thesis, new fundamental insights into the oxide-metal transition processes and structure/composition – reactivity relationship of the three different electrocatalysts were obtained using in-situ/*operando* Raman and XAS techniques. Furthermore, these case studies highlight the need to investigate electrocatalysts under operating conditions, to obtain a detailed understanding of catalytic processes as well as structural changes of the active catalyst material. Our findings aid to the development of new active electrocatalyst materials for a cell reversal tolerant anode as well as CO_2RR electrolysis.

6. Outlook

The results obtained from the operando XAS and Raman studies presented in this thesis have advanced our understanding of dynamic oxidation–reduction behavior and electronic interplay of bifunctional Pt-Ir and Cu_xO foam electrocatalysts under reaction-relevant conditions. Several opportunities arise from these findings that can guide both short- and long-term efforts towards more durable, bifunctional fuel cell anode catalysts with low Ir content as well as efficient and selective CO_2RR catalysts.

Cell reversal tolerant bifunctional Pt-Ir Catalysts

The operando Quick-XANES potential-jump experiments reveal a strong potential-dependence on Pt and Ir oxidation states and different kinetic regimes for bimetallic nanoparticles prepared by the colloidal and wet-impregnation syntheses. Guided by the observation that a decrease in Ir concentration within the bimetallic NPs prepared by the colloidal route is not influencing the HOR-OER bifunctionality, the minimum amount of iridium within the particles should be explored further to reduce the cost and usage of the scarce iridium. Differences in iridium oxidation kinetics between amorphous small NPs and larger crystalline particles point to a role for structural disorder and particle size effects. Systematic synthetic control to tune crystallinity and surface Pt and Ir species could be used to achieve optimal tradeoffs between catalytic activity, metal-oxide transition kinetics and durability. To enhance the cell reversal tolerance and thus the long-term durability, the Pt-Ir catalysts can also be investigated with a carbon-free support material such as TiO_2[266,267] and other titanium-based oxides[36,39], Sb-doped SnO_2[268] or Nb-doped ceria[38] to mitigate carbon corrosion.

Future work on the oxidation-reduction kinetics of Pt and Ir species using Quick-XANES could extend the time window under normal operating conditions with short OER pulses, to be closer to more realistic H_2 starvation scenarios. Coupling accelerated stress test protocols with *operando* techniques can reveal additional degradation pathways such as Pt and Ir dissolution, carbon corrosion or nanoparticle agglomeration. Especially, *operando* X-ray techniques such as small angle X-ray scattering (SAXS) or XRD (for the large wet-impregnation NPs) or pair distribution function (PDF, for the small amorphous colloidal NPs) under the potential jump experiments could be conducted to monitor changes in particle size (SAXS), crystallinity and phase composition (XRD) or neighboring atomic structure (PDF). PDF could be particularly useful for investigating the atomic structure, since EXAFS analysis of the Pt and Ir L3 edge XAS data is not possible due to the overlapping edge energies. Further, the amorphous structure

and small particle size of the colloidal NPs lead to broad XRD patterns making PDF a useful technique.

In addition, the bimetallic Pt-Ir NPs should be evaluated in membrane-electrode assemblies for PEMFCs under cell reversal cycles to validate the *operando* XANES insights from the HER-OER potential jump experiments. Especially, the reductive H_2-atmosphere at the anode in a PEMFC with several starvation cycles and under prolonged holding times can lead to oxide-metal transitions of both Pt and Ir species.[51,53] Therefore, also the long-term monitoring of these catalysts under normal operating conditions should be considered.

Pt-Ir thin films under OER and ORR

The ORR and OER mechanisms on Pt-Ir thin films could be further systematically investigated using Raman spectroscopy by employing isotope labelling (e.g. $^{18}O_2$ or D_2O). With that, more insights into the formation of the bimetallic oxide and role of this oxide under the OER as well as the absence of ORR intermediates can be gained.

With the use case of Pt-Ir catalyst as the oxygen electrode of a URFC, the reversibility of the bimetallic oxide formation is a crucial factor. Thus, several consecutive ORR and OER cycles should be investigated using Raman spectroscopy to understand repeated oxide formation and reduction cycles.

Furthermore, the bimetallic sputtered films should be tested as the oxygen electrode in a full URFC set-up. Cell performance under changing ORR (fuel cell) and OER (water electrolyzer) conditions and collecting respective charging and discharging polarization curves could be done to gain insights into the stability of the bifunctional catalyst under realistic operating conditions, such as elevated temperatures. Ultimately, combining an URFC set-up with in-situ/*operando* Raman spectroscopy can provide novel insights into catalyst oxidation behavior and monitoring of ORR and OER intermediates under more relevant operating conditions.

Cu_xO foams under CO_2RR

In the third part of the thesis the influence of the copper oxide species on the reduction kinetics under CO_2RR was investigated. We could show that high initial amounts of crystalline CuO drastically enhance the reduction kinetics to metallic Cu. Thus, tuning the Cu^{2+}:Cu^{+}:Cu^{0} ratio by the annealing temperature in air can be combined with real-time product analysis (GC/MS or HPLC) to directly link foam reduction to product formation and selectivity. Furthermore, the copper oxide reduction could be monitored by *operando* XRD to investigate the reduction kinetics of the crystalline phases of the Cu_xO foams. *Operando* Raman spectroscopy could be employed for understanding the reduction of the surface copper oxide species. Generally, a

better understanding of the reduction processes of the oxides that occur simultaneously to the formation of selective C_2 products needs to be achieved. Only this will improve systematically the discovery of novel, more efficient CO_2RR catalyst materials.
Combining experiments under continuous CO_2 flow such as in GDE experiments can assess practical hydrocarbon and alcohol production rates under more technically relevant conditions. Coupling this with *operando* X-ray based techniques such as XRD, PDF or XAS could give novel insights into the Cu_xO foam reduction.

In general, CO_2 electrolysis needs to also be enhanced on a more technical level. Further research on the device level to achieve high selectivity of valuable hydrocarbons or alcohols as products in combination with more efficient and selective catalyst materials needs to be developed to become a more industrially relevant process.

Altogether, the discussed directions could build directly on the mechanistic insights reported in this thesis and offer a path from fundamental understanding towards more practical, cost-effective and durable electrocatalysts for cell reversible tolerant PEMFC anodes, URFCs and CO_2RR.

7. References

1 T. Haas, R. Krause, R. Weber, M. Demler and G. Schmid, Technical photosynthesis involving CO2 electrolysis and fermentation, *Nat Catal*, 2018, **1**, 32–39.

2 Umweltbundesamt, Indicator: Greenhouse gas emissions, https://www.umweltbundesamt.de/en/data/environmental-indicators/indicator-greenhouse-gas-emissions#at-a-glance, (accessed 17 February 2025).

3 Hannah Ritchie, Pablo Rosado and Max Roser, Breakdown of carbon dioxide, methane and nitrous oxide emissions by sector, *Our World in Data*, 2020.

4 Federal Ministry for Economic Affairs and Climate, The National Hydrogen Strategy, https://www.bmwk.de/Redaktion/EN/Publikationen/Energie/the-national-hydrogen-strategy.html, (accessed 17 February 2025).

5 Bundesministerium für Wirtschaft und Klimaschutz, Die Nationale Wasserstoffstrategie, https://www.bmwk.de/Redaktion/DE/Wasserstoff/Dossiers/wasserstoffstrategie.html, (accessed 17 February 2025).

6 A. Brüggemann, *Hochlauf der grünen Wasserstoffwirtschaft – wo steht Deutschland?* 475, 2024, (accessed 17 February 2024).

7 S. Wang, A. Z. Weber and X. Peng, Advances and prospects to achieve high-performing and durable proton-exchange-membrane unitized regenerative fuel cells, *Current Opinion in Electrochemistry*, 2023, **40**, 101340.

8 Bundesregierung, Climate-friendly transport, https://www.bundesregierung.de/breg-en/issues/climate-action/climate-friendly-transport-1795842, (accessed 17 February 2025).

9 Umweltbundesamt, Wasserstoff im Verkehr: Häufig gestellte Fragen (FAQs), https://www.umweltbundesamt.de/themen/verkehr/kraftstoffe-antriebe/wasserstoff-im-verkehr-haeufig-gestellte-fragen#einleitung, (accessed 17 February 2025).

10 Statista, Pkw-Neuzulassungen mit Benzinmotor in Deutschland 2024 | Statista, https://de.statista.com/statistik/daten/studie/818600/umfrage/pkw-mit-benzinmotor-neuzulassungen-in-deutschland/, (accessed 17 February 2025).

11 Statista, Zulassungszahlen von Elektroautos 2025 | Statista, https://de.statista.com/statistik/daten/studie/244000/umfrage/neuzulassungen-von-elektroautos-in-deutschland/, (accessed 17 February 2025).

12 M. A. Aminudin, S. K. Kamarudin, B. H. Lim, E. H. Majilan, M. S. Masdar and N. Shaari, An overview: Current progress on hydrogen fuel cell vehicles, *International Journal of Hydrogen Energy*, 2023, **48**, 4371–4388.

13 H2 MOBILITY Deutschland GmbH & Co. KG, H2.LIVE: Hydrogen Stations in Germany & Europe, https://h2.live/en/, (accessed 18 February 2025).

14 E. Wallnöfer-Ogris, F. Poimer, R. Köll, M.-G. Macherhammer and A. Trattner, Main degradation mechanisms of polymer electrolyte membrane fuel cell stacks – Mechanisms, influencing factors, consequences, and mitigation strategies, *International Journal of Hydrogen Energy*, 2024, **50**, 1159–1182.

15 United Nations, The Paris Agreement | United Nations, https://www.un.org/en/climatechange/paris-agreement, (accessed 17 February 2025).

16 S. Nitopi, E. Bertheussen, S. B. Scott, X. Liu, A. K. Engstfeld, S. Horch, B. Seger, I. E. L. Stephens, K. Chan, C. Hahn, J. K. Nørskov, T. F. Jaramillo and I. Chorkendorff, Progress and Perspectives of Electrochemical CO2 Reduction on Copper in Aqueous Electrolyte, *Chemical Reviews*, 2019, **119**, 7610–7672.

17 Umweltbundesamt, *Carbon Capture and Storage in the global climate debate,* https://www.umweltbundesamt.de/sites/default/files/medien/11850/publikationen/ccs_in_the_global_climate_debate_policy_brief.pdf, (accessed 17 February 2025).
18 Y. Yang, Y. Xiong, R. Zeng, X. Lu, M. Krumov, X. Huang, W. Xu, H. Wang, F. J. DiSalvo, J. D. Brock, D. A. Muller and H. D. Abruña, Operando Methods in Electrocatalysis, *ACS Catal.*, 2021, **11**, 1136–1178.
19 Y. Wang, K. S. Chen, J. Mishler, S. C. Cho and X. C. Adroher, A review of polymer electrolyte membrane fuel cells: Technology, applications, and needs on fundamental research, *Applied Energy*, 2011, **88**, 981–1007.
20 M. Janssen, P. Weber and M. Oezaslan, Recent advances of various Pt-based catalysts for oxygen reduction reaction (ORR) in polymer electrolyte membrane fuel cells (PEMFCs), *Current Opinion in Electrochemistry*, 2023, **40**, 101337.
21 J. X. Wang, in *Encyclopedia of Applied Electrochemistry*, ed. G. Kreysa, K. Ota and R. F. Savinell, Springer New York, New York, NY, 2014, pp. 1045–1049.
22 A. Kusoglu and A. Z. Weber, New Insights into Perfluorinated Sulfonic-Acid Ionomers, *Chemical Reviews*, 2017, **117**, 987–1104.
23 W. M. Haynes, D. R. Lide and T. J. Bruno, *CRC handbook of chemistry and physics: a ready-reference book of chemical and physical data.*, CRC Press, Florida, 97th edn., 2016.
24 H. A. Gasteiger, J. E. Panels and S. G. Yan, Dependence of PEM fuel cell performance on catalyst loading, *Journal of Power Sources*, 2004, **127**, 162–171.
25 H. A. Gasteiger, S. S. Kocha, B. Sompalli and F. T. Wagner, Activity benchmarks and requirements for Pt, Pt-alloy, and non-Pt oxygen reduction catalysts for PEMFCs, *Applied Catalysis B: Environmental*, 2005, **56**, 9–35.
26 P. Mandal, B. K. Hong, J.-G. Oh and S. Litster, Understanding the voltage reversal behavior of automotive fuel cells, *Journal of Power Sources*, 2018, **397**, 397–404.
27 T. Joo, L. Hu, B. K. Hong, J.-G. Oh and S. Litster, On the origin of deactivation of reversal-tolerant fuel cell anodes under voltage reversal conditions, *Journal of Power Sources*, 2020, **472**, 228439.
28 A. Taniguchi, T. Akita, K. Yasuda and Y. Miyazaki, Analysis of electrocatalyst degradation in PEMFC caused by cell reversal during fuel starvation, *Journal of Power Sources*, 2004, **130**, 42–49.
29 R. Marić, C. Gebauer, M. Nesselberger, F. Hasché and P. Strasser, Towards a Harmonized Accelerated Stress Test Protocol for Fuel Starvation Induced Cell Reversal Events in PEM Fuel Cells: The Effect of Pulse Duration, *J. Electrochem. Soc.*, 2020, **167**, 124520.
30 J. Bak, H. Kim, S. Lee, M. Kim, E.-J. Kim, J. Roh, J. Shin, C. H. Choi and E. Cho, Boosting the Role of Ir in Mitigating Corrosion of Carbon Support by Alloying with Pt, *ACS Catal.*, 2020, **10**, 12300–12309.
31 C. Qin, J. Wang, D. Yang, B. Li and C. Zhang, Proton Exchange Membrane Fuel Cell Reversal: A Review, *Catalysts*, 2016, **6**, 197.
32 H. Tang, Z. Qi, M. Ramani and J. F. Elter, PEM fuel cell cathode carbon corrosion due to the formation of air/fuel boundary at the anode, *Journal of Power Sources*, 2006, **158**, 1306–1312.
33 Y. Yu, H. Li, H. Wang, X.-Z. Yuan, G. Wang and M. Pan, A review on performance degradation of proton exchange membrane fuel cells during startup and shutdown processes: Causes, consequences, and mitigation strategies, *Journal of Power Sources*, 2012, **205**, 10–23.
34 Chi-Woo Roh, Hee-Eun Kim, Juhyuk Choi, Jinkyu Lim and Hyunjoo Lee, Monodisperse IrOx deposited on Pt/C for reversal tolerant anode in proton exchange membrane fuel cell, *Journal of Power Sources*, 2019, **443**, 227270.

35 F. Du, J. A. Hirschfeld, X. Huang, K. Jozwiak, T. A. Dao, A. Bauer, T. J. Schmidt and A. Orfanidi, Simulative Investigation on Local Hydrogen Starvation in PEMFCs: Influence of Water Transport and Humidity Conditions, *J. Electrochem. Soc.*, 2021, **168**, 74504.

36 T. Ioroi and K. Yasuda, Highly reversal-tolerant anodes using Ti4O7-supported platinum with a very small amount of water-splitting catalyst, *Journal of Power Sources*, 2020, **450**, 227656.

37 H. Schmies, E. Hornberger, B. Anke, T. Jurzinsky, H. N. Nong, F. Dionigi, S. Kühl, J. Drnec, M. Lerch, C. Cremers and P. Strasser, Impact of Carbon Support Functionalization on the Electrochemical Stability of Pt Fuel Cell Catalysts, *Chem. Mater.*, 2018, **30**, 7287–7295.

38 G. Shi, T. Tano, D. A. Tryk, A. Iiyama, M. Uchida and K. Kakinuma, Pt nanorods supported on Nb-doped ceria: A promising anode catalyst for polymer electrolyte fuel cells, *Electrochemistry Communications*, 2024, **163**, 107733.

39 E. Hornberger, A. Bergmann, H. Schmies, S. Kühl, G. Wang, J. Drnec, D. J. S. Sandbeck, V. Ramani, S. Cherevko, K. J. J. Mayrhofer and P. Strasser, In Situ Stability Studies of Platinum Nanoparticles Supported on Ruthenium−Titanium Mixed Oxide (RTO) for Fuel Cell Cathodes, *ACS Catal.*, 2018, **8**, 9675–9683.

40 H. Schmies, A. Bergmann, J. Drnec, G. Wang, D. Teschner, S. Kühl, D. J. S. Sandbeck, S. Cherevko, M. Gocyla, M. Shviro, M. Heggen, V. Ramani, R. E. Dunin-Borkowski, K. J. J. Mayrhofer and P. Strasser, Unravelling Degradation Pathways of Oxide-Supported Pt Fuel Cell Nanocatalysts under In Situ Operating Conditions, *Advanced Energy Materials*, 2018, **8**, 1701663.

41 G. Shen, J. Liu, H. B. Wu, P. Xu, F. Liu, C. Tongsh, K. Jiao, J. Li, M. Liu, M. Cai, J. P. Lemmon, G. Soloveichik, H. Li, J. Zhu and Y. Lu, Multi-functional anodes boost the transient power and durability of proton exchange membrane fuel cells, *Nat Commun*, 2020, **11**, 1191.

42 H. Choi, H. J. Choi, S. Y. Kang, J. Kim, H. Choi, C.-Y. Ahn, H. J. Kang, I. La, O.-H. Kim, Y.-H. Cho and Y.-E. Sung, Optimization of hydrophobic additives content in microporous layer for air breathing PEMFC, *Journal of Electroanalytical Chemistry*, 2024, **952**, 117963.

43 S.-E. Jang and H. Kim, Effect of water electrolysis catalysts on carbon corrosion in polymer electrolyte membrane fuel cells, *J. Am. Chem. Soc.*, 2010, **132**, 14700–14701.

44 J.-G. Oh, W. H. Lee and H. Kim, The inhibition of electrochemical carbon corrosion in polymer electrolyte membrane fuel cells using iridium nanodendrites, *International Journal of Hydrogen Energy*, 2012, **37**, 2455–2461.

45 T. Zhang, S.-C. Li, W. Zhu, Z.-P. Zhang, J. Gu and Y.-W. Zhang, Shape-tunable Pt-Ir alloy nanocatalysts with high performance in oxygen electrode reactions, *Nanoscale*, 2017, **9**, 1154–1165.

46 J. Du, J. Quinson, D. Zhang, F. Bizzotto, A. Zana and M. Arenz, Bifunctional Pt-IrO_2 Catalysts for the Oxygen Evolution and Oxygen Reduction Reactions: Alloy Nanoparticles versus Nanocomposite Catalysts, *ACS Catal.*, 2021, **11**, 820–828.

47 H.-Y. Jung, S. Park and B. N. Popov, Electrochemical studies of an unsupported PtIr electrocatalyst as a bifunctional oxygen electrode in a unitized regenerative fuel cell, *Journal of Power Sources*, 2009, **191**, 357–361.

48 T. Ioroi, N. Kitazawa, K. Yasuda, Y. Yamamoto and H. Takenaka, Iridium Oxide/Platinum Electrocatalysts for Unitized Regenerative Polymer Electrolyte Fuel Cells, *J. Electrochem. Soc.*, 2000, **147**, 2018.

49 T. Ioroi and K. Yasuda, Platinum-Iridium Alloys as Oxygen Reduction Electrocatalysts for Polymer Electrolyte Fuel Cells, *J. Electrochem. Soc.*, 2005, **152**, A1917.

50 G. C. Da Silva, K. J. J. Mayrhofer, E. A. Ticianelli and S. Cherevko, Dissolution Stability: The Major Challenge in the Regenerative Fuel Cells Bifunctional Catalysis, *J. Electrochem. Soc.*, 2018, **165**, F1376-F1384.

51 T. Labi, F. van Schalkwyk, S. M. Andersen, P. Morgen, S. C. Ray and J. Chamier, Increasing fuel cell durability during prolonged and intermittent fuel starvation using supported IrOx, *Journal of Power Sources*, 2021, **490**, 229568.

52 H.-E. Kim, S. Shin and H. Lee, Pt-IrOx catalysts immobilized on defective carbon for efficient reversal tolerant anode in proton exchange membrane fuel cells, *Journal of Catalysis*, 2021, **395**, 404–411.

53 R. Marić, C. Gebauer, F. Eweiner and P. Strasser, A Comparative Study on the Activity and Stability of Iridium-Based Co-Catalysts for Cell Reversal Tolerant PEMFC Anodes, *J. Electrochem. Soc.*, 2023, **170**, 84505.

54 M. Fathi Tovini, A. M. Damjanović, H. A. El-Sayed, B. Strehle, J. Speder, A. Ghielmi and H. A. Gasteiger, Irreducible IrO 2 Anode Co-Catalysts for PEM Fuel Cell Voltage Reversal Mitigation and Their Stability Under Start-Up/Shut-Down Conditions, *J. Electrochem. Soc.*, 2024, **171**, 74510.

55 K. Sasaki, N. Marinkovic, H. S. Isaacs and R. R. Adzic, Synchrotron-Based In Situ Characterization of Carbon-Supported Platinum and Platinum Monolayer Electrocatalysts, *ACS Catal.*, 2016, **6**, 69–76.

56 C. A. Campos-Roldán, A. Gasmi, M. Ennaji, M. Stodel, I. Martens, J.-S. Filhol, P.-Y. Blanchard, S. Cavaliere, D. Jones, J. Drnec and R. Chattot, Metal-oxide phase transition of platinum nanocatalyst below fuel cell open-circuit voltage, *Nature communications*, 2025, **16**, 936.

57 R. Mom, L. Frevel, J.-J. Velasco-Vélez, M. Plodinec, A. Knop-Gericke and R. Schlögl, The Oxidation of Platinum under Wet Conditions Observed by Electrochemical X-ray Photoelectron Spectroscopy, *J. Am. Chem. Soc.*, 2019, **141**, 6537–6544.

58 E. L. Redmond, B. P. Setzler, F. M. Alamgir and T. F. Fuller, Elucidating the oxide growth mechanism on platinum at the cathode in PEM fuel cells, *Phys. Chem. Chem. Phys.*, 2014, **16**, 5301–5311.

59 S. Cherevko, A. R. Zeradjanin, A. A. Topalov, N. Kulyk, I. Katsounaros and K. J. J. Mayrhofer, Dissolution of Noble Metals during Oxygen Evolution in Acidic Media, *ChemCatChem*, 2014, **6**, 2219–2223.

60 T. Fuchs, J. Drnec, F. Calle-Vallejo, N. Stubb, D. J. S. Sandbeck, M. Ruge, S. Cherevko, D. A. Harrington and O. M. Magnussen, Structure dependency of the atomic-scale mechanisms of platinum electro-oxidation and dissolution, *Nat Catal*, 2020, **3**, 754–761.

61 I. Martens, R. Chattot, M. Rasola, M. V. Blanco, V. Honkimäki, D. Bizzotto, D. P. Wilkinson and J. Drnec, Probing the Dynamics of Platinum Surface Oxides in Fuel Cell Catalyst Layers Using in Situ X-ray Diffraction, *ACS Appl. Energy Mater.*, 2019, **2**, 7772–7780.

62 K. Ehelebe, J. Knöppel, M. Bierling, B. Mayerhöfer, T. Böhm, N. Kulyk, S. Thiele, K. J. J. Mayrhofer and S. Cherevko, Platinum Dissolution in Realistic Fuel Cell Catalyst Layers, *Angewandte Chemie*, 2021, **133**, 8964–8970.

63 N. Bhuvanendran, S. Ravichandran, S. S. Jayaseelan, Q. Xu, L. Khotseng and H. Su, Improved bi-functional oxygen electrocatalytic performance of Pt–Ir alloy nanoparticles embedded on MWCNT with Pt-enriched surfaces, *Energy*, 2020, **211**, 118695.

64 D. Bentele, K. Aylar, K. Olsen, E. Klemm and S. H. Eberhardt, PEMFC Anode Durability: Innovative Characterization Methods and Further Insights on OER Based Reversal Tolerance, *J. Electrochem. Soc.*, 2021, **168**, 24515.

65 X. Xu and T. Yu, Platinum–Iridium–Ruthenium Trimetallic Alloy Nanoparticles as Catalysts for Oxygen and Hydrogen Evolution, *ACS Appl. Nano Mater.*, 2025. DOI: 10.1021/acsanm.4c06609.

66 J. Ahn and R. Holze, Bifunctional electrodes for an integrated water-electrolysis and hydrogen-oxygen fuel cell with a solid polymer electrolyte, *J Appl Electrochem*, 1992, **22**, 1167–1174.

67 J. C. Fornaciari, S. Garg, X. Peng, Y. N. Regmi, A. Z. Weber and N. Danilovic, Performance and Durability of Proton Exchange Membrane Vapor-Fed Unitized Regenerative Fuel Cells, *J. Electrochem. Soc.*, 2022, **169**, 54514.

68 T. Reier, M. Oezaslan and P. Strasser, Electrocatalytic Oxygen Evolution Reaction (OER) on Ru, Ir, and Pt Catalysts: A Comparative Study of Nanoparticles and Bulk Materials, *ACS Catal.*, 2012, **2**, 1765–1772.

69 L. Blanco-Redondo, Y. Lobko, K. Veltruská, J. Nováková, M. Mazur, A. M. Darabut, T. Hrbek, M. Dopita, J. Hraníček, Y. Yakovlev, I. Matolínová and V. Matolín, Bifunctional Pt–Ir nanoparticle catalysts for oxygen reduction and evolution reactions: investigating the influence of surface composition on the catalytic properties, *Sustainable Energy Fuels*, 2024, **8**, 797–810.

70 J.-H. Kim, S.-W. Yun, K. Shim, S.-H. You, S.-M. Jung, H. Kweon, S. H. Joo, Y. H. Moon and Y.-T. Kim, Enhanced Activity and Stability of Nanoporous PtIr Electrocatalysts for Unitized Regenerative Fuel Cell, *ACS Appl. Energy Mater.*, 2020, **3**, 1423–1428.

71 M. Roca-Ayats, G. García, J. L. Galante, M. A. Peña and M. V. Martínez-Huerta, Electrocatalytic stability of Ti based-supported Pt3Ir nanoparticles for unitized regenerative fuel cells, *International Journal of Hydrogen Energy*, 2014, **39**, 5477–5484.

72 T. C. Crowtz and J. R. Dahn, Screening Bifunctional Pt Based NSTF Catalysts for Durability with the Rotating Disk Electrode: The Effect of Ir and Ru, *J. Electrochem. Soc.*, 2018, **165**, F854-F862.

73 M. Wesselmark, B. Wickman, C. Lagergren and G. Lindbergh, The impact of iridium on the stability of platinum on carbon thin-film model electrodes, *Electrochimica Acta*, 2013, **111**, 152–159.

74 M. Scohy, S. Abbou, V. Martin, B. Gilles, E. Sibert, L. Dubau and F. Maillard, Probing Surface Oxide Formation and Dissolution on/of Ir Single Crystals via X-ray Photoelectron Spectroscopy and Inductively Coupled Plasma Mass Spectrometry, *ACS Catal.*, 2019, **9**, 9859–9869.

75 M. Wakisaka, H. Suzuki, S. Mitsui, H. Uchida and M. Watanabe, Identification and quantification of oxygen species adsorbed on Pt(111) single-crystal and polycrystalline Pt electrodes by photoelectron spectroscopy, *Langmuir*, 2009, **25**, 1897–1900.

76 Y. B. He, A. Stierle, W. X. Li, A. Farkas, N. Kasper and H. Over, Oxidation of Ir(111): From O-Ir-O Trilayer to Bulk Oxide Formation, *J. Phys. Chem. C*, 2008, **112**, 11946–11953.

77 T. Wittemann, H. İ. Sözen, M. Oezaslan and T. Klüner, Ab initio calculations of the chemisorption of atomic H and O on Pt and Ir metal and on bimetallic Pt_xIr_y surfaces, *Zeitschrift für Naturforschung B*, 2024, **79**, 177–190.

78 Z. Pavlovic, C. Ranjan, Q. Gao, M. van Gastel and R. Schlögl, Probing the Structure of a Water-Oxidizing Anodic Iridium Oxide Catalyst using Raman Spectroscopy, *ACS Catal.*, 2016, **6**, 8098–8105.

79 Z. Pavlovic, C. Ranjan, M. van Gastel and R. Schlögl, The active site for the water oxidising anodic iridium oxide probed through in situ Raman spectroscopy, *Chem. Commun.*, 2017, **53**, 12414–12417.

80 F. Zhao, B. Wen, W. Niu, Z. Chen, C. Yan, A. Selloni, C. G. Tully, X. Yang and B. E. Koel, Increasing Iridium Oxide Activity for the Oxygen Evolution Reaction with Hafnium Modification, *Journal of the American Chemical Society*, 2021, **143**, 15616–15623.

81 S. P. Devarajan, J. A. Hinojosa and J. F. Weaver, STM study of high-coverage structures of atomic oxygen on Pt(111): p(2×1) and Pt oxide chain structures, *Surface Science*, 2008, **602**, 3116–3124.

82 J. M. Hawkins, J. F. Weaver and A. Asthagiri, Density functional theory study of the initial oxidation of the Pt(111) surface, *Phys. Rev. B*, 2009, **79**, 125434.

83 Y.-F. Huang, P. J. Kooyman and M. T. M. Koper, Intermediate stages of electrochemical oxidation of single-crystalline platinum revealed by in situ Raman spectroscopy, *Nat Commun*, 2016, **7**, 12440.

84 A. Kafka and F. Hess, Why alloying with noble metals does not decrease the oxidation of platinum: a DFT-based ab initio thermo-dynamics study, *Phys. Chem. Chem. Phys.*, 2024, **26**, 24631–24648.

85 J. X. Wang, T. E. Springer and R. R. Adzic, Dual-Pathway Kinetic Equation for the Hydrogen Oxidation Reaction on Pt Electrodes, *J. Electrochem. Soc.*, 2006, **153**, A1732.
86 J. Heyrovský, A theory of overpotential, *Recl. Trav. Chim. Pays-Bas*, 1927, **46**, 582–585.
87 J. Tafel, Über die Polarisation bei kathodischer Wasserstoffentwicklung, *Zeitschrift für Physikalische Chemie*, 1905, **50U**, 641–712.
88 T. Erdey-Grúz and M. Volmer, Zur Theorie der Wasserstoff Überspannung, *Zeitschrift für Physikalische Chemie*, 1930, **150A**, 203–213.
89 J. X. Wang, T. E. Springer, P. Liu, M. Shao and R. R. Adzic, Hydrogen Oxidation Reaction on Pt in Acidic Media: Adsorption Isotherm and Activation Free Energies, *J. Phys. Chem. C*, 2007, **111**, 12425–12433.
90 V. Komanicky and V. Latyshev, in *Handbook of Energy Materials*, Springer, Singapore, 2022, pp. 1–32.
91 K. Kunimatsu, H. Uchida, M. Osawa and M. Watanabe, In situ infrared spectroscopic and electrochemical study of hydrogen electro-oxidation on Pt electrode in sulfuric acid, *Journal of Electroanalytical Chemistry*, 2006, **587**, 299–307.
92 R. J. Nichols and A. Bewick, Spectroscopic identification of the adsorbed intermediate in hydrogen evolution on platinum, *Journal of Electroanalytical Chemistry and Interfacial Electrochemistry*, 1988, **243**, 445–453.
93 E. Protopopoff and P. Marcus, Poisoning of the Cathodic Hydrogen Evolution Reaction by Sulfur Chemisorbed on Platinum (110), *J. Electrochem. Soc.*, 1988, **135**, 3073–3075.
94 N. M. Marković, T. J. Schmidt, V. Stamenković and P. N. Ross, Oxygen Reduction Reaction on Pt and Pt Bimetallic Surfaces: A Selective Review, *Fuel Cells*, 2001, **1**, 105–116.
95 H. S. Wroblowa, Yen-Chi-Pan and G. Razumney, Electroreduction of oxygen, *Journal of Electroanalytical Chemistry and Interfacial Electrochemistry*, 1976, **69**, 195–201.
96 Y. Wang, D. Wang and Y. Li, A fundamental comprehension and recent progress in advanced Pt-based ORR nanocatalysts, *SmartMat*, 2021, **2**, 56–75.
97 A. Damjanovic and V. Brusic, Electrode kinetics of oxygen reduction on oxide-free platinum electrodes, *Electrochimica Acta*, 1967, **12**, 615–628.
98 K. Kinoshita, *Electrochemical oxygen technology*, Wiley, New York, 1992.
99 D. B. Sepa, M. V. Vojnovic and A. Damjanovic, Reaction intermediates as a controlling factor in the kinetics and mechanism of oxygen reduction at platinum electrodes, *Electrochimica Acta*, 1981, **26**, 781–793.
100 H. Mistry, A. S. Varela, S. Kühl, P. Strasser and B. R. Cuenya, Nanostructured electrocatalysts with tunable activity and selectivity, *Nat Rev Mater*, 2016, **1**, 1–14.
101 S. Zhu, X. Hu and M. Shao, Impacts of anions on the oxygen reduction reaction kinetics on platinum and palladium surfaces in alkaline solutions, *Phys. Chem. Chem. Phys.*, 2017, **19**, 7631–7641.
102 S. Zhu, X. Hu, L. Zhang and M. Shao, Impacts of Perchloric Acid, Nafion, and Alkali Metal Ions on Oxygen Reduction Reaction Kinetics in Acidic and Alkaline Solutions, *J. Phys. Chem. C*, 2016, **120**, 27452–27461.
103 X. Ge, A. Sumboja, D. Wuu, T. An, B. Li, F. W. T. Goh, T. S. A. Hor, Y. Zong and Z. Liu, Oxygen Reduction in Alkaline Media: From Mechanisms to Recent Advances of Catalysts, *ACS Catal.*, 2015, **5**, 4643–4667.
104 H. Lv, D. Li, D. Strmcnik, A. P. Paulikas, N. M. Markovic and V. R. Stamenkovic, Recent advances in the design of tailored nanomaterials for efficient oxygen reduction reaction, *Nano Energy*, 2016, **29**, 149–165.
105 I. Katsounaros, S. Cherevko, A. R. Zeradjanin and K. J. J. Mayrhofer, Oxygen electrochemistry as a cornerstone for sustainable energy conversion, *Angewandte Chemie International Edition*, 2014, **53**, 102–121.

106M. Gara, E. Laborda, P. Holdway, A. Crossley, C. J. V. Jones and R. G. Compton, Oxygen reduction at sparse arrays of platinum nanoparticles in aqueous acid: hydrogen peroxide as a liberated two electron intermediate, *Phys. Chem. Chem. Phys.*, 2013, **15**, 19487–19495.

107A. Kulkarni, S. Siahrostami, A. Patel and J. K. Nørskov, Understanding Catalytic Activity Trends in the Oxygen Reduction Reaction, *Chemical Reviews*, 2018, **118**, 2302–2312.

108J. Healy, C. Hayden, T. Xie, K. Olson, R. Waldo, M. Brundage, H. Gasteiger and J. Abbott, Aspects of the Chemical Degradation of PFSA Ionomers used in PEM Fuel Cells, *Fuel Cells*, 2005, **5**, 302–308.

109J.-C. Dong, X.-G. Zhang, V. Briega-Martos, X. Jin, J. Yang, S. Chen, Z.-L. Yang, D.-Y. Wu, J. M. Feliu, C. T. Williams, Z.-Q. Tian and J.-F. Li, In situ Raman spectroscopic evidence for oxygen reduction reaction intermediates at platinum single-crystal surfaces, *Nat Energy*, 2019, **4**, 60–67.

110Y.-H. Wang, J.-B. Le, W.-Q. Li, J. Wei, P. M. Radjenovic, H. Zhang, X.-S. Zhou, J. Cheng, Z.-Q. Tian and J.-F. Li, In situ Spectroscopic Insight into the Origin of the Enhanced Performance of Bimetallic Nanocatalysts towards the Oxygen Reduction Reaction (ORR), *Angewandte Chemie International Edition*, 2019, **58**, 16062–16066.

111M. Shao, P. Liu and R. R. Adzic, Superoxide anion is the intermediate in the oxygen reduction reaction on platinum electrodes, *J. Am. Chem. Soc.*, 2006, **128**, 7408–7409.

112K. Kunimatsu, T. Yoda, D. A. Tryk, H. Uchida and M. Watanabe, In situ ATR-FTIR study of oxygen reduction at the Pt/Nafion interface, *Phys. Chem. Chem. Phys.*, 2010, **12**, 621–629.

113D. E. Ramaker, A. Korovina, V. Croze, J. Melke and C. Roth, Following ORR intermediates adsorbed on a Pt cathode catalyst during break-in of a PEM fuel cell by in operando X-ray absorption spectroscopy, *Phys. Chem. Chem. Phys.*, 2014, **16**, 13645–13653.

114H.-C. Tsai, T. H. Yu, Y. Sha, B. V. Merinov, P.-W. Wu, S.-Y. Chen and W. A. Goddard, Density Functional Theory Study of Pt 3 M Alloy Surface Segregation with Adsorbed O/OH and Pt 3 Os as Catalysts for Oxygen Reduction Reaction, *J. Phys. Chem. C*, 2014, **118**, 26703–26712.

115T. H. Yu, R. Torres, B. V. Merinov and W. A. Goddard, Elucidating challenges of reactions with correlated reactant and product binding energies on an example of oxygen reduction reaction, *Journal of Molecular Catalysis A: Chemical*, 2016, **423**, 449–456.

116C. Zhang, X. Shen, Y. Pan and Z. Peng, A review of Pt-based electrocatalysts for oxygen reduction reaction, *Front. Energy*, 2017, **11**, 268–285.

117B.-A. Lu, N. Tian and S.-G. Sun, Surface structure effects of platinum-based catalysts for oxygen reduction reaction, *Current Opinion in Electrochemistry*, 2017, **4**, 76–82.

118B. Garlyyev, M. D. Pohl, V. Čolić, Y. Liang, F. K. Butt, A. Holleitner and A. S. Bandarenka, High oxygen reduction reaction activity of Pt5Pr electrodes in acidic media, *Electrochemistry Communications*, 2018, **88**, 10–14.

119L. Chen, W. Zhao, J. Zhang, M. Liu, Y. Jia, R. Wang and M. Chai, Recent Research on Iridium-Based Electrocatalysts for Acidic Oxygen Evolution Reaction from the Origin of Reaction Mechanism, *Small*, 2024, **20**, e2403845.

120T. Reier, H. N. Nong, D. Teschner, R. Schlögl and P. Strasser, Electrocatalytic Oxygen Evolution Reaction in Acidic Environments – Reaction Mechanisms and Catalysts, *Advanced Energy Materials*, 2017, **7**, 1601275.

121J. Rossmeisl, Z.-W. Qu, H. Zhu, G.-J. Kroes and J. K. Nørskov, Electrolysis of water on oxide surfaces, *Journal of Electroanalytical Chemistry*, 2007, **607**, 83–89.

122J. O. Bockris, Kinetics of Activation Controlled Consecutive Electrochemical Reactions: Anodic Evolution of Oxygen, *J. Chem. Phys.*, 1956, **24**, 817–827.

123T. Naito, T. Shinagawa, T. Nishimoto and K. Takanabe, Recent advances in understanding oxygen evolution reaction mechanisms over iridium oxide, *Inorg. Chem. Front.*, 2021, **8**, 2900–2917.

124Z. Shi, X. Wang, J. Ge, C. Liu and W. Xing, Fundamental understanding of the acidic oxygen evolution reaction: mechanism study and state-of-the-art catalysts, *Nanoscale*, 2020, **12**, 13249–13275.

125H. Ooka, A. Yamaguchi, T. Takashima, K. Hashimoto and R. Nakamura, Efficiency of Oxygen Evolution on Iridium Oxide Determined from the pH Dependence of Charge Accumulation, *J. Phys. Chem. C*, 2017, **121**, 17873–17881.

126Y. Ping, R. J. Nielsen and W. A. Goddard, The Reaction Mechanism with Free Energy Barriers at Constant Potentials for the Oxygen Evolution Reaction at the IrO(2) (110) Surface, *J. Am. Chem. Soc.*, 2017, **139**, 149–155.

127J. A. Gauthier, C. F. Dickens, L. D. Chen, A. D. Doyle and J. K. Nørskov, Solvation Effects for Oxygen Evolution Reaction Catalysis on IrO 2 (110), *J. Phys. Chem. C*, 2017, **121**, 11455–11463.

128H. G. Sanchez Casalongue, M. L. Ng, S. Kaya, D. Friebel, H. Ogasawara and A. Nilsson, In situ observation of surface species on iridium oxide nanoparticles during the oxygen evolution reaction, *Angewandte Chemie International Edition*, 2014, **53**, 7169–7172.

129A. Minguzzi, O. Lugaresi, E. Achilli, C. Locatelli, A. Vertova, P. Ghigna and S. Rondinini, Observing the oxidation state turnover in heterogeneous iridium-based water oxidation catalysts, *Chem. Sci.*, 2014, **5**, 3591.

130A. Minguzzi, C. Locatelli, O. Lugaresi, E. Achilli, G. Cappelletti, M. Scavini, M. Coduri, P. Masala, B. Sacchi, A. Vertova, P. Ghigna and S. Rondinini, Easy Accommodation of Different Oxidation States in Iridium Oxide Nanoparticles with Different Hydration Degree as Water Oxidation Electrocatalysts, *ACS Catal.*, 2015, **5**, 5104–5115.

131K. S. Exner and H. Over, Beyond the Rate-Determining Step in the Oxygen Evolution Reaction over a Single-Crystalline IrO 2 (110) Model Electrode: Kinetic Scaling Relations, *ACS Catal.*, 2019, **9**, 6755–6765.

132T. Shinagawa, A. T. Garcia-Esparza and K. Takanabe, Insight on Tafel slopes from a microkinetic analysis of aqueous electrocatalysis for energy conversion, *Sci Rep*, 2015, **5**, 13801.

133V. Pfeifer, T. E. Jones, S. Wrabetz, C. Massué, J. J. Velasco Vélez, R. Arrigo, M. Scherzer, S. Piccinin, M. Hävecker, A. Knop-Gericke and R. Schlögl, Reactive oxygen species in iridium-based OER catalysts, *Chem. Sci.*, 2016, **7**, 6791–6795.

134V. Pfeifer, T. E. Jones, J. J. Velasco Vélez, R. Arrigo, S. Piccinin, M. Hävecker, A. Knop-Gericke and R. Schlögl, In situ observation of reactive oxygen species forming on oxygen-evolving iridium surfaces, *Chemical science*, 2017, **8**, 2143–2149.

135V. A. Saveleva, L. Wang, D. Teschner, T. Jones, A. S. Gago, K. A. Friedrich, S. Zafeiratos, R. Schlögl and E. R. Savinova, Operando Evidence for a Universal Oxygen Evolution Mechanism on Thermal and Electrochemical Iridium Oxides, *The Journal of Physical Chemistry Letters*, 2018, **9**, 3154–3160.

136V. Pfeifer, T. E. Jones, J. J. Velasco Vélez, C. Massué, M. T. Greiner, R. Arrigo, D. Teschner, F. Girgsdies, M. Scherzer, J. Allan, M. Hashagen, G. Weinberg, S. Piccinin, M. Hävecker, A. Knop-Gericke and R. Schlögl, The electronic structure of iridium oxide electrodes active in water splitting, *Phys. Chem. Chem. Phys.*, 2016, **18**, 2292–2296.

137K. H. Saeed, M. Forster, J.-F. Li, L. J. Hardwick and A. J. Cowan, Water oxidation intermediates on iridium oxide electrodes probed by in situ electrochemical SHINERS, *Chem. Commun.*, 2020, **56**, 1129–1132.

138H. N. Nong, L. J. Falling, A. Bergmann, M. Klingenhof, H. P. Tran, C. Spöri, R. Mom, J. Timoshenko, G. Zichittella, A. Knop-Gericke, S. Piccinin, J. Pérez-Ramírez, B. R. Cuenya, R. Schlögl, P. Strasser, D. Teschner and T. E. Jones, Key role of chemistry versus bias in electrocatalytic oxygen evolution, *Nature*, 2020, **587**, 408–413.

139 O. Kasian, J.-P. Grote, S. Geiger, S. Cherevko and K. J. J. Mayrhofer, The Common Intermediates of Oxygen Evolution and Dissolution Reactions during Water Electrolysis on Iridium, *Angewandte Chemie International Edition*, 2018, **57**, 2488–2491.

140 A. Grimaud, A. Demortière, M. Saubanère, W. Dachraoui, M. Duchamp, M.-L. Doublet and J.-M. Tarascon, Activation of surface oxygen sites on an iridium-based model catalyst for the oxygen evolution reaction, *Nat Energy*, 2017, **2**, 1–10.

141 S. Fierro, T. Nagel, H. Baltruschat and C. Comninellis, Investigation of the oxygen evolution reaction on Ti/IrO2 electrodes using isotope labelling and on-line mass spectrometry, *Electrochemistry Communications*, 2007, **9**, 1969–1974.

142 O. Kasian, S. Geiger, T. Li, J.-P. Grote, K. Schweinar, S. Zhang, C. Scheu, D. Raabe, S. Cherevko, B. Gault and K. J. J. Mayrhofer, Degradation of iridium oxides via oxygen evolution from the lattice: correlating atomic scale structure with reaction mechanisms, *Energy Environ. Sci.*, 2019, **12**, 3548–3555.

143 S. Cherevko, S. Geiger, O. Kasian, A. Mingers and K. J. Mayrhofer, Oxygen evolution activity and stability of iridium in acidic media. Part 2. – Electrochemically grown hydrous iridium oxide, *Journal of Electroanalytical Chemistry*, 2016, **774**, 102–110.

144 S. Geiger, O. Kasian, M. Ledendecker, E. Pizzutilo, A. M. Mingers, W. T. Fu, O. Diaz-Morales, Z. Li, T. Oellers, L. Fruchter, A. Ludwig, K. J. J. Mayrhofer, M. T. M. Koper and S. Cherevko, The stability number as a metric for electrocatalyst stability benchmarking, *Nat Catal*, 2018, **1**, 508–515.

145 K. Schweinar, B. Gault, I. Mouton and O. Kasian, Lattice Oxygen Exchange in Rutile IrO2 during the Oxygen Evolution Reaction, *The Journal of Physical Chemistry Letters*, 2020, **11**, 5008–5014.

146 A. Grimaud, O. Diaz-Morales, B. Han, W. T. Hong, Y.-L. Lee, L. Giordano, K. A. Stoerzinger, M. T. M. Koper and Y. Shao-Horn, Activating lattice oxygen redox reactions in metal oxides to catalyse oxygen evolution, *Nature Chem*, 2017, **9**, 457–465.

147 N. Diklić, A. H. Clark, J. Herranz, D. Aegerter, J. S. Diercks, A. Beard, V. A. Saveleva, P. Chauhan, M. Nachtegaal, T. Huthwelker, D. Lebedev, P. Kayser, J. A. Alonso, C. Copéret and T. J. Schmidt, Surface Ir +5 Formation as a Universal Prerequisite for O 2 Evolution on Ir Oxides, *ACS Catal.*, 2023, **13**, 11069–11079.

148 D. Lebedev, R. Ezhov, J. Heras-Domingo, A. Comas-Vives, N. Kaeffer, M. Willinger, X. Solans-Monfort, X. Huang, Y. Pushkar and C. Copéret, Atomically Dispersed Iridium on Indium Tin Oxide Efficiently Catalyzes Water Oxidation, *ACS central science*, 2020, **6**, 1189–1198.

149 A. Minguzzi, O. Lugaresi, C. Locatelli, S. Rondinini, F. D'Acapito, E. Achilli and P. Ghigna, Fixed energy X-ray absorption voltammetry, *Analytical Chemistry*, 2013, **85**, 7009–7013.

150 H. Ooka, Y. Wang, A. Yamaguchi, M. Hatakeyama, S. Nakamura, K. Hashimoto and R. Nakamura, Legitimate intermediates of oxygen evolution on iridium oxide revealed by in situ electrochemical evanescent wave spectroscopy, *Phys. Chem. Chem. Phys.*, 2016, **18**, 15199–15204.

151 C. Sherwin, V. Celorrio, U. Podbevsek, K. Rigg, T. Hodges, A. Ibraliu, A. J. Telfer, L. McLeod, A. Difilippo, E. C. Corbos, C. Zalitis and A. E. Russell, An optimised Cell for in situ XAS of Gas Diffusion Electrocatalyst Electrodes, *ChemCatChem*, 2024, **16**, e202400221.

152 Y. Hori, in *Vayenas, C.G., White, R.E., Gamboa-Aldeco, M.E. (eds) Modern Aspects of Electrochemistry. Modern Aspects of Electrochemistry, vol 42*, pp. 89–189.

153 B. Ruqia, G. M. Tomboc, T. Kwon, J. Kundu, J. Y. Kim, K. Lee and S.-I. Choi, Recent advances in the electrochemical CO reduction reaction towards highly selective formation of Cx products (X = 1–3), *Chem Catalysis*, 2022, **2**, 1961–1988.

154 M. J. Bennett and J. B. Price, A physical and chemical examination of an ethylene steam cracker coke and of the underlying pyrolysis tube, *J Mater Sci*, 1981, **16**, 170–188.

155 M. Gattrell, N. Gupta and A. Co, A review of the aqueous electrochemical reduction of CO2 to hydrocarbons at copper, *Journal of Electroanalytical Chemistry*, 2006, **594**, 1–19.

156M. K. Birhanu, M.-C. Tsai, A. W. Kahsay, C.-T. Chen, T. S. Zeleke, K. B. Ibrahim, C.-J. Huang, W.-N. Su and B.-J. Hwang, Copper and Copper-Based Bimetallic Catalysts for Carbon Dioxide Electroreduction, *Adv Materials Inter*, 2018, **5**, 1800919.

157R. Kortlever, J. Shen, K. J. P. Schouten, F. Calle-Vallejo and M. T. M. Koper, Catalysts and Reaction Pathways for the Electrochemical Reduction of Carbon Dioxide, *The Journal of Physical Chemistry Letters*, 2015, **6**, 4073–4082.

158S. Bhardwaj, A. Biswas, M. Das and R. S. Dey, Nanostructured Cu foam and its derivatives: emerging materials for the heterogeneous conversion of CO 2 to fuels, *Sustainable Energy Fuels*, 2021, **5**, 2393–2414.

159A. Bagger, W. Ju, A. S. Varela, P. Strasser and J. Rossmeisl, Electrochemical CO2 Reduction: A Classification Problem, *ChemPhysChem*, 2017, **18**, 3266–3273.

160H. Ooka, M. C. Figueiredo and M. T. M. Koper, Competition between Hydrogen Evolution and Carbon Dioxide Reduction on Copper Electrodes in Mildly Acidic Media, *Langmuir : the ACS journal of surfaces and colloids*, 2017, **33**, 9307–9313.

161A. Dutta, M. Rahaman, N. C. Luedi, M. Mohos and P. Broekmann, Morphology Matters: Tuning the Product Distribution of CO 2 Electroreduction on Oxide-Derived Cu Foam Catalysts, *ACS Catal.*, 2016, **6**, 3804–3814.

162S. Ibrahim, A. Dworzak, D. Crespo, F. U. Renner, C. Dosche and M. Oezaslan, Nanoporous Copper Ribbons Prepared by Chemical Dealloying of a Melt-Spun ZnCu Alloy, *J. Phys. Chem. C*, 2022, **126**, 212–226.

163I. E. L. Stephens, A. S. Bondarenko, U. Grønbjerg, J. Rossmeisl and I. Chorkendorff, Understanding the electrocatalysis of oxygen reduction on platinum and its alloys, *Energy Environ. Sci.*, 2012, **5**, 6744.

164R. Reske, H. Mistry, F. Behafarid, B. Roldan Cuenya and P. Strasser, Particle size effects in the catalytic electroreduction of CO_2 on Cu nanoparticles, *J. Am. Chem. Soc.*, 2014, **136**, 6978–6986.

165K. Manthiram, B. J. Beberwyck and A. P. Alivisatos, Enhanced electrochemical methanation of carbon dioxide with a dispersible nanoscale copper catalyst, *J. Am. Chem. Soc.*, 2014, **136**, 13319–13325.

166J. Timoshenko, A. Bergmann, C. Rettenmaier, A. Herzog, R. M. Arán-Ais, H. S. Jeon, F. T. Haase, U. Hejral, P. Grosse, S. Kühl, E. M. Davis, J. Tian, O. Magnussen and B. Roldan Cuenya, Steering the structure and selectivity of CO2 electroreduction catalysts by potential pulses, *Nat Catal*, 2022, **5**, 259–267.

167B. Eren, D. Zherebetskyy, L. L. Patera, C. H. Wu, H. Bluhm, C. Africh, L. Wang, G. A. Somorjai and M. Salmeron, Activation of Cu(111) surface by decomposition into nanoclusters driven by CO adsorption, *Science*, 2016, **351**, 475–478.

168M. Rahaman, A. Dutta, A. Zanetti and P. Broekmann, Electrochemical Reduction of CO 2 into Multicarbon Alcohols on Activated Cu Mesh Catalysts: An Identical Location (IL) Study, *ACS Catal.*, 2017, **7**, 7946–7956.

169A. Dutta, K. Kiran, M. Rahaman, I. Z. Montiel, P. Moreno-García, S. Vesztergom, J. Drnec, M. Oezaslan and P. Broekmann, Insights from Operando and Identical Location (IL) Techniques on the Activation of Electrocatalysts for the Conversion of CO_2: A Mini-Review, *Chimia*, 2021, **75**, 733–743.

170A. Dutta, M. Rahaman, M. Mohos, A. Zanetti and P. Broekmann, Electrochemical CO 2 Conversion Using Skeleton (Sponge) Type of Cu Catalysts, *ACS Catal.*, 2017, **7**, 5431–5437.

171T. T. H. Hoang, S. Ma, J. I. Gold, P. J. A. Kenis and A. A. Gewirth, Nanoporous Copper Films by Additive-Controlled Electrodeposition: CO 2 Reduction Catalysis, *ACS Catal.*, 2017, **7**, 3313–3321.

172C. Reller, R. Krause, E. Volkova, B. Schmid, S. Neubauer, A. Rucki, M. Schuster and G. Schmid, Selective Electroreduction of CO 2 toward Ethylene on Nano Dendritic Copper Catalysts at High Current Density, *Advanced Energy Materials*, 2017, **7**, 1602114.

173Y. Lum, B. Yue, P. Lobaccaro, A. T. Bell and J. W. Ager, Optimizing C–C Coupling on Oxide-Derived Copper Catalysts for Electrochemical CO 2 Reduction, *J. Phys. Chem. C*, 2017, **121**, 14191–14203.

174M. Le, M. Ren, Z. Zhang, P. T. Sprunger, R. L. Kurtz and J. C. Flake, Electrochemical Reduction of CO2 to CH3OH at Copper Oxide Surfaces, *J. Electrochem. Soc.*, 2011, **158**, E45.

175K. W. Frese, Electrochemical Reduction of CO 2 at Intentionally Oxidized Copper Electrodes, *J. Electrochem. Soc.*, 1991, **138**, 3338–3344.

176R. Kas, R. Kortlever, A. Milbrat, M. T. M. Koper, G. Mul and J. Baltrusaitis, Electrochemical CO2 reduction on Cu2O-derived copper nanoparticles: controlling the catalytic selectivity of hydrocarbons, *Phys. Chem. Chem. Phys.*, 2014, **16**, 12194–12201.

177C. W. Li, J. Ciston and M. W. Kanan, Electroreduction of carbon monoxide to liquid fuel on oxide-derived nanocrystalline copper, *Nature*, 2014, **508**, 504–507.

178D. Gao, I. Zegkinoglou, N. J. Divins, F. Scholten, I. Sinev, P. Grosse and B. Roldan Cuenya, Plasma-Activated Copper Nanocube Catalysts for Efficient Carbon Dioxide Electroreduction to Hydrocarbons and Alcohols, *ACS Nano*, 2017, **11**, 4825–4831.

179H. Mistry, A. S. Varela, C. S. Bonifacio, I. Zegkinoglou, I. Sinev, Y.-W. Choi, K. Kisslinger, E. A. Stach, J. C. Yang, P. Strasser and B. R. Cuenya, Highly selective plasma-activated copper catalysts for carbon dioxide reduction to ethylene, *Nat Commun*, 2016, **7**, 12123.

180A. Dutta, M. Rahaman, B. Hecker, J. Drnec, K. Kiran, I. Zelocualtecatl Montiel, D. Jochen Weber, A. Zanetti, A. Cedeño López, I. Martens, P. Broekmann and M. Oezaslan, CO2 electrolysis – Complementary operando XRD, XAS and Raman spectroscopy study on the stability of CuxO foam catalysts, *Journal of Catalysis*, 2020, **389**, 592–603.

181J.-J. Velasco-Vélez, T. Jones, D. Gao, E. Carbonio, R. Arrigo, C.-J. Hsu, Y.-C. Huang, C.-L. Dong, J.-M. Chen, J.-F. Lee, P. Strasser, B. Roldan Cuenya, R. Schlögl, A. Knop-Gericke and C.-H. Chuang, The Role of the Copper Oxidation State in the Electrocatalytic Reduction of CO 2 into Valuable Hydrocarbons, *ACS Sustainable Chem. Eng.*, 2019, **7**, 1485–1492.

182M. Ma, K. Djanashvili and W. A. Smith, Controllable Hydrocarbon Formation from the Electrochemical Reduction of CO2 over Cu Nanowire Arrays, *Angewandte Chemie International Edition*, 2016, **55**, 6680–6684.

183F. Cavalca, R. Ferragut, S. Aghion, A. Eilert, O. Diaz-Morales, C. Liu, A. L. Koh, T. W. Hansen, L. G. M. Pettersson and A. Nilsson, Nature and Distribution of Stable Subsurface Oxygen in Copper Electrodes During Electrochemical CO 2 Reduction, *J. Phys. Chem. C*, 2017, **121**, 25003–25009.

184A. Eilert, F. Cavalca, F. S. Roberts, J. Osterwalder, C. Liu, M. Favaro, E. J. Crumlin, H. Ogasawara, D. Friebel, L. G. M. Pettersson and A. Nilsson, Subsurface Oxygen in Oxide-Derived Copper Electrocatalysts for Carbon Dioxide Reduction, *The Journal of Physical Chemistry Letters*, 2017, **8**, 285–290.

185M. Fields, X. Hong, J. K. Nørskov and K. Chan, Role of Subsurface Oxygen on Cu Surfaces for CO 2 Electrochemical Reduction, *J. Phys. Chem. C*, 2018, **122**, 16209–16215.

186C. Zhan, F. Dattila, C. Rettenmaier, A. Bergmann, S. Kühl, R. García-Muelas, N. López and B. R. Cuenya, Revealing the CO Coverage-Driven C-C Coupling Mechanism for Electrochemical CO2 Reduction on Cu2O Nanocubes via Operando Raman Spectroscopy, *ACS Catal.*, 2021, **11**, 7694–7701.

187Marcel Pourbaix, *Atlas of Electrochemical Equilibria in Aqueous Solutions*, Pergamon Press, Brussels, 1966.

188 T. A. Strobel, E. D. Sloan and C. A. Koh, Raman spectroscopic studies of hydrogen clathrate hydrates, *The Journal of Chemical Physics*, 2009, **130**, 14506.

189 H. S. Jeon, J. Timoshenko, C. Rettenmaier, A. Herzog, A. Yoon, S. W. Chee, S. Oener, U. Hejral, F. T. Haase and B. Roldan Cuenya, Selectivity Control of Cu Nanocrystals in a Gas-Fed Flow Cell through CO2 Pulsed Electroreduction, *J. Am. Chem. Soc.*, 2021, **143**, 7578–7587.

190 A. J. Garza, A. T. Bell and M. Head-Gordon, Is Subsurface Oxygen Necessary for the Electrochemical Reduction of CO2 on Copper?, *The Journal of Physical Chemistry Letters*, 2018, **9**, 601–606.

191 P. Grosse, D. Gao, F. Scholten, I. Sinev, H. Mistry and B. Roldan Cuenya, Dynamic Changes in the Structure, Chemical State and Catalytic Selectivity of Cu Nanocubes during CO2 Electroreduction: Size and Support Effects, *Angewandte Chemie International Edition*, 2018, **57**, 6192–6197.

192 J. Timoshenko and B. Roldan Cuenya, In Situ/Operando Electrocatalyst Characterization by X-ray Absorption Spectroscopy, *Chemical Reviews*, 2021, **121**, 882–961.

193 S.-C. Lin, C.-C. Chang, S.-Y. Chiu, H.-T. Pai, T.-Y. Liao, C.-S. Hsu, W.-H. Chiang, M.-K. Tsai and H. M. Chen, Operando time-resolved X-ray absorption spectroscopy reveals the chemical nature enabling highly selective CO2 reduction, *Nature communications*, 2020, **11**, 3525.

194 S. B. Scott, T. V. Hogg, A. T. Landers, T. Maagaard, E. Bertheussen, J. C. Lin, R. C. Davis, J. W. Beeman, D. Higgins, W. S. Drisdell, C. Hahn, A. Mehta, B. Seger, T. F. Jaramillo and I. Chorkendorff, Absence of Oxidized Phases in Cu under CO Reduction Conditions, *ACS Energy Lett.*, 2019, **4**, 803–804.

195 About XAS - Diamond Light Source, https://www.diamond.ac.uk/industry/Techniques-Available/Spectroscopy/X-ray-spectroscopy-XAS/About-XAS.html, (accessed 2 January 2025).

196 T. Binninger, E. Fabbri, A. Patru, M. Garganourakis, J. Han, D. F. Abbott, O. Sereda, R. Kötz, A. Menzel, M. Nachtegaal and T. J. Schmidt, Electrochemical Flow-Cell Setup for In Situ X-ray Investigations, *J. Electrochem. Soc.*, 2016, **163**, H906-H912.

197 W. A. Caliebe, V. Murzin, A. Kalinko and M. Görlitz, High-flux XAFS-beamline P64 at PETRA III, *AIP Conf. Proc.*, 2019, **2054**, 60031.

198 B. Bornmann, J. Kläs, O. Müller, D. Lützenkirchen-Hecht and R. Frahm, The quick EXAFS setup at beamline P64 at PETRA III for up to 200 spectra per second, *AIP Conf. Proc.*, 2019, **2054**, 40008.

199 A. Kalinko, W. A. Caliebe, R. Schoch and M. Bauer, A von Hamos-type hard X-ray spectrometer at the PETRA III beamline P64, *J Synchrotron Rad*, 2020, **27**, 31–36.

200 B. Ravel and M. Newville, *ATHENA and ARTEMIS*, John Wiley & Sons, Ltd, 2020.

201 A. H. Clark, J. Imbao, R. Frahm and M. Nachtegaal, ProQEXAFS: a highly optimized parallelized rapid processing software for QEXAFS data, *J Synchrotron Rad*, 2020, **27**, 551–557.

202 J. Jaumot, A. de Juan and R. Tauler, MCR-ALS GUI 2.0: New features and applications, *Chemometrics and Intelligent Laboratory Systems*, 2015, **140**, 1–12.

203 W. H. Cassinelli, L. Martins, A. R. Passos, S. H. Pulcinelli, C. V. Santilli, A. Rochet and V. Briois, Multivariate curve resolution analysis applied to time-resolved synchrotron X-ray Absorption Spectroscopy monitoring of the activation of copper alumina catalyst, *Catalysis Today*, 2014, **229**, 114–122.

204 J. Rabeah, V. Briois, S. Adomeit, C. La Fontaine, U. Bentrup and A. Brückner, Multivariate Analysis of Coupled Operando EPR/XANES/EXAFS/UV-Vis/ATR-IR Spectroscopy: A New Dimension for Mechanistic Studies of Catalytic Gas-Liquid Phase Reactions, *Chemistry – A European Journal*, 2020, **26**, 7395–7404.

205 A. Merkys, A. Vaitkus, A. Grybauskas, A. Konovalovas, M. Quirós and S. Gražulis, Graph isomorphism-based algorithm for cross-checking chemical and crystallographic descriptions, *Journal of cheminformatics*, 2023, **15**, 25.

206 A. Vaitkus, A. Merkys and S. Gražulis, Validation of the Crystallography Open Database using the Crystallographic Information Framework, *Journal of applied crystallography*, 2021, **54**, 661–672.
207 A. Vaitkus, A. Merkys, T. Sander, M. Quirós, P. A. Thiessen, E. E. Bolton and S. Gražulis, A workflow for deriving chemical entities from crystallographic data and its application to the Crystallography Open Database, *Journal of cheminformatics*, 2023, **15**, 123.
208 C. Lesage, E. Devers, C. Legens, G. Fernandes, O. Roudenko and V. Briois, High pressure cell for edge jumping X-ray absorption spectroscopy: Applications to industrial liquid sulfidation of hydrotreatment catalysts, *Catalysis Today*, 2019, **336**, 63–73.
209 Peter J. Larkin, *Infrared and Raman Spectroscopy*, Elsevier, Oxford, 2018.
210 Z. Huang, J. Peng, L. Xu and P. Liu, Development and Application of Surface-Enhanced Raman Scattering (SERS), *Nanomaterials*, 2024, **14**, 1417.
211 W. Knoll, Interfaces and thin films as seen by bound electromagnetic waves, *Annual Review of Physical Chemistry*, 1998, **49**, 569–638.
212 M. Moskovits, Surface-enhanced Raman spectroscopy: a brief retrospective, *Journal of Raman Spectroscopy*, 2005, **36**, 485–496.
213 N. Guillot and M. L. de La Chapelle, The electromagnetic effect in surface enhanced Raman scattering: Enhancement optimization using precisely controlled nanostructures, *Journal of Quantitative Spectroscopy and Radiative Transfer*, 2012, **113**, 2321–2333.
214 S. Zou, H. Y. H. Chan, C. T. Williams and M. J. Weaver, Formation and Stability of Oxide Films on Platinum-Group Metals in Electrochemical and Related Environments As Probed by Surface-Enhanced Raman Spectroscopy: Dependence on the Chemical Oxidant, *Langmuir*, 2000, **16**, 754–763.
215 M. Moskovits, D. P. DiLella and K. J. Maynard, Surface Raman spectroscopy of a number of cyclic aromatic molecules adsorbed on silver: selection rules and molecular reorientation, *Langmuir*, 1988, **4**, 67–76.
216 H. Yu, Y. Peng, Y. Yang and Z.-Y. Li, Plasmon-enhanced light–matter interactions and applications, *npj Comput Mater*, 2019, **5**, 1–14.
217 R. Smith, K. L. Wright and L. Ashton, Raman spectroscopy: an evolving technique for live cell studies, *Analyst*, 2016, **141**, 3590–3600.
218 Deutsches Insitut für Normung e.V., *VDI 2221 Blatt 1. Design of technical products and systems - Model of product design*, Beuth Verlag GmbH, Berlin, 2019.
219 *DIN ISO 3601-1:2013-11, Fluidtechnik_- O-Ringe_- Teil_1: Innendurchmesser, Schnurstärken, Toleranzen und Bezeichnung (ISO_3601-1:2012_+ Cor._1:2012)*, DIN Media GmbH, Berlin.
220 J. Quinson, L. Kacenauskaite, J. Bucher, S. B. Simonsen, L. Theil Kuhn, M. Oezaslan, S. Kunz and M. Arenz, Controlled Synthesis of Surfactant-Free Water-Dispersible Colloidal Platinum Nanoparticles by the Co4Cat Process, *ChemSusChem*, 2019, **12**, 1229–1239.
221 J. Quinson, A. Dworzak, S. B. Simonsen, L. Theil Kuhn, K. M. Jensen, A. Zana, M. Oezaslan, J. J. Kirkensgaard and M. Arenz, Surfactant-free synthesis of size controlled platinum nanoparticles: Insights from in situ studies, *Applied Surface Science*, 2021, **549**, 149263.
222 J. K. Mathiesen, J. Quinson, A. Dworzak, T. Vosch, M. Juelsholt, E. T. S. Kjær, J. Schröder, J. J. K. Kirkensgaard, M. Oezaslan, M. Arenz and K. M. Ø. Jensen, Insights from In Situ Studies on the Early Stages of Platinum Nanoparticle Formation, *The Journal of Physical Chemistry Letters*, 2021, **12**, 3224–3231.
223 J. Quinson, S. Neumann, T. Wannmacher, L. Kacenauskaite, M. Inaba, J. Bucher, F. Bizzotto, S. B. Simonsen, L. Theil Kuhn, D. Bujak, A. Zana, M. Arenz and S. Kunz, Colloids for Catalysts: A Concept for the Preparation of Superior Catalysts of Industrial Relevance, *Angewandte Chemie International Edition*, 2018, **57**, 12338–12341.

224M. Oezaslan, F. Hasché and P. Strasser, Oxygen Electroreduction on PtCo 3 PtCo and Pt 3 Co Alloy Nanoparticles for Alkaline and Acidic PEM Fuel Cells, *J. Electrochem. Soc.*, 2012, **159**, B394-B405.

225M. Oezaslan, F. Hasché and P. Strasser, PtCu 3 PtCu and Pt 3 Cu Alloy Nanoparticle Electrocatalysts for Oxygen Reduction Reaction in Alkaline and Acidic Media, *J. Electrochem. Soc.*, 2012, **159**, B444-B454.

226D. J. Morris and P. Zhang, In situ X-ray Absorption Spectroscopy of Platinum Electrocatalysts, *Chemistry - Methods*, 2021, **1**, 162–172.

227F. Nattino and N. Marzari, Operando XANES from first-principles and its application to iridium oxide, *Phys. Chem. Chem. Phys.*, 2020, **22**, 10807–10818.

228D. F. Abbott, D. Lebedev, K. Waltar, M. Povia, M. Nachtegaal, E. Fabbri, C. Copéret and T. J. Schmidt, Iridium Oxide for the Oxygen Evolution Reaction: Correlation between Particle Size, Morphology, and the Surface Hydroxo Layer from Operando XAS, *Chem. Mater.*, 2016, **28**, 6591–6604.

229D. E. Ramaker and D. C. Koningsberger, The atomic AXAFS and Delta(mu) XANES techniques as applied to heterogeneous catalysis and electrocatalysis, *Phys. Chem. Chem. Phys.*, 2010, **12**, 5514–5534.

230H. Imai, K. Izumi, M. Matsumoto, Y. Kubo, K. Kato and Y. Imai, In situ and real-time monitoring of oxide growth in a few monolayers at surfaces of platinum nanoparticles in aqueous media, *J. Am. Chem. Soc.*, 2009, **131**, 6293–6300.

231T. T. T. Hanh, Y. Takimoto and O. Sugino, First-principles thermodynamic description of hydrogen electroadsorption on the Pt(111) surface, *Surface Science*, 2014, **625**, 104–111.

232E. Skúlason, G. S. Karlberg, J. Rossmeisl, T. Bligaard, J. Greeley, H. Jónsson and J. K. Nørskov, Density functional theory calculations for the hydrogen evolution reaction in an electrochemical double layer on the Pt(111) electrode, *Physical chemistry chemical physics : PCCP*, 2007, **9**, 3241–3250.

233Y. Mo, I. C. Stefan, W.-B. Cai, J. Dong, P. Carey and D. A. Scherson, In Situ Iridium L III -Edge X-ray Absorption and Surface Enhanced Raman Spectroscopy of Electrodeposited Iridium Oxide Films in Aqueous Electrolytes, *J. Phys. Chem. B*, 2002, **106**, 3681–3686.

234J. D. E. McIntyre, W. F. Peck and S. Nakahara, Oxidation State Changes and Structure of Electrochromic Iridium Oxide Films, *J. Electrochem. Soc.*, 1980, **127**, 1264–1268.

235C. Powell, *X-ray Photoelectron Spectroscopy Database XPS,Version 4.1, NIST Standard Reference Database 20*, 1989, (accessed 30 November 2023).

236L. Li, H. Liu, C. Qin, Z. Liang, A. Scida, S. Yue, X. Tong, R. R. Adzic and S. S. Wong, Ultrathin Pt x Sn 1– x Nanowires for Methanol and Ethanol Oxidation Reactions: Tuning Performance by Varying Chemical Composition, *ACS Appl. Nano Mater.*, 2018, **1**, 1104–1115.

237L. Da Silva, V. Alves, S. de Castro and J. Boodts, XPS study of the state of iridium, platinum, titanium and oxygen in thermally formed IrO_2+TiO_2+PtO_X films, *Colloids and Surfaces A: Physicochemical and Engineering Aspects*, 2000, **170**, 119–126.

238K. P. Kepp, A Quantitative Scale of Oxophilicity and Thiophilicity, *Inorganic Chemistry*, 2016, **55**, 9461–9470.

239F. Bizzotto, J. Quinson, A. Zana, J. J. K. Kirkensgaard, A. Dworzak, M. Oezaslan and M. Arenz, Ir nanoparticles with ultrahigh dispersion as oxygen evolution reaction (OER) catalysts: synthesis and activity benchmarking, *Catal. Sci. Technol.*, 2019, **9**, 6345–6356.

240Q.-S. Chen, J. Solla-Gullón, S.-G. Sun and J. M. Feliu, The potential of zero total charge of Pt nanoparticles and polycrystalline electrodes with different surface structure: The role of anion adsorption in fundamental electrocatalysis, *Electrochimica Acta*, 2010, **55**, 7982–7994.

241 C. Schneemann, J. Traegner, L. Mindermann, M. Friedrichs-Schucht, B. Tang, A. Dietzel, J. Koehler and M. Oezaslan, A Universal Analytical Model for the Limiting Current Characteristics in Impinging Jet Electrodes, *J. Electrochem. Soc.*, 2025, **172**, 66503.

242 P. Liao, C. Chen, W. Ho, Y. Huang and K. Tiong, Characterization of IrO2 thin films by Raman spectroscopy, *Thin Solid Films*, 1997, **301**, 7–11.

243 Y. S. Huang, S. S. Lin, C. R. Huang, M. C. Lee, T. E. Dann and F. Z. Chien, Raman spectrum of IrO2, *Solid State Communications*, 1989, **70**, 517–522.

244 G. W. Graham, W. H. Weber, J. R. McBride and C. R. Peters, Raman investigation of simple and complex oxides of platinum, *J. Raman Spectrosc.*, 1991, **22**, 1–9.

245 J.-C. Dong, M. Su, V. Briega-Martos, L. Li, J.-B. Le, P. Radjenovic, X.-S. Zhou, J. M. Feliu, Z.-Q. Tian and J.-F. Li, Direct In Situ Raman Spectroscopic Evidence of Oxygen Reduction Reaction Intermediates at High-Index Pt(hkl) Surfaces, *J. Am. Chem. Soc.*, 2020, **142**, 715–719.

246 L. Moriau, M. A. Nazrulla, A. Logar, L. Pavko, M. Bele, N. Hodnik and A. K. Surca, Ir metal nanoparticles and IrO2 for acidic oxygen evolution reaction: Insight from Raman spectroscopy, *Sustainable Materials and Technologies*, 2024, **40**, e00901.

247 M. van der Merwe, R. E. Wibowo, C. E. Jimenez, C. Escudero, G. Agostini, M. Bär and R. Garcia-Diez, Electronic and Structural Property Comparison of Iridium-Based OER Nanocatalysts Enabled by Operando Ir L 3 -Edge X-ray Absorption Spectroscopy, *ACS Catal.*, 2024, **14**, 16759–16769.

248 I. Katsounaros, W. B. Schneider, J. C. Meier, U. Benedikt, P. U. Biedermann, A. A. Auer and K. J. J. Mayrhofer, Hydrogen peroxide electrochemistry on platinum: towards understanding the oxygen reduction reaction mechanism, *Phys. Chem. Chem. Phys.*, 2012, **14**, 7384–7391.

249 A. M. Gómez–Marín and E. A. Ticianelli, A reviewed vision of the oxygen reduction reaction mechanism on Pt-based catalysts, *Current Opinion in Electrochemistry*, 2018, **9**, 129–136.

250 B. A. Sexton, Vibrational spectra of water chemisorbed on platinum (111), *Surface Science*, 1980, **94**, 435–445.

251 Y. Zhang, X. Gao and M. J. Weaver, Nature of surface bonding on voltammetrically oxidized noble metals in aqueous media as probed by real-time surface-enhanced Raman spectroscopy, *J. Phys. Chem.*, 1993, **97**, 8656–8663.

252 H. Y. H. Chan, S. Zou and M. J. Weaver, Mechanistic Differences between Electrochemical and Gas-Phase Thermal Oxidation of Platinum-Group Transition Metals As Discerned by Surface-Enhanced Raman Spectroscopy, *J. Phys. Chem. B*, 1999, **103**, 11141–11151.

253 F. Sugimura, N. Sakai, T. Nakamura, M. Nakamura, K. Ikeda, T. Sakai and N. Hoshi, In situ observation of Pt oxides on the low index planes of Pt using surface enhanced Raman spectroscopy, *Phys. Chem. Chem. Phys.*, 2017, **19**, 27570–27579.

254 P. Sabatier, *La catalyse en chimie organique. Encyclopédie de Science Chimique Appliquée.*, Dunham, QC: Ch. Béranger, 1913.

255 H. Y. Lim, S. O. Park, S. H. Kim, G. Y. Jung and S. K. Kwak, First-Principles Design of Rutile Oxide Heterostructures for Oxygen Evolution Reactions, *Front. Energy Res.*, 2021, **9**. DOI: 10.3389/fenrg.2021.606313.

256 Z. W. Seh, J. Kibsgaard, C. F. Dickens, I. Chorkendorff, J. K. Nørskov and T. F. Jaramillo, Combining theory and experiment in electrocatalysis: Insights into materials design, *Science*, 2017, **355**. DOI: 10.1126/science.aad4998.

257 M. van der Merwe, Y. Lee, R. E. Wibowo, T. Kokumai, A. Efimenko, M. D. Arce, C. E. Jimenez, B. Howchen, R. Suarez Anzorena, I. Lucentini, C. Escudero, G. Schuck, Z. Kochovski, M. Favaro, D. E. Starr, K. Reuter, C. Scheurer, M. Bär and R. Garcia-Diez, Unravelling the mechanistic complexity of the oxygen evolution reaction and Ir dissolution in highly dimensional amorphous hydrous iridium oxides, *Energy Environ. Sci.*, 2025, **18**, 1214–1231.

258 S. Blaseio, C. Dosche, M. Rahaman, K. Kiran, A. Dworzak, B. Mahrt, P. Broekmann, A. Dutta and M. Oezaslan, Impact of Cu + and Cu 2+ species on the oxide-metal transition processes of Cu x O foams during the CO 2 RR probed by operando Quick-XAS, *J. Mater. Chem. A*, 2024, **12**, 28177–28192.

259 A. Gaur, B. D. Shrivastava and S. K. Joshi, Copper K-edge XANES of Cu(I) and Cu(II) oxide mixtures, *J. Phys.: Conf. Ser.*, 2009, **190**, 12084.

260 C. Powell, *X-ray Photoelectron Spectroscopy Database XPS,Version 4.1, NIST Standard Reference Database 20*, 1989, (accessed 20 December 2023).

261 J. A. Torres-Ochoa, D. Cabrera-German, O. Cortazar-Martinez, M. Bravo-Sanchez, G. Gomez-Sosa and A. Herrera-Gomez, Peak-fitting of Cu 2p photoemission spectra in Cu0, Cu1+, and Cu2+ oxides: A method for discriminating Cu0 from Cu1+, *Applied Surface Science*, 2023, **622**, 156960.

262 J. Kaur, A. Khanna, R. Kumar and R. Chandra, Growth and characterization of Cu2O and CuO thin films, *J Mater Sci: Mater Electron*, 2022, **33**, 16154–16166.

263 L. Debbichi, Marco de Lucas, M. C., J. F. Pierson and P. Krüger, Vibrational Properties of CuO and Cu 4 O 3 from First-Principles Calculations, and Raman and Infrared Spectroscopy, *J. Phys. Chem. C*, 2012, **116**, 10232–10237.

264 K. Reimann and K. Syassen, Raman scattering and photoluminescence in Cu2O under hydrostatic pressure, *Physical review. B, Condensed matter*, 1989, **39**, 11113–11119.

265 S. H. Lee, J. C. Lin, M. Farmand, A. T. Landers, J. T. Feaster, J. E. Avilés Acosta, J. W. Beeman, Y. Ye, J. Yano, A. Mehta, R. C. Davis, T. F. Jaramillo, C. Hahn and W. S. Drisdell, Oxidation State and Surface Reconstruction of Cu under CO2 Reduction Conditions from In Situ X-ray Characterization, *J. Am. Chem. Soc.*, 2021, **143**, 588–592.

266 C. E. Moore, J. Eastcott, M. Cimenti, N. Kremliakova and E. L. Gyenge, Novel methodology for ex situ characterization of iridium oxide catalysts in voltage reversal tolerant proton exchange membrane fuel cell anodes, *Journal of Power Sources*, 2019, **417**, 53–60.

267 S.-Y. Huang, P. Ganesan, H.-Y. Jung and B. N. Popov, Development of supported bifunctional oxygen electrocatalysts and corrosion-resistant gas diffusion layer for unitized regenerative fuel cell applications, *Journal of Power Sources*, 2012, **198**, 23–29.

268 J. C. Cruz, S. Rivas, D. Beltran, Y. Meas, R. Ornelas, G. Osorio-Monreal, L. Ortiz-Frade, J. Ledesma-García and L. G. Arriaga, Synthesis and evaluation of ATO as a support for Pt–IrO2 in a unitized regenerative fuel cell, *International Journal of Hydrogen Energy*, 2012, **37**, 13522–13528.

269 Y. Wang, J. Ren, K. Deng, L. Gui and Y. Tang, Preparation of Tractable Platinum, Rhodium, and Ruthenium Nanoclusters with Small Particle Size in Organic Media, *Chem. Mater.*, 2000, **12**, 1622–1627.

270 J. K. Mathiesen, J. Quinson, S. Blaseio, E. T. S. Kjær, A. Dworzak, S. R. Cooper, J. K. Pedersen, B. Wang, F. Bizzotto, J. Schröder, T. L. Kinnibrugh, S. B. Simonsen, L. Theil Kuhn, J. J. K. Kirkensgaard, J. Rossmeisl, M. Oezaslan, M. Arenz and K. M. Ø. Jensen, Chemical Insights into the Formation of Colloidal Iridium Nanoparticles from In Situ X-ray Total Scattering: Influence of Precursors and Cations on the Reaction Pathway, *J. Am. Chem. Soc.*, 2023, **145**, 1769–1782.

271 J. Quinson, L. Kacenauskaite, J. Bucher, S. B. Simonsen, L. Theil Kuhn, M. Oezaslan, S. Kunz and M. Arenz, Controlled Synthesis of Surfactant-Free Water-Dispersible Colloidal Platinum Nanoparticles by the Co4Cat Process, *ChemSusChem*, 2019, **12**, 1229–1239.

272 J. Quinson, S. Neumann, L. Kacenauskaite, J. Bucher, J. J. K. Kirkensgaard, S. B. Simonsen, L. Theil Kuhn, A. Zana, T. Vosch, M. Oezaslan, S. Kunz and M. Arenz, Solvent-Dependent Growth and Stabilization Mechanisms of Surfactant-Free Colloidal Pt Nanoparticles, *Chemistry – A European Journal*, 2020, **26**, 9012–9023.

273 T. Biegler, D. Rand and R. Woods, Limiting oxygen coverage on platinized platinum; Relevance to determination of real platinum area by hydrogen adsorption, *Journal of Electroanalytical Chemistry and Interfacial Electrochemistry*, 1971, **29**, 269–277.

274 R. Woods, Hydrogen adsorption on platinum, iridium and rhodium electrodes at reduced temperatures and the determination of real surface area, *Journal of Electroanalytical Chemistry and Interfacial Electrochemistry*, 1974, **49**, 217–226.

275 J. Zheng, Y. Yan and B. Xu, Correcting the Hydrogen Diffusion Limitation in Rotating Disk Electrode Measurements of Hydrogen Evolution Reaction Kinetics, *J. Electrochem. Soc.*, 2015, **162**, F1470-F1481.

276 G. W. Sievers, A. W. Jensen, J. Quinson, A. Zana, F. Bizzotto, M. Oezaslan, A. Dworzak, J. J. K. Kirkensgaard, T. E. L. Smitshuysen, S. Kadkhodazadeh, M. Juelsholt, K. M. Ø. Jensen, K. Anklam, H. Wan, J. Schäfer, K. Čépe, M. Escudero-Escribano, J. Rossmeisl, A. Quade, V. Brüser and M. Arenz, Self-supported Pt-CoO networks combining high specific activity with high surface area for oxygen reduction, *Nature materials*, 2021, **20**, 208–213.

277 A. W. Jensen, G. W. Sievers, K. D. Jensen, J. Quinson, J. A. Arminio-Ravelo, V. Brüser, M. Arenz and M. Escudero-Escribano, Self-supported nanostructured iridium-based networks as highly active electrocatalysts for oxygen evolution in acidic media, *J. Mater. Chem. A*, 2020, **8**, 1066–1071.

278 F. Neese, The ORCA program system, *Wiley Interdisciplinary Reviews: Computational Molecular Science*, 2012, **2**, 73–78.

279 A. D. Becke, Density-functional exchange-energy approximation with correct asymptotic behavior, *Physical review. A, General physics*, 1988, **38**, 3098–3100.

280 E. van Lenthe, J. G. Snijders and E. J. Baerends, The zero-order regular approximation for relativistic effects: The effect of spin–orbit coupling in closed shell molecules, *J. Chem. Phys.*, 1996, **105**, 6505–6516.

281 S. Grimme, S. Ehrlich and L. Goerigk, Effect of the damping function in dispersion corrected density functional theory, *Journal of Computational Chemistry*, 2011, **32**, 1456–1465.

282 F. Zapata and C. García-Ruiz, The discrimination of 72 nitrate, chlorate and perchlorate salts using IR and Raman spectroscopy, *Spectrochimica acta. Part A, Molecular and biomolecular spectroscopy*, 2018, **189**, 535–542.

283 H.-C. Shin, J. Dong and M. Liu, Porous Tin Oxides Prepared Using an Anodic Oxidation Process, *Advanced Materials*, 2004, **16**, 237–240.

284 H.-C. Shin, J. Dong and M. Liu, Nanoporous Structures Prepared by an Electrochemical Deposition Process, *Adv. Mater.*, 2003, **15**, 1610–1614.

285 H.-C. Shin and M. Liu, Copper Foam Structures with Highly Porous Nanostructured Walls, *Chem. Mater.*, 2004, **16**, 5460–5464.

286 B. Lafuente, R. T. Downs, H. Yang and N. Stone, The power of databases: The RRUFF project, *Highlights in Mineralogical Crystallography*, 2015, 1–30.

8. List of Figures

Figure 1. Schematic drawing of a PEMFC. 19
Figure 2. Schematic drawing of a membrane electrode assembly (MEA). The black dots represent the catalyst nanoparticles, grey spheres depict the carbon support, and the light blue lines show the ionomer film inside the catalyst layer, which usually contains the same polymer (Nafion) as the membrane. 20
Figure 3. Schematic fuel cell voltage changes with time under normal operation and hydrogen starvation/cell reversal. 22
Figure 4. Schematic representation of standard operation at the anode catalyst (**left**) and carbon corrosion occurring as a result of hydrogen starvation (**right**). The blue sphere shows a Pt NP and the grey rectangle the carbon support, that is highly corroded during COR. 22
Figure 5. Schematic representation of the incorporation of an iridium co-catalyst into the anode catalyst layer by (**a**) physical mixing, (**b**) addition to the same support and (**c**) alloying with Pt NPs. 24
Figure 6. Schematic drawing of a URFC in constant gas (CG) mode with the HOR/HER and ORR/OER reaction equations and respective standard potentials. 26
Figure 7. Possible adsorption sites of hydrogen on a platinum (111) surface. Reprinted from Komanicky et al.[90] 29
Figure 8. Reaction pathway for the Oxygen reduction reaction (ORR) proposed by Marković et al.[94] and Wroblowa et al.[95] 30
Figure 9. Proposed reaction mechanisms for the oxygen evolution reaction. Reproduced from Reier et al.[120] 32
Figure 10. Primary pathway of the AEM proposed by Rossmeisl et al.[121] Reprinted from Shi et al. 32
Figure 11. Proposed mechanism of the oxygen evolution reaction (OER) over iridium oxide. Four different colors (red, blue, green, and orange) were used to illustrate four catalytic cycles. (**a**) The red-colored cycle is driven by the redox of the iridium center. (**b**) The blue-colored one proceeds via the redox of the adsorbed O species. (**c**) The green-colored cycle is characterized by the redox of the Ir=O state. (**d**) The orange-colored cycle involves the lattice oxygen, where the orange and black O represent the lattice oxygen and adsorbed oxygen species, respectively. The squares represent the initial state of each cycle, and the dashed lines indicate the dissolution path of iridium species. Reprinted from Naito et al.[123] 34
Figure 12. Possible mechanistic pathways of CO_2RR to C_1 and C_2 products on polycrystalline copper grouped into different colored reaction schemes combined from the works in the top-right legend. Reprinted from Nitopi and Bertheussen et al.[16] 38
Figure 13. Pourbaix diagram for copper at 25 °C. The red arrow illustrates the transition of CuO to metallic Cu via the formation of Cu_2O as the potential is decreased to cathodic values under common conditions during CO_2RR (pH ≈ 7 – 8, 25 C). Reprinted from Pourbaix.[187] 41
Figure 14. Electrochemical Protocols used to investigate oxide-metal transition processes of Cu_xO type materials and the influence on the CO_2RR product formation. 42
Figure 15. Schematic representation of the X-ray absorption process and subsequent scattering of the ejected electron. Reprinted from Diamond Light Source. 48
Figure 16. Set-up of the custom-made electrochemical XAS flow-cell at beamline P64 at DESY. 49

Figure 17. Drawings of the three parts of the electrochemical XAS flow-cell. WE = working electrode, RE = reference electrode and CE = counter electrode. 50
Figure 18. Cross section drawing of the electrochemical XAS flow-cell with arrows showing the flow of electrolyte through the cell. RE = reference electrode. 51
Figure 19. XAS data of a Cu foil at the Cu K-edge (blue). Showing the pre-edge line (green), post-edge line (purple) and binding energy (E_0, orange). 53
Figure 20. Normalized XAS spectrum at the Cu K-edge. Showing the XANES (green) and EXAFS region (red) as well as the orbital transition (1s → 4p) observed at this absorption edge. 53
Figure 21. XAS data of a Cu foil at the Cu K-edge (blue). Showing the atomic background ($\mu_0(E)$) 54
Figure 22. (**a**) k^2-weighted Cu K edge EXAFS data in k-space and (**b**) corresponding Fourier-transformed EXAFS data of a Cu foil. 55
Figure 23. Schematic representation of the MCR-ALS analysis, outlining data set D, the obtained components (S^T) and concentration profiles (C) of the respective components by the constrained ALS optimization. 57
Figure 24. Schematic representation of the light scattering process. 59
Figure 25. Schematic representation of the Raman (Stokes/Anti-Stokes) and Rayleigh scattering processes. 60
Figure 26. (**a**) Standard configuration of a Raman microscope. Reprinted from Smith et al. (**b**) Image of WITec alpha300 RSA confocal microscope. 62
Figure 27. Schematic drawings of the electrochemical Raman Cell in exploded view (**a**) and oblique view (**b**). For the manufacturing of the cell Polyetherketon (PEEK) was used and O-rings made from Viton® are employed, which are stable in acids at pH = 1. 63
Figure 28. Image of the spectro-electrochemical Raman cell under WITec alpha300 RSA confocal microscope. CE = Counter Electrode, WE = Working Electrode and RE = Reference Electrode. 64
Figure 29. TEM micrographs (**top panel**) and respective particle size distributions (**bottom panel**) of the PtIr-colloidal (**a,b**) and PtIr-WI (**c,d**) NPs supported on carbon. The PtIr-WI NPs show two different particle size distributions i.e. a smaller diameter with 3.1 ± 0.3 nm (dark grey line) and a larger diameter with 5.5 ± 0.5 nm (orange line). For the cumulative particle size, the two diameters were weight based on the particle count resulting in 3.1 ± 0.3 nm (black line). 67
Figure 30. (**a**) HOR and (**b**) OER polarization curves of the PtIr-WI (green line), PtIr-colloidal (purple line), commercial IrO_x-TEC (grey line) and commercial Pt-TEC (blue line). The catalyst loading was 8 μg_{metal} cm^{-2}_{geo}. For HOR, LSVs were measured from – 0.02 to + 0.4 $V_{RHE,\ iR\text{-}free}$ at a scan rate of 10 mV s^{-1} and 1600 rpm in H_2-saturated 0.1 M $HClO_4$. The data of the Pt-Ir NPs is overlaying with the diffusion limiting currents (j_{diff}, orange dashed line). The OER polarization curves were measured from 1.2 to 1.6 $V_{RHE,\ iR\ free}$ at 6 mV s^{-1} and 2000 rpm in argon-saturated 0.1 M $HClO_4$. (**c**) Specific activities (SA) and (**d**) Ir-based mass activities (MA) towards OER were determined at 1.50 $V_{RHE,\ iR\text{-}free}$. 69
Figure 31. Operando Quick-XANES spectra of the PtIr-colloidal (**a,c**) and PtIr-WI (**b,d**) NPs recorded at the Pt and Ir L3 edges. Spectra were collected every second and subsequently averaged over 3 s during the potential jump experiments between HER (– 0.02 V_{RHE}, black)

and OER (+ 1.55 V_{RHE}, blue or red for Pt or Ir, respectively) with holding times of 3 s in argon-saturated 0.1 M $HClO_4$ and subsequently averaged by three. 70
Figure 32. Concentration profiles of the Pt^0 and Pt^{2+} (**top**) as well as Ir^{3+} and Ir^{4+} (**bottom**) species obtained by the MCR-ALS analysis of the Pt and Ir L3 edge XANES spectra for the PtIr-colloidal NPs in dependence of the time during the potential jump experiments with 3 s intervals for the first 25 s (**a**,**b**) and the potential jump experiments with 10 s intervals (**c**,**d**). For MCR-ALS analysis of the 3 s jumps one XANES spectrum recorded every second was used. For the 10 s experiment the spectra were averaged to every two seconds, resulting in one point every two seconds. The black dashed lines show the holding times of the potential jumps between HER (– 0.02 V_{RHE}) and OER (+ 1.55 V_{RHE}) in argon-saturated 0.1 M $HClO_4$. 72
Figure 33 Normalized Pt^0 and Pt^{2+} (**top**) as well as Ir^0, Ir^{3+} and Ir^{4+} (**bottom**) species concentrations obtained by the MCR-ALS analysis of the XANES spectra collected from the PtIr-WI NPs in dependence of the time during the potential jump experiments with 3 s for the first 35 s (**a**,**b**) and the potential jump experiments with 10 s for 60 s (**c**,**d**). For MCR-ALS analysis of the 3 s jumps one Pt and Ir L3 edge XANES spectrum recorded every second was used. For the 10 s experiment the spectra were averaged to every two seconds, resulting in one point every two seconds. The black dashed lines show the holding times of the potential jumps between HER (– 0.02 V_{RHE}) and OER (+ 1.55 V_{RHE}) in argon-saturated 0.1 M $HClO_4$. 75
Figure 34. Normalized Pt^0 and Pt^{2+} (**top**) as well as normalized Ir^0, Ir^{3+} and Ir^{4+} (**bottom**) concentrations obtained by the MCR-ALS analysis of the XANES spectra collected from the Pt_3Ir-colloidal (**a**,**b**) and Pt_3Ir-WI NPs (**c**,**d**) during the 3 s potential jump experiments for the first 25 s. For the MCR-ALS analysis one XANES spectrum recorded every second was used resulting in one point per second. The black dashed lines show the holding times of the chronoamperometric potential jumps between HER (– 0.02 V_{RHE}) and OER (+ 1.55 V_{RHE}) in argon-saturated 0.1 M $HClO_4$..... 78
Figure 35. *Operando* Quick-XANES potential jump experiments for 3 s with commercial Pt-TEC (**a**,**b**) and Pt-colloidal NPs (**c**,**d**). Pt L3 edge XANES spectra (**top panel**) were collected every second and subsequently averaged by three. XANES spectra collected during HER are displayed in black and during OER in blue. The insets display the same XANES spectra with a longer energy range. Normalized Pt^0 and Pt^{2+} concentrations obtained by the MCR-ALS analysis in dependence of the time (**bottom panel**). For MCR-ALS analysis one spectrum recorded every second was used. The black dashed lines show the holding times of the potential jumps between HER (– 0.02 V_{RHE}) and OER (+ 1.55 V_{RHE}) in argon-saturated 0.1 M $HClO_4$. 80
Figure 36. *Operando* Ir L3 edge Quick-XANES spectra collected of the commercial IrO_x-TEC (**a**) and Ir-colloidal NPs (**b**). Spectra were recorded every second and subsequently averaged over 3 s during the potential jump experiments between HER (– 0.02 V_{RHE}, black) and OER (+ 1.55 V_{RHE}, red) with holding times of 3 s in argon-saturated 0.1 M $HClO_4$. The insets display the same XANES spectra with a longer energy range. 81
Figure 37. Bifunctionality model for the PtIr NPs prepared by the colloidal and Wet-Impregnation (WI) synthesis routes. Proportion of Ir^0, Ir^{3+} and Ir^{4+} species as well as Pt^0 and Pt^{2+} species present during HER (– 0.02 V_{RHE}) and OER (+ 1.55 V_{RHE}) are schematically represented by the bar diagrams. 84

Figure 38. (**a** and **b**) Ex-situ high-resolution Pt and Ir 4f XPS spectra of the Pt-Ir thin films. Light grey circles represent the measured data, the envelope is shown in black and Pt^0, Pt^{2+} and Pt^{4+} species are plotted in blue, while Ir^0, Ir^{3+} and Ir^{4+} species are displayed in red. (**c**) Quantitative surface analysis of the high-resolution Pt and Ir $4f_{7/2}$ XPS spectra, determining each species (Pt^0, Pt^{2+}, Pt^{4+} and Ir^0, Ir^{3+}, Ir^{4+}). High-resolution Pt and Ir 4f XPS spectra of the monometallic Pt and Ir thin films are displayed in **Figure S2.2**. (**d**) ORR and OER polarization curves of the Pt (blue), PtIr(1:1) (pink), PtIr(3:1) (green) and Ir (red) thin films. The polarization curves were recorded in one scan from 0.05 to 1.6 $V_{RHE,\ iR\ free}$ at a scan rate of 1 mV s^{-1} and a flow rate of 1 mL min^{-1} in O_2-saturated 0.1 M $HClO_4$ using an impinging jet flow cell. 91
Figure 39. In-situ Raman spectra collected from (**a**) pure Ir and (**b**) pure Pt thin films in the potential range of 0.8 – 1.6 V_{RHE} in 0.1 M $HClO_4$. Peak assignments of the respective Raman data at 1.2 and 1.6 V_{RHE} are shown in **Tables 4** and **5**. The position at 933 cm^{-1} is ascribed to the adsorbed ClO4- anion. 98
Figure 40. In-situ Raman spectra collected from (**a**) PtIr(1:1) and (**b**) PtIr(3:1) thin films in the potential range of 0.8 – 1.6 V_{RHE} in 0.1 M $HClO_4$. Peak assignments of the respective thin films at 1.2 and 1.6 V_{RHE} are shown in **Tables 6** and **7**. The position at 933 cm^{-1} is related to the adsorbed ClO4- anion. 102
Figure 41. Optimized geometries of the (**a**) iridium oxo-hydroxo complex, (**b**) platinum oxo-hydroxo complex, (**c**) bimetallic platinum-iridium oxo-hydroxo complex with 1:1 Pt:Ir ratio and (**d**) bimetallic platinum-iridium oxo-hydroxo complex with 3:1 Pt:Ir ratio employed for the calculation of the predicted Raman spectra. 103
Figure 42. Calculated Raman spectra of the (**a**) iridium oxo-hydroxo complex, (**b**) platinum oxo-hydroxo complex, (**c**) bimetallic platinum-iridium oxo-hydroxo complex with 1:1 Pt:Ir ratio and (**d**) bimetallic platinum-iridium oxo-hydroxo complex with 3:1 Pt:Ir ratio. Assignments of the Raman frequencies are displayed in **Tables S2.7 – 10**. 105
Figure 43. (**a**) In-situ Raman spectra of all bimetallic Pt-Ir as well as pure Pt and Ir thin films recorded at 1.6 V_{RHE} in 0.1 M$HClO_4$. (**b**) Computed Raman spectra of the pure iridium oxo-hydroxo complex (orange) and the bimetallic platinum-iridium oxo-hydroxy complex with (blue). (**c**) Vibrations of the strong movement of the μ-oxo bonds correspond to the Raman frequencies at 725 cm^{-1} (pure Ir complex) and 682 cm^{-1} (bimetallic Ir-Pt complex). The arrows show the direction and magnitude of the atomic movement. 110
Figure 44. (**a** and **b**) SEM micrographs of the Cu_xO foam annealed at 200 °C for 12 h in air at low and high magnification. (**c**) XRD profiles (black line) of all annealed Cu_xO foams and the corresponding fits (red dashed line) obtained from the quantitative Rietveld refinement analysis. The references of Cu (#9008468, red), Cu_2O (#1010963, purple) and CuO (#9008961, grey) were taken from the crystal open database (COD).[205-207] Note, the peak at a 2θ value of 54° labelled C(006) arises from the carbon substrate. For the 100- and 200-foams, the peaks at 2θ values of 36°, 42°, 61°, 74° and 78° correspond to the lattice planes of (111), (200), (220), (311) and (222) of a primitive cubic Cu_2O unit cell with a space group of Pn3m. The small peak with 2θ = 43° is assigned to the lattice plane of (111) for face-centered cubic (fcc) copper unit cell with a space group of Fm3m. For the 300- and 450-foams, the additional peaks at 2θ values of 35°, 39°, 49°, 54°, 59°, 66°, 68° and 76° correspond to the lattice planes of (111), (111/200), (202), (020) (202), (311), (220) and (004) of a CuO base-centered monoclinic unit cell with space group C12/c1. For the 450-foam, additional CuO peaks appear at 2θ values of 46°, 65°

and 73° that are ascribed to the lattice planes of (112), (022) and (311), respectively. Reprinted from Blaseio et al. 113
Figure 45. Contributions of the three copper species (Cu^{2+}, Cu^{+}, Cu^{0}) within the in air annealed Cu_xO foams obtained by ex-situ (**a**) quantitative Rietveld refinement analysis of the XRD patterns, (**b**) linear combination fit (LCF) analysis of ex-situ Cu K-edge XANES spectra and (**c**) analysis of the high-resolution Cu $2p_{3/2}$ XPS spectra. Reprinted from Blaseio et al.[252] ... 114
Figure 46. Left panel (a, c, e, g): Series of potential-resolved Cu K-edge XANES spectra of the Cu_xO foams annealed at 100 °C, 200 °C, 300 °C and 450 °C in air. The potential was shifted from + 0.4 V_{RHE} to – 1.2 V_{RHE} at 100 mV and held for 6 – 10 min at each potential, while XAS spectra were collected and subsequently averaged. CO_2-saturated 0.5 M $KHCO_3$ was used as electrolyte solution. **Right panel (b, d, f, h):** Normalized Cu^{0}, Cu^{+} and Cu^{2+} concentration courses obtained by the MCR-ALS analysis of the spectra from the left panel. Reprinted from Blaseio et al.[252] 119
Figure 47. Oxide-metal transition potential in dependence of the annealing temperature for different Cu_xO foams obtained by MCR-ALS (full red squares) analysis. The corresponding Cu^{2+} content of each Cu_xO foam (blue bars) was obtained from LCF analysis of the ex-situ XANES spectra using Cu^{0}, Cu_2O and CuO as reference materials. Reprinted from Blaseio et al.[252] 121
Figure 48. Series of time-resolved Cu K-edge Quick-XANES spectra of 200-foam by jumping from OCP → – 0.2 V_{RHE} (**a**) → – 0.5 V_{RHE} (**c**) → – 1.3 V_{RHE} (**d**) in CO_2-saturated 0.5 M $KHCO_3$. One spectrum was collected every second. (**b, d, f**) Normalized Cu^{0}, Cu^{+} and Cu^{2+} concentrations obtained by the MCR-ALS analysis in dependence of the time at the respective applied potential. Note, the noise in the XAS spectra is caused by the strong bubble formation especially at – 1.3 V_{RHE}, making it difficult to normalize the data in a proper way. Reprinted from Blaseio et al.[252] 123
Figure 49. Time-resolved changes in Cu K-edge XANES spectra of the 200-foam (**a, b)** and 300-foam (**c, d**) by direct switching of the potential from OCP → – 0.5 V_{RHE}. One spectrum was collected every second. (**b**, **d**) Normalized concentration profiles of the Cu^{2+}, Cu^{+} and Cu^{0} species obtained by the MCR-ALS analysis. All measurements were performed in CO_2-saturated 0.5 M $KHCO_3$. Note, the noise in the XAS spectra is caused by the strong bubble formation especially at – 0.5 V_{RHE}, making it difficult to normalize the data in a proper way. Reprinted from Blaseio et al.[252] 125
Figure 50. Series of time-resolved Cu K-edge Quick-XANES spectra of 100-foam (**a, b)** and 300-foam (**c, d**) by direct jumping of the potential from OCP → – 1.3 V_{RHE}. One spectrum was collected every second. (**b**, **d**) Normalized concentration profiles of the Cu^{2+}, Cu^{+} and Cu^{0} species obtained by the MCR-ALS analysis. All measurements were performed in CO_2-saturated 0.5M $KHCO_3$. Note, the noise in the XAS spectra is caused by the strong bubble formation especially at – 1.3 V_{RHE}. This makes it difficult to normalize the data in a proper way. Reprinted from Blaseio et al.[252] 126
Figure 51. Schematic model showing the potential-dependent oxide-metal transition processes of the four differently annealed Cu_xO foams during the potential increment (ΔE = 100 mV) experiments. The transition of Cu^{2+} to Cu^{0} with intermediate Cu^{+} formation is illustrated. From the ex-situ XANES analysis, the initial Cu^{0}:Cu^{+}:Cu^{2+} ratios of the in air annealed Cu_xO foams are 50:39:11 (100 °C), 0:79:21 (200 °C), 0:24:76 % (300 °C) and 0:0:100 (450 °C),

respectively. The pore structure of the foams is depicted by the white spheres. Reprinted from Blaseio et al.[252] 129
Figure 52. Schematic model showing the time-dependent oxide-metal transition processes of the 100 °C, 200 °C and 300 °C in air annealed Cu_xO foams during the potential jump (ΔE > 500 mV) experiments. The fast transition of Cu^{2+} to Cu^0 vs. slower intermediate Cu^+ formation is illustrated for the two different chronoamperometric experiments used in this study. From the ex-situ XANES analysis, the initial Cu^0:Cu^+:Cu^{2+} ratios of the in air annealed Cu_xO foams are 50:39:11 (100 °C), 0:79:21 (200 °C), 0:24:76 (300 °C) and 0:0:100 (450 °C), respectively. The pore structure of the foams is depicted by the white spheres. Reprinted from Blaseio et al.[252] 131

9. List of Tables

***Table 1**. Reaction equations and respective standard potentials for the HOR and ORR.[23] ....* 21
***Table 2**. Possible electrochemical cathode reactions and products obtained during CO_2RR.[16,152,155–158] .....* 37
***Table 3.** Requirement list for the design of the electrochemical Raman cell. .....* 62
***Table 4.** Raman peaks and corresponding type of vibration of the Ir thin film at 1.2 V_{RHE} and 1.6 V_{RHE}. Assignments are based on works by Pavlovic et al.[78] and Zhao et al.[80]. .....* 96
***Table 5.** Raman peaks and corresponding type of vibration obtained from monometallic Pt thin film at 1.2 V_{RHE} and 1.6 V_{RHE}. Assignments are made based on Huang et al.[83], Zhang et al.[248], Graham et al.[241] and our own DFT calculations. .....* 97
***Table 6.** Raman peaks and corresponding type of vibration obtained from the PtIr(1:1) thin film at 1.2 V_{RHE} and 1.6 V_{RHE}. .....* 100
***Table 7.** Raman peaks and corresponding type of vibration of the PtIr(3:1) thin film at 1.2 V_{RHE} and 1.6 V_{RHE}. .....* 101

10. Appendix

10.1. Supporting Information Chapter 4.1.

Experimental

Synthesis of bimetallic Pt-Ir NPs

Pt-Ir and monometallic Ir and Pt colloidal nanoparticles were prepared via the surfactant-free colloidal method generally developed by Wang et al.[269] and advanced by Quinson et al.[221,270–272] The metal precursor salts ($H_2PtCl_6 \times 6H_2O$ and $IrCl_3 \times nH_2O$) were dissolved in an alkaline solution (1 M NaOH) of methanol. For the monometallic NPs each precursor salt was mixed separately. Subsequently, microwave irradiation at 70 °C led to NP formation, followed by immobilization on carbon support (Vulcan® XC-72) using rotary evaporation. The immobilized NPs on the carbon support were left to dry overnight to remove any water residues.

The second method for the preparation of the Pt-Ir alloy NPs on Vulcan® XC-72 was the wet-impregnation – freeze drying – thermal annealing synthesis method, reported previously.[224,225] The commercial Pt/C (29.1 wt.%) catalyst and iridium precursor ($IrCl_3 \times nH_2O$) were dispersed in ultra-purified water using horn-sonication (Branson Digital Sonifier 250d, amplitude of 10 %) for 7 min. The resulting slurry was frozen in liquid nitrogen followed by freeze drying in vacuum (0.021 mbar) for 48 h. The dried powder was annealed in a horizontal three-zone tube furnace (Carbolite Gero Ltd., Model HZS) under reductive atmosphere (5 vol.% H_2/95 vol.% Ar) at a constant flow rate of 120 mL min^{-1} using the following heating protocol: 25 °C to 250 °C at 10 °C min^{-1}, held for 2 h, 250 °C to 500 °C at 10°C min^{-1}, held for 6 h and quenched to cool down to room temperature.

Electrochemical measurements in the RDE set-up

For the electrochemical measurements, about 2 mg of catalyst powder was dispersed in 4.25 mL ultra-purified water and 0.75 mL 2-propanol (Fisher Chemicals, HPLC). The calculated total metal loadings of the homogeneous electrode thin films were 8 $\mu g_{metal}\ cm^{-2}_{geo}$. Electrochemical measurements were conducted in a rotating disk electrode (RDE) set-up using a custom-made three-compartment glass cell, a potentiostat (Biologic, VSP-300) and a RDE rotator (Pine Research Instrumentation). The Pt-Ir catalysts dispersed as a thin catalyst film on a glassy carbon electrode (Ø = 5 mm, Pine Research Instrumentation) were used as the working electrode, a gold mesh as the counter electrode and a mercury-mercury sulfate reference electrode. 0.1 M $HClO_4$ was used as the electrolyte.

Three cyclic voltammetry (CV) profiles were recorded between 0.05 and 1.00 V_{RHE} at 50 mV s^{-1} to determine the electrochemically active surface area (ECSA) from the hydrogen

underpotential deposition (H_{UPD}) method. The H_{UPD} was obtained by assuming pseudo-capacities of 210 µC cm^{-2} (polycrystalline Pt)[273], 179 µC cm^{-2} (polycrystalline Ir)[274] and an estimated value of 195 µC cm^{-2} for the bimetallic PtIr NPs.

The HOR performance was measured by five linear sweep voltammograms from – 0.02 to + 0.4 V_{RHE} at a scan rate of 10 mV s^{-1} and 1600 rounds per minute (rpm) in H_2 saturated 0.1 M $HClO_4$. Since the HOR activity is too high to be measured by the RDE set-up, the obtained polarization curve was compared to the diffusion limited current (j_{diff}).[275] To determine the OER activity, five linear sweep voltammograms from 1.2 to 1.6 V_{RHE} at 6 mV s^{-1} and 2000 rpm in argon saturated 0.1 M $HClO_4$ were measured.

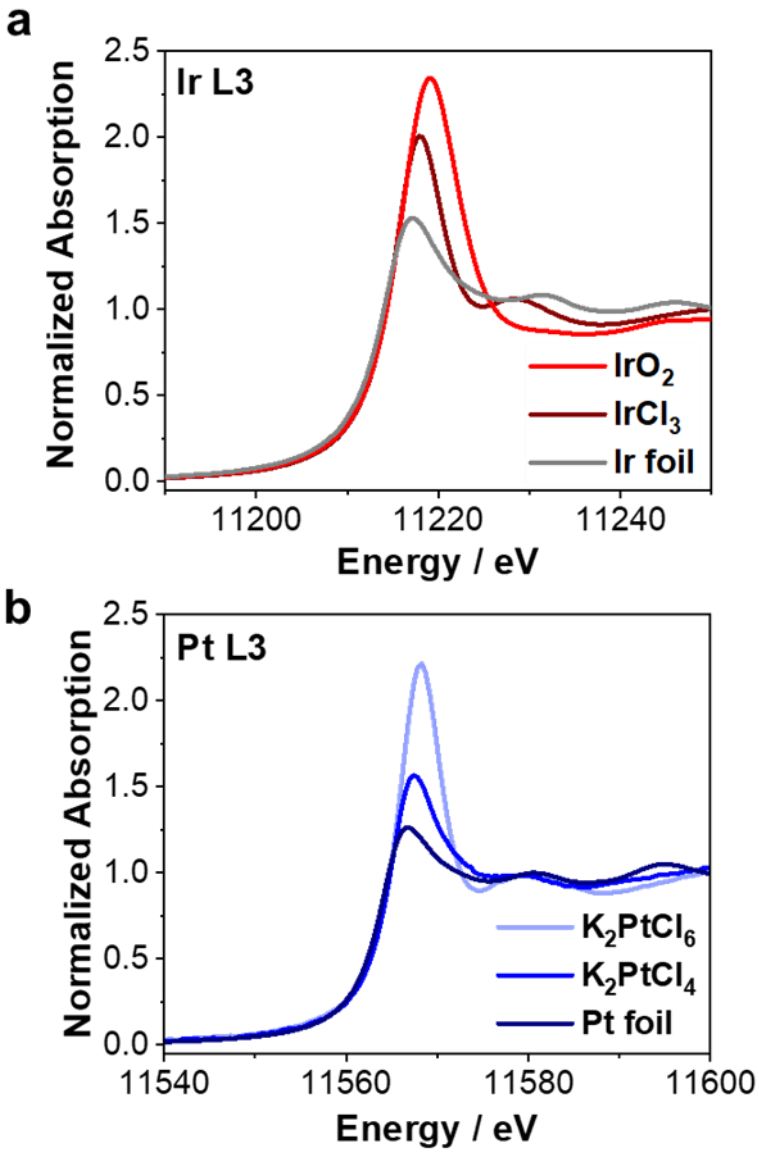

Figure S1.1. *Ex-situ* XAS spectra of the reference materials (IrO_2, $IrCl_3$, Ir foil and K_2PtCl_6, K_2PtCl_4, Pt foil) used for MCR-ALS analysis recorded at the Ir (**a**) and Pt (**b**) L3 edges.

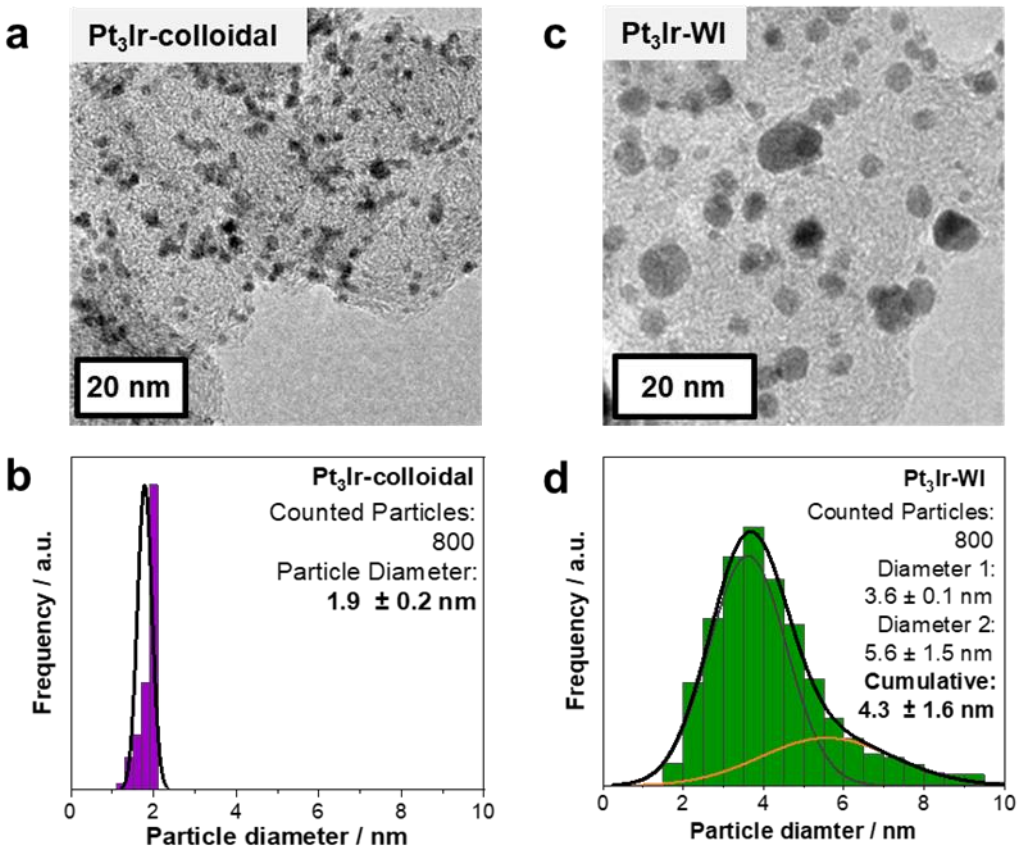

Figure S1.2. TEM micrographs (**top panel**) and respective particle size distributions (**bottom panel**) of the Pt_3Ir-colloidal (**a-b**) and Pt_3Ir-WI (**c-d**) NPs supported on carbon. The Pt_3Ir-WI NPs show two different particle size distributions i.e. a smaller diameter with 3.6 ± 0.1 nm (dark grey line) and a larger diameter with 5.6 ± 1.6 nm (orange line). For the cumulative particle size, the two diameters were weight based on the particle count resulting in 4.3 ± 1.6 nm (black line).

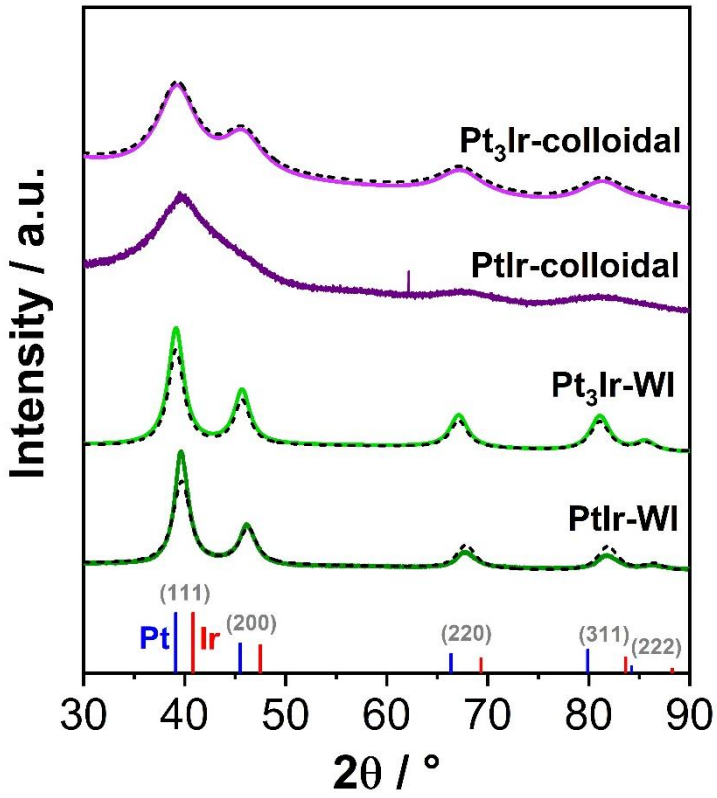

Figure S1.3. XRD profiles of all Pt-Ir NPs prepared by the colloidal (purple) and wet-impregnation (green) routes with the corresponding fits (black dashed lines). The peaks at 2θ values of 40°, 46°, 67°, 82° and 86° correspond to the lattice planes of (111), (200), (220), (311) and (222) of a face-centered cubic (fcc) unit cell with a space group of $Fm\bar{3}m$. The pattern references of fcc Pt (#9008480, blue) and Ir (#9008470, red) were taken from the crystallography open database (COD).[205–207]

Table S1.1. Space group, lattice parameter, crystallite size and composition via Vegard's law determined by quantitative Rietveld refinement analysis of the XRD profiles for the Pt-Ir NPs displayed in **Figure S1.3**. The weighted profile R-factor (R_{wp}) represents the discrepancy index between the calculated and measured data.

sample	space group	lattice parameter / Å	crystallite size / nm	composition via Vegard's law / at.%	R_{wp}
PtIr-colloidal	-	-	-	-	-
Pt_3Ir-colloidal	$Fm\bar{3}m$	3.892 ± 0.001	2.0 ± 0.1	$Pt_{77}Ir_{23}$	6.11
PtIr-WI	$Fm\bar{3}m$	3.887 ± 0.001	4.3 ± 0.2	$Pt_{56}Ir_{44}$	13.70
Pt_3Ir-WI	$Fm\bar{3}m$	3.908 ± 0.004	4.7 ± 0.1	$Pt_{80}Ir_{20}$	6.40

Table S1.2. Elemental EDX analysis confirming the Pt:Ir ratios of the Pt-Ir NPs synthesized by the colloidal and wet-impregnation routes.

Sample	Ir / at.%	Pt / at.%
PtIr-colloidal	51 ± 2	49 ± 2
Pt_3Ir-colloidal	25 ± 2	75 ± 2
PtIr-WI	52 ± 2	48 ± 2
Pt_3Ir-WI	23 ± 2	77 ± 2

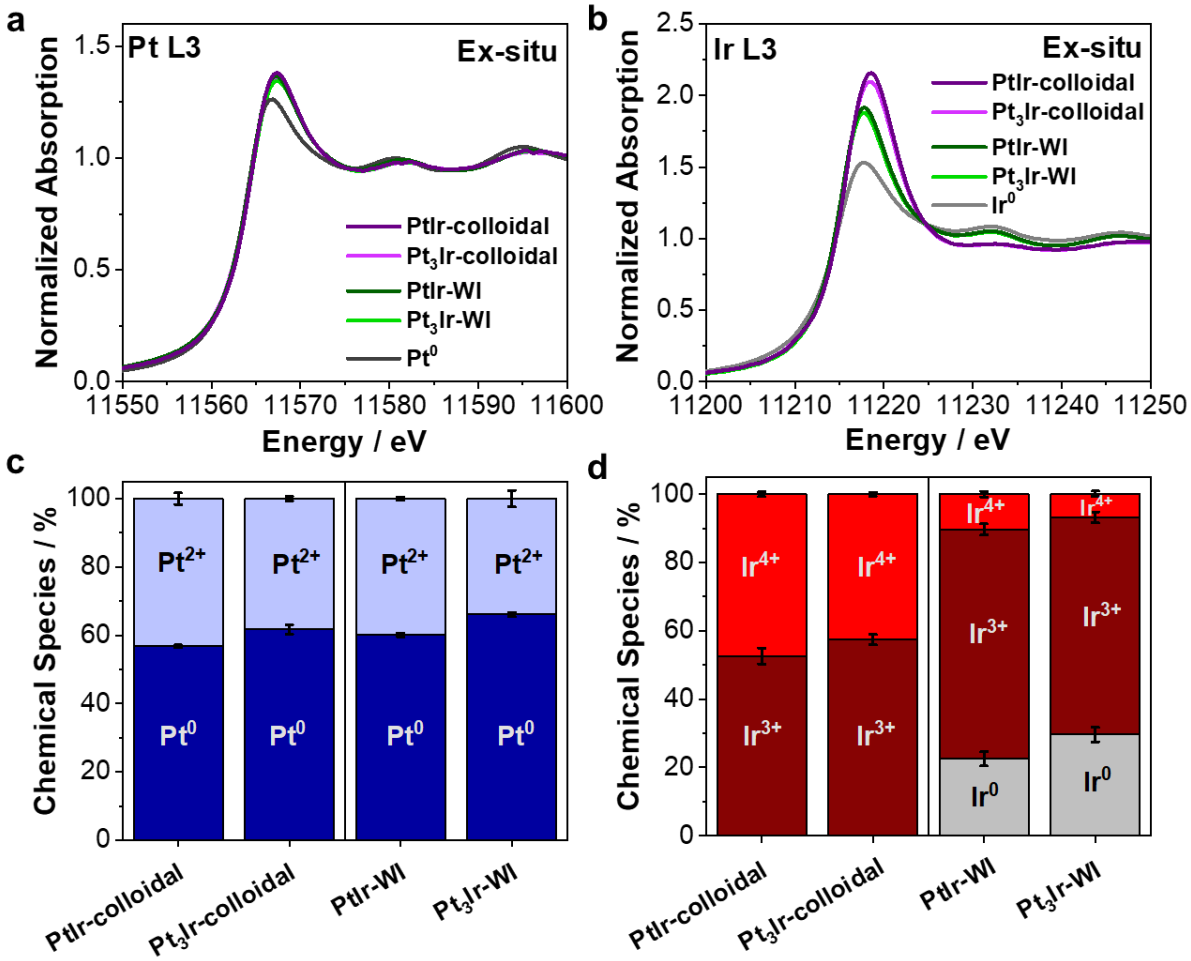

Figure S1.4. Ex-situ XANES data of the PtIr and Pt_3Ir NPs prepared by the colloidal and WI routes. Normalized XANES spectra obtained at the Pt (**a**) and Ir (**b**) L3 edges. Spectra were recorded every second for 10 min and subsequently averaged. (**c**,**d**) Corresponding linear combination fit (LCF) analysis of the Pt and Ir L3 edges XANES spectra using the references in **Figure S1.1**.

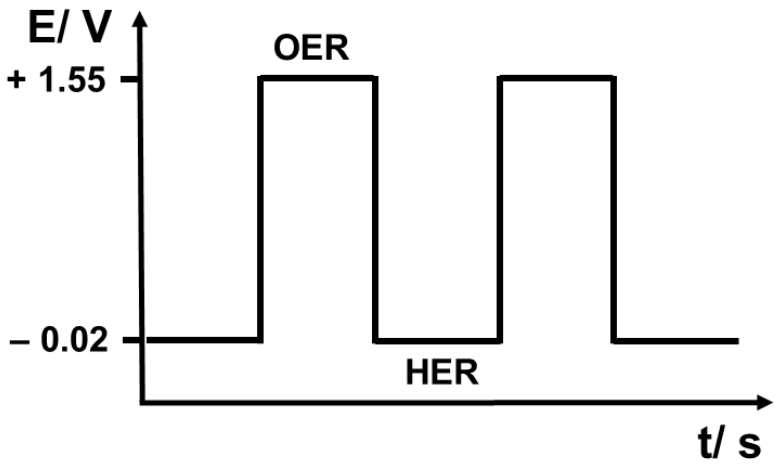

Figure S1.5. Schematic drawing showing the applied potential jumps between HER (– 0.02 V_{RHE}) and OER (+ 1.55 V_{RHE}) every 3 s or 10 s.

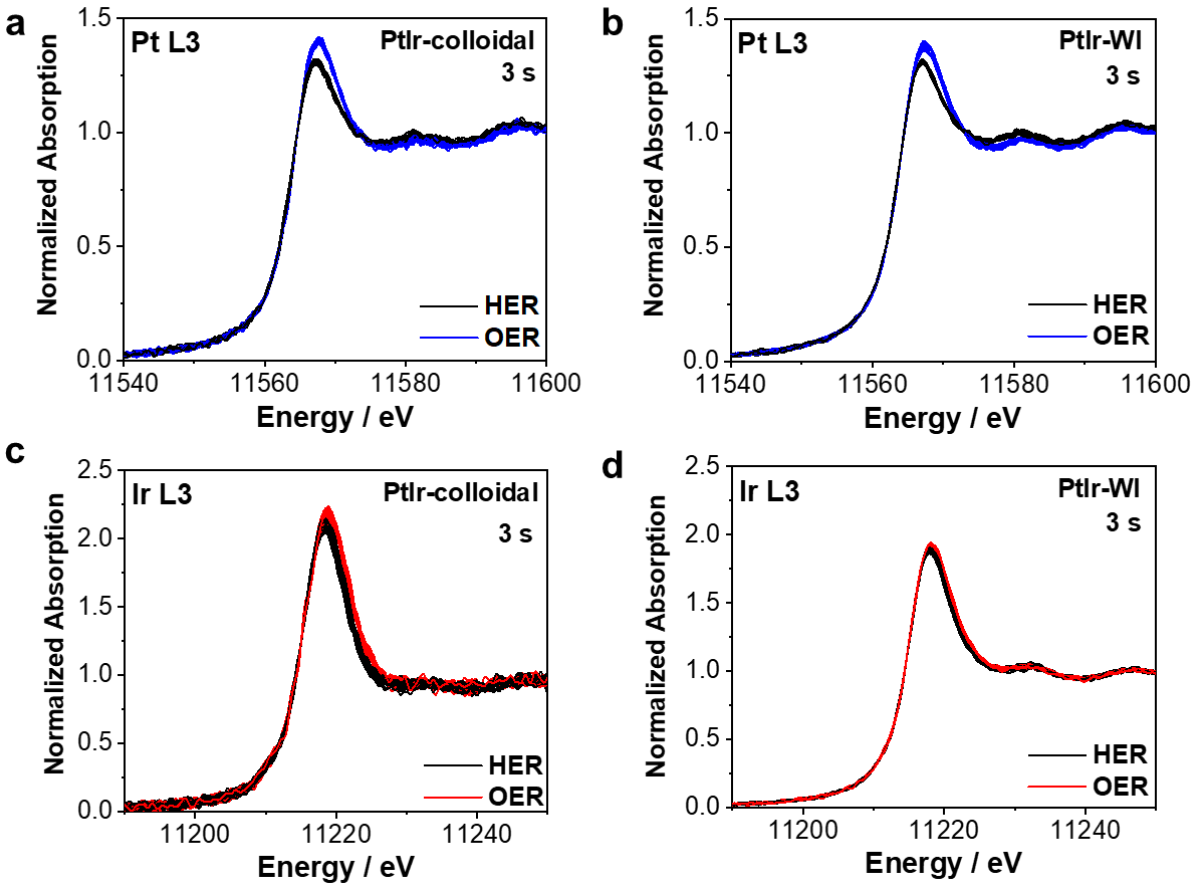

Figure S1.6. Longer range Pt (**top**) and Ir (**bottom**) L3 edges *operando* Quick-XANES spectra of the PtIr-colloidal (**a**,**b**) and PtIr-WI NPs (**c,d**) displayed in **Figure 31**. Spectra were obtained every second and subsequently averaged over 3 s during the potential jump experiments between HER (– 0.02 V_{RHE}, black) and OER (+ 1.55 V_{RHE}, blue/red) with holding times of 3 s in argon-saturated 0.1 M $HClO_4$.

MCR-ALS analysis

After the XANES data matrix was created in MATLAB (spectra are shown in **Figure S1.7, I**), the number of components was estimated from the Eigenvalue and Eigenvector plots in the Singular Value Window of the MCR-ALS Toolbox **(Figure S1.7, II).** Additionally, the purest variable detection method **(Figure S1.7, III)** was used as an initial guess of the spectra in the ALS minimization. Several constraints were applied for the analysis of the XANES spectra: (i) non-negativity of the concentration and MCR-ALS spectra (C and S matrices) and (ii) the total concentration of the components sums up to 1 (100 %) **(Figure S1.7, IV** and **V**). For non-negativity of C and S, fast nonnegativity-constrained least-squares (fnnls) algorithm was selected. To obtain the concentrations of the Pt (Pt^0 and Pt^{2+}) and Ir (Ir^0, Ir^{3+} and Ir^{4+}) species directly through the MCR-ALS method, the spectra of the references shown in **Figure S1.1** were fixed as components in the equality constraints **(Figure S1.7, V**). After ALS optimization was run **(Figure S1.7, VI),** the percentage of variance (r^2) at optimum was confirmed to be 99 % or higher.

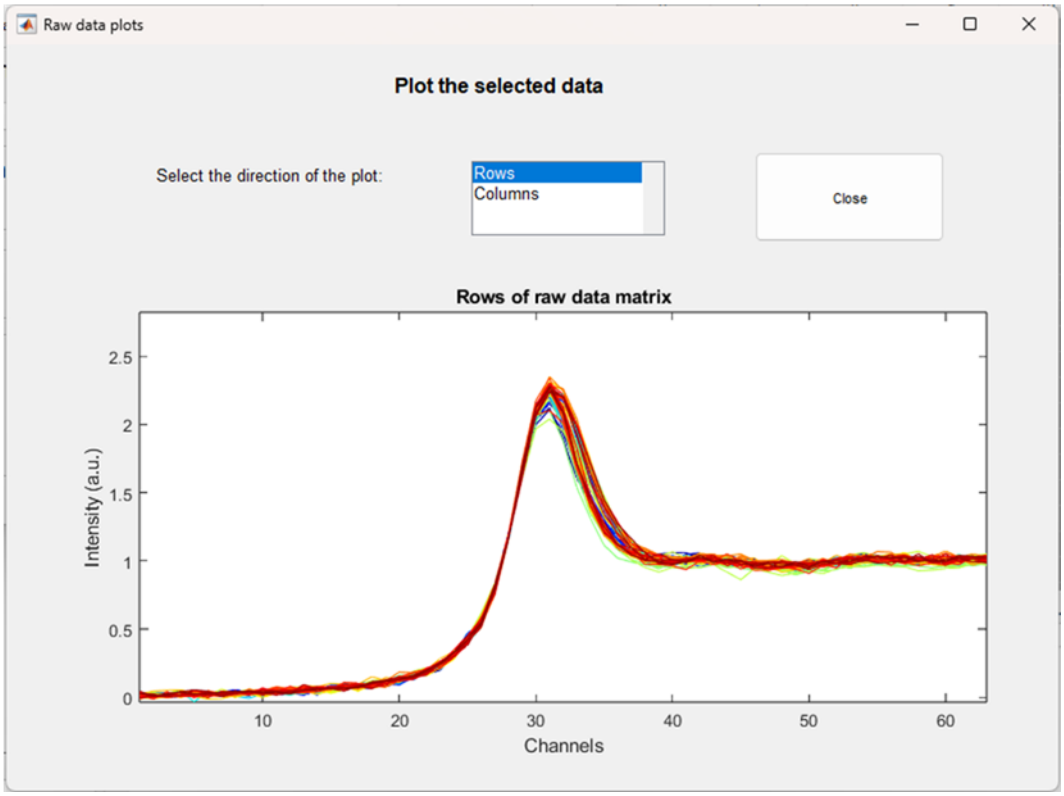

II

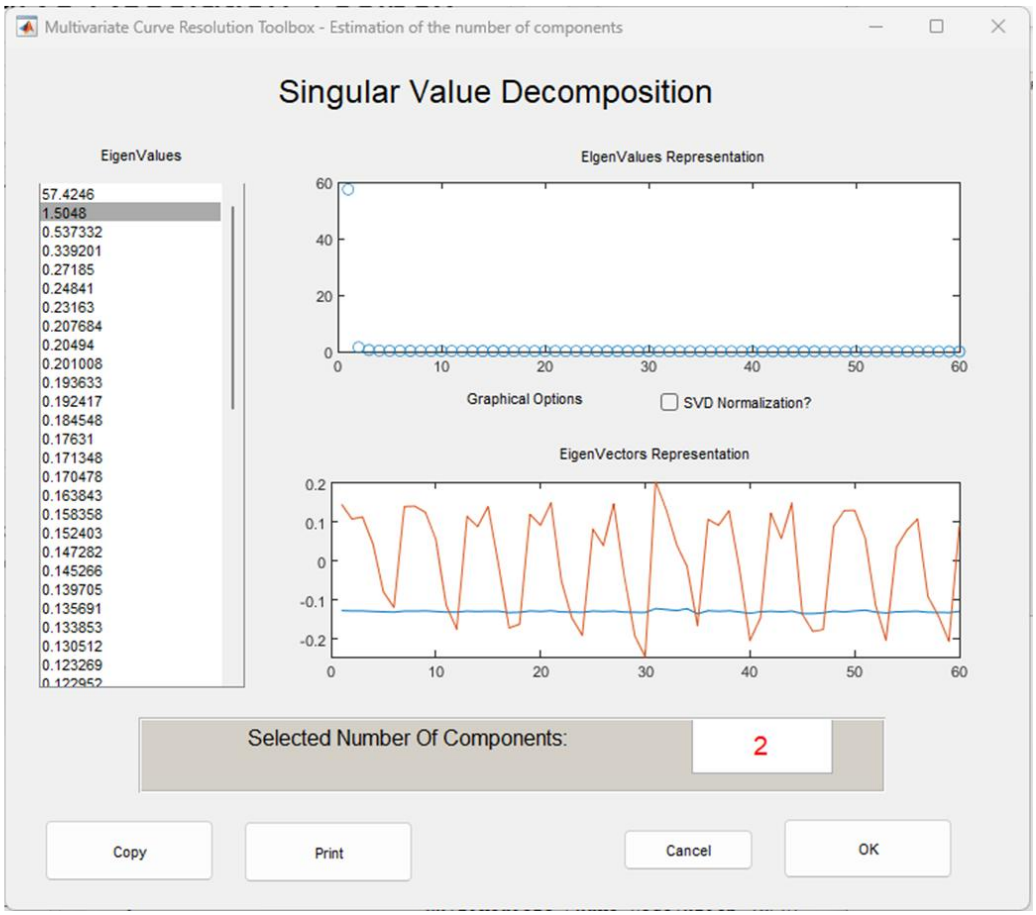
Multivariate Curve Resolution Toolbox - Estimation of the number of components
Singular Value Decomposition
EigenValues
57.4246
1.5048
0.537332
0.339201
0.27185
0.24841
0.23163
0.207684
0.20494
0.201008
0.193633
0.192417
0.184548
0.17631
0.171348
0.170478
0.163843
0.158358
0.152403
0.147282
0.145266
0.139705
0.135691
0.133853
0.130512
0.123269
EigenValues Representation
Graphical Options
SVD Normalization?
EigenVectors Representation
Selected Number Of Components:
2
Copy
Print
Cancel
OK

III

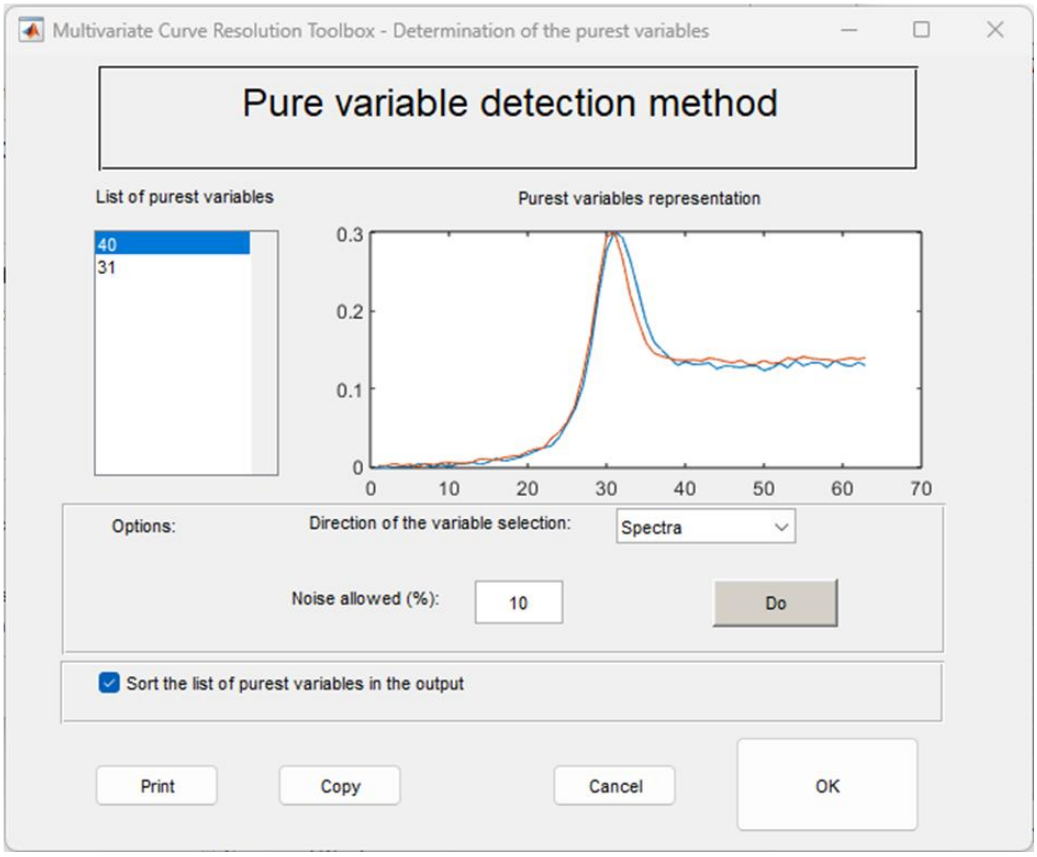
Multivariate Curve Resolution Toolbox - Determination of the purest variables
Pure variable detection method
List of purest variables
40
31
Purest variables representation
Options:
Direction of the variable selection:
Spectra
Noise allowed (%):
10
Do
Sort the list of purest variables in the output
Print
Copy
Cancel
OK

IV

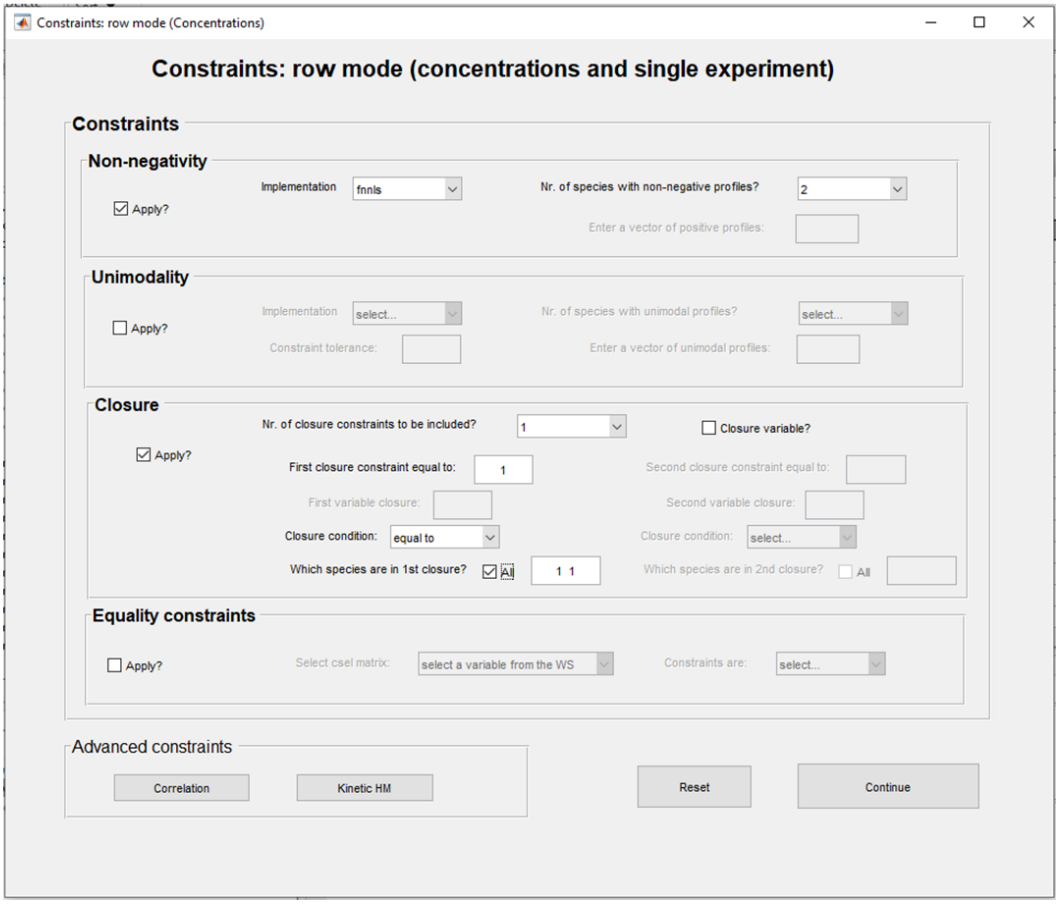
Constraints: row mode (Concentrations)
Constraints: row mode (concentrations and single experiment)
Constraints
Non-negativity
Apply?
Implementation
fnnls
Nr. of species with non-negative profiles?
2
Enter a vector of positive profiles:
Unimodality
Apply?
Implementation
select...
Nr. of species with unimodal profiles?
select...
Constraint tolerance:
Enter a vector of unimodal profiles:
Closure
Apply?
Nr. of closure constraints to be included?
1
Closure variable?
First closure constraint equal to:
1
Second closure constraint equal to:
First variable closure:
Second variable closure:
Closure condition:
equal to
Closure condition:
select...
Which species are in 1st closure?
All
1 1
Which species are in 2nd closure?
All
Equality constraints
Apply?
Select csel matrix:
select a variable from the WS
Constraints are:
select...
Advanced constraints
Correlation
Kinetic HM
Reset
Continue

V

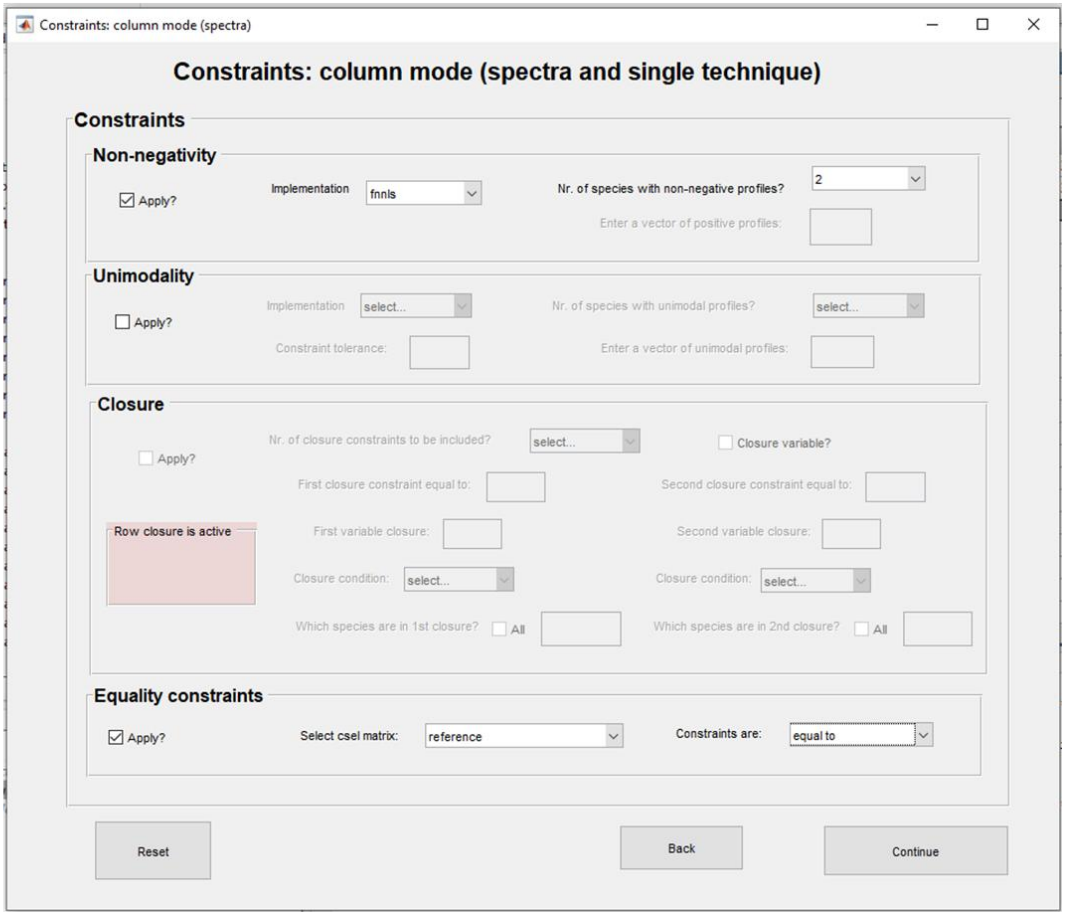
Constraints: column mode (spectra)
Constraints: column mode (spectra and single technique)
Constraints
Non-negativity
Apply?
Implementation
fnnls
Nr. of species with non-negative profiles?
2
Enter a vector of positive profiles:
Unimodality
Apply?
Implementation
select...
Nr. of species with unimodal profiles?
select...
Constraint tolerance:
Enter a vector of unimodal profiles:
Closure
Apply?
Nr. of closure constraints to be included?
select...
Closure variable?
First closure constraint equal to:
Second closure constraint equal to:
Row closure is active
First variable closure:
Second variable closure:
Closure condition:
select...
Closure condition:
select...
Which species are in 1st closure?
All
Which species are in 2nd closure?
All
Equality constraints
Apply?
Select csel matrix:
reference
Constraints are:
equal to
Reset
Back
Continue

VI

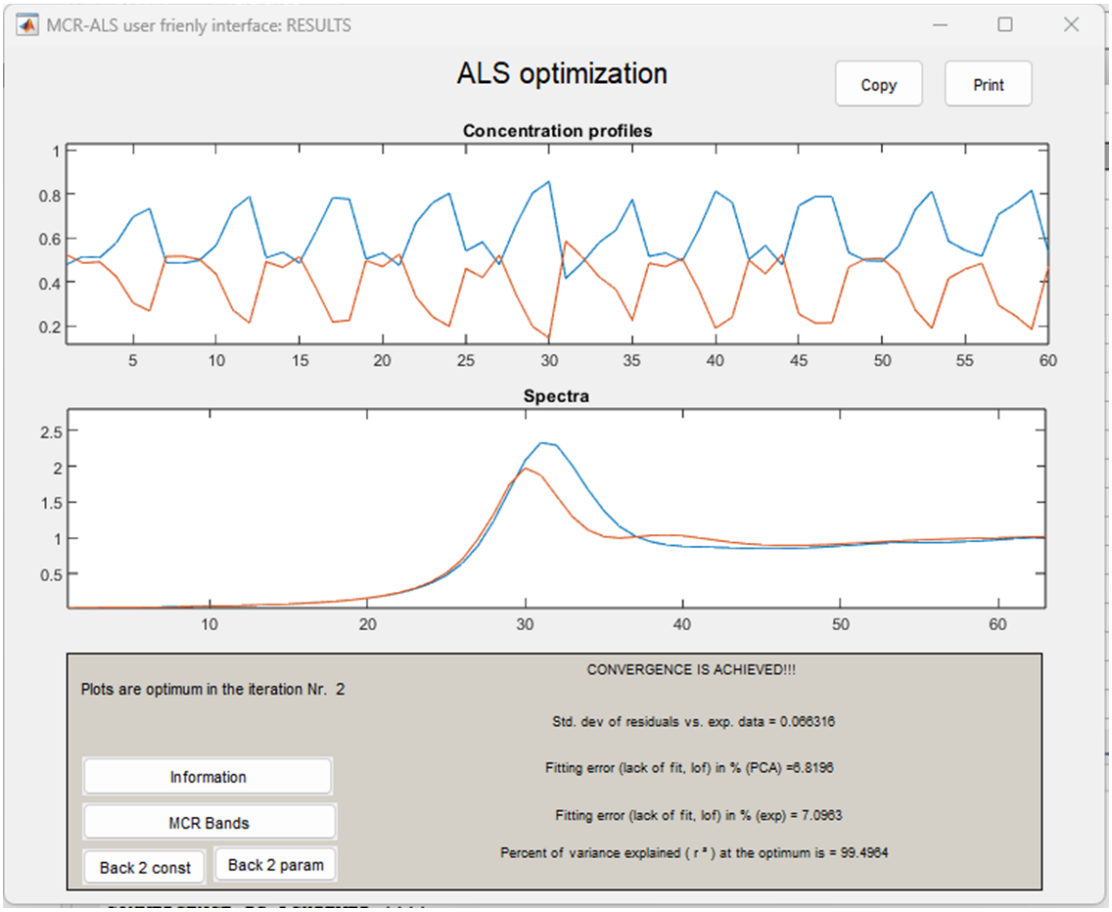

Figure S1.7. Example MCR-ALS analysis steps (**I** – **VI**) for the Ir L3 edge XANES spectra of the Pt_3Ir-colloidal NPs recorded during the 3 s potential jump experiment using the MCR-ALS GUI 2.0 MATLAB script[202].

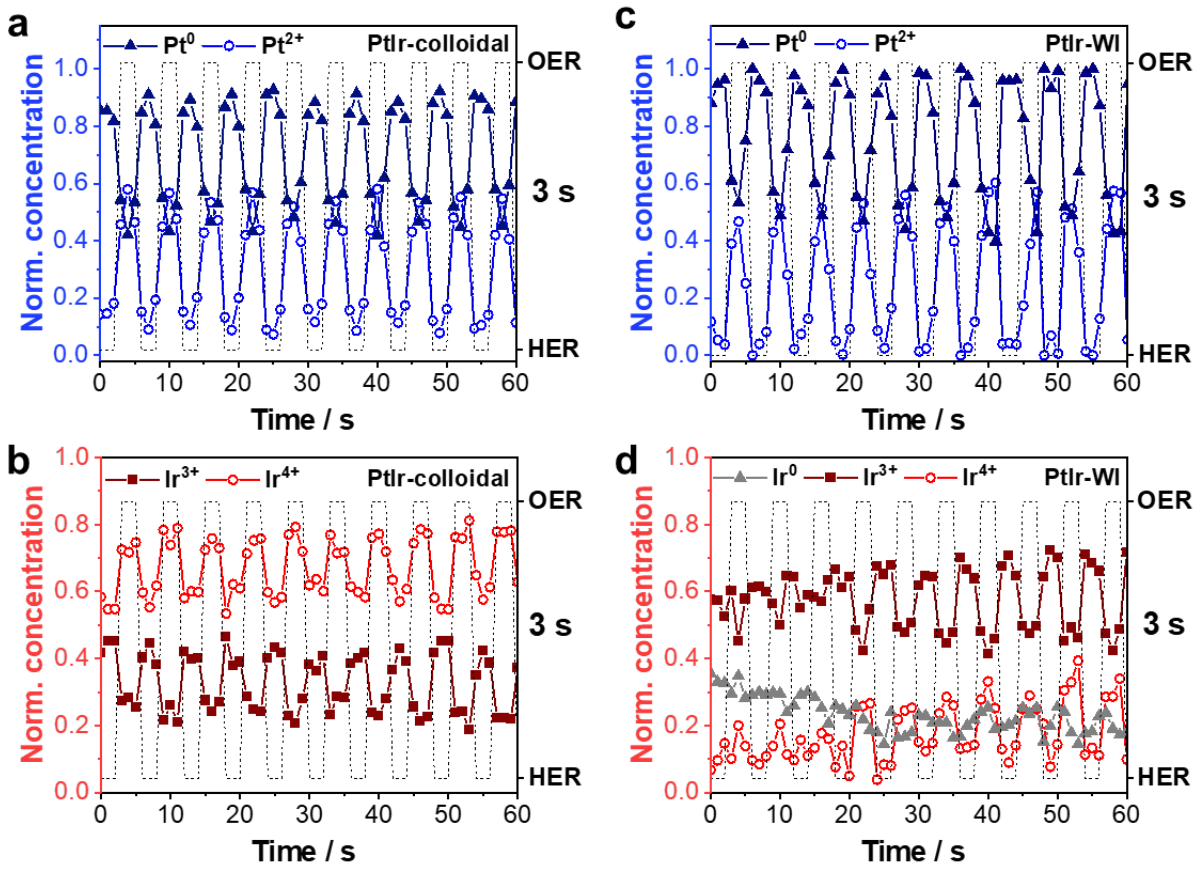

Figure S1.8. Normalized Pt^0 and Pt^{2+} (**top**) and Ir^0, Ir^{3+} and Ir^{4+} (**bottom**) species concentrations for the PtIr-colloidal (**a**,**b**) and PtIr-WI (**c**,**d**) NPs during the 3 s potential jump experiments for 60 s in argon-saturated 0.1 M $HClO_4$. One Pt or Ir L3 edge XANES spectrum recorded every second was used for the analysis. The black dashed lines show the holding times of the potential jumps between HER (– 0.02 V_{RHE}) and OER (+ 1.55 V_{RHE}).

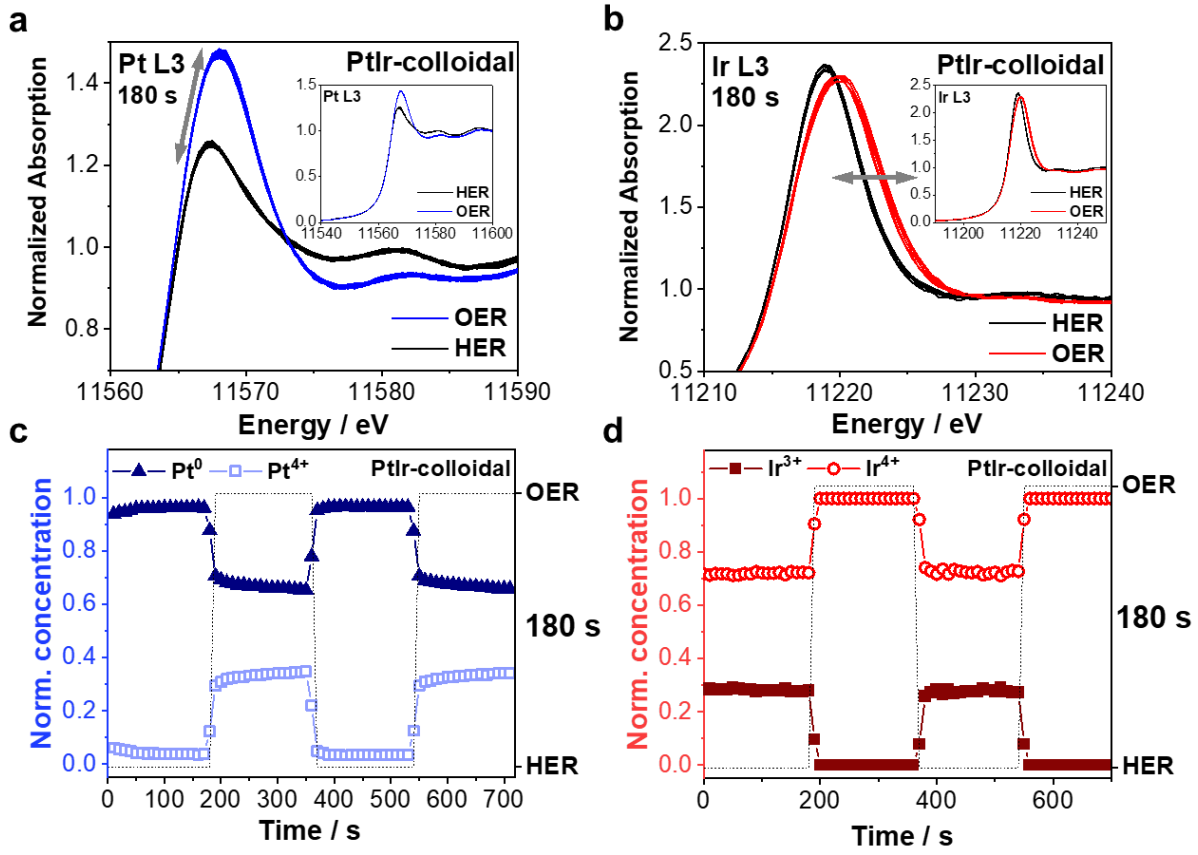

Figure S1.9. *Operando* Quick-XANES potential jump experiments for 180 s with PtIr-colloidal NPs. Pt (**a**) and Ir (**b**) L3 edge XANES spectra were collected every second and subsequently averaged over 180 s. XANES spectra collected during HER are displayed in black and during OER in blue or red, respectively. The insets display the same XANES spectra with a longer energy range. The bottom panel shows the normalized Pt^0 and Pt^{2+} (c) as well as Ir^{3+} and Ir^{4+} (**d**) concentrations obtained by the MCR-ALS analysis in dependence of the time. For the analysis ten XANES spectra were averaged resulting in one point every 10 s. The black dashed lines show the holding times of the potential jumps between HER (– 0.02 V_{RHE}) and OER (+ 1.55 V_{RHE}) in argon-saturated 0.1 M $HClO_4$.

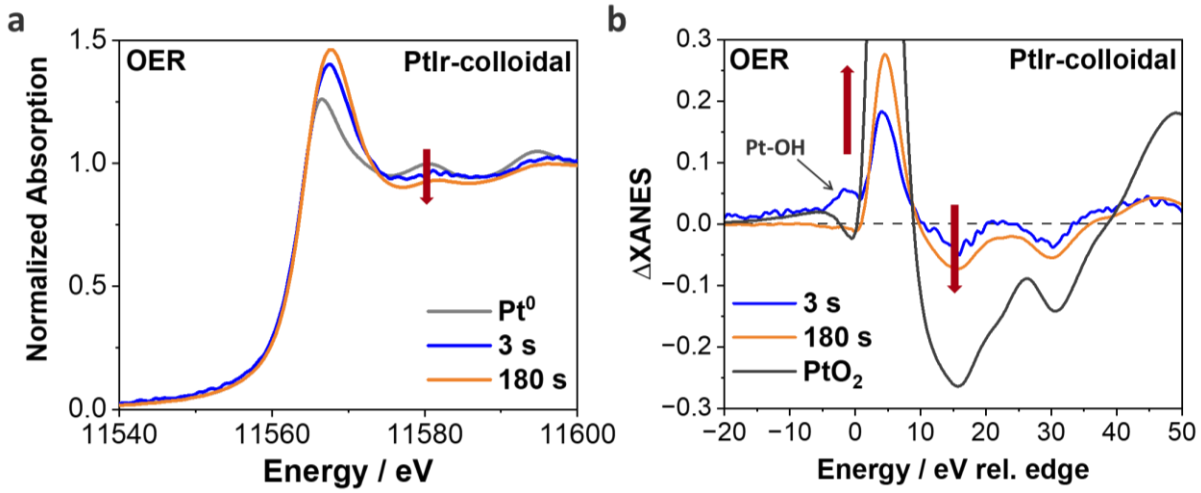

Figure S1.10. Pt L3 edge XANES (**a**) and ΔXANES (**b**) data of the PtIr-colloidal NPs recorded at + 1.55 V_{RHE} with holding times of 3 s (blue) and 180 s (orange) in argon-saturated 0.1 M $HClO_4$. The ΔXANES spectrum of PtO_2 (dark grey) is plotted as a reference.

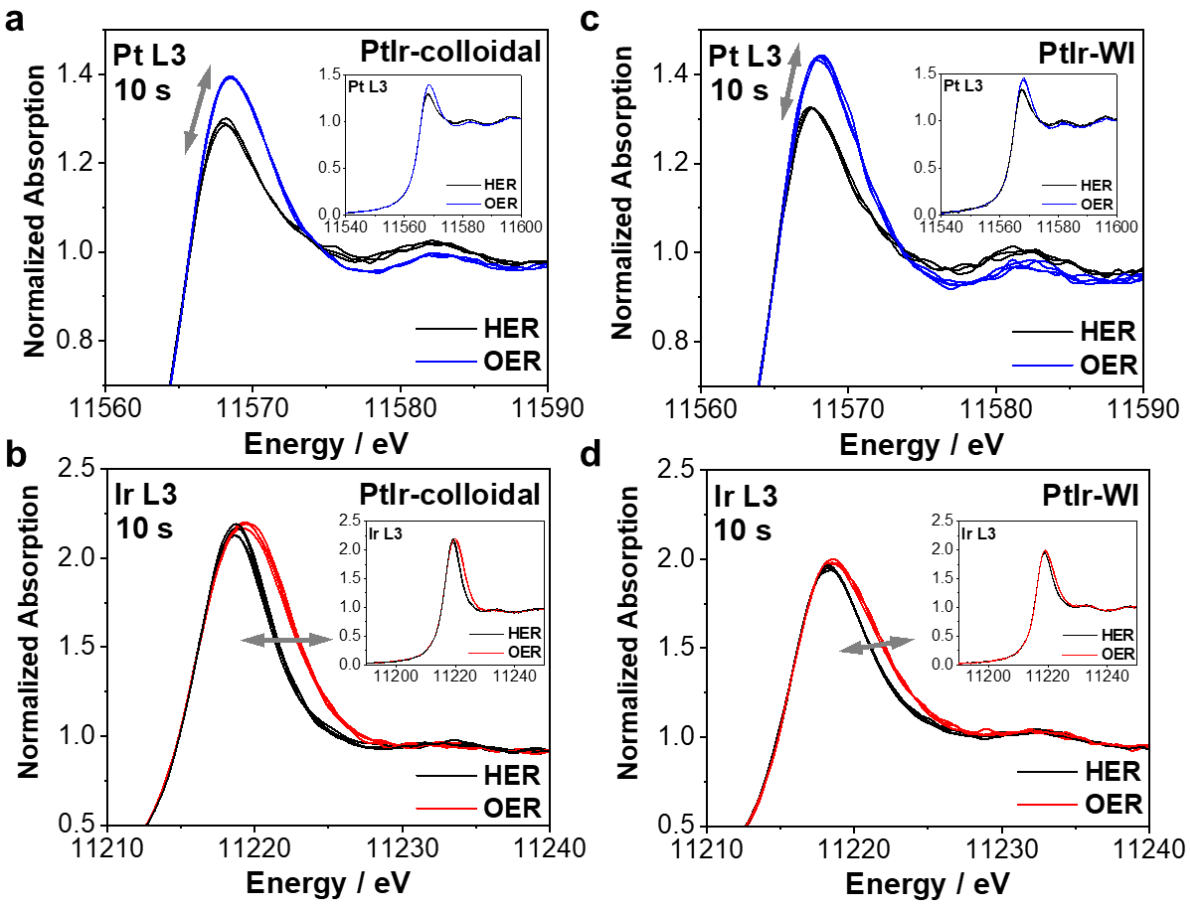

Figure S1.11. *Operando* Quick-XANES spectra of the PtIr-colloidal (**a,c**) and PtIr-WI (**b,d**) NPs recorded at the Pt and Ir L3 edges. Spectra were collected every second and subsequently averaged over 10 s during the potential jump experiments between HER (– 0.02 V_{RHE}) and OER (+ 1.55 V_{RHE}) with holding times of 10 s in argon-saturated 0.1 M $HClO_4$. Spectra collected during HER are plotted in black and during OER in blue or red for Pt or Ir, respectively. The insets show the same XANES spectra with a longer energy range.

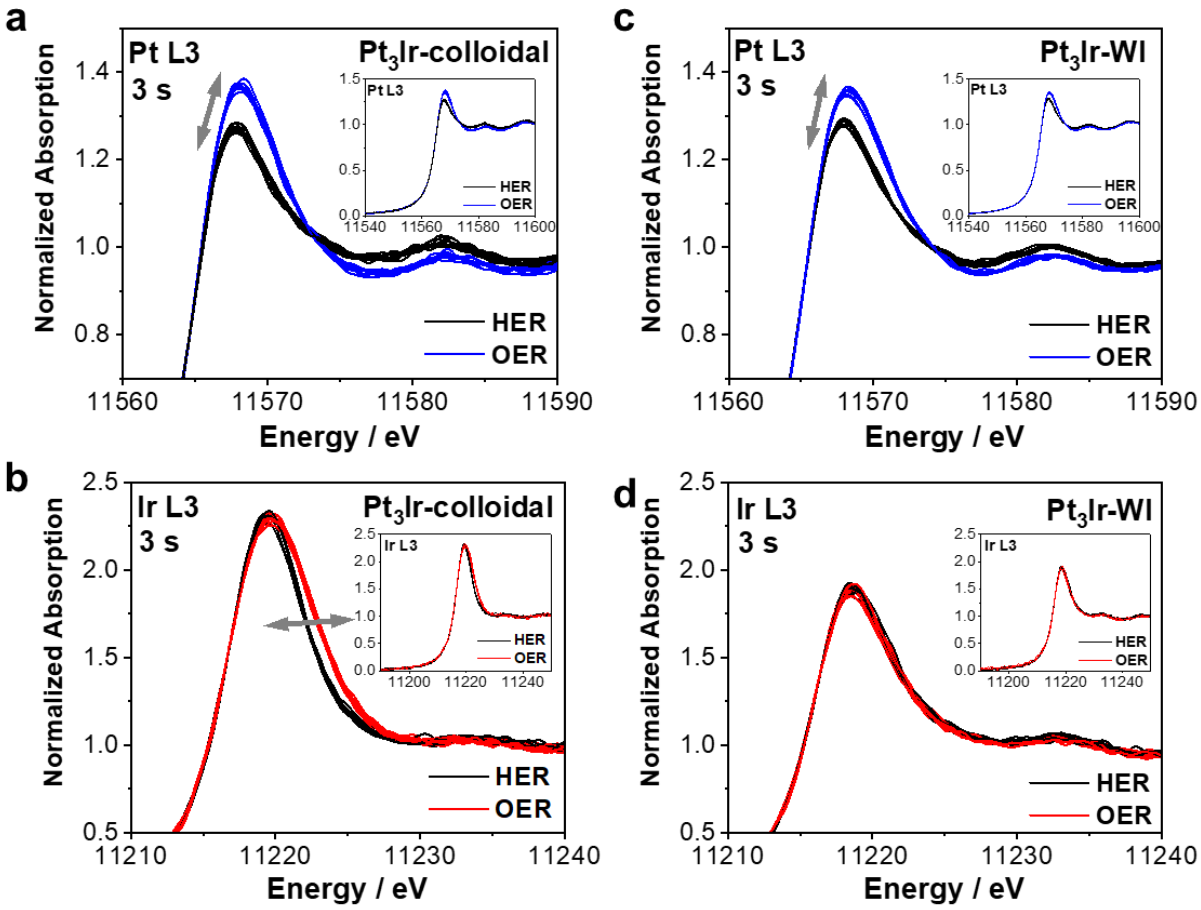

Figure S1.12. *Operando* Quick-XANES spectra of the Pt_3Ir-colloidal (**a**,**c**) and Pt_3Ir-WI (**b**,**d**) NPs recorded at the Pt and Ir L3 edges. Spectra were collected every second and subsequently averaged over 3 s during the potential jump experiments between HER (– 0.02 V_{RHE}) and OER (+ 1.55 V_{RHE}) with holding times of 3 s in argon saturated 0.1 M $HClO_4$. Spectra collected during HER are plotted in black and during OER in blue or red for Pt or Ir, respectively. The insets show the same XANES spectra with a longer energy range.

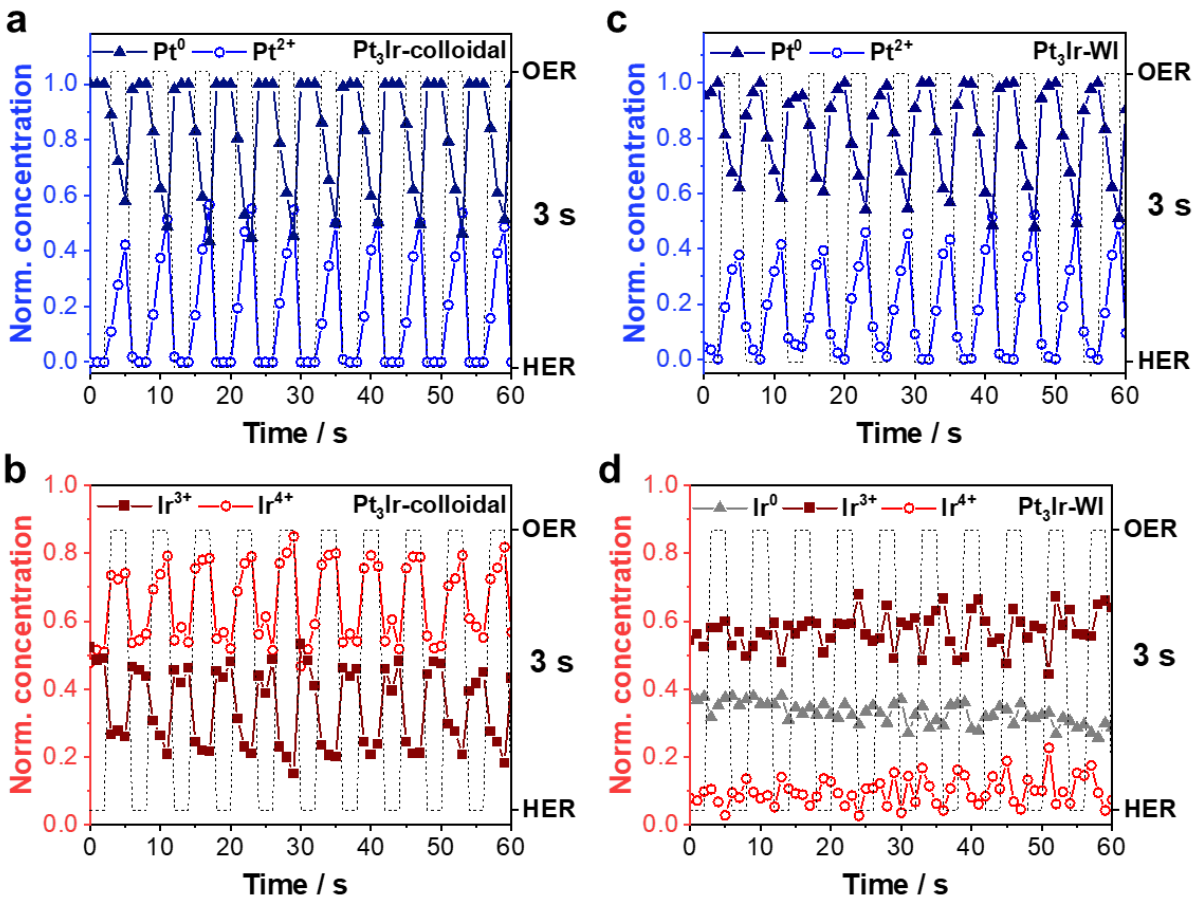

Figure S1.13. Normalized Pt^0 and Pt^{2+} (**top**) and Ir^0, Ir^{3+} and Ir^{4+} (**bottom**) species concentrations for the Pt_3Ir-colloidal (**a**,**b**) and Pt_3Ir-WI (**c**,**d**) NPs during the 3 s potential jump experiments for 60 s in Ar-saturated 0.1 M $HClO_4$. One Pt or Ir L3 edge XANES spectrum recorded every second was used for the analysis. The black dashed lines show the holding times of the potential jumps between HER (– 0.02 V_{RHE}) and OER (+ 1.55 V_{RHE}).

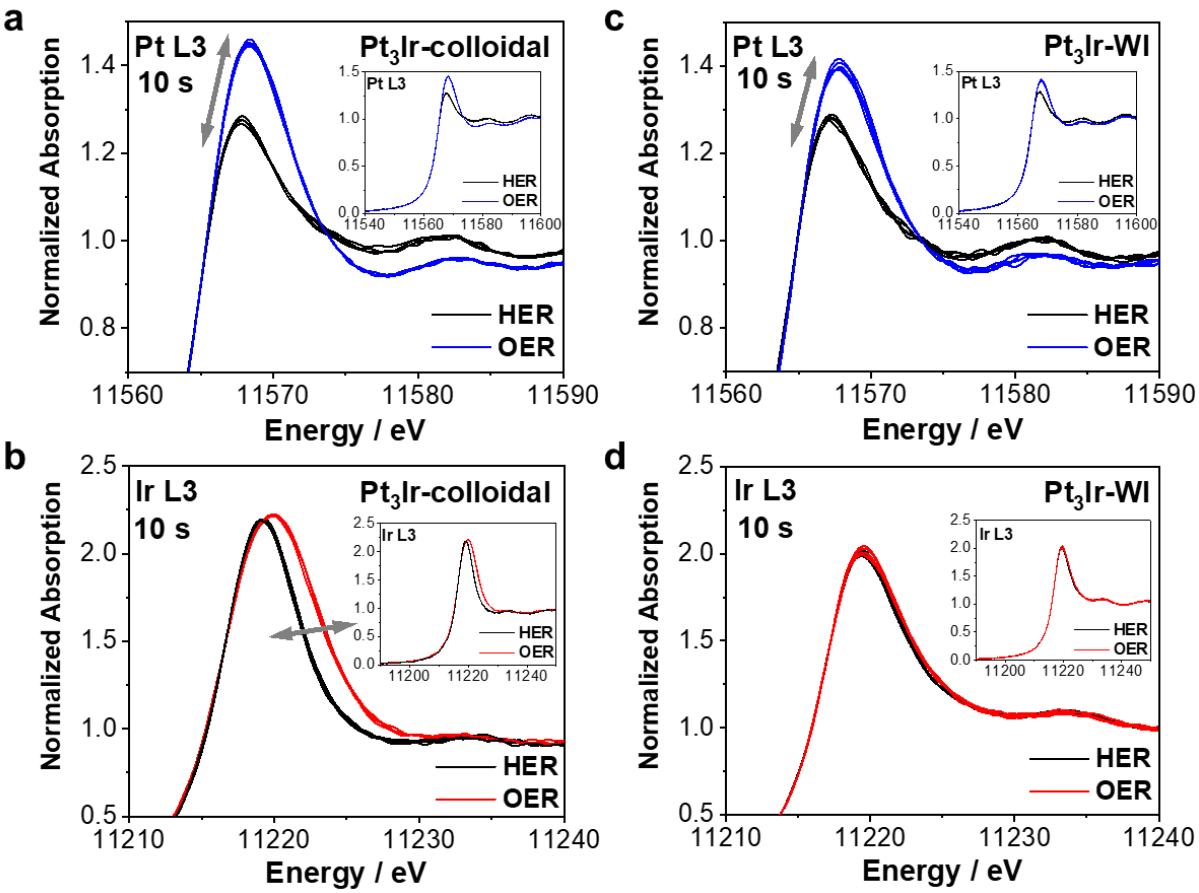

Figure S1.14. *Operando* Quick-XANES spectra of the Pt_3Ir-colloidal (**a**,**c**) and Pt_3Ir-WI (**b**,**d**) NPs recorded at the Pt and Ir L3 edges. Spectra were collected every second and subsequently averaged over 10 s during the potential jump experiments between HER (– 0.02 V_{RHE}) and OER (+ 1.55 V_{RHE}) with holding times of 10 s in Ar-saturated 0.1 M $HClO_4$. Spectra collected during HER are plotted in black and during OER in blue or red for Pt or Ir, respectively. The insets show the same XANES spectra with a longer energy range.

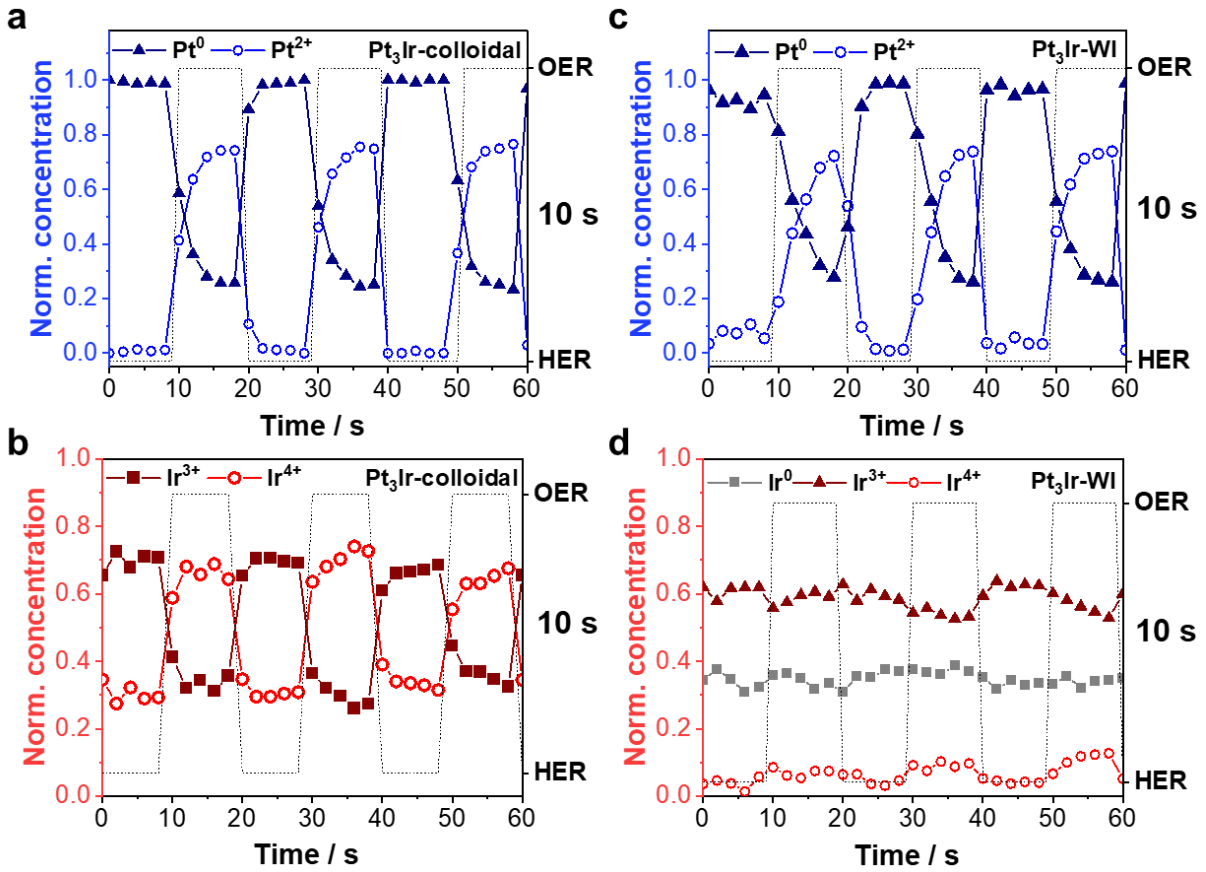

Figure S1.15. Normalized Pt^0 and Pt^{2+} (**top**) and Ir^0, Ir^{3+} and Ir^{4+} (**bottom**) concentrations obtained by the MCR-ALS analysis of the Pt and Ir L3 edge XANES spectra collected from (**a**, **b**) Pt_3Ir-colloidal NPs and (**c**, **d**) Pt_3Ir-WI NPs during the potential jump experiments with 10 s in Ar-saturated 0.1 M $HClO_4$. For the analysis two XANES spectra were averaged resulting in one point every 2 s. The black dashed lines show the holding times of the potential jumps between HER (– 0.02 V_{RHE}) and OER (+ 1.55 V_{RHE}).

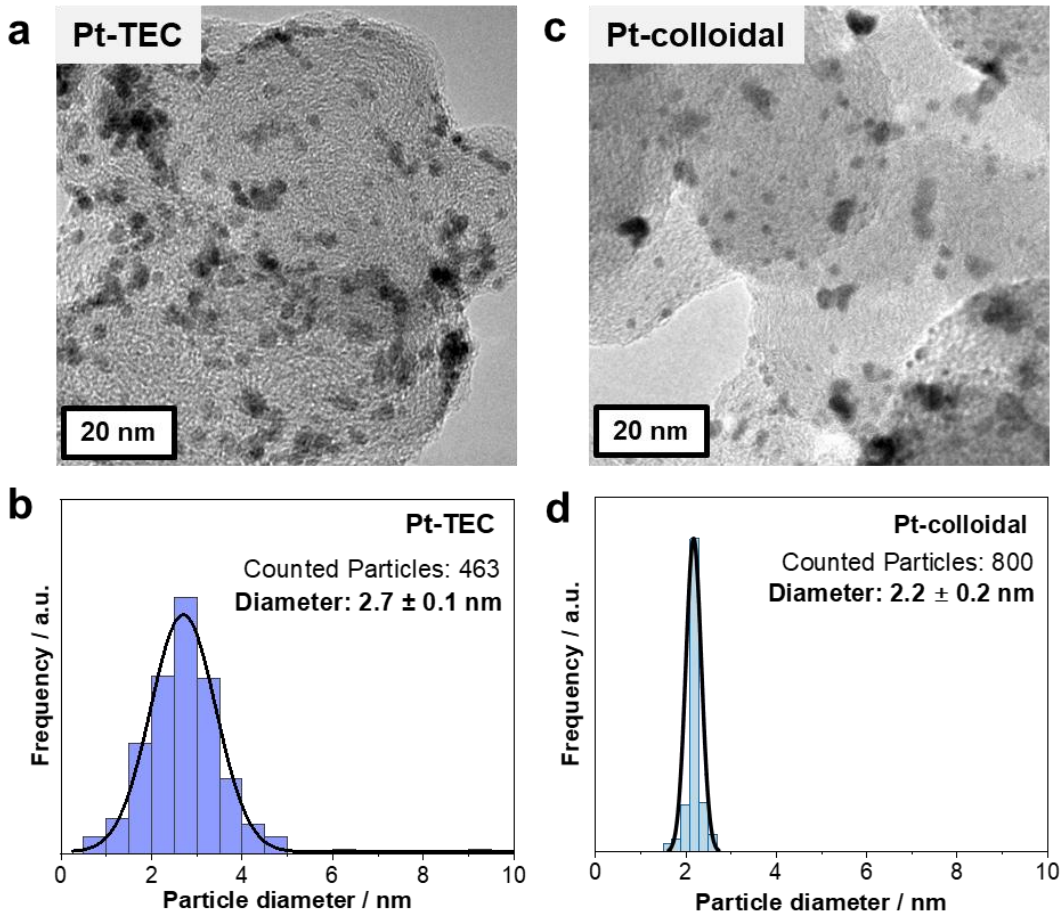

Figure S1.16. TEM micrographs (**top panel**) and respective particle size distributions (**bottom panel**) of the Pt-TEC (**a**,**b**) and Pt-colloidal (**c**,**d**) NPs supported on carbon.

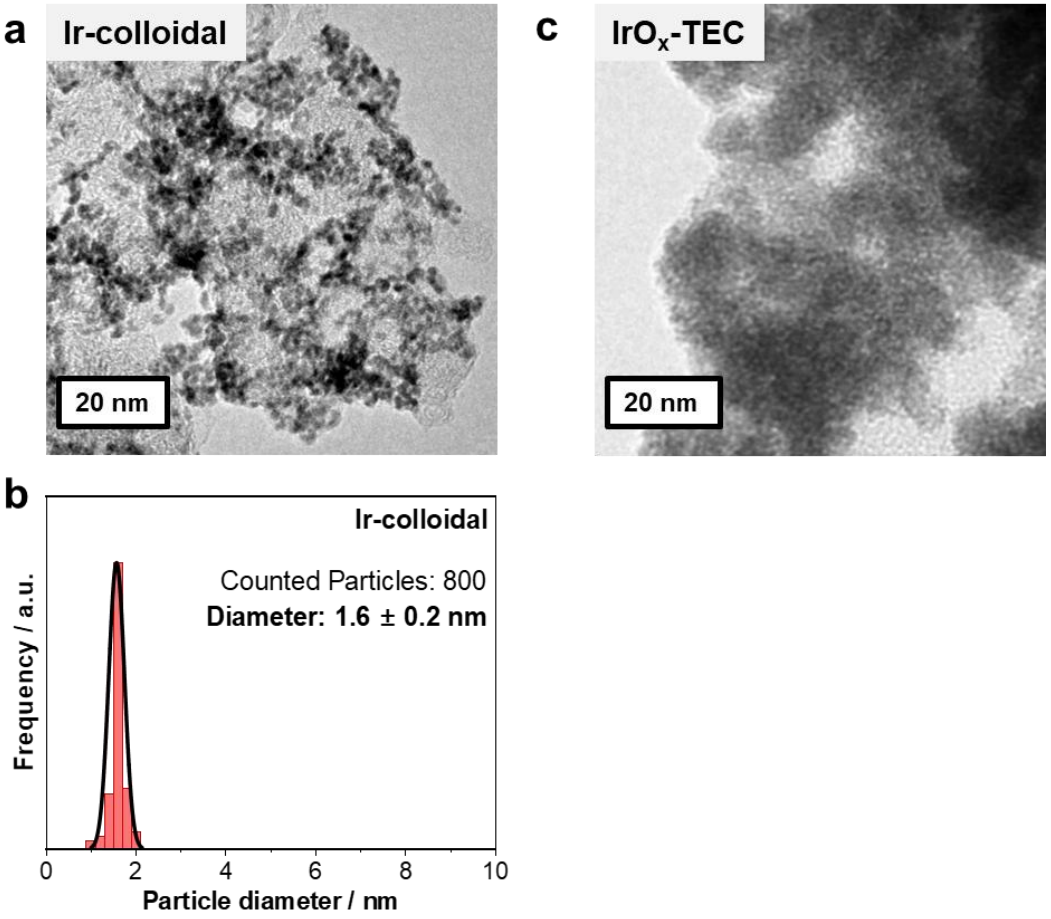

Figure S1.17. TEM micrographs (**top panel**) and respective particle size distributions (**bottom panel**) of the Ir-colloidal (**a**,**b**) and commercial IrO_x-TEC (**c**) NPs supported on carbon.

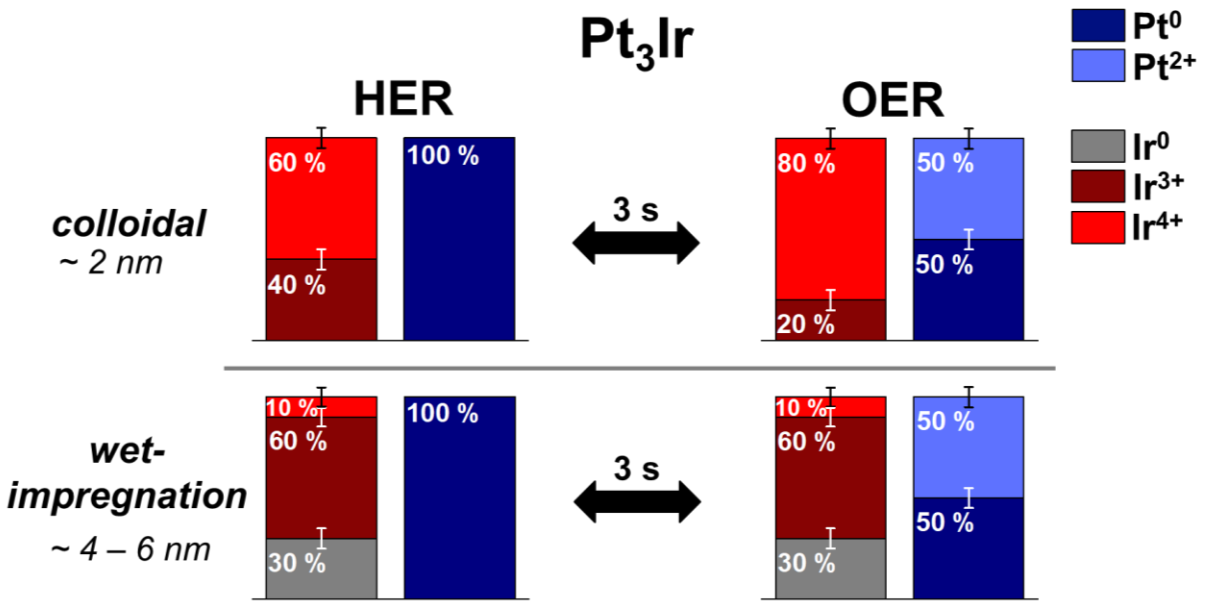

Figure S1.18. Bifunctionality model for the Pt_3Ir NPs prepared by the colloidal and wet-impregnation (WI) synthesis routes. Proportion of Ir^0, Ir^{3+} and Ir^{4+} species as well as Pt^0 and Pt^{2+} species present during HER (– 0.02 V_{RHE}) and OER (+ 1.55 V_{RHE}) are schematically represented by the bar diagrams.

10.2. Supporting Information Chapter 4.2.

Experimental

Thin film preparation

Bimetallic and monometallic thin films were deposited without heating using two magnetrons with planar targets of Ir (MaTeck, 99.95 %) and Pt (MaTeck, 99.95 %) by physical vapor deposition (PVD) in a Leybold Univex 300 instrument. The layers of the bimetallic films were deposited with Pt:Ir ratios 1:1 and 3:1 using alternating sputtering onto a gas diffusion layer (GDL, Freudenberg, H23C6), as described previously by Sievers et al.[276,277] The alternating process was repeated 50 times resulting in a total loading of 0.4 mg_{metal} cm^{-2}_{geo}.

Electrochemical measurements of the Pt-Ir thin films in an impinging jet flow cell

Electrochemical measurements were conducted in a custom-made impinging jet flow cell setup[241] equipped with a potentiostat (Biologic, VSP-300) and a syringe pump (KD Scientific, Legato 210). The three-electrode arrangement consisted of Pt-Ir thin films as a working electrode, gold mesh as a counter electrode and mercury-mercury sulfate reference electrode (ALS-Japan, RE-2CP). The reference electrode was calibrated against a reversible hydrogen electrode using a poly-Pt electrode in H_2-saturated 0.1 M $HClO_4$. The Pt-Ir thin films were glued onto a polished glassy carbon (GC) substrate using a conductive colloidal gold paste (Plano GmbH, #16022). All potentials are referred to the reversible hydrogen electrode (RHE) and were corrected for the iR-drop. In a pre-conditioning step, all catalysts were electrochemically treated by 100 potential cycles between 0.05 V_{RHE} and 1.40 V_{RHE} with a scan rate of 100 mV s^{-1} in argon-saturated 0.1 M $HClO_4$. Afterwards, five cyclic voltammetry (CV) profiles were recorded between 0.05 and 1.40 V_{RHE} at 50 mV s^{-1} to determine the electrochemically active surface area (ECSA) derived from the hydrogen underpotential deposition (H_{UPD}). The H_{UPD} was obtained from integrating the hydrogen ad-/desorption region, correcting it by the double layer current and assuming pseudo-capacities of 210 µC cm^{-2} for poly-crystalline Pt[273], 179 µC cm^{-2} for poly-crystalline Ir[274], 195 µC cm^{-2} for Pt:Ir ratio of 1:1 and 202 µC cm^{-2} for Pt:Ir ratio of 3:1, respectively. In addition, the ORR and OER polarization curves were measured in one linear sweep voltammogram (LSV) from 0.05 to 1.60 V_{RHE} at a scan rate of 1 mV s^{-1} and a flow rate of 1 mL min^{-1} in O_2-saturated 0.1 M $HClO_4$.

DFT

All theoretical calculations were performed with the ORCA software package.[278] The B3LYP hybrid functional was employed for the geometry optimization of the clusters.[279] The geometry optimization convergence threshold was set to $5 \cdot 10^{-6}$ E_H for the energy criterium and 10^{-4} E_H/a_0

for the gradient. D3-Grimme dispersion correction with zero damping and ZORA relativistic correction were used to model all electrons explicitly.[280,281] The lowest possible spin state was assumed in all calculations. Raman spectra were calculated using numerical frequency calculations.

Table S2.1. Experimental acquisition parameters for survey and high-resolution XPS measurements.

spectrum	energy range / eV	step size / eV	pass energy / eV	dwell time / ms	no. of scans
Survey	- 10 – 1350	1	100	10	5
Pt & Ir4f	55 – 85	0.02	10	50	20
O 1s	525 – 540	0.02	10	50	10
C 1s	279 – 298	0.02	10	50	5

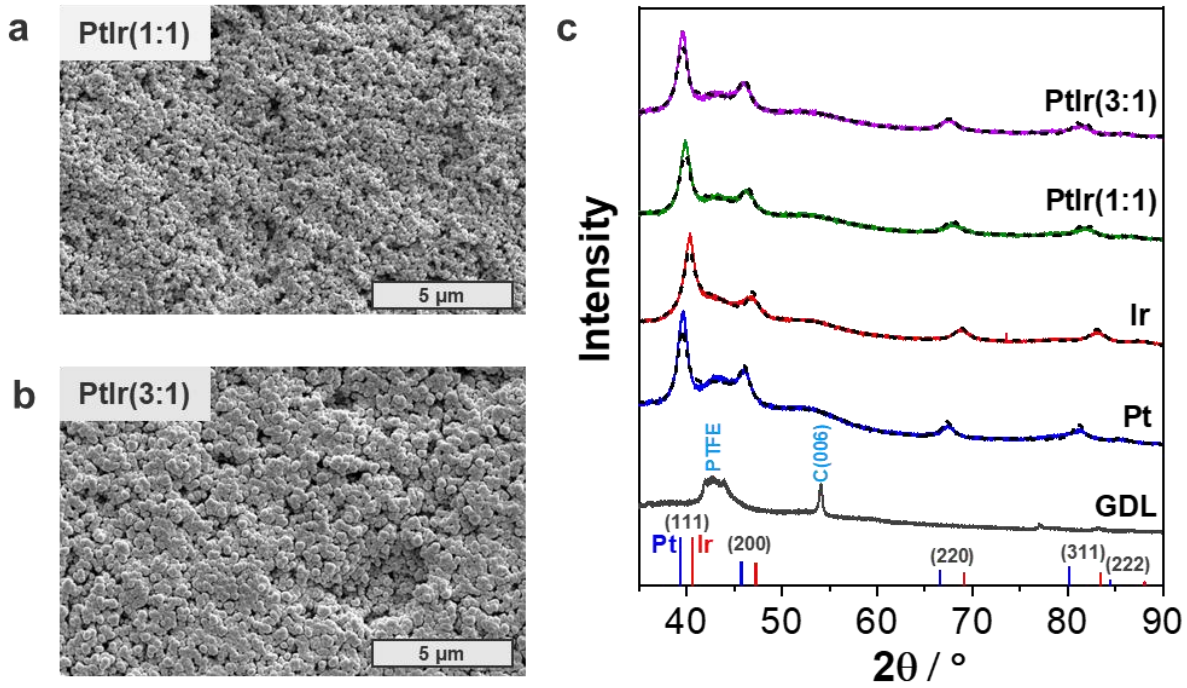

Fig. S2.1. (**a** and **b**) Top-view low magnification SEM micrographs of the Pt-Ir thin films with atomic Pt:Ir ratios of 1:1 and 3:1. (**c**) XRD profiles of the sputtered PtIr(1:1) (green), PtIr(3:1) (purple), Ir (red) and Pt (blue) thin films with the best fits (black dashed lines) obtained from the quantitative Rietveld refinement analysis. Note, that the peaks at 2θ values of around 42 – 44° and ~54° are ascribed to the amorphous PTFE and C(006) graphite of the GDL substrate, respectively. The pattern references of face-centered cubic (fcc) Pt (#9008480, blue) and Ir (#9008470, red) were taken from the crystal open database (COD).[205–207]

Table S2.2. Thin film composition obtained by µ-XRF with three ~20 µm spot measurements. The characteristic L_α lines of Pt and Ir were used for quantitative analysis.

sample	Pt content / at.%	Ir content/ at.%
PtIr(1:1)	47 ± 2	53 ± 2
PtIr(3:1)	75 ± 1	25 ± 1
Pt	100	0
Ir	0	100

Table S2.3. Space group, lattice parameter, crystallite size, phase quantity and composition via Vegard's law determined by quantitative Rietveld refinement analysis of the XRD profiles for the Pt-Ir thin films displayed in **Figure S2.1c**. The weighted profile R-factor (R_{wp}) represents the discrepancy index between the calculated and measured data.

sample	phase	space group	lattice parameter / Å	crystallite size / nm	Quantity / wt.%	composition via Vegard's law	R_{wp}
PtIr(1:1)	PtIr	$Fm\bar{3}m$	3.919 ± 0.001	6.1 ± 0.2	51 ± 1	$Pt_{95}Ir_{05}$	4.80
	PtIr	$Fm\bar{3}m$	3.872 ± 0.001	7.2 ± 0.2	49 ± 1	$Pt_{40}Ir_{60}$	
PtIr(3:1)	PtIr	$Fm\bar{3}m$	3.923 ± 0.001	6.0 ± 0.1	59 ± 1	$Pt_{100}Ir_{0}$	5.16
	PtIr	$Fm\bar{3}m$	3.879 ± 0.001	8.2 ± 0.3	41 ± 1	$Pt_{52}Ir_{48}$	
Pt	Pt	$Fm\bar{3}m$	3.923 ± 0.001	5.1 ± 0.1	-	Pt_{100}	5.22
Ir	Ir	$Fm\bar{3}m$	3.841 ± 0.001	4.5 ± 0.1	-	Ir_{100}	4.70

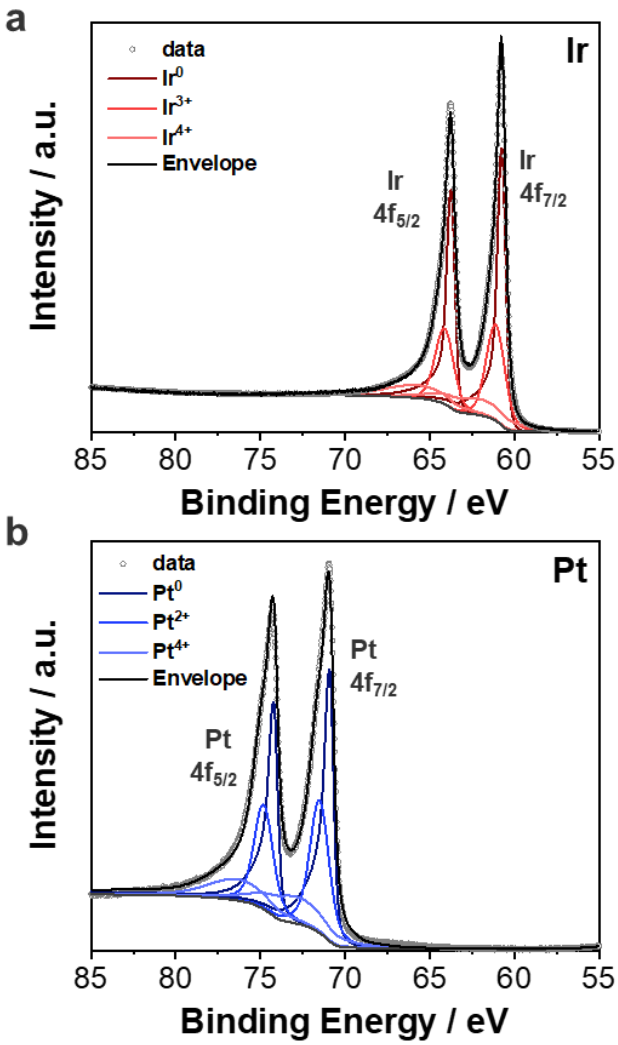

Figure S2.2. Ex-situ high-resolution Ir and Pt 4f XPS spectra of the monometallic (**a**) Ir and (**b**) Pt thin films. Light grey circles represent the measured data, the envelope is shown in black. The Ir^0, Ir^{3+} and Ir^{4+} species are displayed in red, while Pt^0, Pt^{2+} and Pt^{4+} species are plotted in blue.

Table S2.4. Underpotential deposition of hydrogen (H_{UPD}) as well as ORR and OER specific activities (SA) of the Pt, PtIr(1:1), PtIr(3:1) and Ir thin films with a total metal loading of 0.4 mg_{metal} cm^{-2}_{geo}. The H_{UPD} was obtained from cyclic voltammetry measurements shown in **Figure S2.3**. The roughness factor (RF) was obtained by dividing the H_{UPD} by the geometric surface area (0.196 cm^2). SA values towards ORR were determined at 0.90 $V_{RHE, iR\text{-}free}$ and towards OER at 1.50 $V_{RHE, iR\text{-}free}$.

Sample	H_{UPD} / cm^2	Roughness factor (RF)	SA_{ORR} / µA cm^{-2}_{HUP} at 0.90 $V_{RHE, iR\text{-}free}$	SA_{OER} / µA cm^{-2}_{HUP} at 1.50 $V_{RHE, iR\text{-}free}$
Pt	3.8 ± 0.2	19	54	5
PtIr(3:1)	7.6 ± 0.4	39	88	9
PtIr(1:1)	11.0 ± 0.2	56	57	34
Ir	5.0 ± 0.6	26	3	286

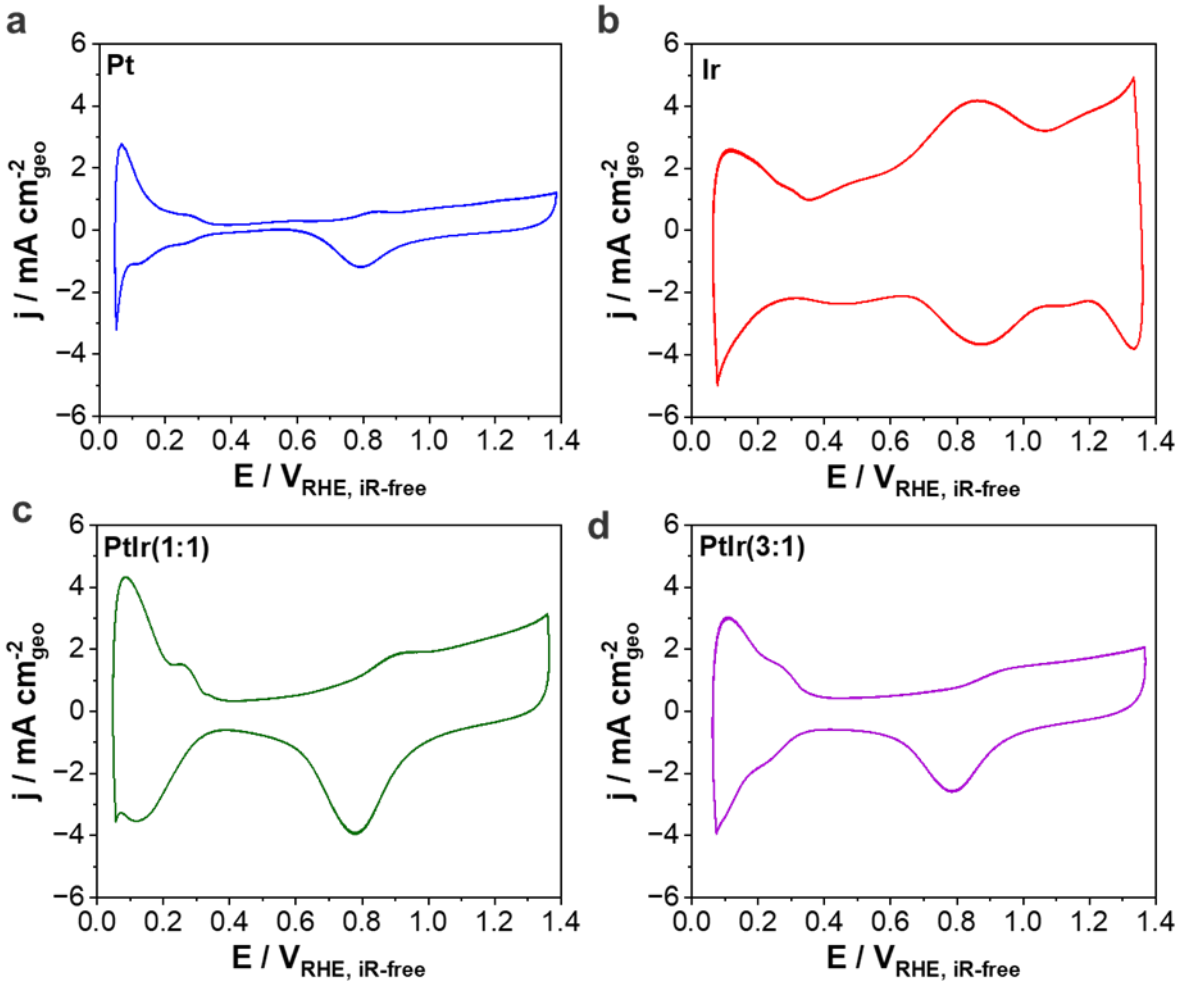

Figure S2.3. Cyclic voltammetry (CV) profiles of the (**a**) Pt, (**b**) Ir, (**c**) PtIr(1:1) and (**d**) PtIr(3:1) thin films (total metal loading of 0.4 mg_{metal} cm^{-2}_{geo}) recorded at 50 mV s^{-1} using an impinging jet flow cell static Ar-saturated 0.1 M $HClO_4$ solution electrolyte. The H_{UPD} region between 0.06 and 0.4 $V_{RHE,iR\text{-}free}$ is observed for all thin films.

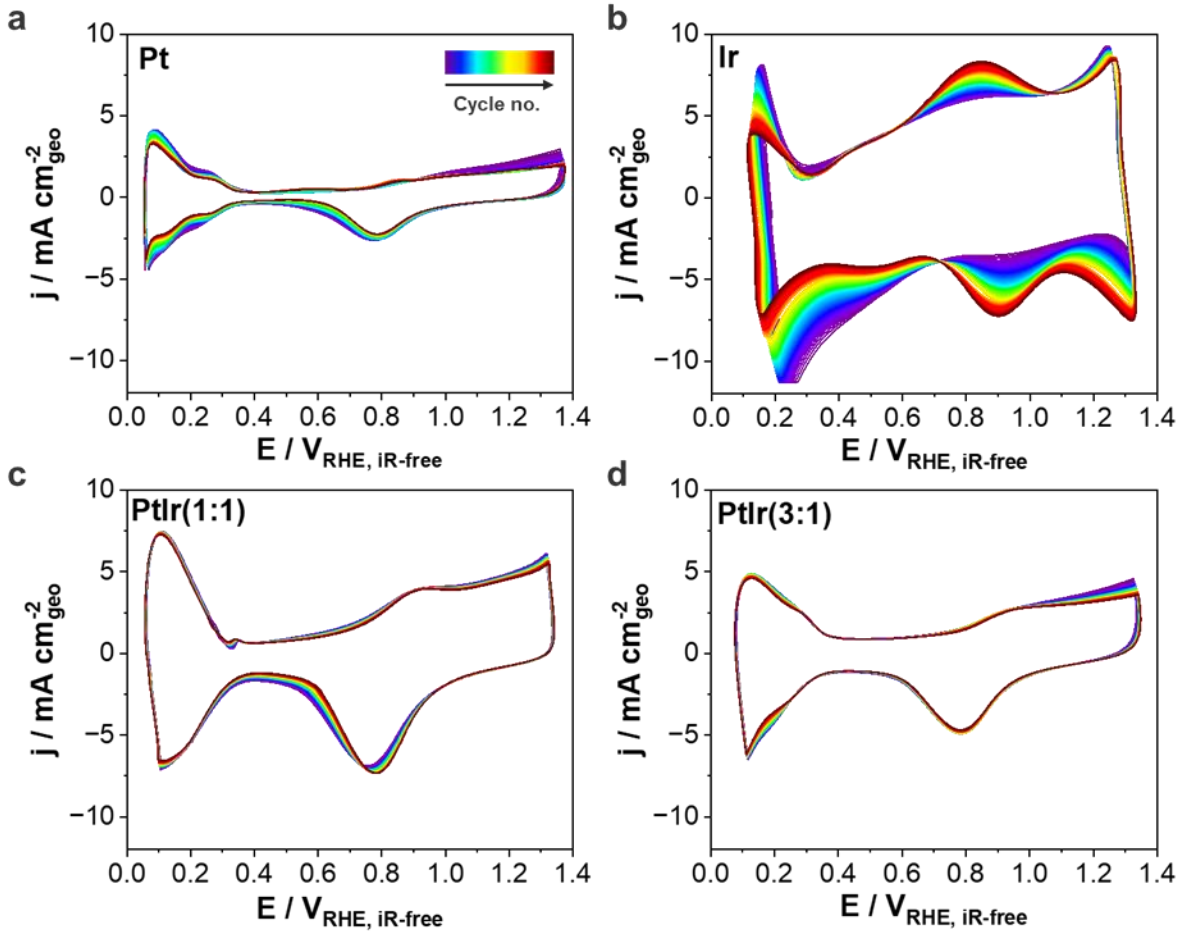

Figure S2.4. Pre-conditioning protocol with 100 cyclic voltammetry (CV) profiles at 100 mV s^{-1} using an impinging jet flow cell in static Ar-saturated 0.1 M $HClO_4$ electrolyte. Evolution of the CV profiles of (**a**) Pt, (**b**) Ir, (**c**) PtIr(1:1) and (**d**) PtIr(3:1) thin films.

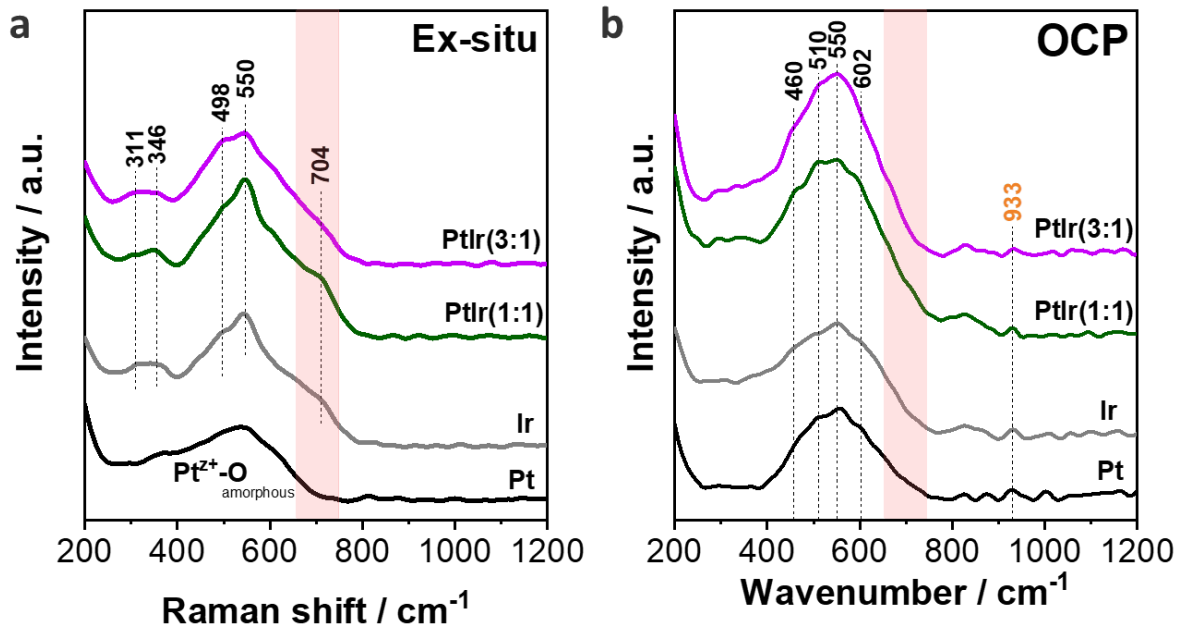

Figure S2.5. Raman spectra of PtIr(1:1) (green), PtIr(3:1) (pink), Pt (blue) and Ir (red) thin films obtained (**a**) ex-situ and (**b**) in-situ at OCP in 0.1 M $HClO_4$. The peak labelled at 933 cm^{-1} is assigned to adsorbed ClO_4^- anion (**Figure S2.6**). The red region shows the disappearance of the Raman band at 704 cm^{-1} with exposure to the electrolyte. Peak assignments are summarized in **Table S2.5**.

Table S2.5. Raman peaks and corresponding modes of vibration for both Pt-Ir, Pt and Ir thin-films ex-situ and in-situ (at OCP) measurements as shown in **Figure S2.5**.

Raman shift / cm^{-1}	**Mode of vibration**	**Ref.**
311	Ir-O bend	78
346	Ir-O bend	78
460	ClO_4^- adsorbed on Ir surface	246,282
498	Ir^{4+}-O stretch	78
550	IrO_2 E_g)	78,242,243
602	Ir^{3+}-OH-Ir^{4+} stretch	78
704	IrO_2 (B_{2g})	78,242,243
933	ClO_4^-	83,109,110,245

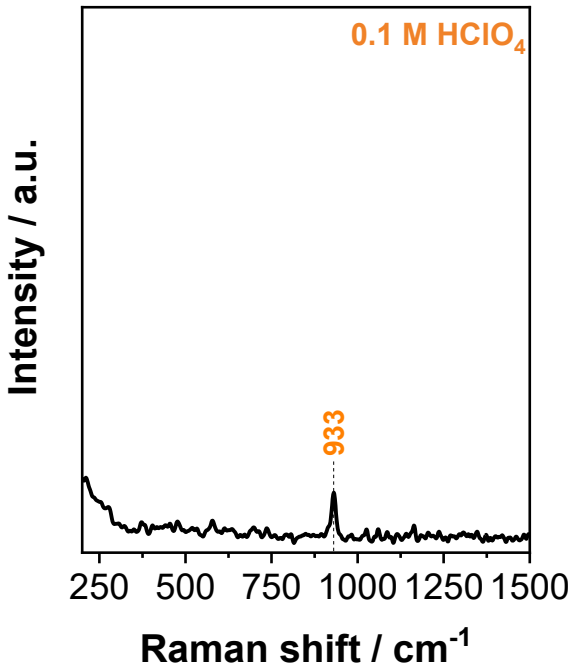

Figure S2.6. Raman spectrum collected of 0.1 M $HClO_4$ solution. The peak at 933 cm^{-1} is assigned to ClO_4^- which is in agreement with the literature.[83,109,245,246]

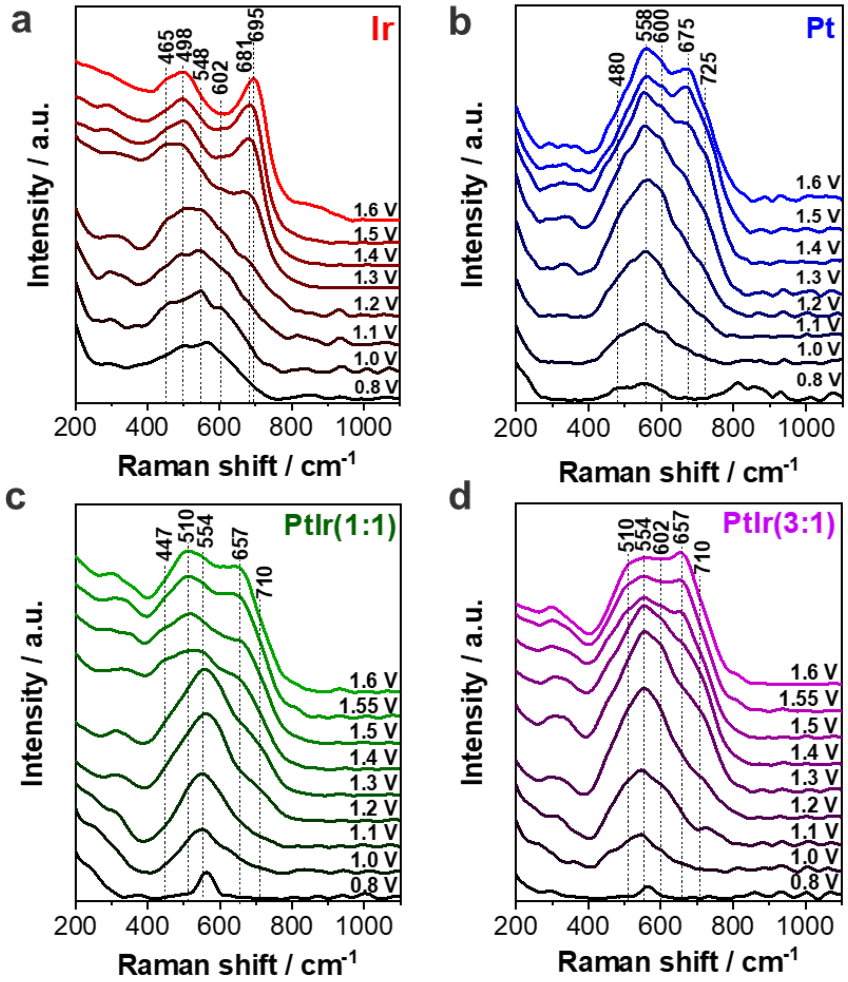

Figure S2.7. Detailed evolution of in-situ Raman spectra collected from (**a**) Ir, (**b**) Pt, (**c**) PtIr(1:1) and (**d**) PtIr(3:1) thin films in the potential range of 0.8 – 1.6 V_{RHE} in 0.1 M $HClO_4$. Each potential was held for around 4 minutes while Raman spectra were collected every 5 s and subsequently averaged. Peak assignments are shown in **Tables 4 – 7**.

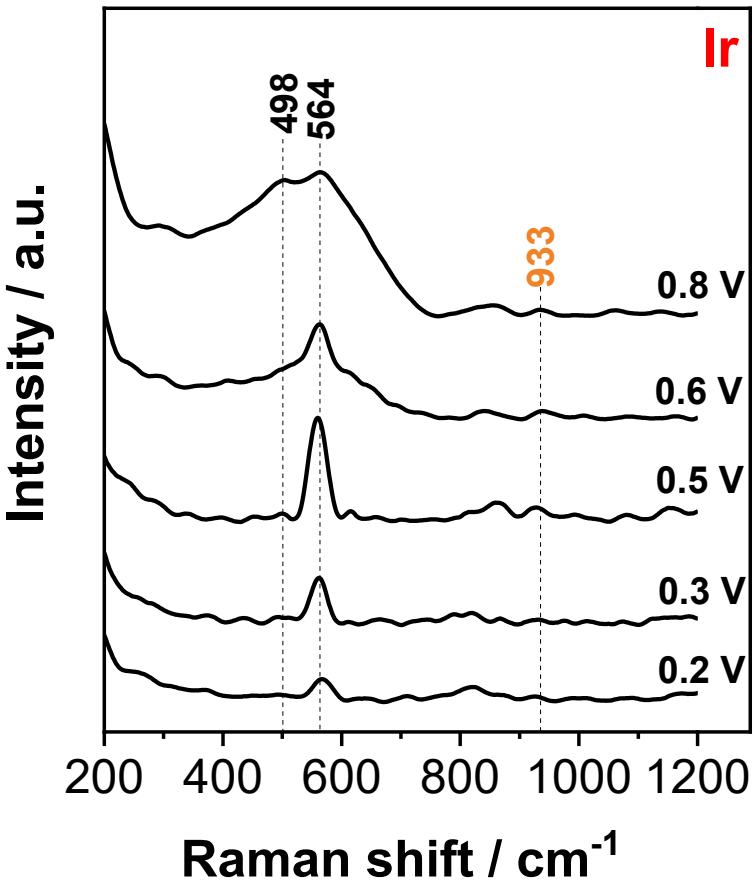

Figure S2.8. In-situ Raman spectra collected from the monometallic Ir thin film in the potential range from 0.2 – 0.8 V_{RHE} in 0.1 M $HClO_4$. The Raman band at 564 cm^{-1} is assigned to pure Ir^{3+}-OH and formation of the band at 498 cm^{-1} is associated with Ir^{4+} center formation.[78,79] The position at 933 cm^{-1} is labelled where the adsorbed ClO_4^- anion is expected. Due to the low intensity and high background, it is likely in the noise of the Raman data.

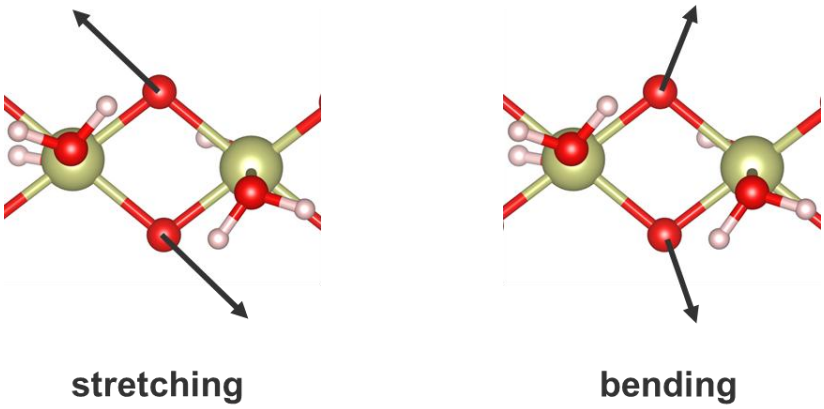

Figure S2.9. Vibrations of the strong movement of the μ-oxo bonds. The arrows show the direction of the atomic movement of the stretching (left) and bending (right) motions. Iridium, oxygen and hydrogen are denoted with gold, red and white spheres, respectively.

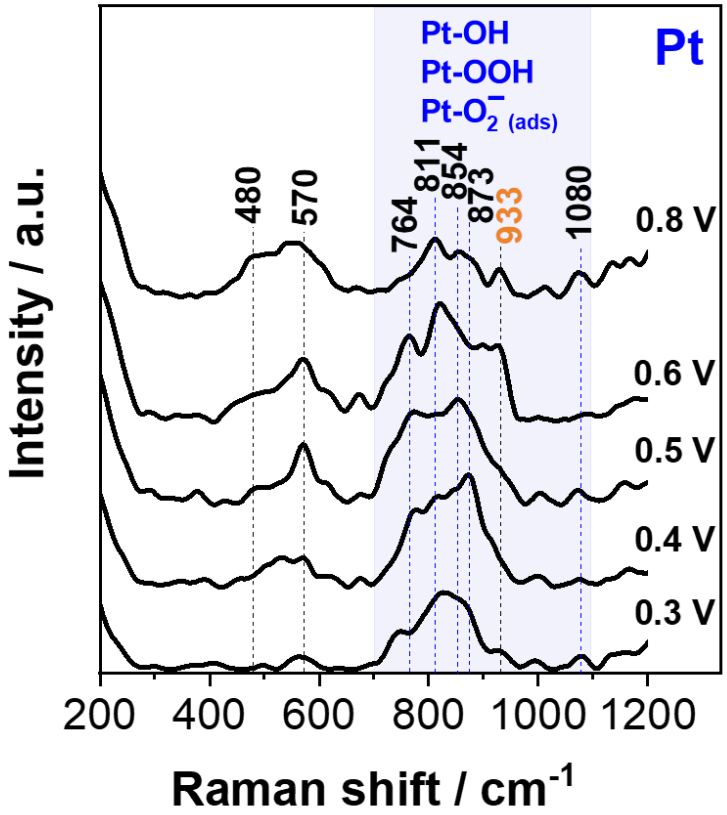

Figure S2.10. In-situ Raman spectra collected from the monometallic Pt thin film between 0.3 – 0.8 V_{RHE} in 0.1 M $HClO_4$. The blue marked area shows the Raman shift region where adsorbed oxygen species are expected.[83,109,110,245] Peak assignments are shown in **Table S2.6**.

Table S2.6. Summary of the Raman peaks for the monometallic Pt thin film between 0.3 V_{RHE} and 0.8 V_{RHE} (**Figure S2.10**), corresponding modes of vibration and respective references of the assignments.

Raman shift / cm^{-1}	Mode of vibration	Ref.
480	Pt-O (oxide)	244
570	Pt-O (oxide)	83,245,252
764	$Pt\text{-}OOH_{(ads)}$	109,110,245
811	$Pt\text{-}O^{-}_{2(ads)}$	83,110
854	$Pt\text{-}O^{-}_{2(ads)}$	83,110
873	$Pt\text{-}O^{-}_{2(ads)}$	83,110
933	ClO^{-}_{4}	83,109,110,245
1080	$Pt\text{-}OH_{(ads)}$	109

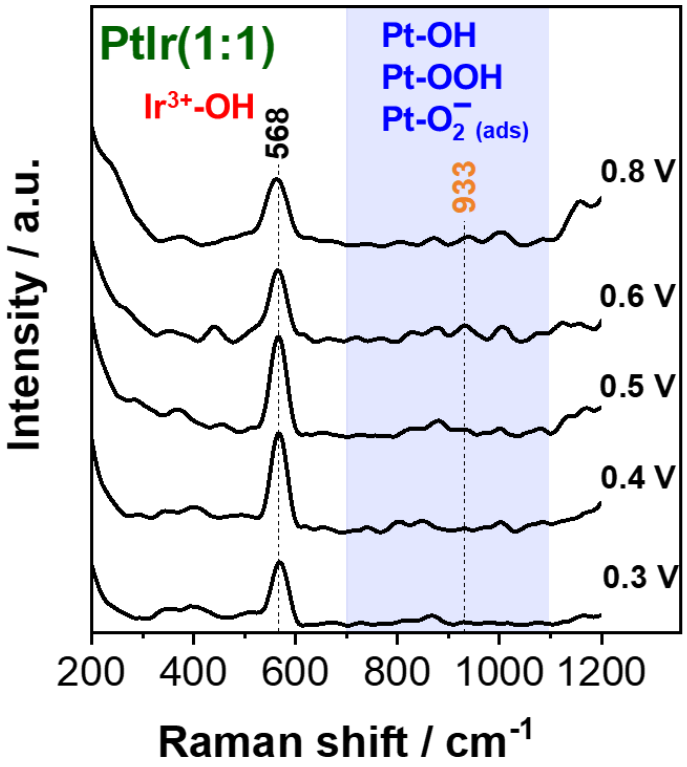

Figure S2.11. In-situ Raman spectra collected from the PtIr(1:1) thin film by holding the potential from 0.3 V_{RHE} to 0.8 V_{RHE} with 100 mV steps in 0.1 M $HClO_4$. The Raman band at 568 cm^{-1} is assigned to Ir^{3+}-OH species (red). The expected formation of adsorbed oxygen species on platinum are denoted with a blue marked area.[83,109,110,245] At the Raman shift of 933 cm^{-1}, the adsorbed ClO_4^- anion might be expected, which is hidden in the signal-to-noise ratio.

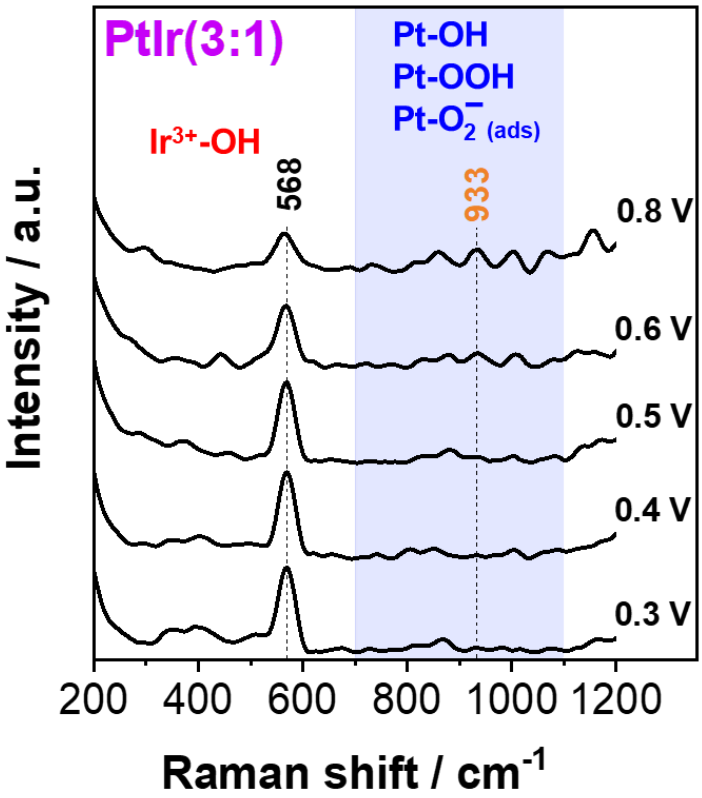

Figure S2.12. Potential-resolved series of in-situ Raman spectra for the PtIr(3:1) thin film in 0.1 M $HClO_4$. The Ir^{3+}-OH species (red) is visible by the Raman band at 568 cm^{-1}. Due to the low intensity and high background, the peak at 933 cm^{-1} (orange label) assigned to adsorbed ClO_4^- anion is likely in the noise of the Raman data. The blue marked area shows the Raman shift region, adsorbed oxygen species appear on the platinum surface.[83,109,110,245]

Table S2.7. Strongest DFT predicted Raman frequencies and mode of vibration for the iridium oxo-hydroxo complex shown in **Figure 42a**.

Raman shift / cm^{-1}	**Mode of vibration**
525	Ir-O-Ir antisymmetric stretch
725	Ir-O-Ir symmetric stretch

Table S2.8. According to the DFT calculations, strongest Raman frequencies and modes of vibration for the platinum oxo-hydroxo complex displayed in **Figure 42b**.

Raman shift / cm^{-1}	**Mode of vibration**
505	Pt-O-Pt antisymmetric stretch + Pt-O-Pt bend
572	Pt-O-Pt symmetric stretch + Pt-O-Pt bend
606	Pt-O-Pt symmetric stretch + Pt-O-Pt bend
645	Pt-O-Pt symmetric stretch + Pt-O-Pt bend

Table S2.9. Strongest DFT predicted Raman frequencies and mode of vibration for the platinum-iridium oxo-hydroxo complex with 1:1 Pt:Ir ratio shown in **Figure 42c**.

Raman shift / cm^{-1}	**Mode of vibration**
430	Ir-O-Pt bend
494	Ir-O-Pt bend
542	Ir-O-Pt bend+ Ir-O-Pt antisymmetric stretch
595/604	Ir-O-Pt bend
629	Ir-O-Pt bend + Ir-O-Pt symmetric stretch
664	Ir-O-Pt symmetric stretch
682	Ir-O-Pt symmetric stretch

Table S2.10. Summary of the strongest DFT predicted Raman frequencies and the respective modes of vibration for the platinum-iridium oxo-hydroxo complex with 3:1 Pt:Ir ratio from **Figure 42d**.

Raman shift / cm^{-1}	**Mode of vibration**
430	Ir-O-Pt bend
470	Ir-O-Pt bend
507	Ir-O-Pt symmetric stretch + Ir-O-Pt bend + Pt-O-Pt antisymmetric stretch
521	Pt-O-Pt bend + Ir-O-Pt antisymmetric stretch + Ir-O-Pt symmetric stretch
592/606	Ir-O-Pt symmetric stretch + Pt-O-Pt symmetric stretch + Pt-O-Pt symmetric stretch
620	Pt-O-Pt bend + Ir-O-Pt bend

10.3. Supporting Information Chapter 4.3.

*This chapter is reprinted in an adapted form from Blaseio et al. in J. Mater. Chem. A, 2024, **12**, 28177–28192. https://doi.org/10.1039/D4TA02217C*

Experimental

Cu_xO foam preparation

Cu_xO foams were prepared by electrodeposition onto activated graphite sheets (0.25 mm thick, Alfa Aesar, 99.8 %) using the dynamic hydrogen bubble template approach.[161,168,283–285] Activation of the carbon foil substrates was achieved by a thermal treatment at 550 °C for 12 h in air, followed by rinsing in an acetone/water mixture (1:1 volume ratio) and subsequent drying at 100 °C for 1 h. For electrodeposition the carbon foil with a geometric surface area of 1 cm^2 was exposed to a Cu plating bath containing 0.2 M $CuSO_4x5H_2O$ (Sigma-Aldrich, ACS grade) and 1.5 M H_2SO_4 (Sigma-Aldrich, ACS grade). As a counter electrode a Cu plate (5 cm x 5 cm) and as the reference electrode an Ag/AgCl (Metrohm, 3 M KCl) were used. The galvanostatic deposition process was carried out for 5 s at a current density of – 3.0 A cm^{-2} normalized by the geometric electrode surface area. Afterwards, all Cu foam samples were thoroughly dried in an Ar flow (Carbagas, 99.999 %) followed by the thermal annealing treatment in a tube furnace (GERO GmbH) at temperatures of 100 °C, 200 °C, 300 °C or 450 °C for 12 h in air, respectively. Dependent on the temperature during the thermal annealing, Cu_xO foams with varying oxidation states are prepared.

CO_2RR Electrolysis

The CO_2 electrolysis experiments were conducted using a custom-built, airtight glass cell (H-type). The three-electrode setup included a leakless Ag/AgCl (3 M KCl) reference electrode (EDAQ), a Pt foil (15mm x 5mm) as a counter electrode, and the graphite-supported annealed Cu_xO foam catalysts (5 s deposition time at – 3.0 A cm^{-2}) as the working electrodes. To prevent any chloride ion contamination in the working electrolyte solution from the Ag/AgCl (3 M KCl) reference electrode, ion exchange chromatography (IC) was employed, with a detection limit of 100 ppb Cl anions. Before starting electrolysis, both the cathodic and anodic compartments were filled with 30 mL of 0.5 M $KHCO_3$ electrolyte solution (ACS grade, Sigma Aldrich) and were saturated with CO_2 gas (99.999 %, Carbagas, Switzerland). The catholyte and anolyte were separated by a polymer membrane (Nafion 117, Sigma Aldrich). The potentiostatic CO_2 electrolysis was performed using a potentiostat (Metrohm Autolab 302N, The Netherlands), while the current interrupt method (Autolab Nova) was utilized to determine and compensate for the iR drop.

For CO_2RR product analysis, the headspace gas from the catholyte compartment was vented with CO_2, allowing the gaseous electrolysis products to be transferred into the gas sampling loop of the gas chromatograph (SRI Instruments, GC 8610C). The GC was equipped with a packed Hayesep D column and FS-INNOPEG 2000 column for separating the gaseous and non-volatile (alcohols) products respectively. Argon (Carba Gas, 99.9999 %) served as the carrier gas. For quantifying all gaseous CO_2RR products, a flame ionization detector (FID) coupled to a methanizer was used, while hydrogen was quantified using a thermal conductivity detector (TCD).

The partial current density for each gaseous electrolysis product was calculated using the following equation:

$$I_0\,(i) = X_i.\ n_i.\ F.\ Vm \tag{14}$$

where $X_i.$ is the volume fraction of the product measured via online GC using a calibration gas mixture in argon (Carbagas), $n_i.$ is the number of electrons involved in forming the product, Vm is the molar CO_2 gas flow rate and F is the Faraday constant. The partial current density was normalized to the total current density, providing the Faradaic Efficiency (FE%) for each product. Gas samples were analyzed every 20 minutes during steady-state CO_2 electrolysis. Non-volatile alcohols were measured using a second FID detector (without methanizer). After electrolysis, an aliquot of the electrolyte was injected into the FS-INNOPEG 2000 column using a microliter syringe. Non-volatile ionic liquid products, such as formate, that accumulated in the catholyte during CO_2 electrolysis were analyzed using ion exchange chromatography coupled with a conductivity detector. The setup included a Metrohm Advanced Modular Ion Chromatograph with an L-7100 pump and a Metrosep A Supp 7-250 column.

Table S3.1. Experimental acquisition parameters for survey and high-resolution XPS and Auger measurements performed for all annealed Cu_xO foams.

spectrum	energy range / eV	step size / eV	pass energy / eV	dwell time / ms	no. of scans
survey	- 10 – 1350	1.0	100	10	5
O 1s	525 – 540	0.02	10	50	10
C 1s	279 – 298	0.02	20	50	5
Cu 2p	925 – 965	0.05	10	50	10
Cu LMM	900 – 930	0.05	10	50	10

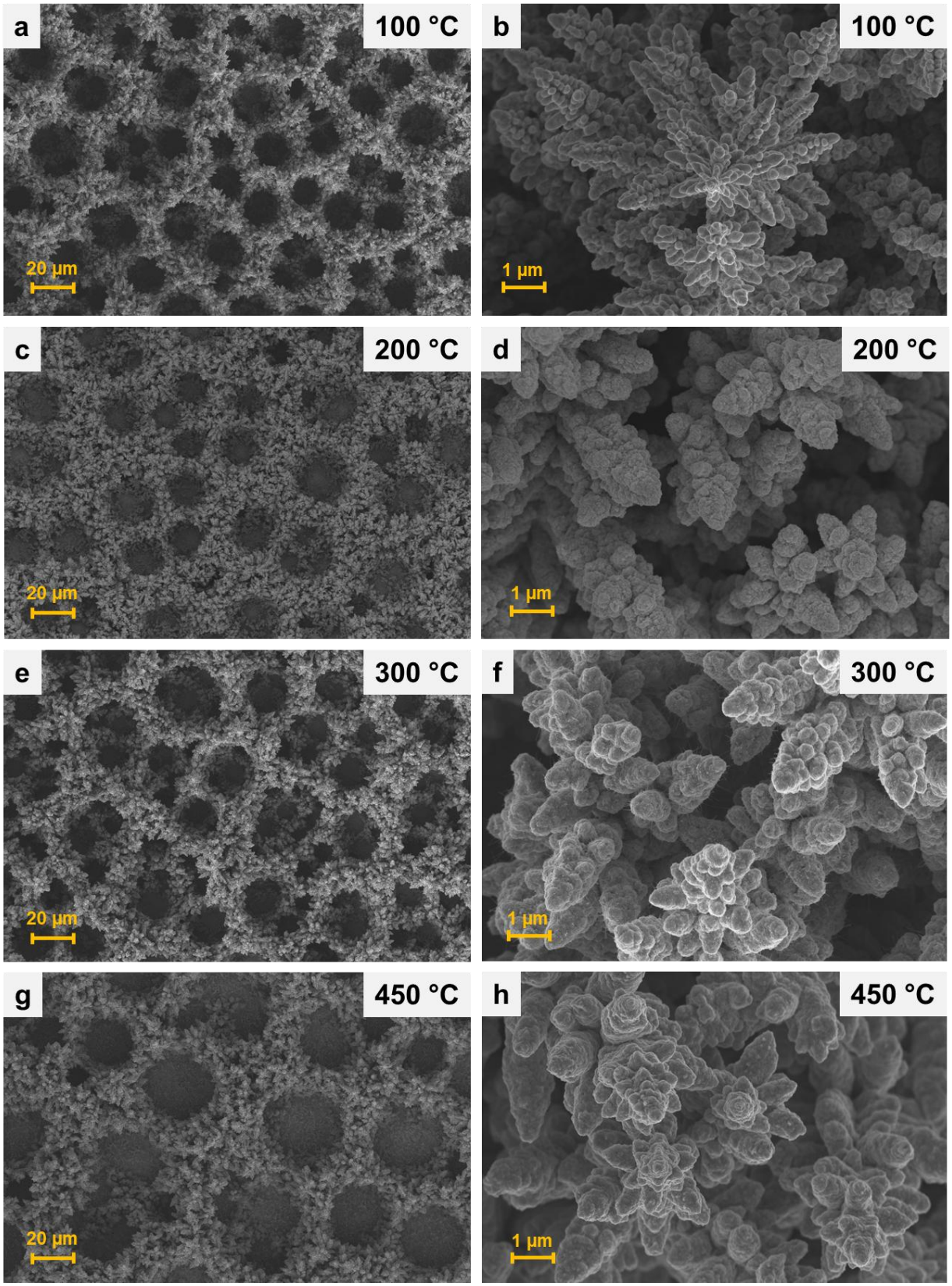

Figure S3.1. SEM micrographs of the in air annealed Cu_xO foams at 100 °C (a-b), 200 °C (c-d), 300 °C (e-f) and 450 °C (g-h) at low and high magnification. Reprinted from Blaseio et al.[258]

Table S3.2. Crystallite size, space group, lattice parameter and phase quantity determined by the quantitative Rietveld refinement analysis of the XRD profiles for the in air annealed Cu_xO foams displayed **Figure 44** in the main part of the thesis. The weighted profile R-factor (R_{wp}) represents the discrepancy index between the calculated and measured data.

sample	phase	space group	lattice parameter / Å	crystallite size / nm	quantity / wt. %	R_{wp}
100-foam	Cu	Fmm	3.619 ± 0.001	45 ± 5	5 ± 1	13.82
	Cu_2O	$Pn\bar{3}m$	4.273 ± 0.001	51 ± 1	95 ± 1	
	CuO	-	-	-	-	
200-foam	Cu	$Fm\bar{3}m$	3.617 ± 0.001	55 ± 11	2 ± 1	14.03
	Cu_2O	$Pn\bar{3}m$	4.272 ± 0.001	69 ± 1	98 ± 1	
	CuO	-	-	-	-	
300-foam	Cu	-	-	-	-	10.15
	Cu_2O	$Pn\bar{3}m$	4.275 ± 0.001	41 ± 1	21 ± 1	
	CuO	C12/c1	4.673 ± 0.001 3.459 ± 0.001 5.146 ± 0.001	16 ± 1	34 ± 1	
		C12/c1	4.689 ± 0.001 3.429 ± 0.001 5.138 ± 0.001	23 ± 1	45 ± 1	
450-foam	Cu	-	-	-	-	13.80
	Cu_2O	$Pn\bar{3}m$	4.202 ± 0.001	30 ± 4	8 ± 1	
	CuO	C12/c1	4.663 ± 0.003 3.470 ± 0.003 5.139 ± 0.004	13 ± 1	51 ± 4	
		C12/c1	4.691 ± 0.002 3.432 ± 0.001 5.139 ± 0.002	31 ± 4	41 ± 4	

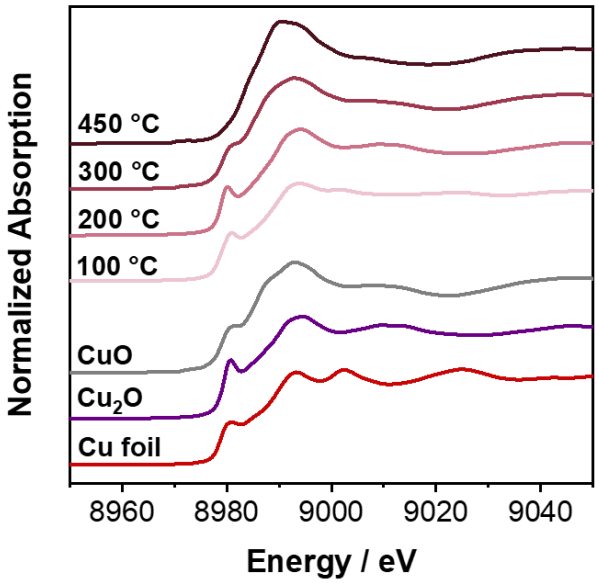

Figure S3.2. Ex-situ Cu K-edge XANES spectra of various air annealed Cu_xO foams at 100 °C, 200 °C, 300 °C and 450 °C in comparison with the Cu foil, Cu_2O and CuO reference materials. The spectra were collected every second for 6-10 min and subsequently averaged. Reprinted from Blaseio et al.[258]

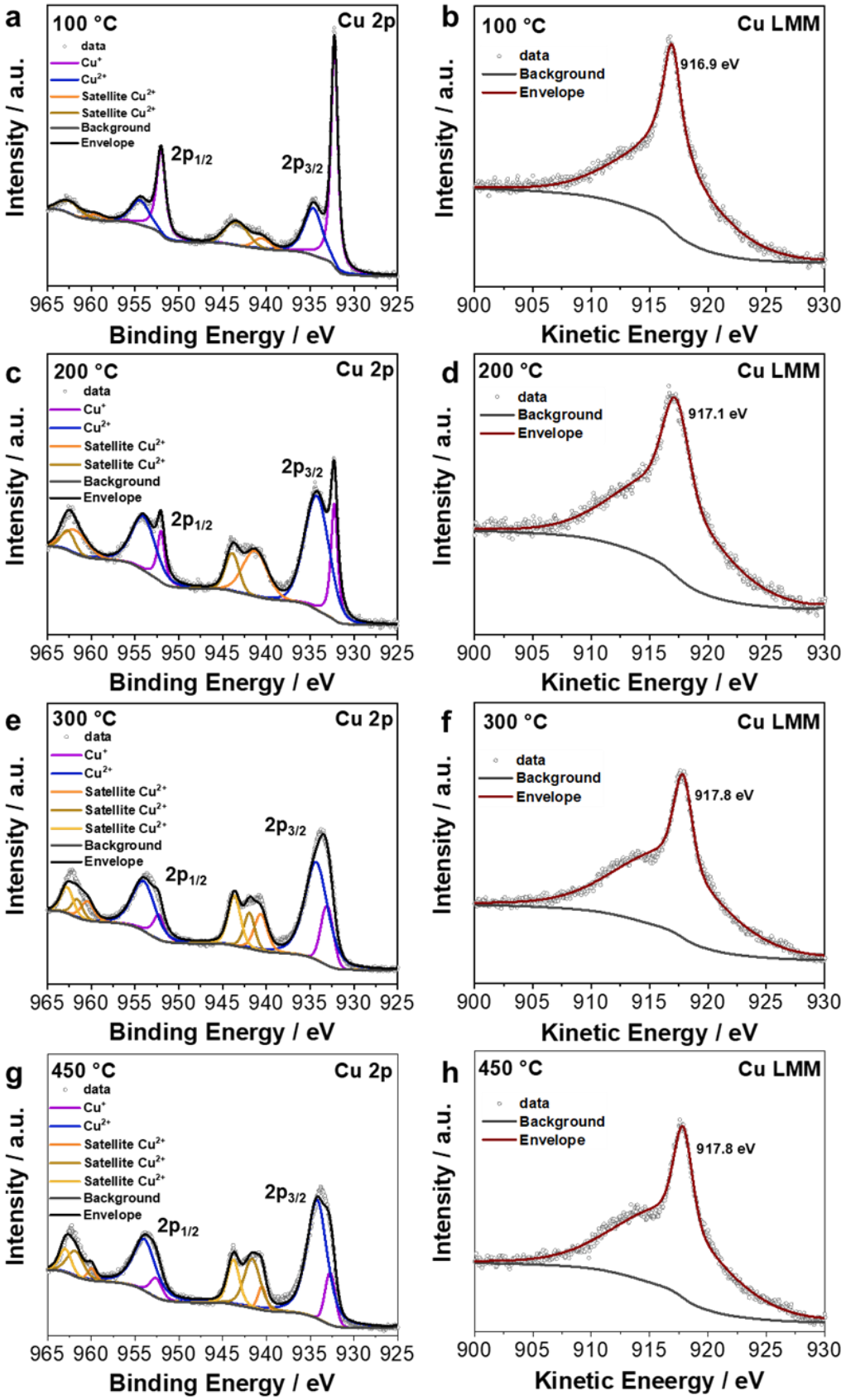

Figure S3.3. High-resolution (**left**) Cu 2p XPS and (**right**) Cu LMM Auger spectra of the air annealed Cu_xO foams at 100 °C (**a, b**), 200 °C (**c, d**), 300 °C (**e, f**) and 450 °C (**g, h**). Reprinted from Blaseio et al.[258]

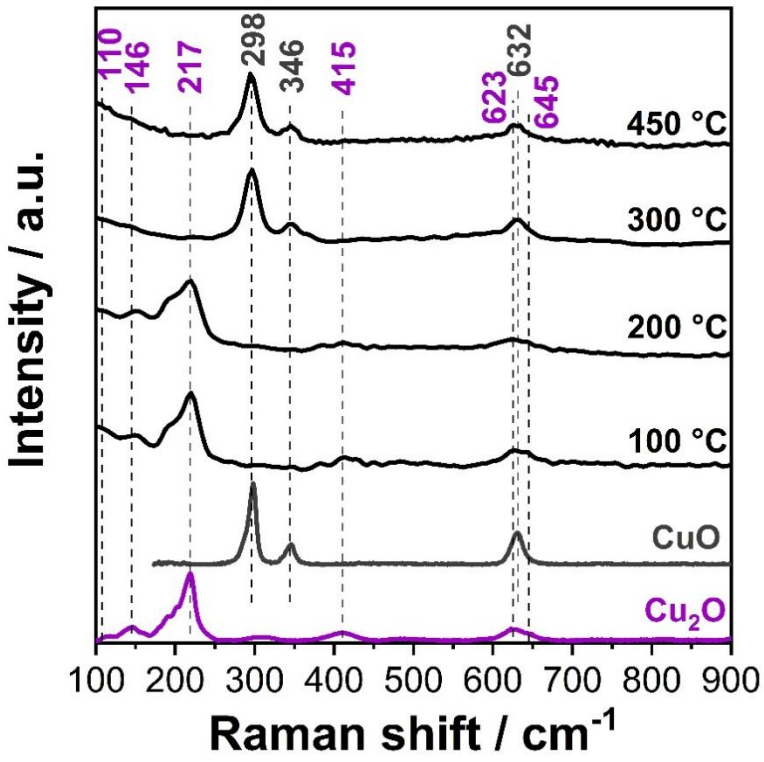

Figure S3.4. Ex-situ Raman spectra of the Cu_xO foams annealed in air at 100 °C, 200 °C, 300 °C and 450 °C (black lines). Cu_2O [#R140763] (purple) and CuO [#R120076] (grey) reference spectra obtained from the Ruff data base.[286] Reprinted from Blaseio et al.[258]

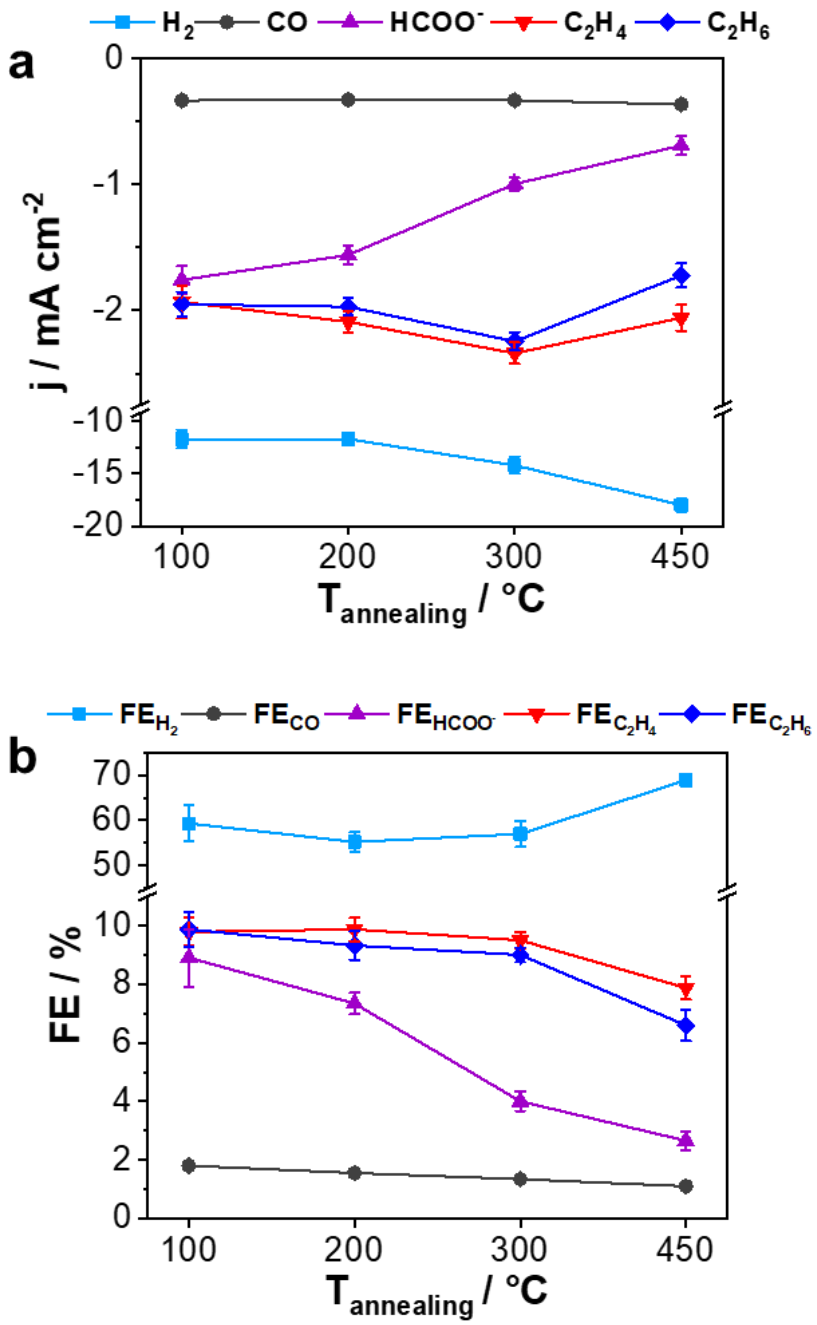

Figure S3.5. H_2, C_1 and C_2 product distribution after 2 h CO_2RR electrolysis at – 0.87 V_{RHE} carried out in CO_2-saturated 0.5 M $KHCO_3$ represented as partial current densities (a) and Faradaic efficiencies (FEs) (b) in dependence on the annealing temperature in air of the Cu_xO foams. In some cases, the error bars are smaller than the data points. Reprinted from Blaseio et al.[258]

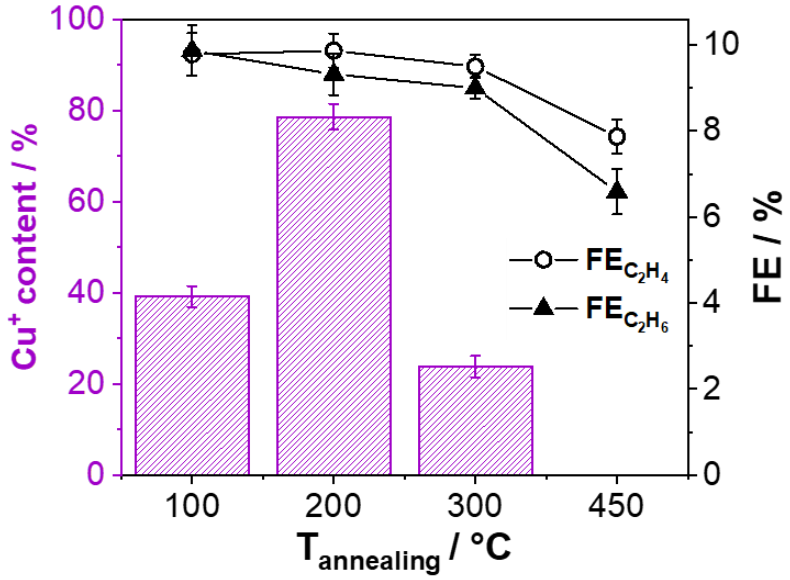

Figure S3.6. Faradaic efficiencies (FEs) of ethylene and ethane after 2 h CO_2RR electrolysis at – 0.87 V_{RHE} carried out in CO_2-saturated 0.5 M $KHCO_3$ in dependence on the annealing temperature of the Cu_xO foams. The corresponding Cu^+ content of each Cu_xO foam (purple bars) was obtained from LCF analysis of the ex-situ XANES spectra using Cu^0, Cu_2O and CuO as reference materials. Reprinted from Blaseio et al.[258]

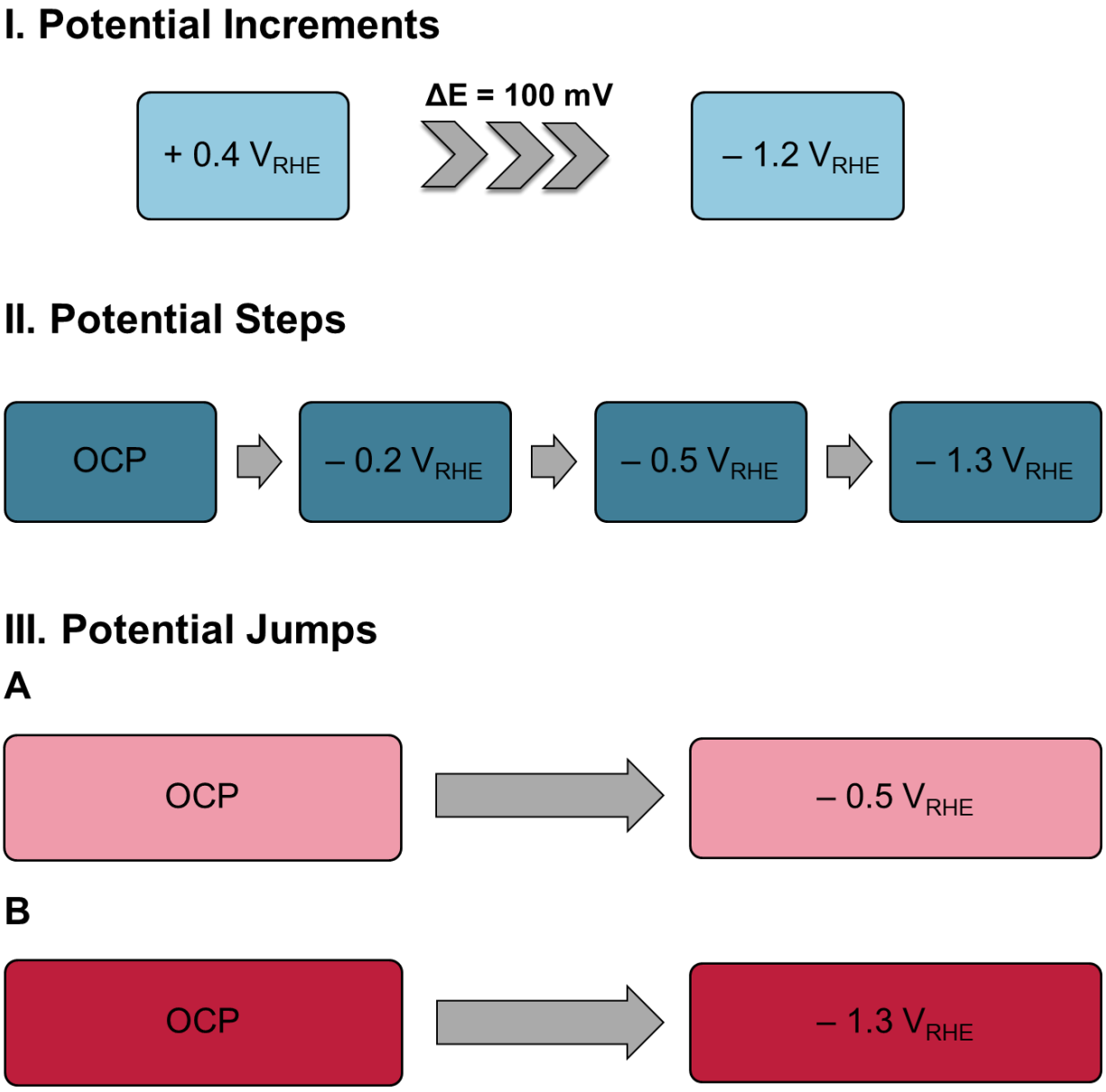

Figure S3.7. Different types of potential control experiments carried out to investigate the oxide to metal transition dynamics of Cu species probed by operando Quick-XAS. Reprinted from Blaseio et al.[258]

MCR-ALS Analysis

After the XAS data matrix was created in MATLAB (spectra are shown in Fig. S8, I), the number of components were estimated from the Eigenvalue and Eigenvector plots in the Singular Value Window of the MCR-ALS Toolbox (Fig. S8, II). Additionally, the purest variable detection method (Fig. S8, III) is used as an initial guess of the spectra in the ALS minimization. Several constraints were applied for the analysis of the XAS spectra: (i) non-negativity of the concentration and MCR-ALS spectra (C and S matrices) and (ii) the total concentration of the components sums up to 1 (100 %) (Fig. S8, IV and V). For non-negativity of C and S, fast non-negativity-constrained least-squares (fnnls) algorithm was selected. To obtain the concentrations of the three copper species (Cu^0, Cu^+ and Cu^{2+}), directly through the MCR-ALS method, the spectra of the references shown in Fig. S2 were fixed as components in the equality constraints (Fig. S8, V). After ALS optimization was run (Fig. S8, VI), the percentage of variance (r^2) at optimum was confirmed to be 99.9 % or higher.

II

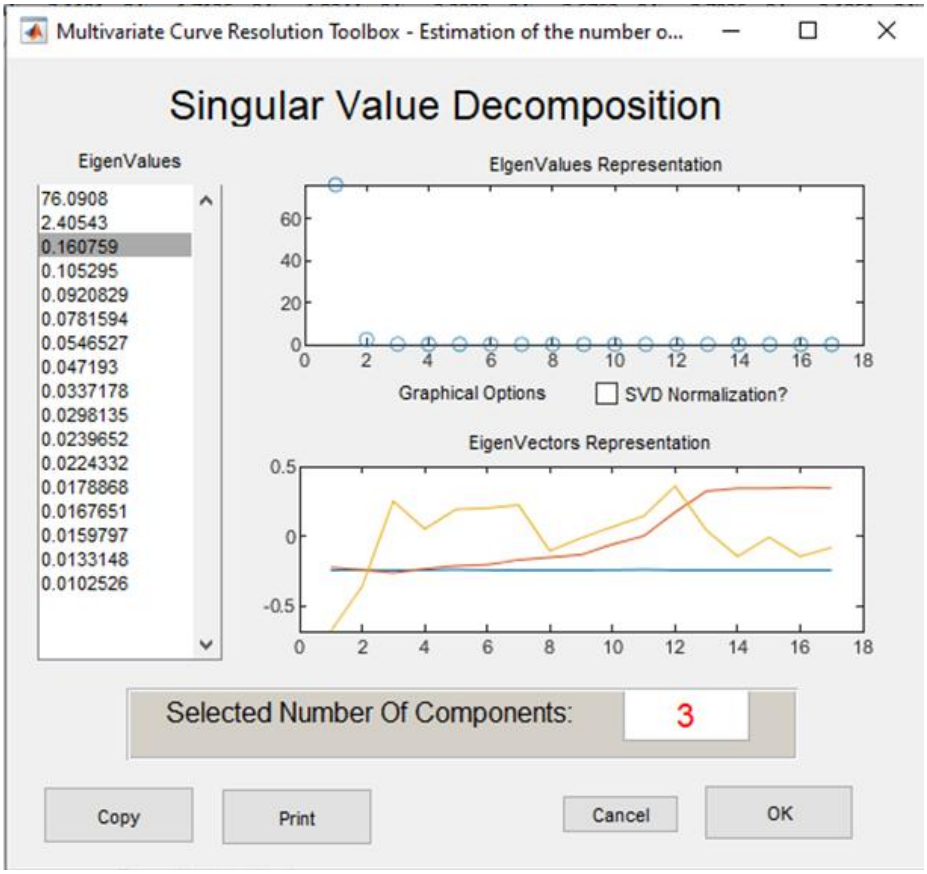
Multivariate Curve Resolution Toolbox - Estimation of the number o...
Singular Value Decomposition
EigenValues
76.0908
2.40543
0.160759
0.105295
0.0920829
0.0781594
0.0546527
0.047193
0.0337178
0.0298135
0.0239652
0.0224332
0.0178868
0.0167651
0.0159797
0.0133148
0.0102526
EIgenValues Representation
Graphical Options
SVD Normalization?
EigenVectors Representation
Selected Number Of Components:
3
Copy
Print
Cancel
OK

III

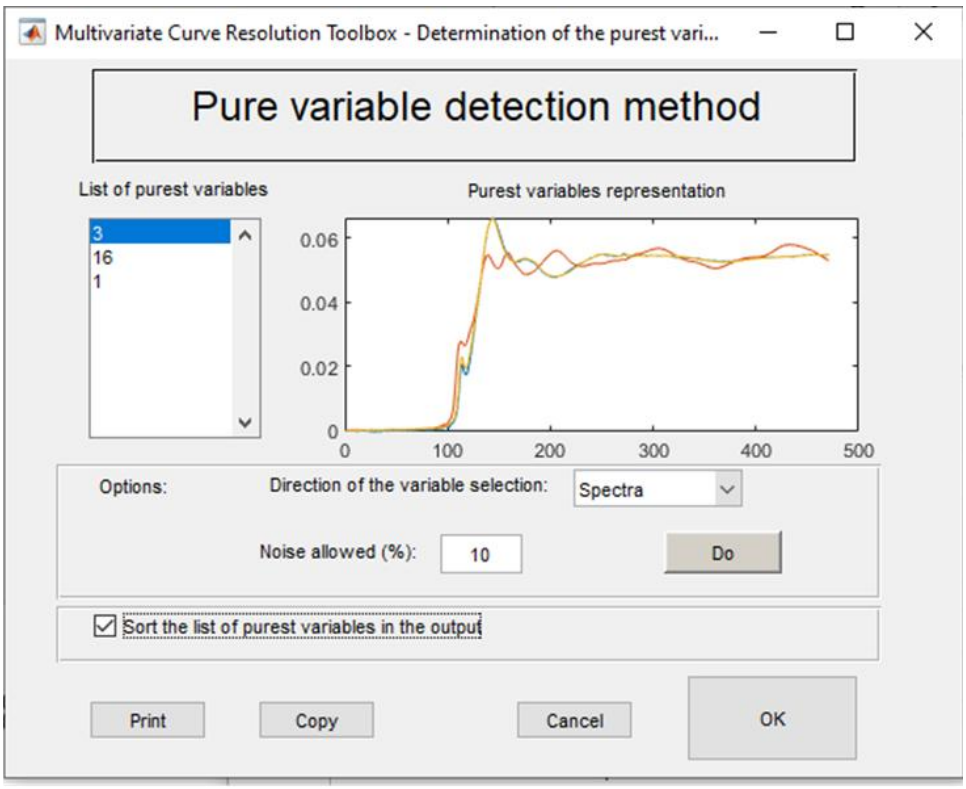
Multivariate Curve Resolution Toolbox - Determination of the purest vari...
Pure variable detection method
List of purest variables
3
16
1
Purest variables representation
Options:
Direction of the variable selection:
Spectra
Noise allowed (%):
10
Do
Sort the list of purest variables in the output
Print
Copy
Cancel
OK

IV

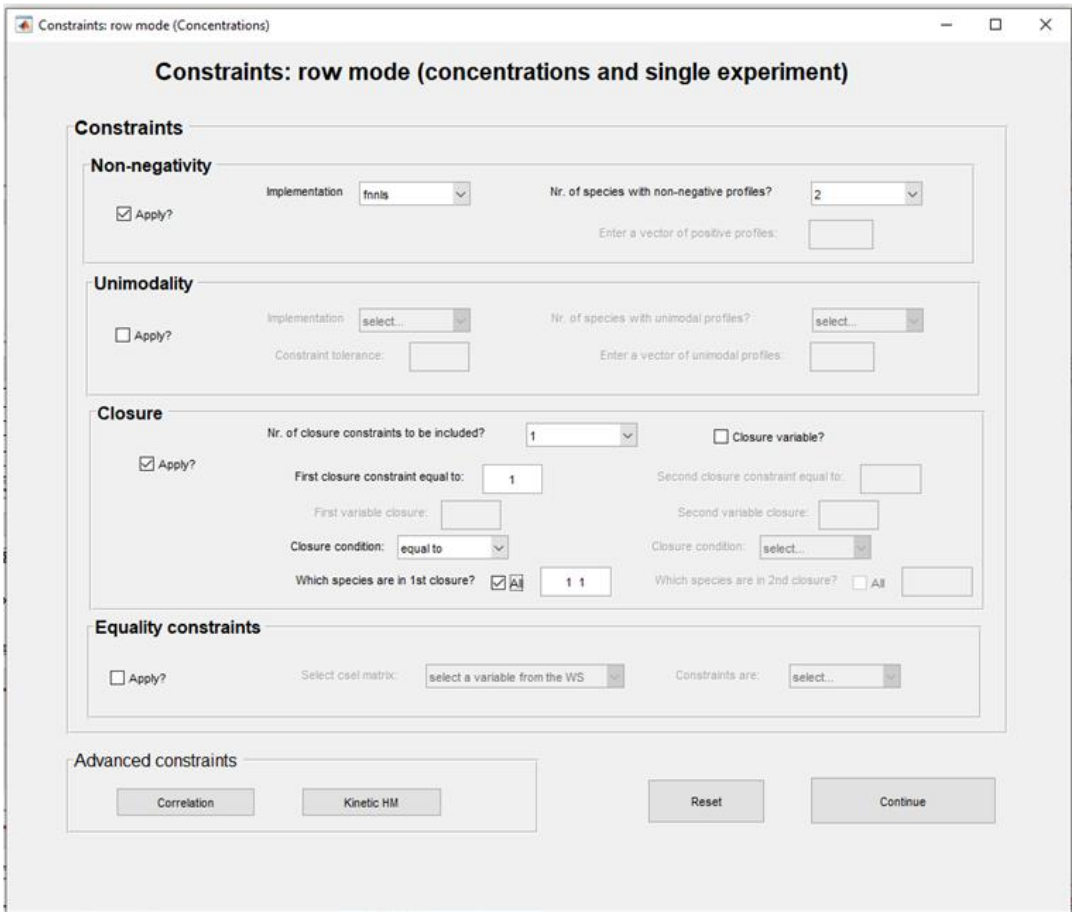
Constraints: row mode (Concentrations)
Constraints: row mode (concentrations and single experiment)
Constraints
Non-negativity
Apply?
Implementation
fnnls
Nr. of species with non-negative profiles?
2
Enter a vector of positive profiles:
Unimodality
Apply?
Implementation
select...
Nr. of species with unimodal profiles?
select...
Constraint tolerance:
Enter a vector of unimodal profiles:
Closure
Apply?
Nr. of closure constraints to be included?
1
Closure variable?
First closure constraint equal to:
1
Second closure constraint equal to:
First variable closure:
Second variable closure:
Closure condition:
equal to
Closure condition:
select...
Which species are in 1st closure?
All
1 1
Which species are in 2nd closure?
All
Equality constraints
Apply?
Select csel matrix:
select a variable from the WS
Constraints are:
select...
Advanced constraints
Correlation
Kinetic HM
Reset
Continue

V

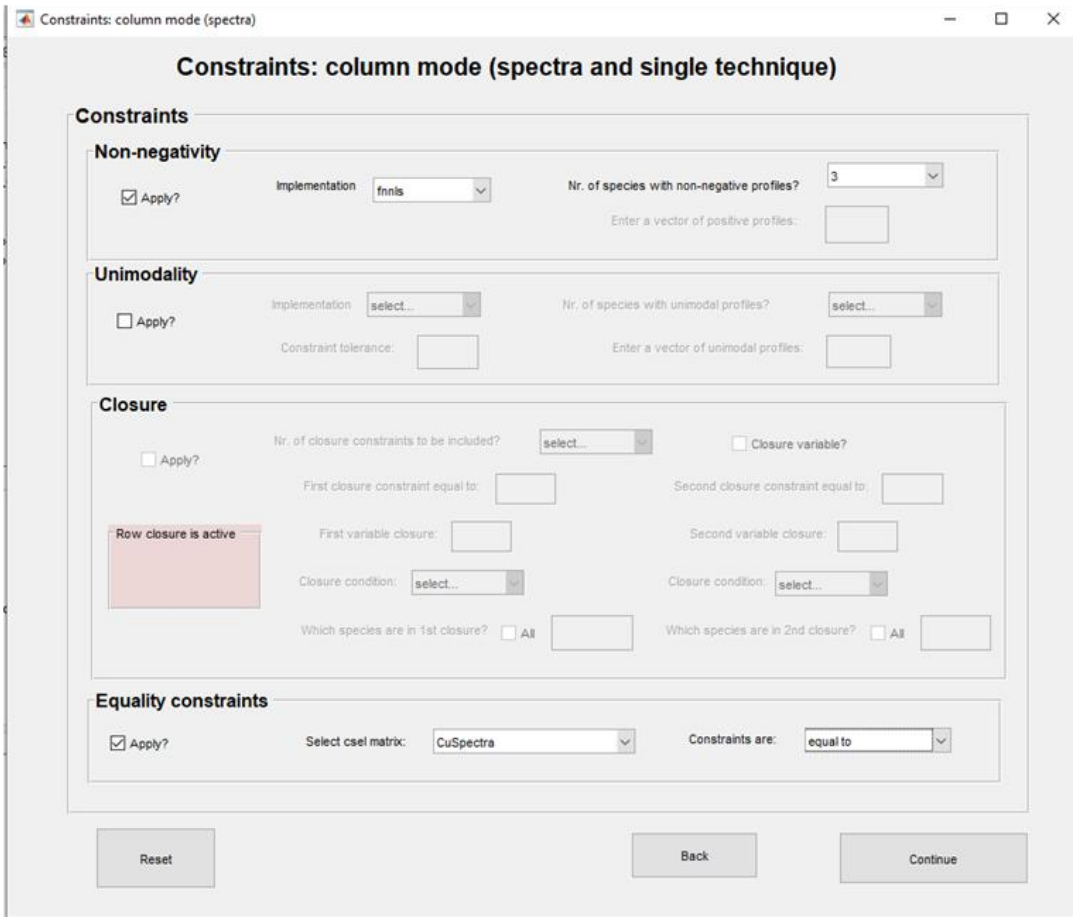
Constraints: column mode (spectra)
Constraints: column mode (spectra and single technique)
Constraints
Non-negativity
Apply?
Implementation
fnnls
Nr. of species with non-negative profiles?
3
Enter a vector of positive profiles:
Unimodality
Apply?
Implementation
select...
Nr. of species with unimodal profiles?
select...
Constraint tolerance:
Enter a vector of unimodal profiles:
Closure
Apply?
Nr. of closure constraints to be included?
select...
Closure variable?
First closure constraint equal to:
Second closure constraint equal to:
Row closure is active
First variable closure:
Second variable closure:
Closure condition:
select...
Closure condition:
select...
Which species are in 1st closure?
All
Which species are in 2nd closure?
All
Equality constraints
Apply?
Select csel matrix:
CuSpectra
Constraints are:
equal to
Reset
Back
Continue

VI

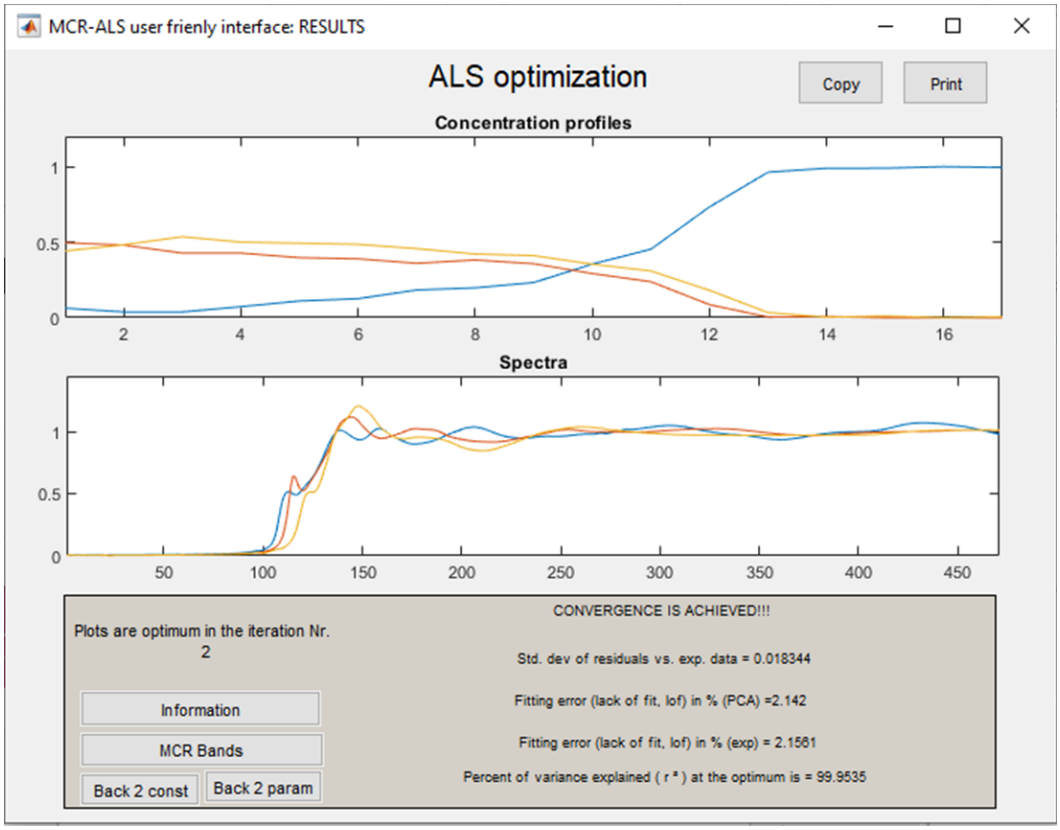

Figure S3.8. Example MCR-ALS analysis steps (**I** – **VI**) for the Cu K-edge XANES spectra of the 200-foam recorded during the potential increment experiment using the MCR-ALS GUI 2.0 MATLAB script[202]. Reprinted from Blaseio et al.[258]

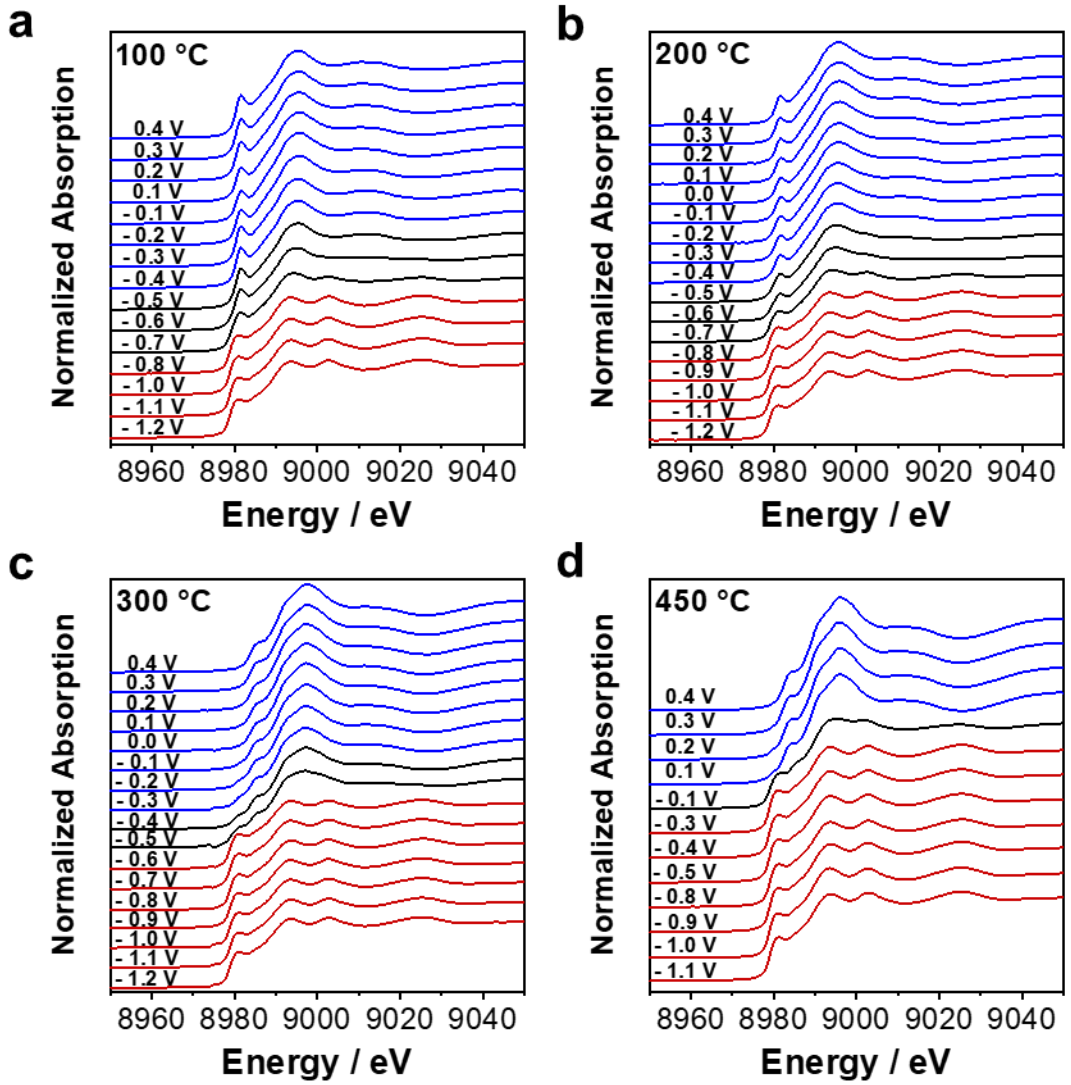

Figure S3.9. Potential-resolved series of Cu K-edge XANES spectra of the Cu_xO foams annealed at 100 °C (a), 200 °C (b), 300 °C (c) and 450 °C (d) for 12 h in air. The potential was shifted from + 0.4 V_{RHE} to – 1.2 V_{RHE} at 100 mV and held for 6 – 10 min at each potential, while XAS spectra were collected and subsequently averaged. Spectra of the oxidized and electrochemically reduced Cu_xO foams are shown in blue and red, respectively. The XANES data during the transition to metallic copper are denoted in black. Reprinted from Blaseio et al.[258]

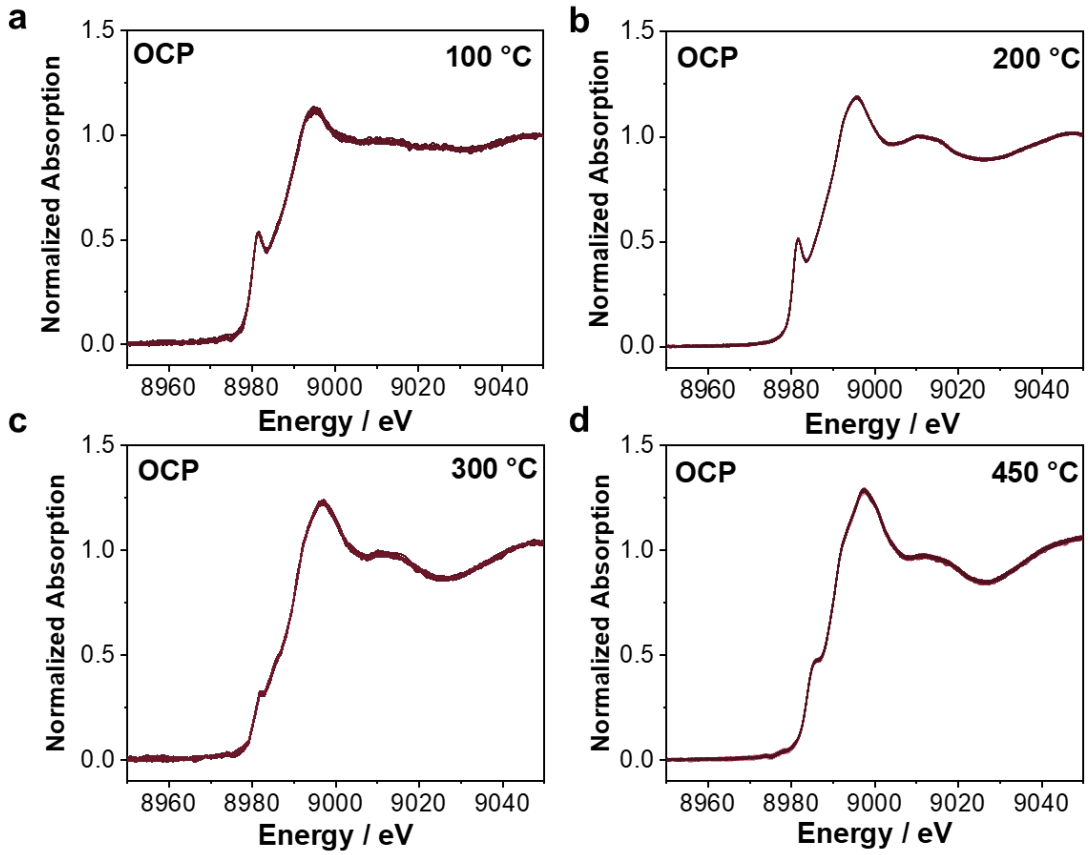

Figure S3.10. Cu K-edge XANES spectra of Cu_xO foams annealed for 12 h in air at 100 °C (a), 200 °C (b), 300 °C (c) and 450 °C (d) obtained at OCP for 300 s in CO_2-saturated 0.5 M $KHCO_3$. Reprinted from Blaseio et al.[258]

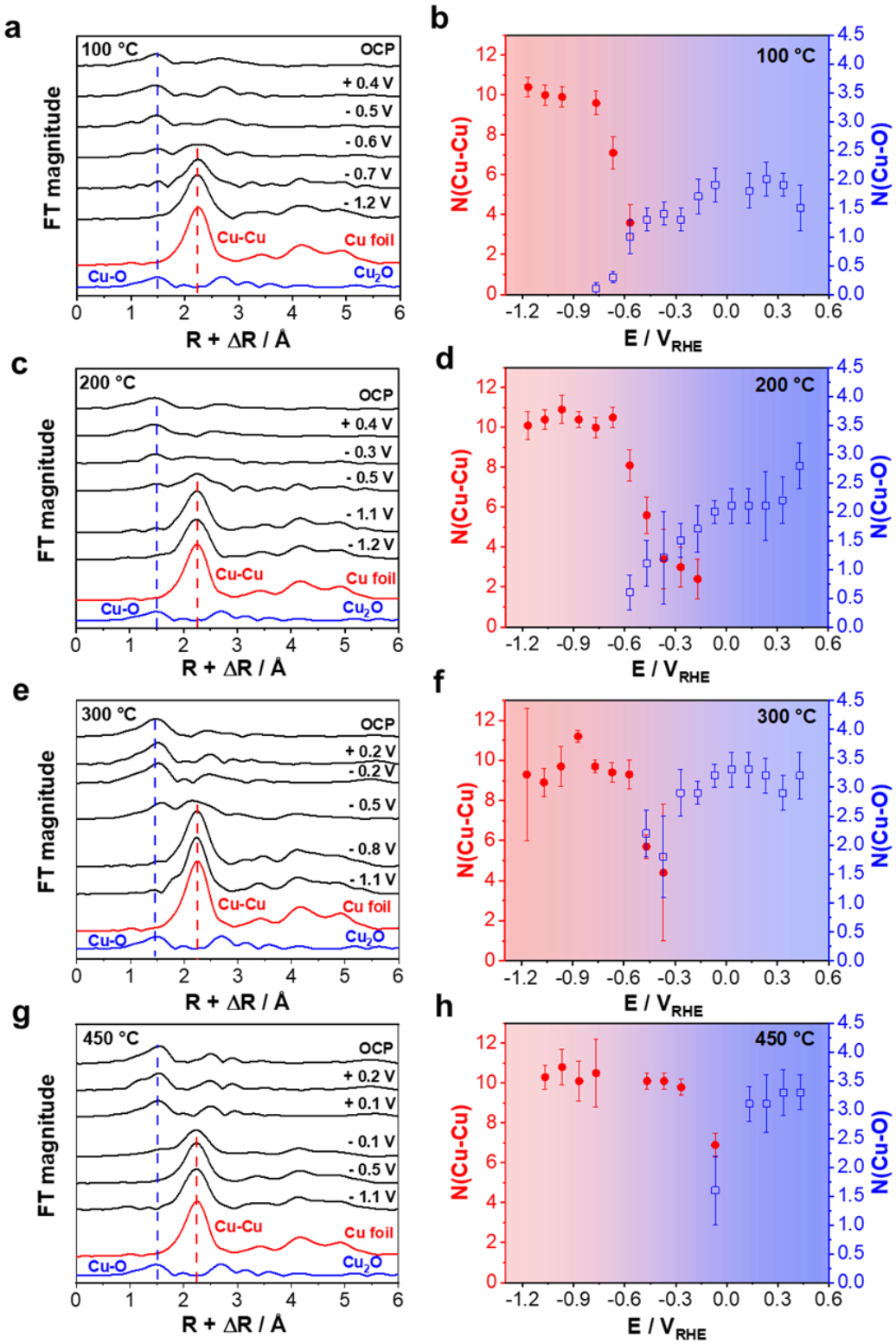

Figure S3.11. (**left**) Fourier-transform magnitudes of the k^2-weighted EXAFS data at the Cu K-edge and (**right**) potential-dependent course of the coordination numbers of the Cu-Cu and Cu-O bonds for Cu_xO foams annealed in air at 100 °C (**a, b**), 200 °C (**c, d**), 300 °C (**e, f**), and 450 °C (**g, h**) obtained from the potential increment experiments (ΔE = 100 mV, see **Figure S3.7**) in CO_2-saturated 0.5 M $KHCO_3$. Metallic Cu (red) and Cu_2O (blue) are shown as comparison. The IFEFF6 data for EXAFS fitting analysis, were determined from Cu (#9008468), Cu_2O (#1010963) and CuO (#9008961) taken from the crystal open database (COD).[205–207] Reprinted from Blaseio et al.[258]

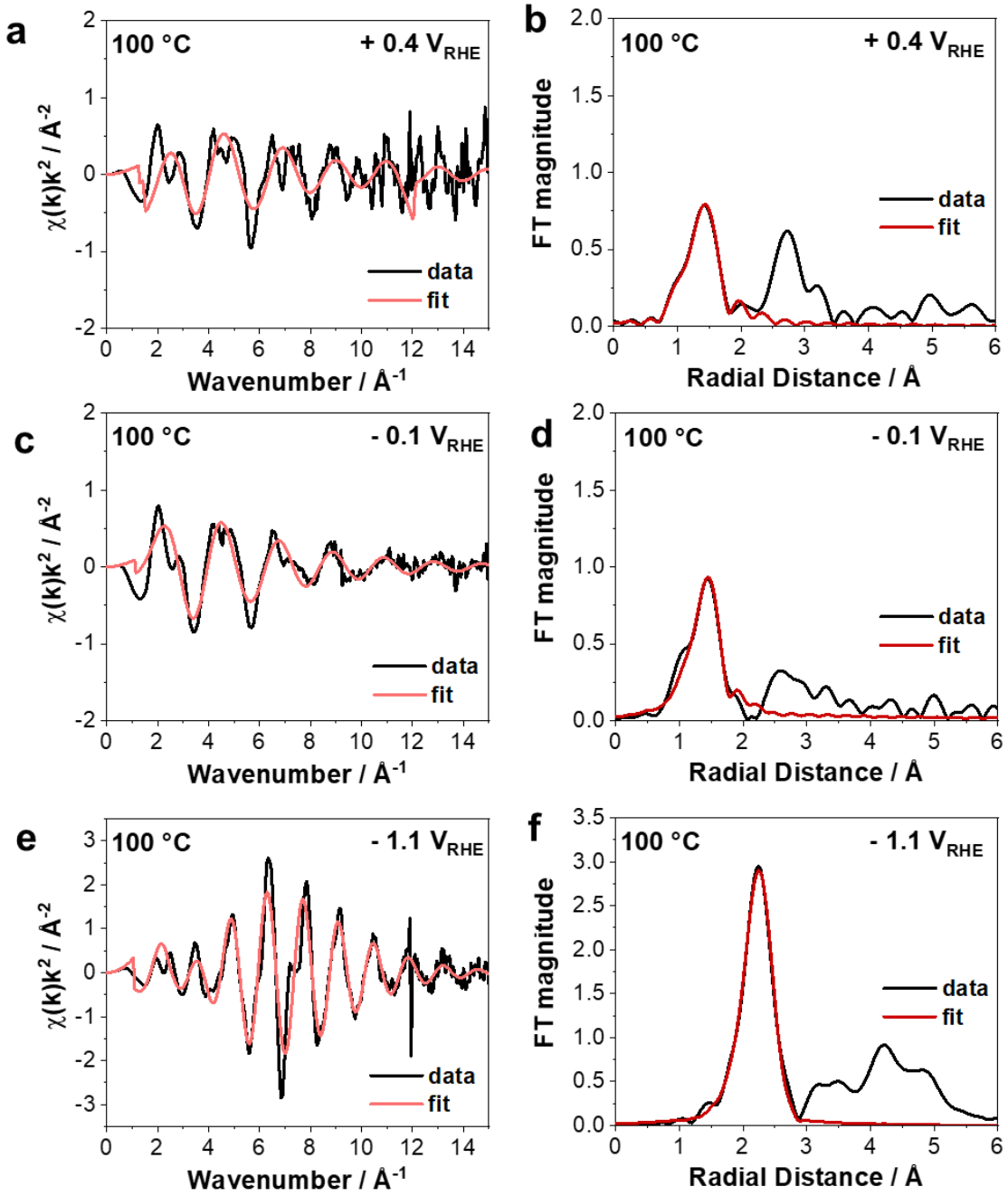

Figure S3.12. (left) k^2-weighted Cu K-edge EXAFS data in k-space and (right) the corresponding Fourier-transformed EXAFS data for the Cu_xO foam annealed in air at 100 °C at + 0.4 V_{RHE} (a, b) and – 0.1 V_{RHE} (c, d) and – 1.1 V_{RHE} (e, f). At potentials from + 0.4 V_{RHE} to – 0.5 V_{RHE} the data was fitted between 1 and 2 Å. From – 0.6 V_{RHE} the fitting range was extended to 3 Å to allow fitting of the metallic Cu. Reprinted from Blaseio et al.[258]

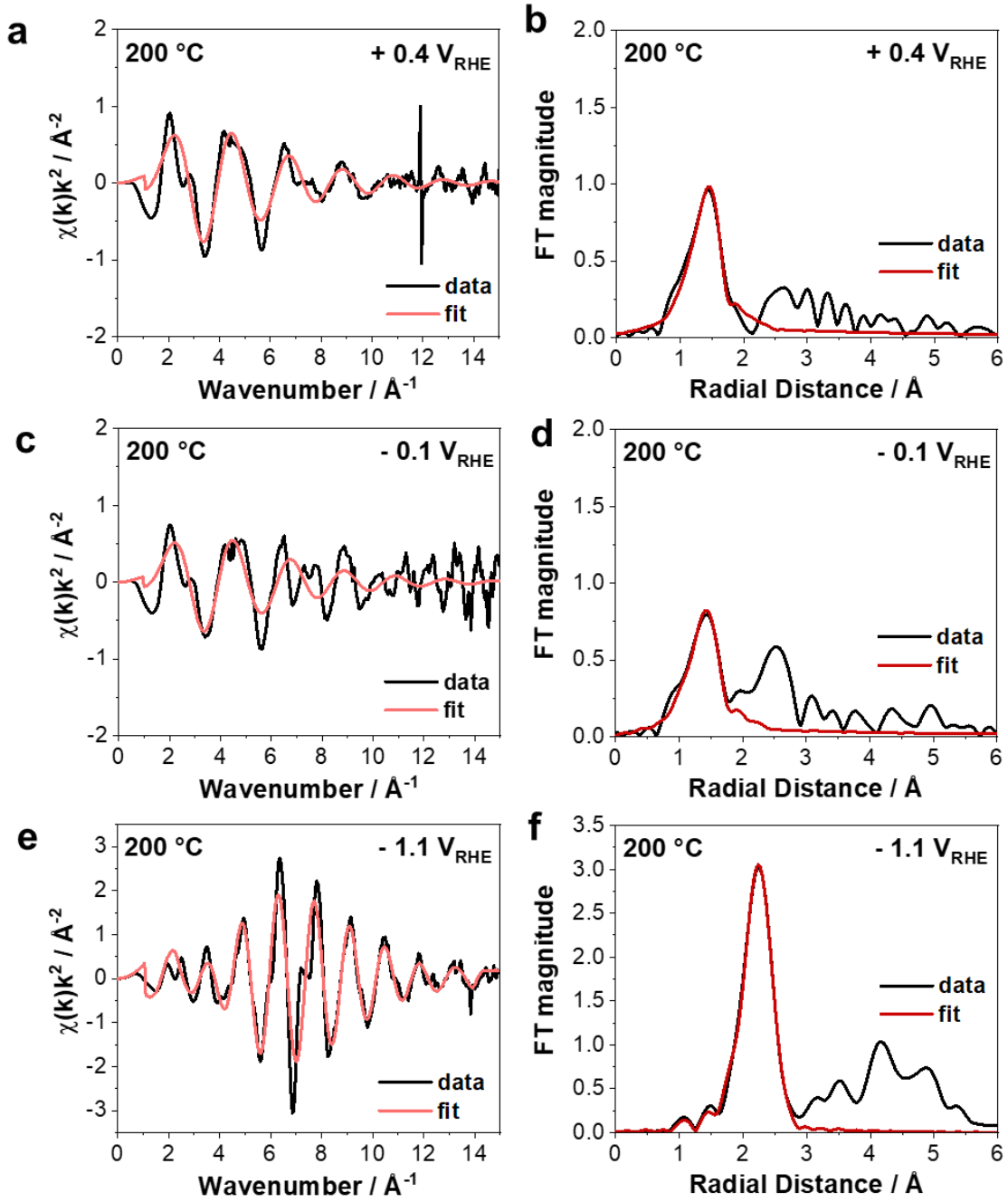

Figure S3.13. (left) k^2-weighted Cu K-edge EXAFS data in k-space and (right) the corresponding Fourier-transformed EXAFS data for the Cu_xO foam annealed in air at 200 °C at + 0.4 V_{RHE} (a, b) and – 0.1 V_{RHE} (c, d) and – 1.1 V_{RHE} (e, f). At potentials from + 0.4 V_{RHE} to – 0.1 V_{RHE} the data was fitted between 1 and 2 Å. From – 0.2 V_{RHE} the fitting range was extended to 3 Å to allow fitting of the metallic Cu. Reprinted from Blaseio et al.[258]

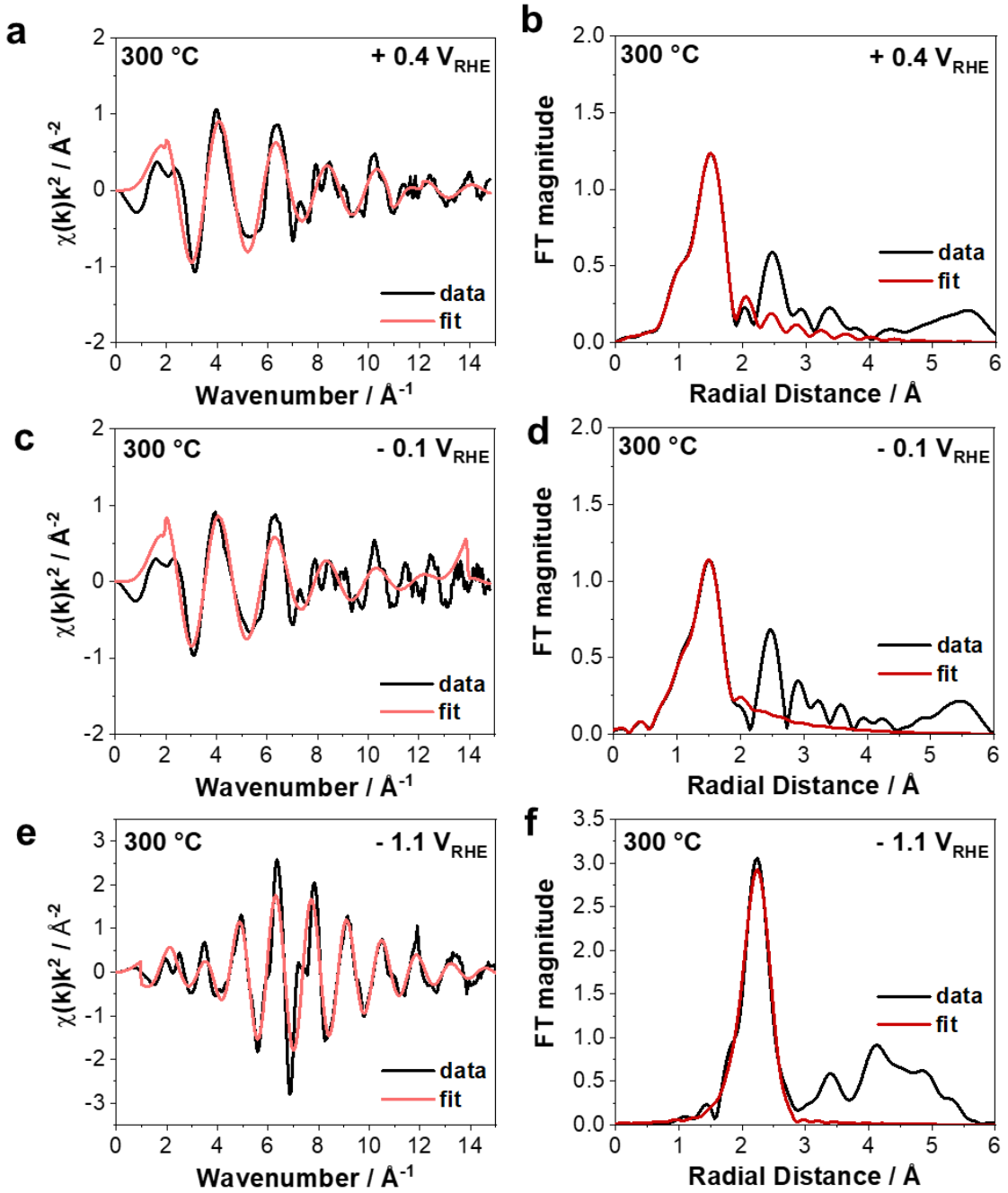

Figure S3.14. (left) k^2-weighted Cu K-edge EXAFS data in k-space and (right) the corresponding Fourier-transformed EXAFS data for the Cu_xO foam annealed in air at 300 °C at + 0.4 V_{RHE} (a, b) and – 0.1 V_{RHE} (c, d) and – 1.1 V_{RHE} (e, f). At potentials from + 0.4 V_{RHE} to – 0.3 V_{RHE} the data was fitted between 1 and 2 Å. From – 0.4 V_{RHE} the fitting range was extended to 3 Å to allow fitting of the metallic Cu. Reprinted from Blaseio et al.[258]

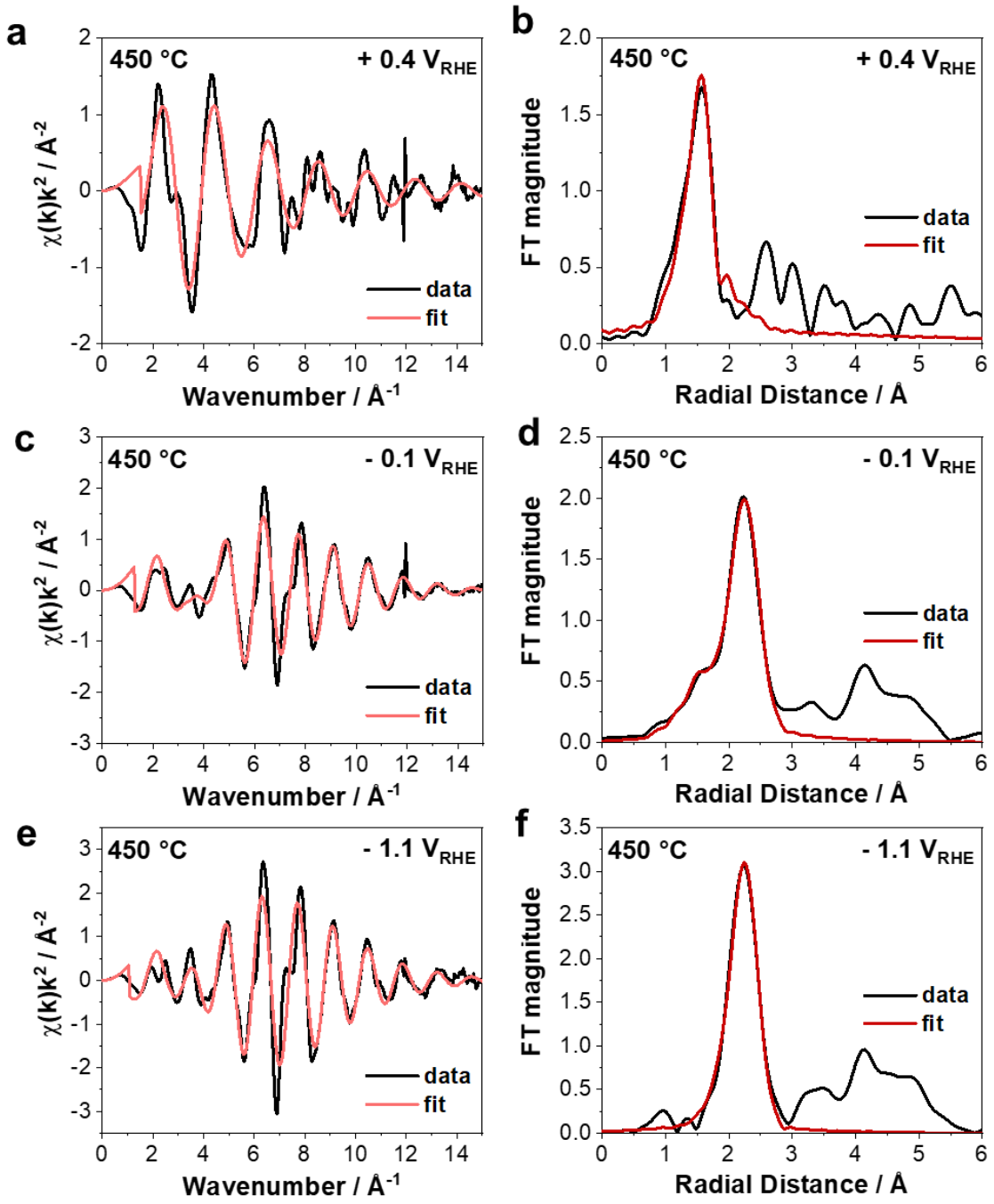

Figure S3.15. (left) k^2-weighted Cu K-edge EXAFS data in k-space and (right) the corresponding Fourier-transformed EXAFS data for the Cu_xO foam annealed in air at 450 °C at + 0.4 V_{RHE} (a, b) and – 0.1 V_{RHE} (c, d) and – 1.1 V_{RHE} (e, f). At potentials from + 0.4 V_{RHE} to + 0.1 V_{RHE} the data was fitted between 1 and 2 Å. From – 0.1 V_{RHE} the fitting range was extended to 3 Å to allow fitting of the metallic Cu. Reprinted from Blaseio et al.[258]

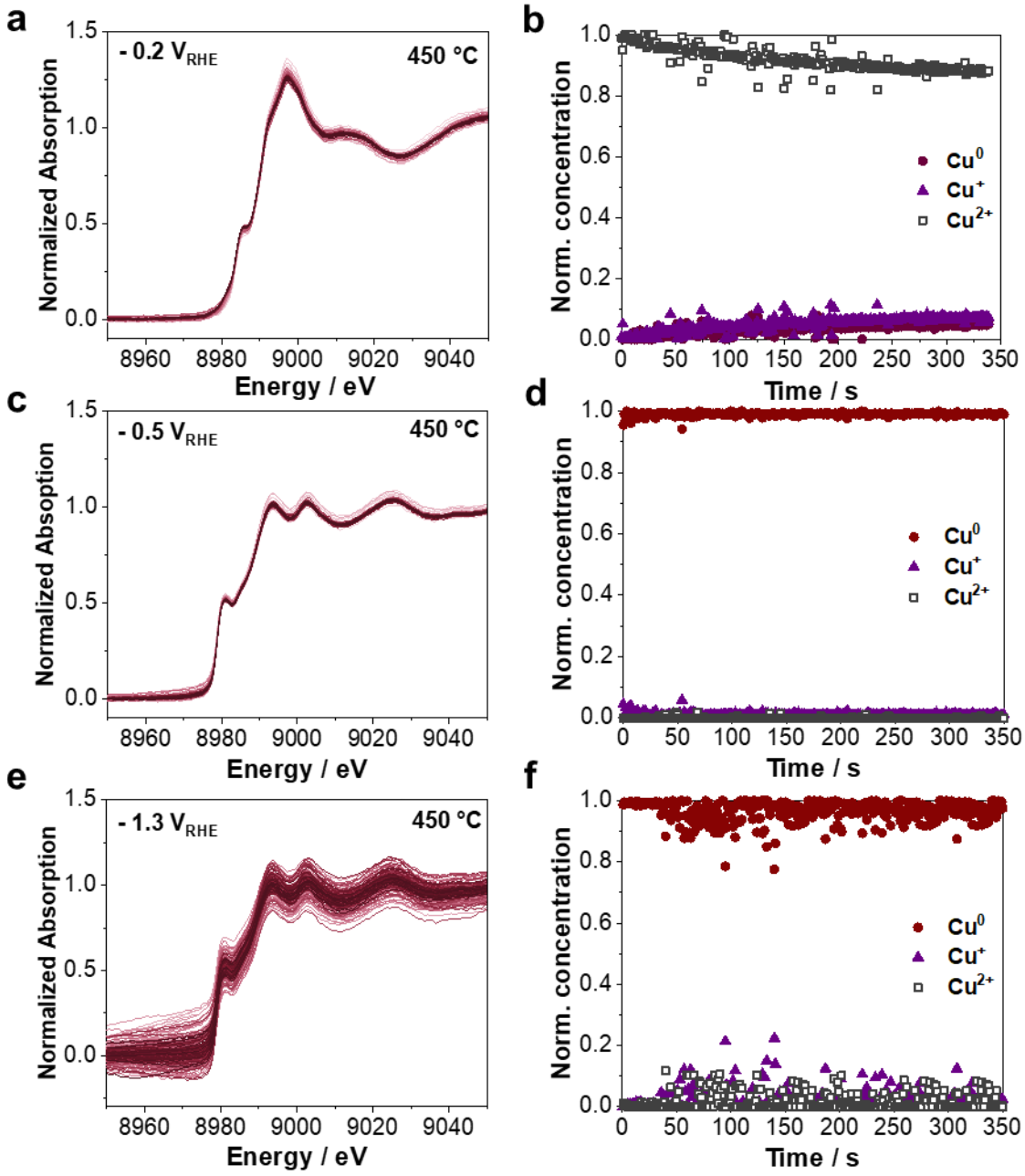

Figure S3.16. Potential step experiments (ΔE > 100 mV, see Fig. S7) of the Cu_xO foam annealed at 450 °C in air. Potentials were jumped from OCP → – 0.2 V_{RHE} → – 0.5 V_{RHE} → – 1.3 V_{RHE} in CO_2-saturated 0.5 M $KHCO_3$. (a, c, e) Cu K-edge Quick-XANES spectra collected at each potential step. One spectrum was collected every second. (b, d, f) Course of the time-resolved normalized concentration profiles of the three copper species (Cu^0, Cu^+ and Cu^{2+}) obtained from the MCR-ALS analysis. Note, the noise in the XAS spectra is caused by the strong bubble formation especially at – 1.3 V_{RHE}, which makes it difficult to normalize the data in a proper way. Reprinted from Blaseio et al.[258]

Table S3.3. EXAFS fit results for Cu_xO foam annealed at 100 °C for 12 h in air including first nearest neighboring coordination shell (N), atomic distance (R), mean squared bond length disorder (σ^2), shift of energy (ΔE_0) at the corresponding edge and R_f - factor (closeness of the fit as quality parameter) as a function of the applied potential during the potential increment experiment (ΔE = 100 mV) in CO_2-saturated 0.5 M $KHCO_3$. The corresponding EXAFS data are shown in **Figure S3.11** and **Figure S3.12**. For all fits the amplitude factor S_0^2 was 0.89.

E / V_{RHE}	**pair**	**N**	**R / Å**	**σ^2 / $*10^{-4}$ Å^2**	**ΔE_0 / eV**	**R_f**
OCP	O-Cu	2.0 ± 0.3	1.862 ± 0.018	36 ± 28	9.0 ± 2.2	0.009
+ 0.4	O-Cu	1.5 ± 0.4	1.843 ± 0.001	21 ± 37	6.4 ± 3.2	0.002
+ 0.3	O-Cu	1.9 ± 0.2	1.860 ± 0.016	44 ± 11	7.5 ± 1.1	0.010
+ 0.2	O-Cu	2.0 ± 0.3	1.860 ± 0.017	52 ± 16	6.7 ± 1.4	0.011
+ 0.1	O-Cu	1.8 ± 0.3	1.862 ± 0.018	32 ± 17	4.6 ± 1.9	0.005
– 0.1	O-Cu	1.9 ± 0.3	1.867 ± 0.023	38 ± 20	4.8 ± 2.0	0.011
– 0.2	O-Cu	1.7 ± 0.3	1.860 ± 0.016	33 ± 18	4.9 ± 2.1	0.011
– 0.3	O-Cu	1.3 ± 0.2	1.850 ± 0.006	11 ± 18	6.0 ± 2.4	0.012
– 0.4	O-Cu	1.4 ± 0.2	1.852 ± 0.008	15 ± 14	6.2 ± 1.9	0.011
– 0.5	O-Cu	1.3 ± 0.2	1.861± 0.017	13 ± 19	8.7 ± 2.2	0.015
– 0.6	O-Cu	1.0 ± 0.3	1.866 ± 0.018	33 ± 41	8.6 ± 1.8	0.008
	Cu-Cu	3.6 ± 0.9	2.569 ± 0.081	88 ± 19		
– 0.7	O-Cu	0.3 ± 0.1	1.842 ± 0.015	29 ± 20	6.5 ± 1.3	0.018
	Cu-Cu	7.1 ± 0.8	2.560 ± 0.008	96 ± 10		
– 0.8	O-Cu	0.1 ± 0.1	1.843 ± 0.023	75 ± 53	3.9 ± 0.7	0.006
	Cu-Cu	9.6 ± 0.6	2.541 ± 0.005	91 ± 6		
– 1.0	Cu-Cu	9.9 ± 0.5	2.539 ± 0.003	92 ± 4	3.8 ± 0.6	0.004
– 1.1	Cu-Cu	10.0 ± 0.5	2.545 ± 0.003	91 ± 4	4.4 ± 0.5	0.004
– 1.2	Cu-Cu	10.4 ± 0.5	2.540 ± 0.003	95 ± 4	4.9 ± 0.5	0.003

Table S3.4. EXAFS fit results for Cu_xO foam annealed at 200 °C for 12 h in air including first nearest neighboring coordination shell (N), atomic distance (R), mean squared bond length disorder (σ^2), shift of energy (ΔE_0) at the corresponding edge and R_f - factor (closeness of the fit as quality parameter) as a function of the applied potential during the potential increment experiment (ΔE = 100 mV) in CO_2-saturated 0.5 M $KHCO_3$. The corresponding EXAFS data are shown in **Figure S3.11** and **Figure S3.13**. For all fits the amplitude factor S_0^2 was 0.89.

E / V_{RHE}	**pair**	**N**	**R / Å**	**σ^2 / $*10^{-4}$ Å²**	**ΔE_0 / eV**	**R_f**
OCP	O-Cu	2.1 ± 0.3	1.869 ± 0.025	43 ± 15	4.8 ± 1.6	0.009
+ 0.4	O-Cu	2.8 ± 0.4	1.872 ± 0.027	56 ± 18	5.2 ± 1.6	0.008
+ 0.3	O-Cu	2.2 ± 0.4	1.869 ± 0.025	52 ± 23	3.9 ± 2.1	0.011
+ 0.2	O-Cu	2.1 ± 0.6	1.869 ± 0.025	53 ± 41	3.9 ± 3.3	0.011
+ 0.1	O-Cu	2.1 ± 0.3	1.869 ± 0.025	52 ± 16	4.0 ± 1.6	0.006
0.0	O-Cu	2.1 ± 0.4	1.873 ± 0.029	55 ± 31	4.5 ± 2.7	0.008
– 0.1	O-Cu	2.0 ± 0.2	1.865 ± 0.021	58 ± 18	3.5 ± 1.6	0.002
– 0.2	O-Cu	1.7 ± 0.4	1.884 ± 0.040	45 ± 36	8.0 ± 2.4	0.032
	Cu-Cu	2.4 ± 1.0	2.562 ± 0.005	90 ± 37		
– 0.3	O-Cu	1.5 ± 0.3	1.873 ± 0.029	29 ± 29	6.8 ± 2.0	0.007
	Cu-Cu	3.0 ± 1.0	2.555 ± 0.005	88 ± 31		
– 0.4	O-Cu	1.2 ± 0.8	1.895 ± 0.051	51 ± 43	7.4 ± 3.4	0.042
	Cu-Cu	3.4 ± 1.5	2.585 ± 0.034	68 ± 39		
– 0.5	O-Cu	1.4 ± 0.6	1.888 ± 0.044	73 ± 65	8.7 ± 1.8	0.019
	Cu-Cu	5.6 ± 1.0	2.576 ± 0.025	99 ± 17		
– 0.6	O-Cu	0.6 ± 0.3	1.872 ± 0.006	44 ± 76	5.5 ± 1.0	0.005
	Cu-Cu	8.1 ± 0.8	2.545 ± 0.029	94 ± 8		
– 0.7	Cu-Cu	10.5 ± 1.1	2.552 ± 0.007	95 ± 9	4.7 ± 1.2	0.012
– 0.8	Cu-Cu	10.0 ± 0.5	2.543 ± 0.003	85 ± 4	4.3 ± 0.6	0.003
– 0.9	Cu-Cu	10.4 ± 0.4	2.546 ± 0.002	90 ± 3	4.4 ± 0.4	0.001
– 1.0	Cu-Cu	10.9 ± 0.7	2.553 ± 0.004	94 ± 5	5.2 ± 0.7	0.004
– 1.1	Cu-Cu	10.4 ± 0.5	2.545 ± 0.004	90 ± 4	4.3 ± 0.6	0.003
– 1.2	Cu-Cu	10.1 ± 0.7	2.544 ± 0.005	88 ± 6	4.2 ± 0.7	0.004

Table S3.5. EXAFS fit results for Cu_xO foam annealed at 300 °C for 12 h in air including first nearest neighboring coordination shell (N), atomic distance (R), mean squared bond length disorder (σ^2), shift of energy (ΔE_0) at the corresponding edge and R_f - factor (closeness of the fit as quality parameter) as a function of the applied potential during the potential increment experiment (ΔE = 100 mV) in CO_2-saturated 0.5 M $KHCO_3$. The corresponding EXAFS data are shown in **Figure S3.11** and **Figure S3.14**. For all fits the amplitude factor S_0^2 was 0.89.

E / V_{RHE}	**pair**	**N**	**R / Å**	**σ^2 / *10^{-4} Å^2**	**ΔE_0 / eV**	**R_f**
OCP	O-Cu	2.8 ± 0.4	1.926 ± 0.021	46 ± 17	1.1 ± 1.9	0.004
+ 0.4	O-Cu	3.2 ± 0.4	1.938 ± 0.009	34 ± 14	1.9 ± 1.6	0.003
+ 0.3	O-Cu	2.9 ± 0.3	1.947 ± 0.007	27 ± 15	0.3 ± 1.3	0.007
+ 0.2	O-Cu	3.2 ± 0.3	1.939 ± 0.009	42 ± 10	2.0 ± 1.3	0.004
+ 0.1	O-Cu	3.3 ± 0.3	1.941 ± 0.007	46 ± 10	2.4 ± 1.3	0.004
0.0	O-Cu	3.3 ± 0.3	1.937 ± 0.011	41 ± 11	2.4 ± 1.1	0.003
– 0.1	O-Cu	3.2 ± 0.2	1.940 ± 0.008	46 ± 10	2.2 ± 0.9	0.002
– 0.2	O-Cu	2.9 ± 0.2	1.933 ± 0.015	39 ± 10	2.0 ± 1.0	0.004
– 0.3	O-Cu	2.9 ± 0.4	1.948 ± 0.001	48 ± 19	0.7 ± 1.7	0.004
– 0.4	O-Cu	1.8 ± 0.7	1.920 ± 0.027	42 ± 53	8.1 ± 2.7	0.023
	Cu-Cu	4.4 ± 3.4	2.553 ± 0.002	72 ± 32		
– 0.5	O-Cu	2.2 ± 0.4	1.948 ± 0.010	56 ± 19	9.0 ± 1.3	0.005
	Cu-Cu	3.7 ± 0.5	2.556 ± 0.007	79 ± 10		
– 0.6	Cu-Cu	9.3 ± 0.7	2.556 ± 0.005	89 ± 6	4.0 ± 0.8	0.009
– 0.7	Cu-Cu	9.4 ± 0.5	2.539 ± 0.004	87 ± 4	4.1 ± 0.6	0.006
– 0.8	Cu-Cu	9.7 ± 0.3	2.542 ± 0.002	86 ± 3	4.2 ± 0.4	0.002
– 0.9	Cu-Cu	11.2 ±0.3	2.544 ± 0.002	85 ± 3	4.2 ± 0.3	0.002
– 1.0	Cu-Cu	9.7 ± 1.0	2.544 ± 0.007	84 ± 9	4.4 ± 1.2	0.017
– 1.1	Cu-Cu	8.9 ± 0.7	2.556 ± 0.005	81 ± 6	3.7 ± 0.9	0.012
– 1.2	Cu-Cu	9.3 ± 3.3	2.556 ± 0.023	86 ± 30	4.8 ± 3.8	0.019

Table S3.6. EXAFS fit results for Cu_xO foam annealed at 450 °C for 12 h in air including first nearest neighboring coordination shell (N), atomic distance (R), mean squared bond length disorder (σ^2), shift of energy (ΔE_0) at the corresponding edge and R_f - factor (closeness of the fit as quality parameter) as a function of the applied potential during the potential increment experiment (ΔE = 100 mV) in CO_2-saturated 0.5 M $KHCO_3$. The corresponding EXAFS data are shown in **Figure S3.11** and **Figure S3.15**. For all fits the amplitude factor S_0^2 was 0.89.

E / V_{RHE}	**pair**	**N**	**R / Å**	**σ^2 / *10^{-4} Å^2**	**ΔE_0 / eV**	**R_f**
OCP	O-Cu	3.3 ± 0.4	1.937 ± 0.010	33 ± 15	8.2 ± 0.4	0.009
+ 0.4	O-Cu	3.3 ± 0.3	1.937 ± 0.011	34 ± 14	8.8 ± 1.3	0.010
+ 0.3	O-Cu	3.3 ± 0.4	1.937 ± 0.011	35 ± 14	8.7 ± 1.3	0.014
+ 0.2	O-Cu	3.1 ± 0.5	1.940 ± 0.007	31 ± 18	9.7 ± 1.8	0.016
+ 0.1	O-Cu	3.1 ± 0.3	1.943 ± 0.004	39 ± 16	10.3 ± 1.5	0.008
– 0.1	O-Cu	1.6 ± 0.6	1.914 ± 0.020	91 ± 55	6.0 ± 1.1	0.008
	Cu-Cu	6.9 ± 0.6	2.548 ± 0.006	88 ± 7		
– 0.3	Cu-Cu	9.8 ± 0.4	2.540 ± 0.003	86 ± 4	4.5 ± 0.5	0.003
– 0.4	Cu-Cu	10.1 ± 0.4	2.542 ± 0.003	89 ± 3	4.6 ± 0.4	0.003
– 0.5	Cu-Cu	10.1 ± 0.4	2.542 ± 0.003	89 ± 3	4.7 ± 0.5	0.003
– 0.8	Cu-Cu	10.5 ± 1.7	2.553 ± 0.011	96 ± 14	5.9 ± 1.7	0.022
– 0.9	Cu-Cu	10.1 ± 1.0	2.543 ± 0.006	86 ± 8	4.7 ± 1.1	0.008
– 1.0	Cu-Cu	10.8 ± 0.9	2.537 ± 0.019	86 ± 7	3.9 ± 1.0	0.009
– 1.1	Cu-Cu	10.3 ± 0.6	2.542 ± 0.004	87 ± 5	4.3 ± 0.7	0.007

11. Hazardous Materials

Chemical	CAS-No.	Pictograms	H statements	P statements
2-Propanol	67-63-0		H225, H319, H336	P210, P233, P305+P351+P338
Acetone	67-64-1		H225, H319, H336	P210, P233, P240, P241, P242, P305+P351+P338
Chloroplatinic acid hexahydrate ($H_2PtCl_6x6H_2O$)	18497-13-7		H301, H314, H317, H334	P260, P272, P280, P303+P361+P353, P304+P340+P310, P305+P351+P338
Copper(II) sulfate hydrate ($CuSO_4x5H_2O$	23254-43-5		H302, H318, H410	P264, P273, P280, P301+P312, P305+P351+P338, P391
Colloidal gold paste	108-88-3 141-78-6 64-17-5 107-98-2 7440-57-5		H225, H361d, H304, H315, H373, H319	P201, P202, P210, P240, P241, P242, P243, P260, P261, P264, P271, P280, P312, P314, P321, P331, P362, P301+P310, P302+P352, P303+P361+P353, P304+P340, P308+P313, P332+P313, P370+P378, P405, P403+P233, P403+P235, P501
Iridium(III) chloride hydrate ($IrCl_3xnH_2O$)	14996-61-3		H319	P305+P351+P338
Perchloric acid ($HClO_4$)	7601-90-3		H271, H290, H302, H314, H373	P210, P280, P301+P312, P303+P361+P353, P305+P351+P338
Platinum nanoparticles on Carbon (Pt/C)	7440-06-4 1333-86-4		H228, H315, H317, H319, H334, H335, H351, H372	P201, P202, P210, P240, P241, P260, P264, P270, P271, P272, P280, P284, P302+P352, P304+P340,

				P305+ P351+P338, P308+P313, P314, P332+P313, P337+P313, P342+P313, P362+P364, P370+P378, P304+P233, P405, P501
Sodium Hydroxide (NaOH)	1310-73-2		H290, H314, H318	P234, P260, P280, P303+P361+P353, P304+P340+P310, P305+P351+P338
Sulfuric acid (H_2SO_4)	7664-93-9		H290, H314, H318	P234, P280, P303+P361+P353, P304+P340+P310, P305+P351+P338

11.1. Hazardous Statements

H225	Highly flammable liquid and vapour.
H228	Flammable solid.
H271	May cause fire or explosion; strong oxidizer.
H290	May be corrosive to metals.
H301	Toxic if swallowed.
H302	Harmful if swallowed.
H304	May be fatal if swallowed and enters airways.
H314	Causes Severe skin burns and eye damage.
H315	Causes Skin irritation.
H317	May cause an allergic skin reaction.
H318	Causes serious eye damage.
H319	Causes serious eye irritation.
H334	May cause allergy or asthma symptoms or breathing difficulties if inhaled.
H335	May cause respiratory irritation.
H336	May cause drowsiness or dizziness.
H351	Suspected of causing cancer.
H361d	Suspected of damaging the unborn child.
H372	Causes Damage to organs (respiratory system) through prolonged or repeated exposure.
H373	May cause damage to organs (Thyroid) through prolonged or repeated exposure.
H410	Very toxic to aquatic life with long lasting effects.

11.2. Precautionary Statements

P201	Obtain special instructions before use.
P202	Do not handle until all safety precautions have been read and understood.
P210	Keep away from heat, hot surfaces, sparks, open flames and other ignition sources. No smoking.
P233	Keep container tightly closed.
P234	Keep only in original packaging.
P240	Ground/bond container and receiving equipment.
P241	Use explosion-proof electric/ventilating/lightning/equipment.
P242	Use only non-sparking tools.
P243	Take precautionary measures against static discharge.
P260	Do not breathe dust.
P261	Avoid breathing dust/fume/gas/mist/vapors/spray.
P264	Wash skin thoroughly after handling.
P270	Do not eat drink or smoke when using this product.
P271	Use only outdoors or in a well-ventilated area.
P272	Contaminated work clothing should not be allowed out of the workplace.
P273	Avoid release to the environment.
P280	Wear protective gloves/ protective clothing/ eye protection/ face protection.
P284	[In case of inadequate ventilation] wear respiratory protection.
P301+P310	IF SWALLOWED: Immediately call a POISON CENTER/doctor/…
P301 + P312	If swallowed: Call a poison center / doctor if you feel unwell.
P302 + P352	If on skin: Wash with plenty of water.
P303 + P361 + P353	If on skin (or hair): Take off immediately all contaminated clothing. Rinse skin with water.
P304 + P340 + P310	If inhaled: Remove person to fresh air and keep comfortable for breathing. Immediately call a POISON CENTER/ doctor.
P305 + P351 + P338	If in eyes: Rinse cautiously with water for several minutes. Remove contact lenses, if present and easy to do. Continue rinsing.
P308 + P313	If exposed or concerned: Get medical advice/attention.
P312	Call a POISON CENTER/doctor/…/if you feel unwell.
P314	Get medical advice / attention if you feel unwell.
P321	Specific treatment (see … on this label).
P331	Do NOT induce vomiting.
P332 + P313	If skin irritation occurs: Get medical advice/attention.
P333 + P313	If skin irritation or rash occurs: Get medical advice/attention.
P337 + P313	If eye irritation persists: Get medical advice/attention.

P342 + P313	If experiencing respiratory symptoms: Call a poison center/doctor.
P362 + P364	Take off contaminated clothing and wash before reuse.
P362	Take off contaminated clothing.
P370 + P378	In case of fire: Use carbon dioxide (for initial stage of fire only), water spray of fog, dry chemical powder, foam fire system to extinguish.
P391	Collect spillage.
P403 + P233	Store in a well-ventilated place. Keep container tightly closed.
P403+P235	Store in a well-ventilated place. Keep cool.
P405	Store locked up.
P501	Dispose of contents/container in accordance with related laws and local/regional regulations.

12. Acknowledgements

First, I would like to express my sincere appreciation to Prof. Dr. Mehtap Oezaslan for the opportunity to complete my PhD thesis in her group. Thank you for giving me the chance to delve into the field of operando/in-situ electrocatalysis, that was completely unfamiliar to me at the start of my PhD. Your mentoring, support and discussions have enriched my PhD thesis at every stage. I am deeply grateful to you, for all the opportunities you have given me.

I would like to extend my sincere thanks to Prof. Dr. Katsuyoshi Kakinuma. I very much appreciate your effort in reviewing this thesis.

My sincerest gratitude goes to all my colleagues in the Technical Electrocatalysis group for their contributions to my research work, their endless support, their ideas and the many fruitful discussions in the PVZ office. I will always remember our incredible trips to Hawaii and Tokyo as well as the cycling tours into the Elm and Harz. Especially, I would like to thank Jochen Klein for managing countless beamtimes across Europe with me. It was a pleasure to work with you throughout the last 4 years, and I have many great memories. Furthermore, I would like to extend my thanks to Marek Janssen, Christian Schneeman and Giulia Ioselli – you have always encouraged me, motivated me and helped me with my endless questions about electrochemistry.

My deepest appreciation also goes to my parents, Susann and Bernd and my sister, Lydia. Even though you hardly understood what I did during my PhD and in my studies, you were always extremely supportive, excited to read my publications and believed in me every step of the way.

Lastly, words cannot express my gratitude to my boyfriend Tammo. You have been my rock throughout the last years. You always listened calmly to my complaints and cheered me up when I was shattered and wanted to give up. Our conversations kept me motivated and your optimism and positivity are endless. You always gave me strength and helped me through setbacks, calmed me when everything was overwhelming and taught me to focus on the important things in life when it was tough for me. Without your invaluable engineering and programming expertise parts of this thesis would not have been possible. Thank you for everything, I am looking forward to our next chapters!

13. Declaration on oath

I hereby declare and affirm that this doctoral dissertation is my own work and that I have not used any aids and sources other than those indicated. If electronic resources based on generative artificial intelligence (gAI) were used in the course of writing this dissertation, I confirm that my own work was the main and value-adding contribution and that complete documentation of all resources used is available in accordance with good scientific practice. I am responsible for any erroneous or distorted content, incorrect references, violations of data protection and copyright law or plagiarism that may have been generated by the gAI.

Hiermit versichere ich an Eides statt, die vorliegende Dissertationsschrift selbst verfasst und keine anderen als die angegebenen Quellen und Hilfsmittel benutzt zu haben. Sofern im Zuge der Erstellung der vorliegenden Dissertationsschrift generative Künstliche Intelligenz (gKI) basierte elektronische Hilfsmittel verwendet wurden, versichere ich, dass meine eigene Leistung im Vordergrund stand und dass eine vollständige Dokumentation aller verwendeten Hilfsmittel gemäß der Guten wissenschaftlichen Praxis vorliegt. Ich trage die Verantwortung für eventuell durch die gKI generierte fehlerhafte oder verzerrte Inhalte, fehlerhafte Referenzen, Verstöße gegen das Datenschutz- und Urheberrecht oder Plagiate.

26.05.2025 Sonja Blascio

Date, Signature